ISSN 1173-5996

2-D Analysis of Composite Steel - Concrete Beams in Fire

by
Richard Welsh

Supervised by
Associate Professor Andrew Buchanan
and
Associate Professor Peter Moss

Fire Engineering Research Report 01/8
March 2001

This report was presented as a project report as part of the
M.E. (Fire) degree at the University of Canterbury

School of Engineering
University of Canterbury
Private Bag 4800
Christchurch, New Zealand

Phone 643 364-2250
Fax 643 364-2758
www.civil.canterbury.ac.nz

ABSTRACT

This report investigates the behaviour of composite steel – concrete beams at elevated temperatures using the finite element program SAFIR. The finite element analysis carried out in this report is two dimensional and investigates the effects of an envelope of support conditions under varying thermal exposure.

Composite steel – concrete construction is a common and popular form of construction used around the world. It is well understood that this form of construction has good inherent fire resistance. At this stage, it is not well understood how the fire resistance mechanisms work and how changes in material properties influence the behaviour of the composite beam. It is the intention of this report to provide some detail on single span, two dimensional, beam behaviour in relation to material properties, support conditions and thermal exposure.

The analysis of this report was conducted using SAFIR, a non-linear finite element program developed at the University of Liege, Belgium. A 610 UB 101 steel beam with a 120mm thick composite concrete floor slab is exposed to three sided heating to simulate the effects of a compartment fire. The composite beams with moment and axial restraint perform poorly in comparison to beams with only moment restraint, axial restraint or no restraint in linear heating rates. In the ISO 834 fire, the beams with axial restraint performed poorly in comparison to those *without* axial restraint due to the high axial forces experienced because of thermal elongation. The axially restrained – moment resisting case performed poorly in both scenarios due to high compression stresses in the steel section caused by thermal bowing and thermal elongation.

It was also found that when the EC3 Proportional and EC3 Yield Limit stresses were reached in the steel section, that displacements, axial force and bending moments along the section were affected.

ACKNOWLEDGEMENTS

I would like to thank the following people who have helped me with my project:

- Associate Professor Andrew Buchanan for supervising my project and always being available to offer invaluable assistance and guidance.

- Associate Professor Peter Moss for being the associate supervisor for my report and providing me with invaluable assistance in finite element modelling, structural theory and especially with methodically proof reading this report.

- The New Zealand Fire Service for their financial assistance in providing me with a scholarship.

- The members of the *SAFIR* club, Bevan Jones, Jenny Sepultro, Linus Lim, for their ideas and help, as well as providing me with company in the wee small hours of the morning.

- And finally, to my parents and family for their unwavering support and guidance over the years. Without their help this would not have been possible.

TABLE OF CONTENTS

LIST OF FIGURES

LIST OF TABLES

NOMENCLATURE

Latin Symbols

Symbol	Description	Units
a_c	depth to plastic neutral axis	mm^2
A_g	gross area of cross section	mm^2
A_t	total area of internal compartment surfaces	m^2
A_v	area of openings	m^2
b_{ec}	effective slab width	mm
c_p	specific heat	J/kgK
e'	eccentricity	mm
e_f	fuel load	MJ/m^2
E_c	elastic modulus of concrete	GPa
E_s	elastic modulus of steel	GPa
f'_c	compressive strength of concrete	MPa
f_y	yield strength of steel	MPa
f_r	tensile strength of concrete	MPa
G	nominal dead load	kN/m
H_v	height of windows	m
I	moments of inertia	mm^4
k	relative stiffness of the spring compared to that of the beam	
K	stiffness of the member	N/m
k_c	parameter to account for compartment linings	
k_θ	characteristic strength reduction factor	
l	effective length of member	m
L	span of member length	m
M*	applied moments	kNm
M_n	nominal moment capacity	kNm
n	steel/concrete stiffness ratio	
P	axial force	kN
P_{cr}	buckling load	kN

Q	live load	kN/m
t	time	sec
T	temperature	^{o}C
t_d	bottom slab depth	mm
t_e	time equivalent exposure to the ISO 834 fire	min
t_t	top slab depth	mm
w_u	uniformly distributed load	kN/m
y	depth	mm
y'	elastic neutral axis	mm

Greek Symbols

Symbol	Description	Unit
α	thermal expansion coefficient	$^{o}C^{-1}$
δ	deflection	mm
ε	strain	
ϕ	curvature	m^{-1}
λ	thermal conductivity	W/mK
ν	Poisson's ratio	
θ	material temperature	^{o}C
ρ	density	kg/m^3
σ	stress	MPa
ψ_u	live load reduction factor	

1 INTRODUCTION

1.1 Composite Steel – Concrete Construction

The methods in the construction of steel and composite structures have significantly changed over the past ten years. Developments in composite floor systems and advances in fabrication technology have made steel framed buildings with composite floor construction extremely competitive. During this same period the development and application of fire engineering techniques has brought about a significant reduction in the cost of protecting steel frames. With these developments in fire engineering, sophisticated finite element programs have been developed to aid the design of structures at elevated temperatures.

It has been observed from real fire events and tests carried out that composite steel – concrete construction has good inherent fire resistance. Bailey et al (1999) states that there is a growing opinion that the structural contribution of modern composite floor systems is under-utilised when designing for the fire limit state. When designing structures for elevated temperatures it is pertinent that reliable and well documented practices be adhered to. For this reason these new finite element models must be able to predict behaviour observed in real fires to validate their usefulness.

In this project I have not only sought to analyse composite beam behaviour at elevated temperatures but also validate it with behaviour observed in real fire events. The ultimate goal is to provide some understanding into the behaviour of composite steel – concrete beams under varying thermal exposure with an envelop of support conditions so that in the future more rational design methodology for such structures is available.

1.2 Impetus for the research

Steel beams with composite concrete slabs are a popular method of construction around the world. It has been observed in many tests and real fire events that modern composite steel framed structures have good inherent fire resistance. If sufficient information can be gained about the inherent fire resistance of composite steel framed buildings then significant reductions in the costs

of protecting the steel frame can be made making this form of construction a much more viable option to the developer.

1.3 Objective of this research

- The first objective of this research is to investigate the behaviour of composite steel and concrete beams in fire using a two dimensional thermal and structural finite element model.

- The second objective of this research is to validate the predicted behaviour from the finite element analysis with behaviour observed in real fire events.

- The scope of this research covers the behaviour of:

1. Support conditions; a 610 UB 101 beam with a 120mm thick composite concrete slab is subjected to three linear heating rates with four different end support conditions and simulating until collapse. The end support conditions used were the *pin – pin* and *pin - roller* simply supported cases as well as the *fixed – fixed* and the *fixed – slide* moment resisting end supports.

2. Axial springs; this investigates the roll of axial restraint upon the simply supported composite section where the boundary support conditions are the *pin – roller* and *pin – pin* supports (zero axial restraint $\rightarrow \infty$).

3. ISO 834 fire; this investigates the influence of a more severe fire growth on the composite section utilising the initial four support conditions and simulating until collapse. The ISO 834 fire was selected because it is an internationally recognised standard fire growth model.

4. ISO 834 fire with cooling phase; this investigates the influence of a cooling phase introduced to the fire model prior to collapse of the composite beam. The beam was again analysed with the initial four support conditions.

The thermal and structural analysis in this project is conducted with a non-linear finite element code, SAFIR, developed by Jean-Marc Franssen at the University of Liege, Belgium.

1.4 Organisation of this report

This report consists of ten chapters. Chapter 2 provides a review of steel and concrete material properties at elevated temperatures. Chapter 3 provides a review of the composite beam layout and dicretisation of the cross section model. SAFIR, the finite element program used to model the composite section at elevated temperatures has also been discussed.

Chapter 4 discusses observed composite beam behaviour in real fires as well providing background into previous research conducted in this field. Chapter 5 reports the results of the observed composite beam behaviour with four support conditions in a linear heating rate fire growth. Chapter 6 reports the observed results of the composite beam behaviour with simply supported axial restraint in a linear heating rate fire growth.

Chapter 7 reports the results of the observed composite beam behaviour with four support conditions in an ISO 834 standard fire growth curve. Chapter 8 discusses the results of the observed composite beam behaviour with four support conditions in an ISO 834 standard fire growth curve with a cooling phase.

Chapter 9 discusses the problems that were encountered in the finite element modelling and describes solutions to these problems. Chapter 10 describes the conclusions and findings of this report and makes recommendations for future research.

2 PROPERTIES OF MATERIALS AT ELEVATED TEMPERATURES.

2.1 Introduction

This section describes the ambient and temperature dependent mechanical properties of the structural steel and siliceous concrete models used in the SAFIR analysis. SAFIR uses the Eurocode (EC2: 1993 and EC3: 1995) relationships to simulate the temperature dependent non-linear effects of the material.

2.2 Steel Mechanical Properties.

2.2.1 Introduction.

This section describes the ambient and temperature dependent mechanical properties of the structural steel model used in the SAFIR analysis. SAFIR uses the Eurocode (EC3: 1995) relationships to simulate the temperature dependent non-linear effects of the material. The constitutive laws and stress-strain relationships for the structural steel are defined in relation to temperature.

2.2.2 Ambient Properties.

The ambient properties of the steel model are tabulated below in Table 2.2.1. These values have been entered directly into the input data files for the SAFIR simulations.

Table 2.2.1 Ambient steel properties

Property	Nomenclature	Value	Unit
610 UB 101 Yield Strength	F_y	275	MPa
Reinforcing Mesh	F_y	430	MPa
Poisson's Ratio	ν	0.3	-
Elastic Modulus	E_{steel}	210	GPa
Density	ρ	7850	Kg/m^3

2.2.3 EC3 1995 Properties at Elevated Temperatures.

The Eurocode (EC3: 1995) specifies that for heating rates between 2 and 50°C/min, the strength and deformation properties of steel at elevated temperatures shall be obtained from the stress-strain relationship shown in Figure A.1, Appendix A.. This relationship should be used to determine resistance to tension, compression, moment or shear. Table A.1, Appendix A, gives the reduction factors, relative to the appropriate value at 20°C, for the stress-strain relationship for structural steel at elevated temperatures given in Figure A.1, Appendix A, as follows:

- effective yield strength, relative to yield strength at 20°C: $k_{y,\theta} = f_{y,\theta}/f_y$
- proportional limit, relative to yield strength at 20°C: $k_{p,\theta} = f_{p,\theta}/f_y$
- modulus of elasticity, relative to the elastic modulus at 20°C: $k_{E,\theta} = E_{a,\theta}/E_a$

The variation of these three reduction factors with temperature is illustrated in **Figure 2.2.1**. This model has been used for the 610 UB 101 steel beam SAFIR model.

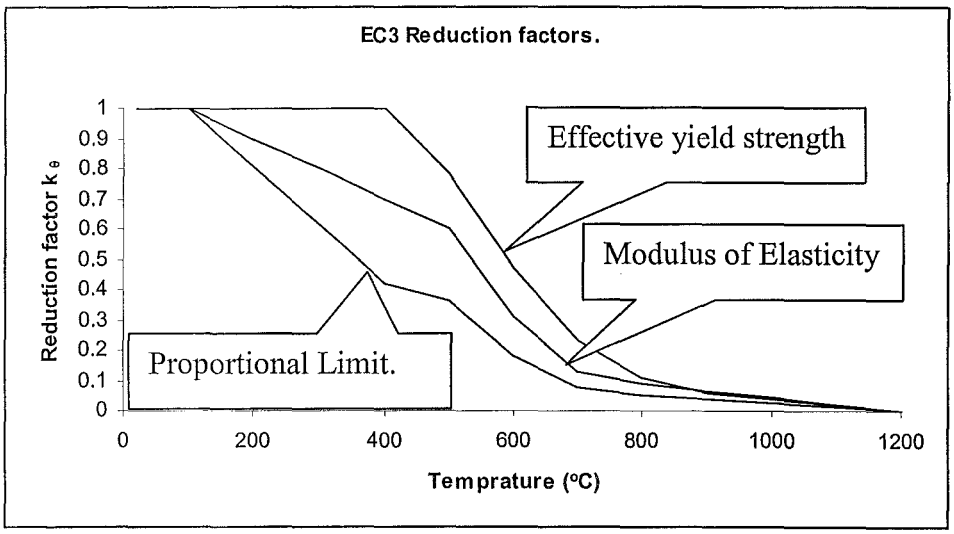

Figure 2.2.1 Reduction factors for the stress-strain relationship of steel at elevated temperatures (EC3: 1995).

2.3 Steel Thermal Properties.

2.3.1 Introduction

This section describes the thermal properties used by SAFIR from the Eurocode (EC3: 1995) for the structural steel model. These thermal properties are shown below.

2.3.2 Thermal Conductivity – λ.

The thermal conductivity is dependent on steel composition as well as the steel temperature. **Figure 2.3.1** shows that the EC3 steel model has a linear reduction in thermal conductivity from 54 W/mK at 20°C to 27.3 W/mK at 800°C. The equations for thermal conductivity from Eurocode (EC3: 1995) are shown below.

$\lambda = 54\text{-}3.33E\text{-}2*\theta_a$ (W/mK). for $20°C \leq \theta_a < 800°C$. [Equation 2.1]

$\lambda = 27.3$ (W/mK). for $800°C \leq \theta_a \leq 1200°C$. [Equation 2.2]

where θ_a is the material temperature.

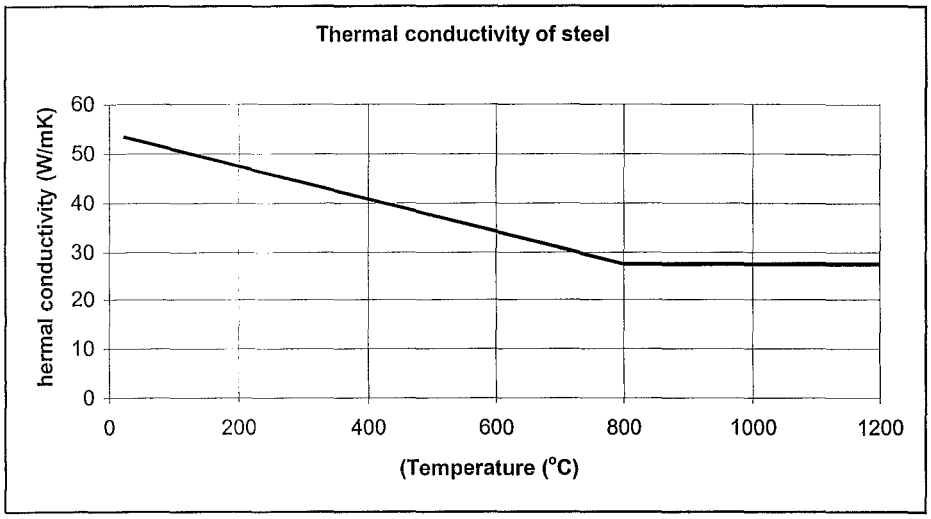

Figure 2.3.1 EC3 Thermal conductivity of steel as a function of temperature.

2.3.3 *Specific Heat c_s.*

Figure 2.3.2 shows that the specific heat of steel varies with temperature. The specific heat of steel is independent of steel composition. Specific heat is the ability of the steel to absorb heat. At 730°C there is a metallurgical change in the steel that causes a peak specific heat. The equations from the Eurocode (EC3: 1995) for the specific heat relationships are shown below.

c_s = 425+7.73E-1*θ_a – 1.69E-3*θ_a 2+2.22E-6*θ_a 3. for 20°C ≤ θ_a < 600°C. J/kgK [Equation 2.3]

c_s = 666+13002/(738-θ_a) for 600°C ≤ θ_a < 735°C. J/kgK [Equation 2.4]

c_s = 545+17820/(θ_a–731) for 735°C ≤ θ_a < 900°C. J/kgK [Equation 2.5]

c_s = 650 for 900°C < θ_a J/kgK [Equation 2.6]

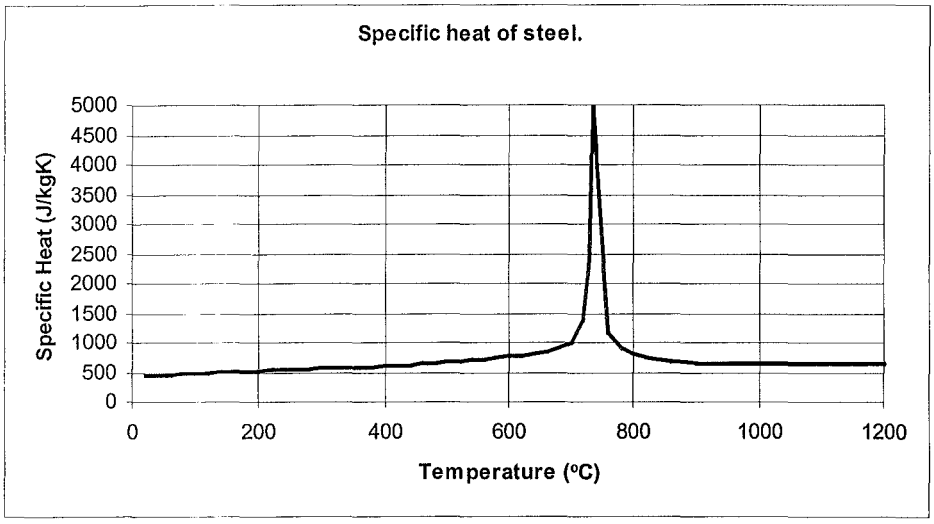

Figure 2.3.2 EC3 Specific heat of steel as a function of temperature

2.3.4 Thermal Elongation $\Delta l / l$.

The thermal elongation of steel, $\Delta l / l$, is determined from the following equations from the Eurocode (EC3: 1995). The discontinuity in the thermal elongation is due to a phase transformation that occurs in the steel in the temperature range between 750°C and 860°C as shown in Figure 2.3.3.

$\Delta l / l = 1.2E\text{-}5*\theta_a + 0.4E\text{-}8*\theta_a^2 - 2.416E\text{-}4$ For $20°C \leq \theta_a < 750°C$. [Equation 2.7]

$\Delta l / l = 1.1E\text{-}2.$ For $750°C \leq \theta_a < 860°C$. [Equation 2.8]

$\Delta l / l = 2E\text{-}5*\theta_a - 6.2E\text{-}3.$ For $860°C \leq \theta_a < 1200°C$. [Equation 2.9]

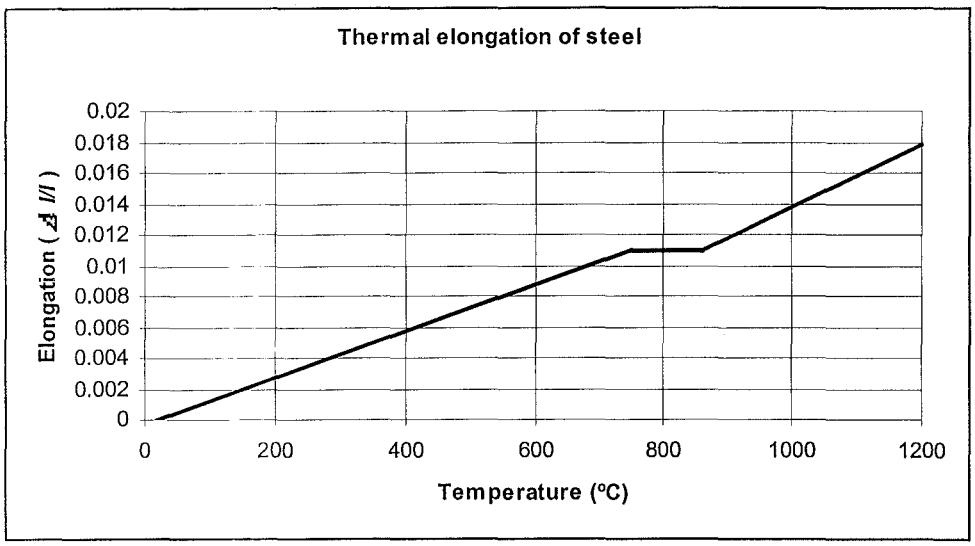

Figure 2.3.3 EC3 Thermal elongation of steel as a function of temperature.

2.4 Concrete Mechanical Properties.

2.4.1 Introduction.

This section describes the ambient and temperature dependent mechanical properties of the siliceous aggregate concrete and reinforcing steel model used in the SAFIR analysis. The SAFIR code mechanical concrete properties are based on the Eurocode (EC2: 1993) relationships.

2.4.2 Ambient properties.

Table 2.4.1 shows the ambient properties of the siliceous concrete model. These values have been entered directly into the input data files for the SAFIR simulations.

Table 2.4.1 Ambient concrete properties.

Property	Nomenclature	Value	Unit
Concrete			
Concrete crushing strength	f'_c	25	MPa
Concrete tensile strength	f_t	0.5	MPa
Elastic Modulus	E_{conc}	23.5	GPa
Density	ρ	2300	kg/m^3
Reinforcing Steel			
Reinforcing Mesh	f_y	430	MPa
Elastic Modulus	E_{steel}	210	GPa
Poisson's Ratio	ν	0.3	-
Density	ρ	7850	kg/m^3

2.4.3 EC2 1993 Properties at Elevated Temperatures.

Values for the temperature dependant reduction of the characteristic compressive strength of concrete, and of the characteristic strength of hot rolled reinforcing steel are given in this section.

The Eurocode (EC2: 1993) specifies that the following temperature dependent material properties are only relevant between 20°C and 1200°C.

Concrete.

The stress-strain relationship for siliceous aggregate concrete at elevated temperatures is illustrated in Figure A.2 and Table A.2 in Appendix A. The reduction of the characteristic compressive strength of concrete as a function of the temperature θ is allowed for by the coefficient $k_c(\theta)$ for which:

$$f'_{ck}(\theta) = k_c(\theta) f'_c(20^oC) \qquad \text{[Equation 2.10].}$$

Where: $k_c(\theta) = 1.0$ for $20^oC \leq \theta \leq 100^oC$.

$k_c(\theta) = (1600-\theta)/1500$ for $100^oC \leq \theta \leq 400^oC$.

$k_c(\theta) = (900-\theta)/625$ for $400^oC \leq \theta \leq 900^oC$.

$k_c(\theta) = 0$ for $900^oC \leq \theta \leq 1200^oC$.

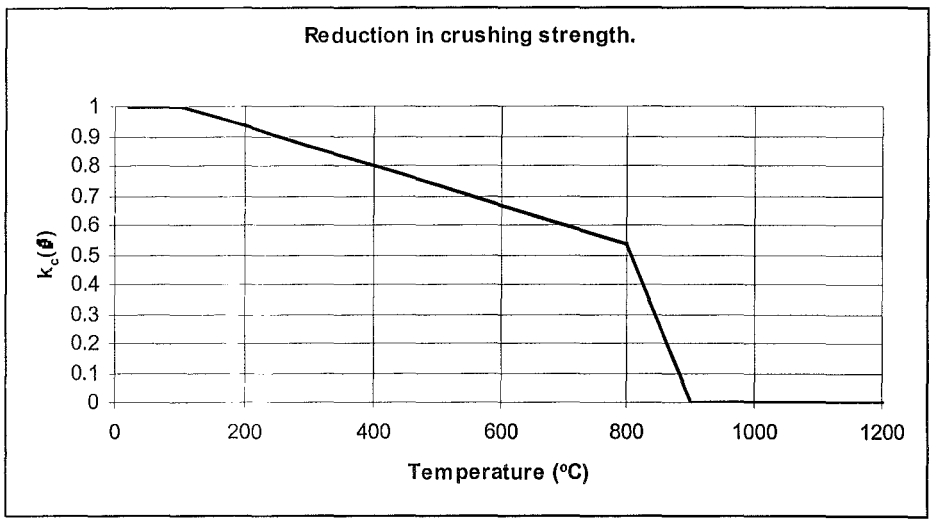

Figure 2.4.1 Coefficient $k_c(\theta)$ allowing for decrease of compressive strength (f_{ck}) (EC2: 1993).

The reduction of the characteristic tensile strength of concrete as a function of the temperature θ is allowed for by the coefficient $k_{ct}(\theta)$ for which:

$$f'_{ct}(\theta) = k_{ct}(\theta) f_r(20^oC) \qquad \text{[Equation 2.11].}$$

where: $k_{ct}(\theta) = 1.0$ for $20^oC \leq \theta \leq 100^oC$.

$k_c(\theta) = (600-\theta)/500$ for $100^oC \leq \theta \leq 600^oC$.

$k_c(\theta) = 0$ for $600^oC \leq \theta \leq 1200^oC$.

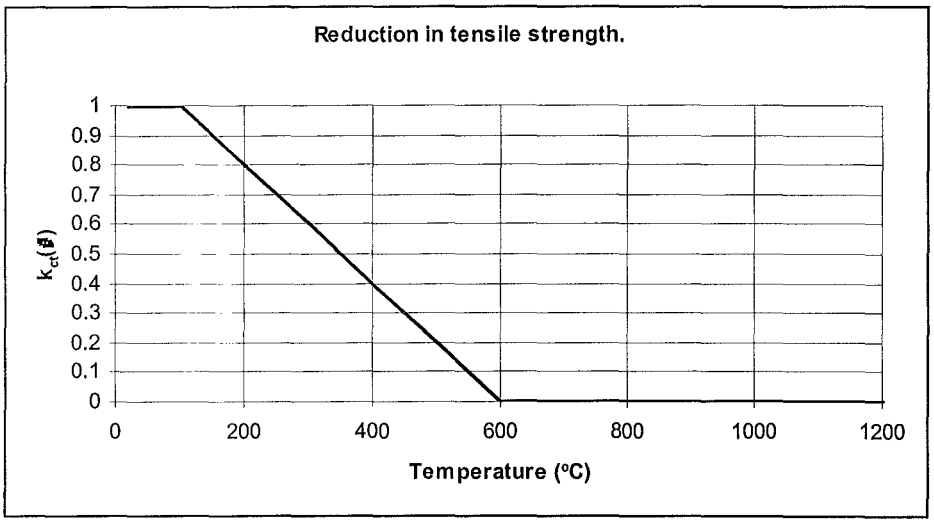

Figure 2.4.2 Coefficient $k_{ct}(\theta)$ allowing for decrease of tensile strength (f_{ct}) (EC2: 1993).

Reinforcing steel.

The stress-strain relationship for hot rolled reinforcing steel at elevated temperatures is illustrated in Figure A.3 and Table A.3 in Appendix A. For a given steel temperature, the stress-strain curves are defined by three parameters:

- the slope of the linear elastic range $E_s(\theta)$ for reinforcing steel,
- the proportional limit $\sigma_{spr}(\theta)$ and
- the maximum stress level $f_y(\theta)$.

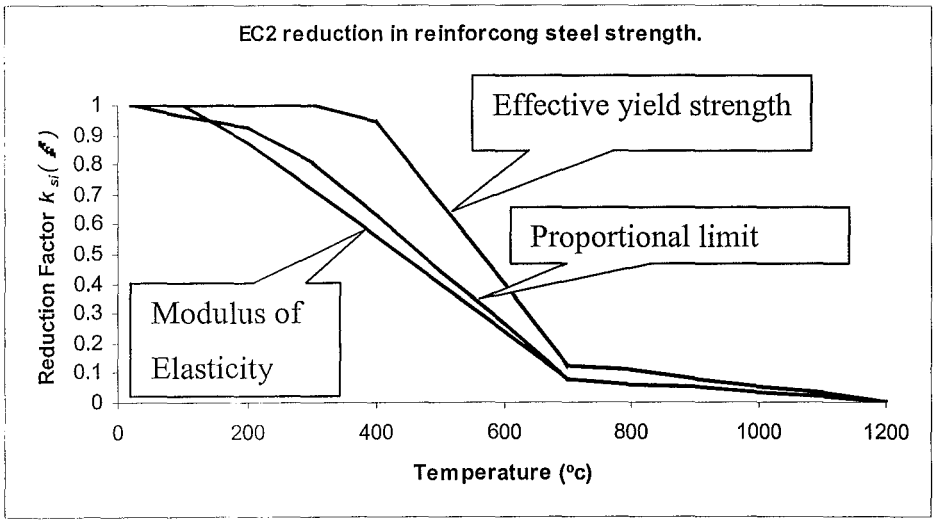

Figure 2.4.3 Reduction factors for the stress strain relationship of hot rolled reinforcing steel at elevated temperatures.

The reduction of the characteristic strength of a reinforcing steel as a function of the temperature θ is allow for by the coefficient $k_s(\theta)$ for which:

$$f_{sk}(\theta) = k_s(\theta) f_{yk}(20^oC) \qquad \text{[Equation 2.12].}$$

For tension reinforcement in beams and slabs where $\varepsilon_{s,fi} \geq 2\%$, the strength reduction is recommended as given below

Where $k_s(\theta) = 1.0$ for $20^oC \leq \theta \leq 350^oC$.

$k_s(\theta) = (6650-9\theta)/3500$ for $350^oC \leq \theta \leq 700^oC$.

$k_s(\theta) = (1200-\theta)/5000$ for $700^oC \leq \theta \leq 1200^oC$.

For reinforcement in compression zones of beams and slabs the strength reduction at 0.2% proof strain is recommended as shown below. This also applies for tension reinforcement where $\varepsilon_{s,fi} < 2\%$ when using the simplified or general calculation methods.

where: $k_c(\theta) = 1.0$ for $20^{\circ}C \leq \theta \leq 100^{\circ}C$.

$k_c(\theta) = (1100-\theta)/1000$ for $100^{\circ}C \leq \theta \leq 400^{\circ}C$.

$k_c(\theta) = (8300-12\theta)/5000$ for $400^{\circ}C \leq \theta \leq 650^{\circ}C$.

$k_c(\theta) = (1200-\theta)/5500$ for $650^{\circ}C \leq \theta \leq 1200^{\circ}C$.

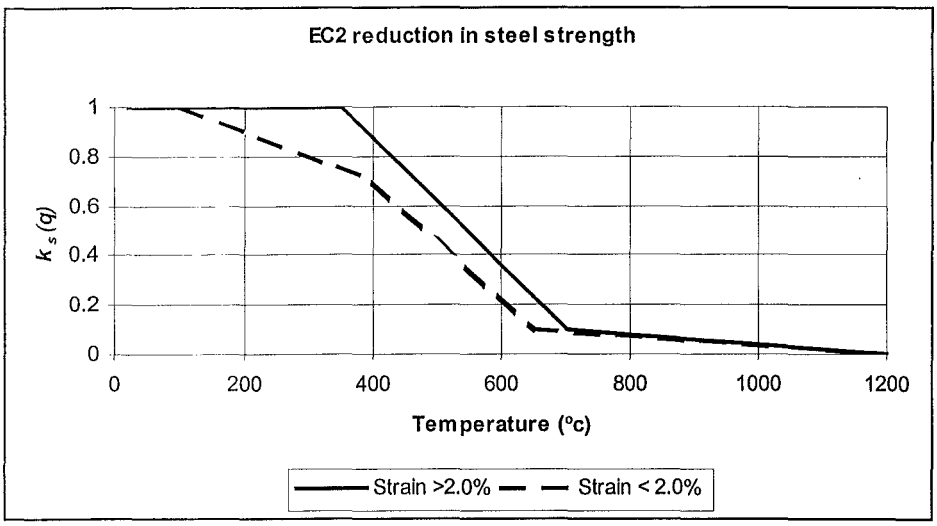

Figure 2.4.4 Coefficient $k_s(\theta)$ allowing for decrease of characteristic strength (f_{yk}) (EC2: 1993).

2.5 Concrete Thermal Properties

2.5.1 Introduction.

This section describes the thermal properties used by SAFIR from the Eurocode (EC2: 1993) for the siliceous aggregate concrete model. The thermal properties of this material SAFIR are shown below.

2.5.2 Concrete Thermal Conductivity (λ_c)

The thermal conductivity of concrete is temperature dependent and varies due to the type of aggregate. For concrete with siliceous aggregates the thermal conductivity model is described by the following relationship and shown below in Figure 2.5.1.

$\lambda_c = 2 - 0.24\theta/120 + 0.012(\theta/120)2$ *(W/mK)* *for* $20^oC < \theta \leq 1200^oC$ [Equation 2.13].

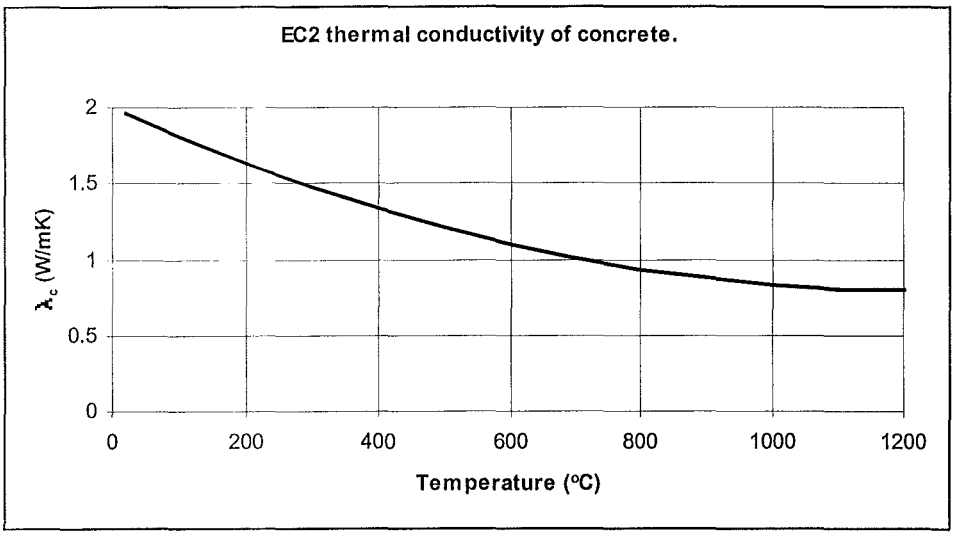

Figure 2.5.1 EC2 Thermal conductivity of concrete as a function of temperature.

2.5.3 Concrete Specific Heat c_c

The specific heat of concrete (c_c) varies over a broad range depending on the moisture content which for EC2 concrete is a maximum of 2%. The following relationships show the EC2 concrete specific heat. Between 100°C and 200°C there is a peak in specific heat due to water being driven off as shown in Figure 2.5.2.

$c_c = 900 + 80\theta/120 - 4(\theta/120)^2$ *(J/kgK)* for $20°C < \theta \leq 1200°C$ [Equation 2.14]

Between 100°C and 200°C there is a peak in specific heat due to the water being driven off

$c_{c,peak}$ = 1875 J/kgK for a humidity of 2% of concrete weight.

$c_{c,peak}$ = 2750 J/kgK for a humidity of 4% of concrete weight.

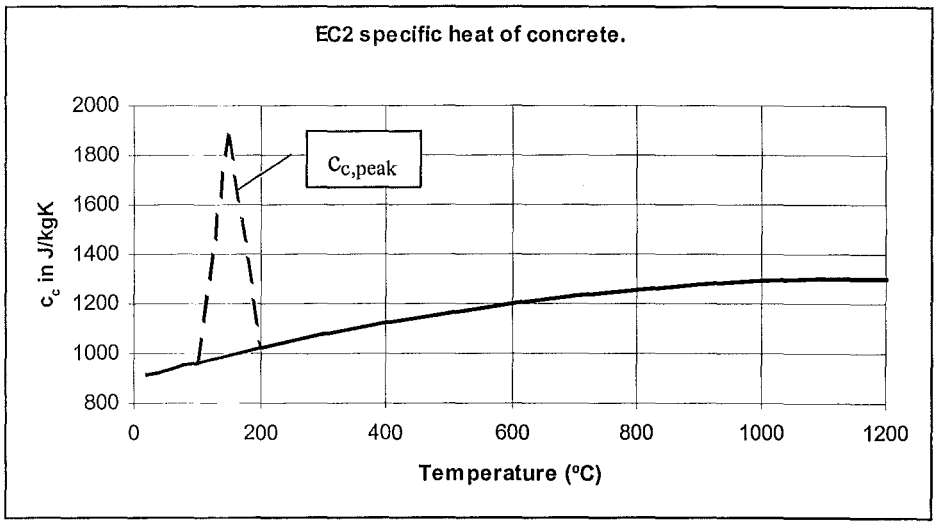

Figure 2.5.2 EC2 Specific heat of concrete as a function of temperature.

2.5.4 Concrete Thermal Elongation (Δl/l).

The relationships below and in Figure 2.5.3 show the thermal elongation of siliceous concrete as a function of temperature as proposed by the Eurocode (EC2: 1993). This model is non-linear up to 700°C where it becomes constant.

$(\Delta l/l)_c = (-1.8E\text{-}4) + (9E\text{-}6*\theta) + (2.3E\text{-}11\theta^3)$ for $20°C < q \leq 700°C$. [Equation 2.15].

$(\Delta l/l)_c = 14E\text{-}3$ for $700°C < q \leq 1200°C$. [Equation 2.16].

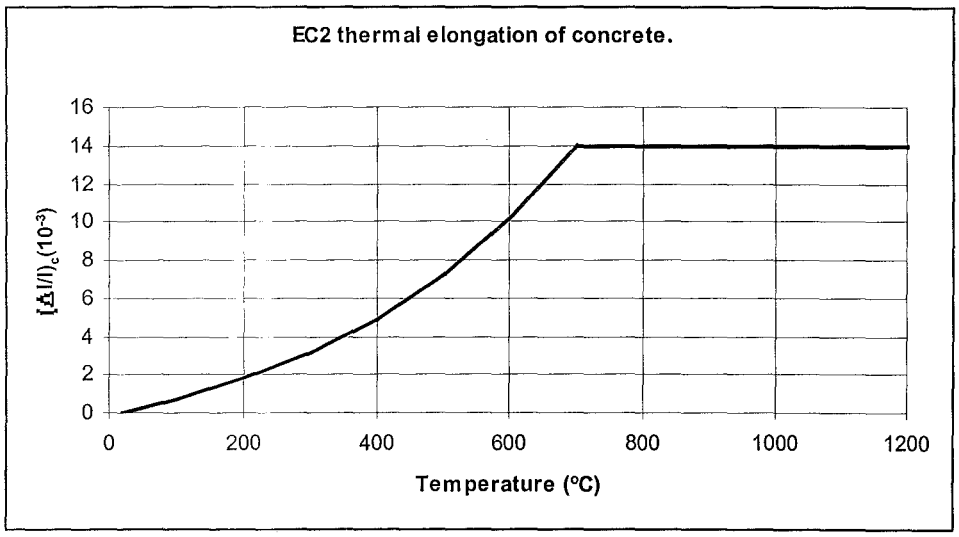

Figure 2.5.3 EC2 Thermal elongation of concrete as a function of temperature.

3 COMPOSITE BEAM MODEL AND ANALYSIS METHOD

3.1 Introduction

This section of the report describes the composite beam layout, dicretisation and gravity loading used in the SAFIR program. The fire growth models are also described in this section. These models are used in the SAFIR thermal analysis. Manual calculations of section properties have been compared with those obtained from SAFIR. A description of the SAFIR finite element program is given and a comparison of mesh discretisations made

3.2 Composite Beam Layout and Section Components.

The beam studied in this report is an 8.2m long composite 610 UB 101 steel beam supporting a 120mm thick concrete deck. It is an internal gravity beam from a typical steel framed New Zealand office building that was constructed in 1988 as described by Stevenson (1993). Figure 3.2.1 shows the floor plan of the building. The span between the gravity beam and the perimeter beams is 8.9m and the secondary beams are spaced at approximately 2.56m centres. It is assumed that there is full composite action between the steel beam and the concrete slab. It is also assumed that the gravity load is uniformly distributed over the gravity beam rather than point loads from the secondary beams.

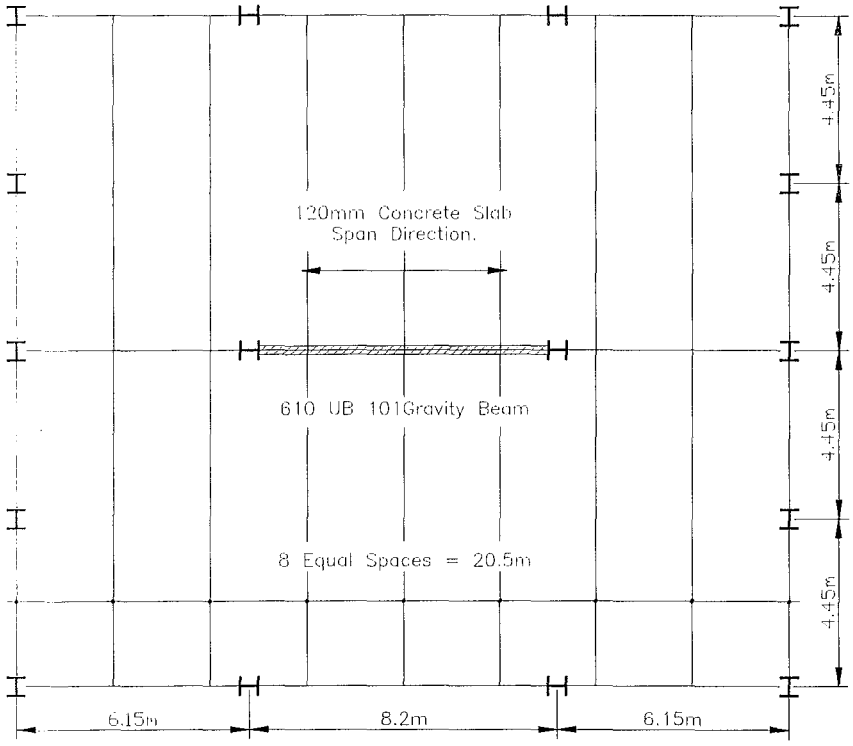

Figure 3.2.1 Layout plan of building, from Stevenson (1993).

The 17 storey office building has all the structural members protected against fire with insulating materials. The suspended ceilings in the building will also provide protection to the steel framing. The analysis in this report examines the behaviour of the beam *without* fire protection.

Figure 3.2.2 shows the beam – column joint connection for the gravity beam. The connection has been designed as simply supported in the real structure but for the purposes of this report four support conditions will be analysed, namely *pin – pin*, *pin – roller*, *fixed – fixed* and *fixed – slide* support conditions. While some of these support conditions are unrealistic they form an envelope of possible support conditions.

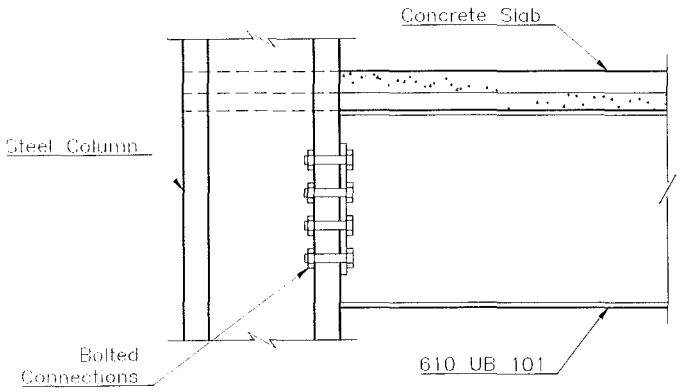

Figure 3.2.2 Beam - column joint elevation.

Figure 3.2.3 shows a section through the beam and the composite slab. The proprietary profile decking is Diamond Hi-Bond. Figure 3.2.1 shows that the span between the gravity beam and the perimeter beams is 8.9m centre to centre. From NZS 3404:1997 (clause 13.4.2.1) positive moment regions with a slab on both sides have an effective slab width for flexural contribution of the lesser of 0.25 times the beam span or the beam centre line distance. Therefore the effective slab width is taken as 2.05m which is 0.25 times the beam span of 8.2m. The effective width has been used as the discretisation width for the slab in the 2-D analysis as shown in Figure 3.2.4

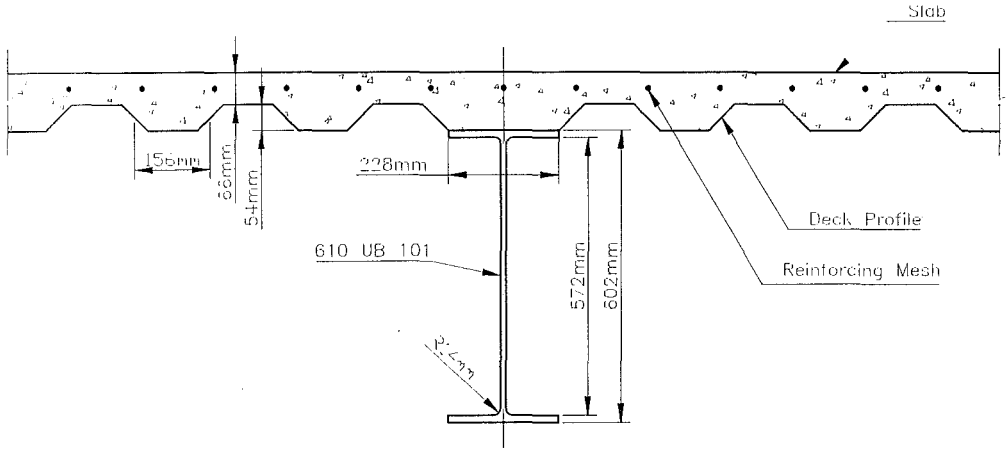

Figure 3.2.3 Section through composite slab.

Figure 3.2.4 shows that the section has been modified for the SAFIR discretisation. The reason for the modification is to cut down on the computational effort required in modelling the deck profile for the SAFIR runs. The deck profile has been entered into the model as a slab (Slab 2), of an equivalent area to the actual deck profile. The bottom slab was included so that equivalent thermal affects and thus losses in strength in the top slab could be taken into account. The

reinforcing mesh was added into the model as an equivalent area of reinforcing steel centred at the same height as the actual case. No modification was made in modelling the 610 UB 101 except that the root fillets were modelled as equivalent area triangles rather than their actual circular profile. This will have little effect on the thermal and structural output. See Section *3.8 "FEM Thermal Discretisation."* for details of discretisation.

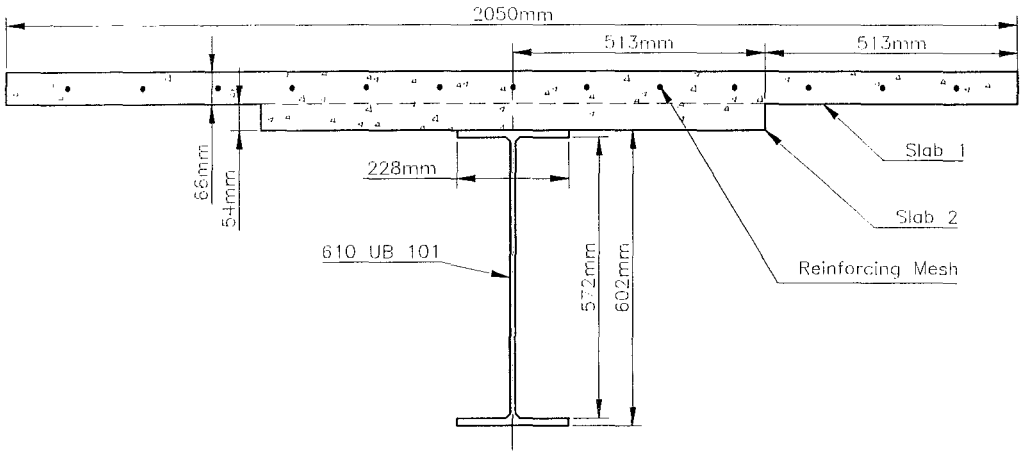

Figure 3.2.4 Discretised composite section

3.3 Gravity Load

For specific fire engineering the New Zealand loading code NZS 4203:1992 requires that:

For the period of time during a fire emergency when the structure is subjected to elevated temperatures and designated members are required to remain stable, the affected members shall be designed for the following combination of factored load.

$$\mathbf{G} + \mathbf{Q_u}$$

Where:

G = Dead Load.

$Q_u = \psi_u Q$

Q = Live load.

ψ_u = 0.4 for office buildings.

The gravity load to be used in the analysis is a uniformly distributed load along the whole length of the beam. With partial or unsymmetrical loading there are more variables to consider which would obscure the basic behaviour sought in this report.

Table 3.3.1 Calculation of UDL.

Component of load	**Value**	**Unit**	**kN/m**
Slab + Deck	2.5	kPa	22.25
610 UB 101	0.99	kN/m	0.99
Self imposed dead load. (SDL)	2.00	kPa	17.8
Live Load	2.5	kPa	
Adjustment for $Q_u = \psi Q$	0.4*2.5	kPa	8.9
Total	5.62	kPa	50.00

The self imposed dead load covers those items that are fixed to the structure but do not contribute to the load carrying capacity of the structure, for example pipe work and ducting. The self-imposed dead load is high at 2.0 kPa but as per NZS 4203:1992 Section 2.4.3.5 *The most adverse distribution of live load shall be considered in the design.* Therefore the design load to be used in this report is 50 kN/m leaving a total load of 410kN (5.62 kPa).

3.4 Fire Growth Models

3.4.1 Introduction

Two standard types of fire model have been used in this report to simulate thermal effects on composite beam behaviour. The first model used is a linear heating rate model and the second model is the ISO 834 standard fire test. The fire models, which are entered into the SAFIR thermal analysis can be input as a series of time - temperature points, in a separate data file, or are contained within the code itself, for example the ISO 834 Standard fire. The temperature relates to the gas temperature of the fire that surrounds the structure. This gas temperature is uniform throughout the depth of the section and is considered, for the purposes of this report, to be the upper layer gas temperature in a two-zone model.

3.4.2 Linear heating rates.

Figure 3.4.1 shows the linear heating rate fire growth models. This fire growth model has been selected as it has been used in other reports, Rotter et al (1999), as it is useful for determining section behaviour at a constant rate of temperature increase. The heating rates used in this report are 5°C per minute, 10°C per minute and 20°C per minute to model the effects of increased thermal exposure. The 5°C per minute model gives slow changes in section behaviour due to a better uniformity between gas temperature and average section temperature, so that all variations in behaviour can be well defined and understood. The 5°C per minute case will form the base case for this report to which all other simulations will compared.

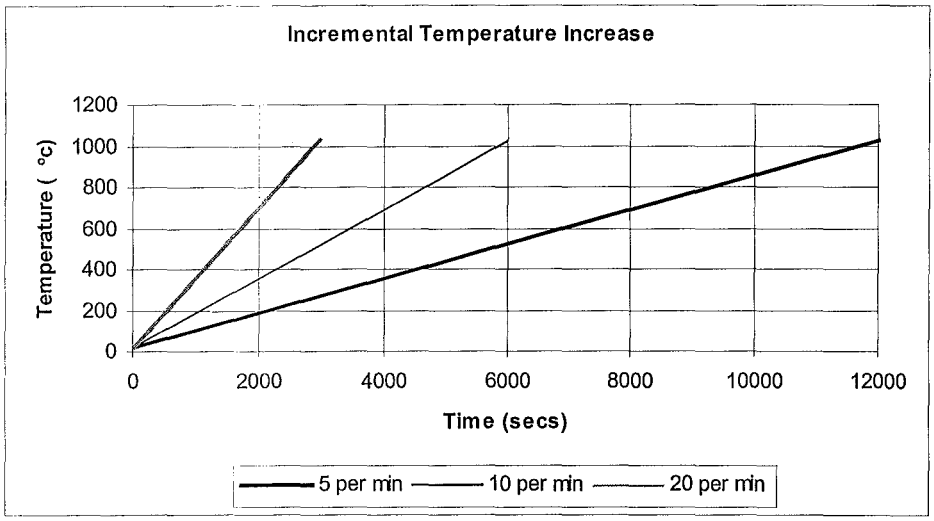

Figure 3.4.1 Linear heating rate versus time.

The thermal analyses were run for reasonably long periods of fire duration, up to 3 hours in some cases, so that failure would occur in the structural analysis as shown later in this report. Note that the term failure in this report is defined as the time when the stiffness matrix of the finite element analysis is no longer positive.

The linear heating rate has been used as the base case for the four support cases in Section 5 *SUPPORT CONDITONS* as well as being used in Section 6 *AXIAL SPRINGS* "".

3.4.3 ISO 834 Standard Fire.

Figure 3.4.2 shows the ISO 834 (ISO: 1975) standard fire which has been included as a case of simulations in this report as it is an internationally recognised and tested standard fire. Initially the ISO 834 fire will subject the composite section to a much more rigorous test than the linear heating rate fire. This is due to the rapid fire growth within the initial stages of the fire.

The ISO 834 fire is a non-linear rapid growth fire where in the early stages of fire growth is comparable with a temperature increment of approximately 212°C per minute for the first two minutes. The rate of change in fire growth is also reasonably rapid, meaning that where the structure is able to withstand the initial thermal exposure the average steel and concrete temperature will become more uniform with gas temperature as fire duration proceeds. Due to the different heating rates there will be more of a lag between the average material temperature and that of the gas temperature than was found in the linear heating rate cases. The ISO 834 fire growth model has been used as the base case for the four support cases in Section 7 *ISO 834 STANDARD FIRE.*

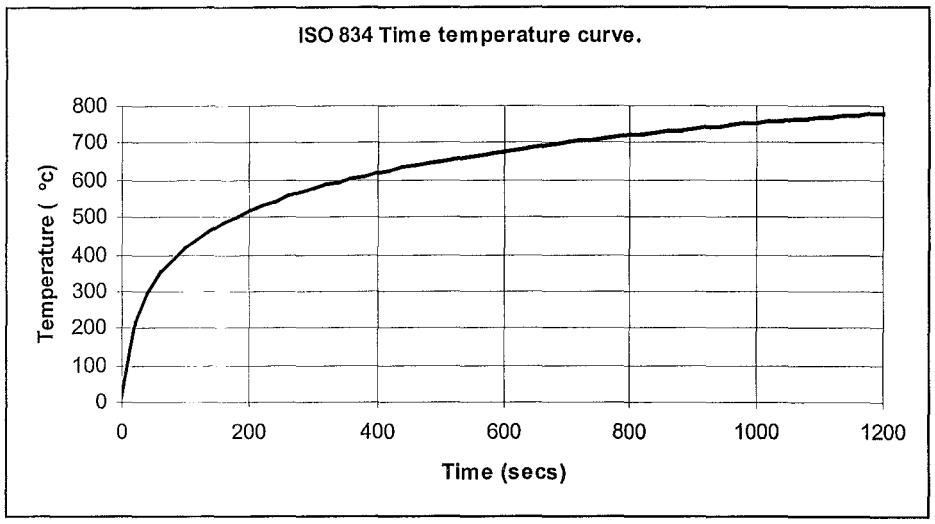

Figure 3.4.2 ISO 834 Time temperature curve.

In the ISO 834 specification (ISO 1975) the temperature T (°C) is defined by

$$T = 345\log_{10}(8t+1)+T_0 \qquad \text{[Equation 3.1]}.$$

A cooling phase was also introduced to the standard fire and used to model the beam behaviour with the four support cases in Section 8 *COOLING PHASE BEHAVIOUR*. Figure 3.4.3 shows that the ISO 834 fire growth duration is 600 seconds and then there is a linear cooling phase. 600 seconds was selected as the fire growth time as the composite section fails at 660 seconds with *pin – pin* supports as shown in Section 6.2 "*Pin – Pin Supports*". The linear decay rate used in the formation of this time temperature curve is from the Eurocode (EC1: 1994). The Eurocode suggests a decay rate $(dT/dt)_{ref}$ for fires with a burning period of less than half and hour is 625°C per hour. At 600 seconds the ISO 834 fire temperature is 678°C leaving a cooling duration of 3793 seconds (63.2 minutes) to reach 20°C. The total simulation time is 4393 seconds (73.2 minutes).

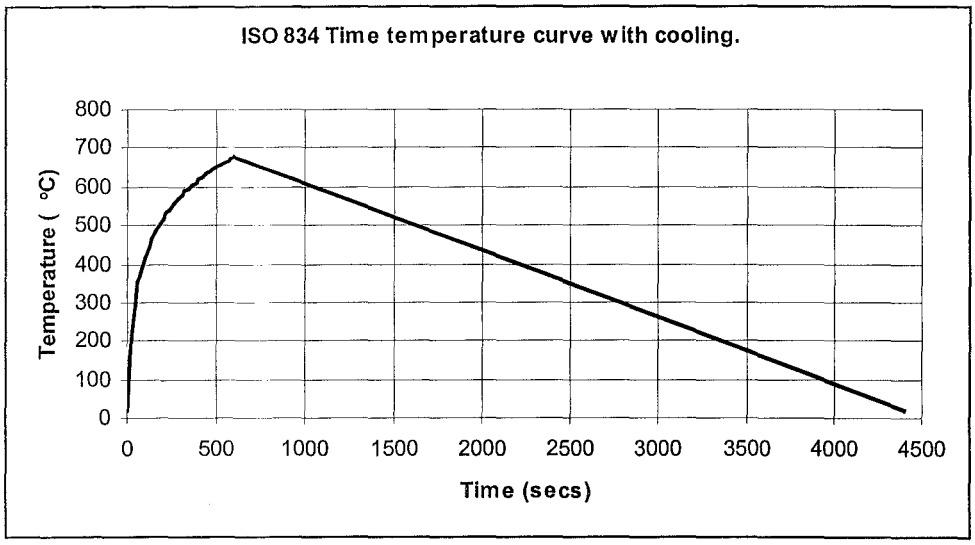

Figure 3.4.3 ISO 834 Time temperature curve with cooling.

Described in Buchanan (2001) from the CIB formula published by the CIB W14 group (CIB, 1986), derived by Pettersson (1973) based on the ventilation parameters of the compartment and the fuel load the equivalent time of exposure to an ISO 834 fire test t_e (min) is given by:

$$t_e = k_c w e_f \qquad \text{[Equation 3.2]}$$

where e_f is the fuel load (MJ/m^2 of floor area)

k_c is a parameter to account for different compartment linings

w is the ventilation factor (m-0.25) given by

$$w = A_f/(A_v A_t H_v^{0.5})^{0.5} \qquad \text{[Equation 3.3]}$$

where A_f is the floor area of the compartment (m^2)

A_v is the total area of openings in the walls (m^2)

A_t is the total area of the internal bounding surfaces of the compartment (m^2)

H_v is the height of the windows (m).

The time equivalence of fire exposure for 600 seconds (10 minutes) gives a fuel load of approximately 115MJ/m^2 for the ISO 834 fire with a cooling phase. A value of 0.4 was used for k_c, which is the CIB W14 (CIB: 1986), parameter for steel buildings. The floor area used in the equations is based on the assumptions made by Stevenson (1993) in which the maximum floor area used in the calculations was 150m^2 compared to the actual floor area of the building is 373.1m^2. The reason for doing this is that the CIB W14 formulae is empirical and is only valid in small compartments. The ventilation area was assumed to be 20% of the floor area with the window height being 2.0m as there is no obtainable data for these parameters. This left a ventilation area of 30m^2 and a total area for the surfaces of 451m^2. Buchanan (2001) states that this method is a crude approximation and is not intended for unprotected steelwork. Stevenson estimates that the fire load of the building is 720MJ/m^2. This is the upper limit recommended by the SCI (1990).

The calculated fuel load is low in comparison to that of the 720MJ/m^2 as recommended by the SCI (1990) because of the fire duration limitation of 10 minutes.

3.4.4 Thermal Boundary.

The composite section is thermally exposed on three faces, as shown in Figure 3.4.4. This type of thermal exposure simulates a fire on only one floor at a time. It will provide a higher thermal gradient through the section where the steel temperatures will be a lot higher than the concrete temperatures, due to the relative thermal properties of the two materials. This is only during the fire

growth stage. In the decay phase of a fire the internal concrete temperature may still rise due to the stored energy within the concrete. The steel will cool very quickly in the decay phase relative to the concrete, this will introduce new forces and axial loads into the structure as analysed in Section 8 *COOLING PHASE BEHAVIOUR.*

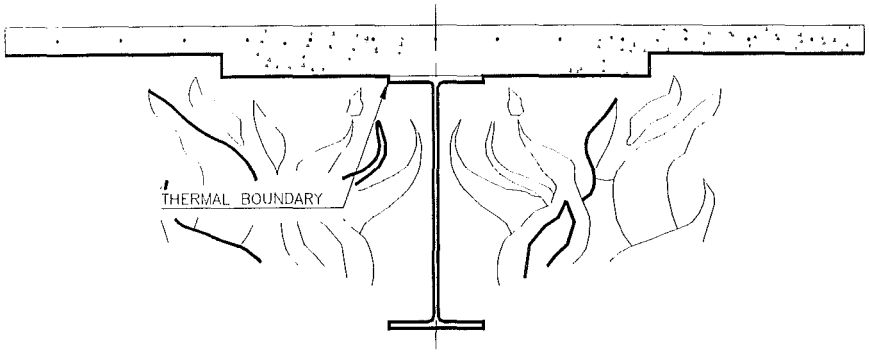

Figure 3.4.4 Thermal boundary of composite section.

3.5 Neutral Axis & Section Properties

3.5.1 Introduction

A manual elastic calculation was undertaken to find the neutral axis height. This is used as the height of the pin supports in the computer model. In reality the line of support will lie in the middle of the web of the primary gravity beam with a cleat plate welded to the steel column. There is also a second line of thrust that occurs somewhere in the plane of the slab and this is taken into account as shown later in this section.

3.5.2 Manual Calculation

The elastic neutral axis and section capacity was manually calculated using the second moment of area method calculations shown in Section 3.5.3. The concrete stiffness ratio, n, was found by comparing the elastic modulus of the steel with that of the concrete and finding an effective width for the concrete slabs relative to the steel. Table 3.5.1 shows the material properties for the steel and the concrete used to find the elastic neutral axis for the composite section.

Table 3.5.1 Material properties used in determining the elastic neutral axis.

Material Properties					
610 101 UB 275 Grade Steel Beam			120mm Hi-bond Concrete Slab		
Property	**Value**	**Unit**	**Property**	**Value**	**Unit**
E_{steel}	210	GPa	E_{conc}	23.5	GPa
F_y	275	MPa	$f'c$	25	MPa
Area	13000	Mm^2	f_r	0.5	MPa
I_{xx}	761E6	Mm^4	Top Slab effective width b_{ec}	2050	mm
			Bottom slab effective width b_{ec}	1025	mm
			Top slab ratio b_{ec}/n	229.4	mm
			Bottom slab ratio b_{ec}/n	114.7	mm
			Top slab depth t_t	66	mm
n (E_{steel} /E_{conc})	8.936		Bottom slab depth t_d	54	mm

Table 3.5.2 shows the concrete slab areas as a ratio of the steel to concrete tangent modulus. The depth to the component neutral axis, ***y***, is from the top of the composite section.

Table 3.5.2 Section properties I.

Component	**Area (mm^2)**	***y*** **(mm)**	***Ay*** **(mm3)**	***A(y-y')²*** **(mm^4)**	***I_{xx}*** **(mm^4)**
Top Slab	15140.7	33	4.996E+05	3.767E+08	5.496E+06
Bottom Slab	6193.9	93	5.760E+05	5.916E+07	1.505E+06
Steel Beam	13000.0	421	5.473E+06	6.893E+08	7.610E+08
Total	34334.6		6.549E+06	1.125E+09	1.125E+09
					1.893E+09

Table 3.5.3 Section properties II

Property	Value	Unit
y'	191	mm
I_{xx}	1.893E+09	mm^4
I_{xx}	0.001893	m^4

Note that the 191mm is from the top of the composite section.

3.5.3 Formulae

Below is the formulae used in determining the second moment of area and the elastic neutral axis.

$$y' = \sum Ay / A_{total} \qquad \text{[Equation 3.4]}$$

where y' is the composite section neutral axis.
y is centroid of a component.
A_{total} is the total relative composite section area.

$$I_{xx} = \sum I + \sum A(y - y')^2 \qquad \text{[Equation 3.5]}$$

where I_{xx} is the second moment of area for the composite section.
I is the second moment of area of a component.

3.5.4 SAFIR Elastic Neutral Axis (zero axial force support height).

An elastic neutral axis was also determined using SAFIR. The SAFIR analytical neutral axis was found by adjusting the support height ('y' 0 – 0 node line) of the composite section in the *Filename.tem* SAFIR input file and then running a structural *pin – roller* analysis. Then results from the structural *pin – roller* simulation were opened in Microsoft Excel and the centre line stresses

selected and tabulated to find the neutral axis, where the stress is zero. The neutral axis was found by adjusting the support height and re-running the structural simulation until the pre-determined support height is the same as the neutral axis.

3.5.5 Results

The results of the analysis show that SAFIR calculates the neutral axis of the section at 162 mm above the neutral axis of the steel beam. Unexpectedly there is a 68mm difference in neutral axis height. Manual calculations give a neutral axis height of 230mm above the neutral axis of the steel beam. Due to the difference in neutral axis heights a comparison in the effect of neutral axis height was made in SAFIR. The comparison was made using the same mesh discretisation with the same linear heating rate of 20°C per minute while adjusting the y_0 node line height. This is effectively taking the same *Filename.tem* file and adjusting the y_0 node line height. The SAFIR neutral axis height was compared with the manually calculated neutral axis height for the *pin – pin* support condition. See Figure 5.2.1 for support schematic.

Figure 3.5.1 shows that there is a significant difference in output between the two lines of thrust. The manually calculated neutral axis gives a better fire resistance and displays more of the beams behaviour. The SAFIR neutral axis shows that the beam fails a lot earlier on in the fire.

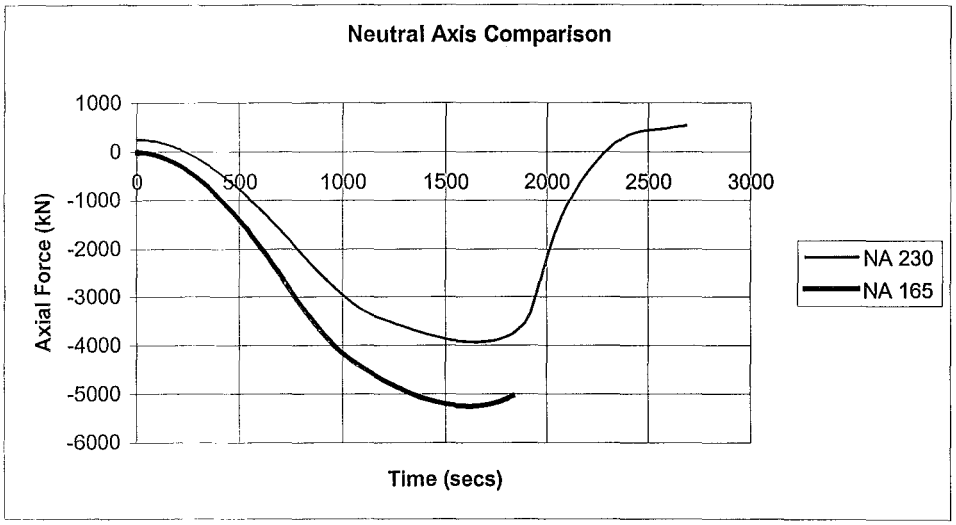

Figure 3.5.1 Axial force comparison of elastic neutral axis.

3.5.6 Conclusions

The results show that the SAFIR neutral axis is lower down the web of the steel beam than the manually calculated neutral axis. This concurs with the scenario of the support height being at the cleat plate height which is welded to the column. The manually calculated elastic neutral axis is probably more realistic taking into account the second line of thrust through the plane of the concrete slab. For this reason the manually calculated elastic neutral axis will be used as the line of thrust for the rest of the analysis.

The SAFIR output is very sensitive to the line of thrust used in the input files. It would be pertinent to make a study of this behaviour but it falls outside the scope of this report.

3.6 Moment Calculations & Deflections

3.6.1 Introduction.

Based on the cold properties used in finding the elastic neutral axis in the previous section, the ambient temperature ultimate flexural capacity in bending for the section can be found manually. The initial displacements for the simply supported case can be found and used to compare with the SAFIR output data.

3.6.2 Ultimate Flexural Capacity Calculation.

The initial step is the calculation of the location of the plastic neutral axis (PNA). This is found by comparing the compressive resistance of the concrete slab with the tensile resistance of the steel section.

Compression

The compression force in positive bending is made up of contributions from the two concrete slabs and the reinforcing mesh. The reinforcing mesh has been neglected in these calculations as its contribution is very small and will not affect the location of the lever arm adversely. Note that the

reinforcing mesh has only been added to those simulations where regions of negative bending moment is expected.

Slab 1	Slab 2	
$C = 0.85f'_c b_{ec} t$	$C = 0.85f'_c b_{ec} t$	[Equation 3.6]
$C = 0.85x25x2.05x66$	$C = 0.85x25x1.025x54$	
$C = 2875kN$	$C = 1176kN$	

Total compression force equals 2875 + 1176 = 4051kN in the concrete slabs.

Tension

The tension force in positive bending is made up mainly from the contribution from the 610 UB 101. For this report the concrete has a small tensile capacity, but for the calculation of the flexural capacity it will make very little difference, approximately 9.5kN of tensile capacity from slab 2. For this reason concrete tensile action has been neglected from these calculations and is considered to be zero. This is a conservative assumption.

$T = Af_y$	[Equation 3.7].
$T = 13000x275 = 3575kN.$	$3575 < 4051$ $\therefore$ NA lies in the slab.

$$\therefore\ a_c = \frac{3{,}575{,}000 - 2{,}875{,}000}{0.85 * 25 * 1025} = 32.1mm$$ into Slab 2.

The neutral axis for the compression force has been calculated at:

Part	Area (mm^2)	y (mm)	Ay (mm^3)
Slab 1	2050*66 = 135.3E3	33	4464.9E3
Slab 2	1025*32 = 32.9E3	33+32.1/2 = 49.05	1613.9E3
Totals	148.6E3		6078.8E3

Compressive neutral axis = 6078.8/148.6 = 40.9mm.

Moment

$$e' = \frac{602}{2} + 120 - 40.9 = 380.1mm$$

$Mn = Te'$ [Equation 3.8].

$M_n = 3575*0.3801 = 1358.9\ kNm.$

$\phi M_n = 0.85x1358.9 = 1155.0\ kNm.$

where ϕ is a safety factor.

Design Loads.

$w_u = 50\ kN/m.$

$M^* = wl2/8$ [Equation 3.9].

$M^* = 420.3\ kNm$

$\therefore M^* < \phi M_n.$

The load ratio is 420.3 kNm / 1155 kNm = 0.364.

3.6.3 Simply Supported Deflection.

The ambient temperature mid span deflection for the simply supported (*pin – roller*) case can be manually calculated from the formula below. Figure 5.3.1 shows the support schematic for the *pin – roller* case. The section and material properties used below are derived from *3.5 Neutral Axis & Section Properties*. The Elastic Modulus, *E*, value is for steel, as the section properties have been determined by using the E_{conc} / E_{steel} ratio, ***n***, for the slab areas.

$$\delta = \frac{5}{384}\frac{wL^4}{EI} \qquad \text{[Equation 3.10]}$$

$$\therefore \delta = \frac{5}{384}\frac{50{,}000x8.2^4}{210E9x1.893E-3} = 7.4mm$$

The manually calculated mid span ambient temperature deflection of the beam is 7.4mm. Results obtained from SAFIR for the same support case give an initial deflection of 8.6mm. The manually calculated and SAFIR deflections are reasonably close.

3.7 SAFIR Computer Code.

3.7.1 Introduction

SAFIR is the computer code used for the analysis in this report, Franssen et al (2000). SAFIR is a special purpose computer program for the analysis of structures under ambient and elevated temperature conditions. The Finite Element Method (FEM) based program can be used to study the behaviour of one, two and three-dimensional structures. The program was developed at the University of Liege, Belgium, and is today viewed as the second generation of structural fire codes developed in Liege.

As a finite element program, SAFIR accommodates various elements for different idealisation, calculation procedures and various material models for incorporating stress-strain behaviour. The elements include 2-D solid elements, 3-D solid elements, beam elements, shell elements and truss elements. The stress-strain material laws are generally linear-elliptic for steel and non-linear for concrete.

3.7.2 Analysis Procedure

Using the program, the analysis of a structure exposed to fire may consist of several steps. The first step involves predicting the temperature distribution inside the structural members, referred

to as 'thermal analysis'. The torsional analysis may be necessary for 3-D beam elements, a section subject to warping and where the warping function table and torsional stiffness of the cross section are not available. The last part of the analysis, termed the 'structural analysis', is carried out for the main purpose of determining the response of the structure due to gravity load and thermal exposure.

3.7.3 Thermal Analysis

This analysis is usually performed while the structure is exposed to fire. For a complex structure, the sub-structuring technique is used, where the total structure is divided in to several substructures and a temperature calculation is performed successively for each of the substructures. This kind of situation does not arise in a structure where the members are made of different sections. For example, a frame with reinforced concrete columns, prestressed main beams and structural steel secondary beams, will require separate temperature analysis for each of the section types. From these analyses, the temperatures across the cross section are obtained and are stored for subsequent structural analysis where these sections are present. The thermal analysis is being made using 2-D solid elements, to be used later, on cross sections of BEAM elements or on the thickness of shell elements.

3.7.4 Structural analysis at elevated temperature

For each calculation, the loads are applied to the structure, described as BEAM, TRUSS and SHELL elements. The temperature history of the structure, due to fire, is read from the files created during the thermal analysis. As the computational strategy is based on a step-by-step procedure, the following information can be obtained until failure occurs in the structure:

- Displacement at each node of the structure
- Axial and shear forces and bending moments at integration points in each finite element
- Strains, stresses and tangent modulus in each mesh at integration points of each finite element.

3.7.5 *Capabilities of SAFIR*

Capabilities concerning the temperature analysis

In SAFIR, plane sections, as well as three dimensional structures, can be analysed. Plane sections are discretised by triangular and or quadrilateral (rectangular and non-rectangular) elements allowing most cross sectional shapes. Although not used in this report, three dimensional structures are discretised using solid elements (prismatic and non-prismatic) with 6 or 8 nodes. Each element is assigned its own material and composite sections can be constructed. The most recent versions of SAFIR allow for user defined materials.

The thermal exposure is defined as a function of time with gas temperatures assigned to each time step. Standard curves (ISO 834, ASTM E119, ULCS-101) are predetermined in the code and any other time – temperature curve can be introduced through data points. A cooling phase can be introduced into the model as well.

The variation of material properties with temperature, as well as the evaporation of moisture can be considered in the model. Thermal performance of materials such as steel, reinforced concrete and composite sections can be analysed.

Capabilities concerning the structural analysis

As stated in the thermal capabilities, plane or three dimensional structures can be analysed. The structure can be discretised by means of four different elements. Truss elements, made of one single material with one uniform temperature per element; beam elements, either pure steel, reinforced concrete or composite steel sections; solid elements in which only thermo-elastic material laws are possible; and shell membrane elements.

Large displacements are considered for truss, beam and shell elements. The effects of thermal strains (thermal restraint) can be accounted for in the model. The material properties are non-linearly temperature dependent and unloading is parallel to the elastic loading branch. Local failure of a structural member that does not endanger the safety of the whole structure can be handled by means of the arc length technique.

Nodal coordinates can be introduced in the Cartesian or cylindrical system of axes. Imposed displacement (prescribed degrees of freedom) can be introduced and structures with external support inclined at an angle to the global axes can be analysed. Residual stresses (initial strains) in members can be accounted for in the model. Pre-stressed structures can also be analysed in SAFIR.

3.7.6 Common features in all analysis.

Thermal and mechanical properties of steel and concrete according to the Eurocode (EC2: 1993, EC3: 1995, and EC4: 1994) are embedded in the code and can be used directly in the models. The same temperature or the same displacement can be imposed at two different nodes by the use of a master-slave relationship.

Optimisation of the matrix in order to reduce computational effort and bandwidth can be performed by the program using internal renumbering of the of the system equations. The program comes with it's own pre-processing and post-processing capabilities. These are the SAFIRwizard and DIAMOND2001 codes respectively. Other pre-processors are under development at the moment. Where required, and usually essential, the Microsoft Excel program can be used to obtain and plot element stresses from the *structural.out* files as has been done for this project. Element temperatures can also be obtained in this manner from the *thermal.out* file.

3.7.7 Sign Conventions

Global and local axis

The Cartesian systems of coordinates are used for the Global axis when defining a structure that is to be analysed using SAFIR. For 2-D problems, as used in the simulations contained in this report, the axes are named G1and G2, while the local axes are named L1 and L2. Applied force and the displacements are positive in the direction of G1 and G2. The applied moment and rotations are positive in a counter-clockwise direction.

Stresses

The stresses are positive in tension. Axial forces, obtained as a summation of the stresses, are also positive in tension. Bending moments in the beam elements are positive when fibres having a positive local coordinate are in tension.

The terminology used in this report is that the '*positive bending moment*' as stated from here on in this report are when fibres having a negative local coordinate are in tension, ie classic, simply supported beam bending. The term '*negative bending moment*' will be used to describe those moments where fibres that have a positive local displacement are in tension, ie the end of span moment of a redundant support. Note that SAFIR plots positive moments on a negative scale, for this reason the graphs in this report show positive moment plotted on a negative scale.

3.7.8 Convergence Criteria.

In order for convergence to be obtained, a tolerance value has to be specified in the input files. An iterative procedure is used so that a solution can be obtained at each time step, which is also set in the input files. A good precision value for the tolerance is dependent on the structure being analysed and information from preliminary runs. Intuitively the finer the time step, and the greater the precision, the more computationally demanding and precise the simulation becomes. A balance has to be obtained between computational effort and reasonable precision for the simulation. This can be achieved on a trial and error basis by running successive simulations with greater precision and smaller time steps, until the user finds the change in the solution acceptable.

3.7.9 Element Theory and Formulations.

Two element types have been used in the simulations. For the composite section the BEAM element was chosen and for the axial spring a TRUSS element was selected.

The TRUSS Element.

The truss element is straight with two end nodes. The geometry is defined by the position of these end nodes. The cross sectional area and material type completely define each truss element. Only one material, one temperature and one strain is present in each element.

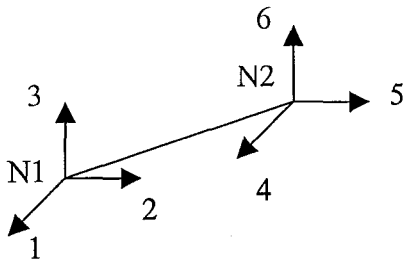

Figure 3.7.1 Truss element - Degrees of freedom at nodes.

All integrations are made analytically and hence no points of integration are given in the program for truss elements. The strain in the element is uniform.

The BEAM Element.

The beam element is straight in its undeformed geometry. Three nodes define its position in space. The two end nodes, N1 and N2, and a third node N4 defining the position of the local y axis of the beam. The node N3 is used to support an additional degree of freedom.

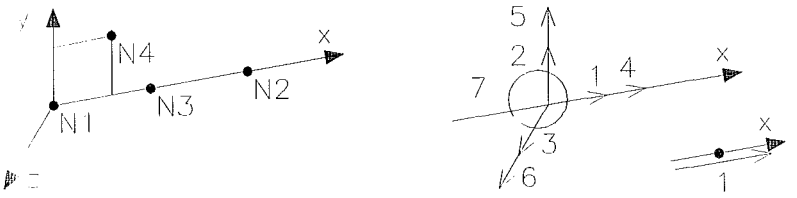

(a) (b) nodes N1, N2 node N3

Figure 3.7.2 Beam element: (a) Local axes (b) Degrees of freedom at nodes.

The fibre model is used to describe the geometry of the cross section. The cross section of the beam is subdivided into small fibres (triangles, quadrilaterals or both). In these simulations quadrilaterals were used to discretise the steel 610 UB 101 and the concrete slab. The root fillets of

the UB were modelled using triangles. The material behaviour of each fibre is calculated at the centre of the fibre and it is constant for the whole fibre, thus a fine mesh is required at points of high thermal exposure and stress. Each fibre can have its own material, which allows for the building of composite sections as described in this report.

Assumptions for the beam element.

- The Bernoulli Hypothesis is considered, ie. the cross section remains plane under bending moment.
- Plastifications are only considered in the longitudinal direction of the member.

3.8 FEM Thermal Discretisation.

3.8.1 Introduction.

In the initial stages of this report an investigation was undertaken to find the minimal number of 2-D solid elements required for the thermal analysis to provide good solutions for the structural analysis. Three mesh discretisations for thermal analysis were constructed using the SAFIR pre-processors, *SAFIRwizard* (Franssen et al, 2000) and *Sapphire* (Mason 1999). These pre-processors were used to create finer or coarser meshes for the cross section of the composite beam for the thermal analysis. Reducing the number of finite elements in the thermal analysis increases the speed of the SAFIR structural modelling and decreases the amount of data requiring manual reduction especially in determining the stresses which can only really be managed in *Microsoft Excel* at this stage.

The thermal mesh discretisations form a cross section of the composite member to be later used in the structural analysis. Table 3.8.1 shows the finest discretisation, Mesh A, which was constructed of 1373 nodes encompassing 1246 2-D solid elements. Table 3.8.2 shows the second finest discretisation, Mesh B, which was constructed of 512 nodes encompassing 426 2-D solid elements. Table 3.8.3 shows a coarse mesh, Mesh C, which was constructed using 460 nodes encompassing 377 2-D solid elements.

A structural analysis was undertaken on the three thermal discretisations and outputs for the axial force, bending moment and displacements at mid span were plotted. This involved running structural models with '*pin – pin*' and '*pin – roller*' end fixations, see Figure 5.2.1and Figure 5.3.1 for support schematics. The results were compared to see if a reduction in the use of elements used in the thermal analysis would have a detrimental impact on the structural results. The *pin – pin* and *pin - roller* end supports were used, as they are the boundary conditions for the simply supported case. Any ambiguities in the structural outputs should be discovered at these boundaries.

A 20 ^{o}C per minute linear heating rate was used as the fire growth model for the thermal analysis for the mesh comparison. This is a fairly rapid rate of temperature increase, so the average temperature increase of the two materials will be very different due to the large thermal mass of the concrete. Therefore any discrepancies due to mesh discretisation should be evident.

Table 3.8.1 Mesh A element discretisation.

Element	Y Axis Elements	Z Axis Elements	Total Elements
Top Slab	11	74	814
Bottom Slab	5	52	260
Top Flange	3	24	72
Web	12	2	24
Root Fillet	2	2	4
Bottom Flange	3	24	72
		SUM	1246

Table 3.8.2 Mesh B element discretisation.

Element	Y Axis Elements	Z Axis Elements	Total Elements
Top Slab	4	54	216
Bottom Slab	3	42	126
Top Flange	2	14	28
Web	12	2	24
Root Fillet	2	2	4
Bottom Flange	2	14	28
		SUM	426

Table 3.8.3 Mesh C element discretisation.

Element	Y Axis Elements	Z Axis Elements	Total Elements
Top Slab	4	53	212
Bottom Slab	3	41	123
Top Flange	1	13	13
Web	12	1	12
Root Fillet	2	2	4
Bottom Flange	1	13	13
		SUM	377

3.8.2 Results.

Figure 3.8.1 and Figure 3.8.2 show the output from the structural analysis. It can be seen that even due to the differences in mesh discretisation, there is very little difference in the structural analysis output.

Mesh A is by far the most time and computationally expensive discretisation to use and there seems to be very little benefit in proceeding with it. Mesh C gives good results but there is some scepticism about using only a single layer of elements to model the top and bottom flanges of the 610 UB 101. The extra layer or elements in the flanges as shown in Mesh B takes little extra time to

analyse. For these reasons Mesh B is considered to be the most favourable, and it will be the thermal discretisation to be used for the rest of the analysis carried out in this report.

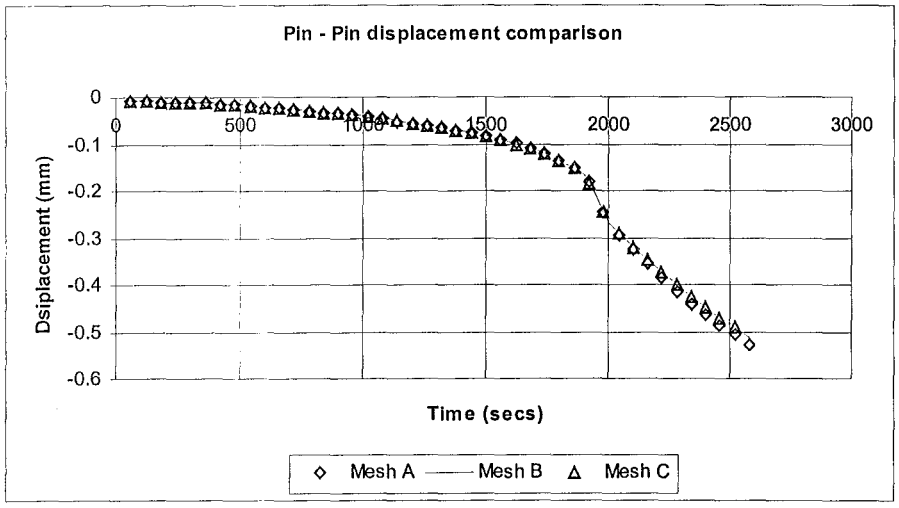

(a) Displacement comparison.

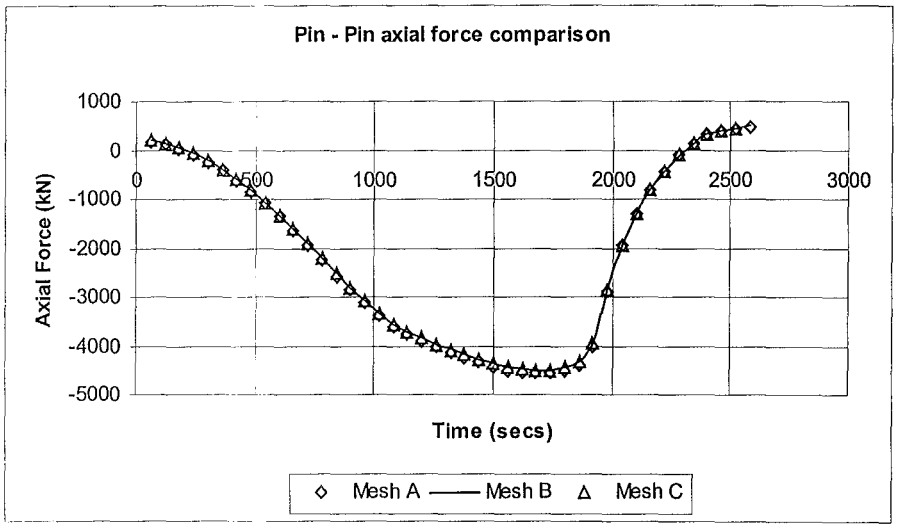

(b) Axial force comparison.

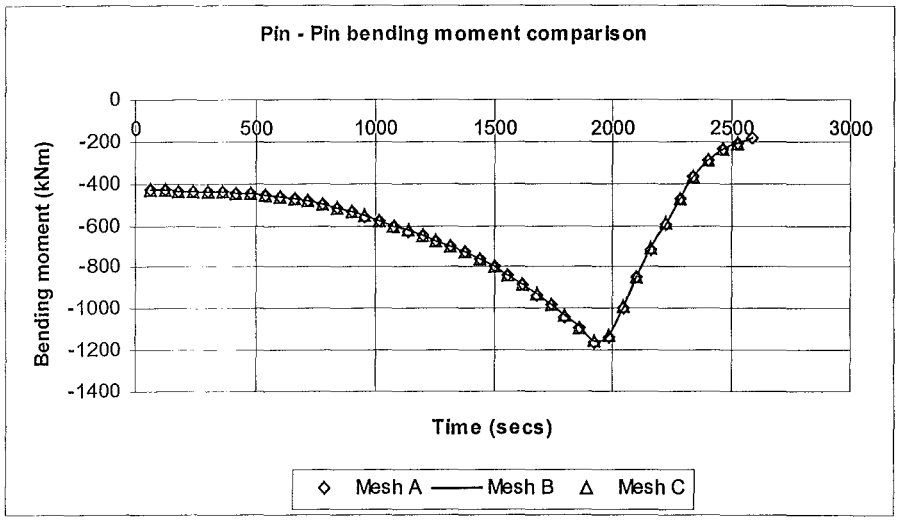

(c) Bending moment comparison.

Figure 3.8.1 Pin - pin support comparison of results at 20°C per minute.

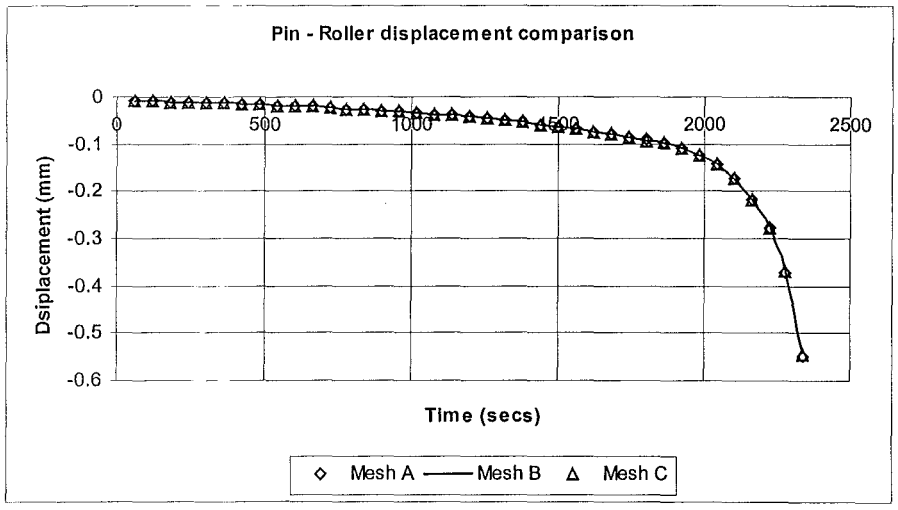

(a) Displacement comparison.

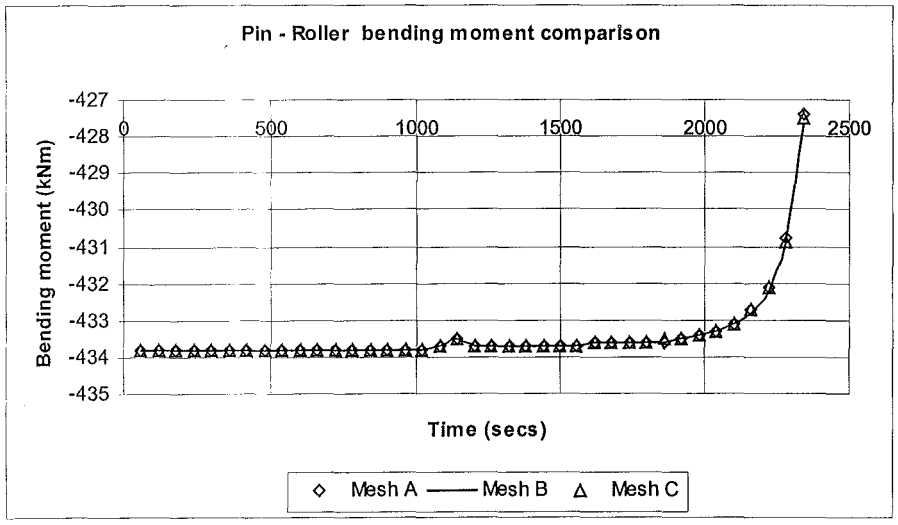

(b) Bending moment comparison.

Figure 3.8.2 Pin - roller support comparison of results at 20°C per minute.

3.8.3 Summary.

The outputs are nearly identical and the savings in calculation and data reduction time make finding a good discretisation a worthwhile exercise. In cases where there are expected to be areas of negative bending moment, reinforcing steel has been introduced to the discretisation. As noted earlier the EC2 (1993) welded mesh is equivalent to 430 grade, 6mm diameter bars at 150mm centres. The discretised reinforcing steel is equivalent in area and has been placed to replicate the actual reinforcing mesh.

3.9 FEM Structural Discretisation.

For the structural discretisation, beam elements have been used for the composite section and a truss element was used for the axial spring. The section was comprised of 41 beam elements, 200mm long, making up the 8.2m long beam. The beam elements have been discretised with two points of integration leading to greater precision of results. The truss element used for the spring was a 200mm diameter circular EC3 steel section with a length of one metre, see Section 6 *AXIAL SPRINGS* for analysis.

As stated the analysis carried out compares an envelope of boundary support conditions. The supports used were placed at the ends of the span, therefore continuity effects have not been analysed in this report. See Section 5 *SUPPORT CONDITONS* for analysis.

The major disadvantage with beam elements is that plane shapes remain plane during the analysis, thus local buckling cannot be modelled. This can, however, be achieved through the use of shell elements at a time and computational cost. Unfortunately this type of analysis falls outside the scope of this report and has not been covered.

4 BEHAVIOUR OF COMPOSITE SECTIONS IN FIRE

4.1 Introduction

In this section of the report observed composite beam behaviour in real fires has been included so that comparison can be made with the finite element analysis in this report. Previous research of composite beam behaviour in fire as well as the material constitutive laws has also been included.

4.2 Real and test fire events in Composite Construction Buildings.

4.2.1 Introduction

In this section the observed behaviour, as described in Bailey et al (1999), from two real British fire events as well as the BRE Cardington Test Facility tests at Bedford have been included. The reason for providing this information is so that comparisons can be made later between the analytical results found in this report and observed behaviour in real fire scenarios.

4.2.2 Broadgate Phase 8 Fire, London

The Broadgate Phase 8 fire occurred in 1990. The fire developed in a partly completed 14 storey office block on the Broadgate development in London. The fire originated in a large site hut on the first floor of the building. Fire temperatures were estimated to be over 1000°C. No structural failure occurred and the integrity of the floor was maintained during the fire. Most of the repair cost was a result of smoke damage rather than being attributed to the structural frame.

The floor was constructed using composite long span lattice trusses and composite beams supporting a composite floor slab. The floor was designed to have 90 minutes fire resistance. At the time of the fire the passive fire protection to the steelwork was incomplete. It was concluded that the structural steel temperature did not exceed 600°C and that the bolted connections did not exceed 540°C. The steel beams had a maximum measures permanent deflection of 270mm with signs of local buckling of the bottom flange and web near the supports. It was concluded that the behaviour

of the beams was strongly influenced by the restraint to thermal expansion of the surrounding cooler structure.

The fabricated steel trusses that supported the floor slab had a maximum permanent deflection of 552mm over a span of 13.5m. Some components of the trusses showed signs of buckling which was due to thermal expansion provided by other members of the truss which caused additional compressive axial forces.

The floor slab consisted of a profiled metal deck, concrete and mesh composite construction. The maximum deformation of the slab was 600mm and some failure in the reinforcement was observed. Steam release and the effects of thermal restraint and differential expansion caused debonding between the metal deck and the concrete in some areas.

A mixture of cleat and end plate connections were used in the construction of the building. No connections failed in the fire but deformation was evident. Some fracturing was also evident. This was attributed to tensile stresses caused during cooling. The connections that displayed fracturing were still able to transfer shear.

4.2.3 Churchill Plaza Fire.

This fire occurred in 1991 in the Mercantile Credit Insurance Building, Churchill Plaza, Basingstoke. This twelve storey building was constructed in 1988 and the steel beams that supported the composite floor had passive protection while the underside of the floor was unprotected. The building was designed to have a 90 minute fire resistance rating.

In this event the fire started on the eighth floor and quickly spread to the tenth floor as the glazing failed. The fire was comparatively cool due to the large areas of ventilation. The protection materials worked well and there was no permanent deformation of the steel. Again the composite floor deck showed signs of debonding from the concrete floor slab, thought mainly to be due to steam from the concrete. No structural repair was required to the steelwork.

4.2.4 BRE Cardington Test Facility Tests.

The tests involved the construction of a eight storey structural steel frame with composite concrete floor slabs. The building was designed and constructed based on a typical modern office building. The footprint of the building covered 21m x 45m and was 33m high. The length of the building was split into five equal bays and the breadth of the building was divided into three bays. The two outer bays were 6m wide while the centre bay was 9m wide. A 9m x 2.5m lift well was placed centrally and two 4m x 4.5m stairwells were placed at either end of the building. The structure was designed as a braced frame.

The beams were designed as simply-supported acting compositely with the floor slab. The composite floor consisted of 0.9mm thick steel deck with an overall 130mm thick slab. Anti-crack mesh was specified as the slab reinforcement consisting of 6mm diameter wires at 200mm centres. Sandbags, with a mass of 11kN, were used to simulate the applied load during the tests.

The objectives of the test program were:

- To provide data to verify computer models of steel frame behaviour in fire.
- To demonstrate the behaviour of large scale structures in fire.
- To provide the basis for the preparation of a more rational design methodology for steel framed buildings under fire conditions.

In all six tests were carried out. These fire tests included a restrained beam, a plane frame, 1st corner, 2nd corner, a large compartment and a large compartment (office). For this report the details of the tests themselves are not important but the observed behaviours become relevant in the comparison with the analytical data in this report.

Results from the tests showed that the beams act compositely with the slab in normal fire conditions. Many of the beams in the tests were unprotected and there was no evidence of structural collapse. The maximum recorded steel temperature was over 1100°C.

As shown in Figure 4.2.1 many of the internal beams showed signs of local buckling in the lower flange and in part of the web in close proximity to the connections. The local buckling was

caused by restraint to thermal expansion and enhanced by negative moments caused by thermally induced curvature and connection restraint. Due to buckling it is recommended that connections are designed as simply supported for fire design. It is suggested that under large deflections the steel beams act in a catenary fashion and that the connections act in tension as will be described later in this report. This enabled the beams provide better fire resistance than was anticipated in the Cardington tests.

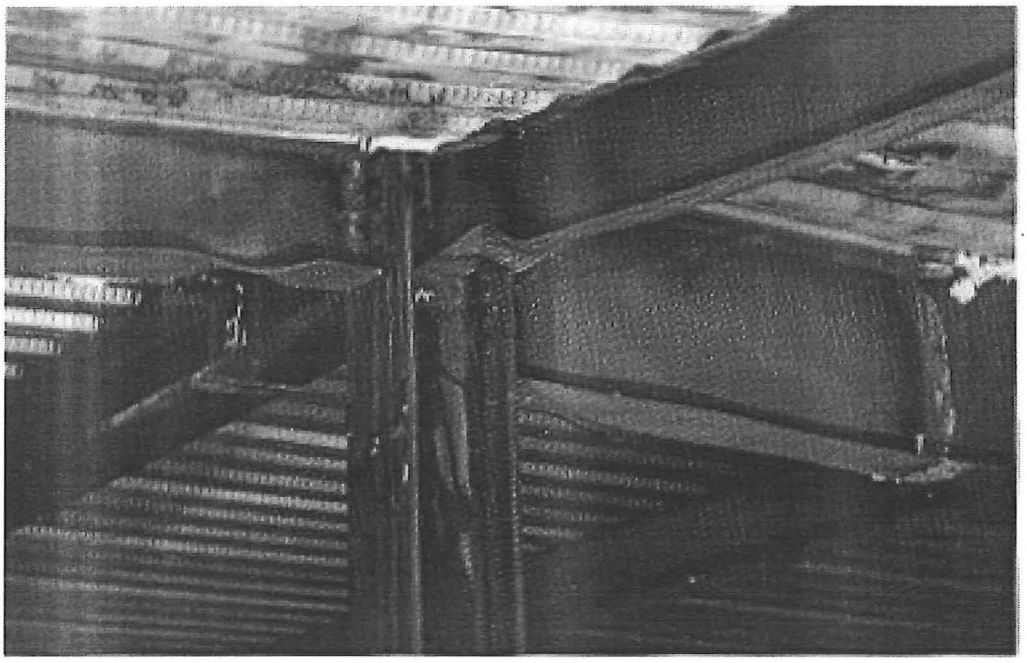

Figure 4.2.1 Local buckling in the bottom flange and web (Bailey et al: 1999).

The composite floor slab performed well during all of the tests reinforcing the fact that composite construction has good inherent fire resistance. The membrane characteristics of the slab had a beneficial effect on the performance of the unprotected beams. Initially the slab uses its full moment capacity to bridge across the weakening heated beam. As the displacements increase further the slab then acts as a tensile membrane through the mesh reinforcement.

Tensile membrane action only occurs when a local area of the slab is heated and there is sufficient restraining effect around the perimeter of the heated area. This action is a 3 D effect and is therefore outside the scope of this report. Whilst not fully understood, tensile membrane action makes the 2 D analysis of composite structures in fire conservative.

4.2.5 Summary

In summary the two real fire events as well as the Cardington fire tests show that composite steel and concrete beam construction have good fire resistance. It is apparent that the steel beams fail by local buckling near the connections due to the axial forces in conjunction with the bending stresses caused by thermal gradients as well as connection restraint inducing negative moments. As the beam begins to fail in bending the slab bridges the loss in strength initially. The slab then acts as a tensile membrane through the reinforcing mesh. This in conjunction with the catenary action of the steel gives the composite good fire resistance under thermal and gravity loading.

4.3 Composite Steel – Concrete Beam Behaviour in Fires.

4.3.1 Introduction

The analysis undertaken in this report is two-dimensional single span finite element model and therefore is a model of the member acting alone as an isolated structure. The analysis simulates a local fire event. This may be quite different to a real fire scenario where hot upper layer gas build up will affect most of the compartments' structural elements, depending on compartment size.

Buchanan (2001) suggests that the fire itself may induce loads in a structure. Restraint from the surrounding cooler structure prevents thermal expansion. Flexural members may also become tension members after large deformations have occurred. Such loads are most likely to occur in steel structures because steel members tend to heat more rapidly than other construction materials. Large restraint forces are attributed to concrete forces because of the thermal inertia of the concrete and its ability to store heat.

The load ratio of a member is loading imposed on the member at a given time as a proportion of the loads that would cause collapse. Buchanan (2001) suggests that most building have a load ratio of 0.5 or less leaving substantial redundancy not only in the members directly affected in the fire event but the entire the structure. When buildings are designed to resist extreme events such as earthquake, snow or wind loading or a combination of loads, the redundancy in the members increase.

Rotter et al (1999) found that interactions within large redundant structures inevitably occurs and that these interactions can completely change the response of the structure, meaning that very sophisticated structural design may be required. The responses that affect the structure are a loss of material strength, the relative stiffness of the adjacent parts of the structure, developments of large deflections, buckling and temperature gradients.

Rotter et al (1999) suggest that the determinate structure collapses when the most highly stressed components of the composite section reach the thermally reduced local strength. In a redundant structure, provided that there is adequate ductility and the structure doesn't suffer form instability, extensive redistribution of load may take place through various load paths when yielding occurs at a single location. Under thermal exposure large deformations may occur without a loss in capacity where a structure is very redundant.

In addition to the response of the structure being dependent on the materials being used, the end connections, redundancy and load paths, the structural behaviour is also dependent on the thermal exposure. The sequence of the fire event, the severity, flame spread and growth rate all affect the structure differently, adding even more variables to this complicated problem. In structural design to resist fire, the common assumption is that the fire will be localised through effective compartmentation.

4.3.2 Thermal Expansion

Composite beams are designed to take their load in bending and shear. Under thermal exposure large compressive axial forces develop in the section of fully or partially axially restrained members due to thermal expansion. During the cooling phase these forces become tensile due to contraction. Initially the steel beam will expand quicker due to its thermal properties but due to the slabs larger area it will induce greater axial forces at lower temperatures.

Rotter et al (1999) suggest that thermal expansion forces may become very large where axial restraint exists and that for a fully restrained steel element compressive yield under thermal expansion occurs at a temperature of only:

$$\Delta T_y = \frac{\sigma_y}{E\alpha}$$ [Equation 4.1]

in which ΔT_y = the temperature rise to cause yield

α = the thermal expansion coefficient

E = the elastic modulus of the steel.

The change in temperature required to cause yield from this relationship is very low. Therefore high stress development in fires is expected from even partially restrained members.

4.3.3 Thermal Buckling

Rotter et al (1999) suggest that when an elastic beam with rigid axial restraint at its ends is heated, compressive stresses develop. Buckling load of the composite structure can be obtained from the relationship presented by Rotter et al (1999).

$$EA\alpha\Delta TL = \frac{\pi^2 EI}{l^2} = \pi^2 EA\left(\frac{r}{l}\right)^2$$ [Equation 4.2].

in which l = effective length of the beam and depends on the restraint conditions.

The elastic modulus of the concrete and steel are temperature dependent as per the Eurocode models (EC2, 1993 and EC3, 1995). The above relationship therefore cannot be so simply defined, as the thrust is non-linear and dependent on thermal expansion and elastic modulus. The stability of the section is dependent on the tangent modulus condition. Rotter et al therefore present this relationship. This model has been used later in this report to check if beam failure is caused by buckling.

$$\int E_T(T,\sigma)\alpha(T)dT = \pi^2\left(\frac{r}{l}\right)^2 E_T(T,\sigma) \qquad \text{[Equation 4.3]}$$

in which $E_T(T,\sigma)$ = the tangent modulus which varies with temperature and stress state.

In reality rigid axial restraint is impossible to achieve. Real structures offer only a limited amount of axial restraint. If the restraint to axial expansion can be represented by a linear translational spring of stiffness k_t for an elastic beam with an unchanging modulus, the compressive axial stress developed by thermal expansion becomes:

$$\sigma = \frac{E\alpha T}{\left(1+\frac{EA}{k_t L}\right)} \qquad \text{[Equation 4.4].}$$

The critical buckling temperature increment is modified to become

$$\Delta T_{cr} = \frac{\pi^2}{\alpha}\left(\frac{r}{l}\right)^2\left(1+\frac{EA}{k_t L}\right) \qquad \text{[Equation 4.5].}$$

Rotter et al (1999) report that for an axially restrained beam with a uniformly distributed load, the effects of heating show a growth of mid span deflection with temperature. A constant modulus elastic behaviour was adopted for these tests. A critical buckling temperature can be clearly identified, and that once achieved, there is a rapid growth in deflection leading to a large deformation state. The axial force in the beam increases with temperature but is close to constant in the post-buckling zone, and additional thermal expansion is absorbed in additional deflection rather than causing increased stresses. In a real fire scenario, for a local fire, in the heating of an axially restrained member, this phenomenon is helpful as it means that adjacent structural elements will not be damaged. Rotter et al (1999) conclude by saying that buckling is good for the structure.

4.3.4 Thermal Gradients

In most real fire situations fire heats the floor and beams from below. This causes temperature differentials through the section. These temperature differentials lead to thermally induced bending or thermal bowing which may increase or decrease deflections.

Rotter et al (1999) suggest that a beam which is axially and rotationally unrestrained at its ends and subjected to a linear thermal gradient which is constant along the length, produces a uniform curvature given by $\phi=\alpha T_y$ where T_y is the gradient of temperature through the beam depth. No stresses are induced and a hot lower surface leads to downward bowing. This scenario has been analysed using SAFIR and the results are shown in sections 6 through 9 of this report.

Rotter et al (1999) also suggest that if the beam is only rigidly restrained against end rotations (the *fixed - slide* case examined in this report), no deflections develop at all in the beam. The beam remains perfectly straight and a constant bending moment is induced throughout the length of the beam $EI\alpha T_y$. The stresses associated with a hot lower surface are the bottom fibre in compression, and in the concrete first cracking occurs on the top unheated surface.

When the beam is rotationally unrestrained the thermal curvature due to a uniform gradient (with no net temperature rise), given by αTy, causes a deflection δy in an axially free beam of

$$\delta_y = \frac{1}{\alpha T_y}\left(1-\cos\frac{\alpha T_y L}{2}\right) \qquad \text{[Equation 4.6].}$$

and in large displacement evaluation this causes the distance between the supports to reduce by

$$\delta_x = L-\frac{2}{\alpha T_y}\left(\sin\frac{\alpha Y_y L}{2}\right) \qquad \text{[Equation 4.7]}$$

Rotter et al (1999) believe that for a *pin – pin* type support arrangement where the beam is axially restrained but rotationally unrestrained, thermal gradients will produce axial tension whereas a uniform temperature rise will cause uniform axial compression. The deformed shape may not give a clear indication whether the beam is in axial compression or tension due to thermal gradients.

Some of these forces may contribute to the load carrying capacity of the beam while others may just induce stresses.

The capacity of a composite section is defined by its sectional properties and its material properties. As temperatures increase the yield and ultimate strength of the steel decreases leading to a loss in strength. The elastic modulus also decreases with temperature, which causes a loss in stiffness.

4.3.5 Large Deflections

As described by Rotter et al (1999), under fire conditions axially restrained beams develop large deflections for several reasons. Thermal expansion in both the steel and the concrete cause large compression forces that lead to buckling which forces the beam down. The main cause of axial restraint is the extensive concrete slab. Due to its high thermal inertia provides an extensive cold surround to the fire. The average temperature of the slab is a lot lower than that of the steel in a typical fire growth event but due to the slabs large cross sectional area induces a lot higher axial forces in the structure. However, as the fire reaches its decay phase, the concrete slab may keep increasing in temperature while the steel beam will cool down. This acts as a heat source for the steel and axial forces may become higher in the decay phase of the fire. The thrust in the slab can be two-dimensional. Slab deflections may increase through cracking leading to significant reductions in strength and rotational restraint.

Reductions in stiffness may lead to a reduction in the rate of deflection due to the reduction in axial force. This may also lead to a decrease in bending moments induced from P-δ effects.

4.3.6 Sources of Restraint

Effective compartmentation of the fire event leads to high axial restraint. If the surrounding structure remains at ambient temperatures this will provide axial restraint to the affected section. Rotter et al (1999) suggest that this restraint may be almost considered rigid.

4.3.7 Strain

When modelling material mechanical behaviour an analytical description is required for the relationship between stresses and strains. Anderburg (1988) and Schneider (1988) have produced models for steel and concrete behaviour where the deformation process at transient high temperature conditions can be described by three strain components, which are separately found in different steady state tests. The three test parameters are the heating process, application and control of load and control of strain.

Constant temperature tests of materials can be carried out in four possible regimes:

(1) Determine stress-strain relationship with stress rate control.
(2) Determine stress-strain relationship with strain rate control.
(3) Creep test - load is kept constant and the deformations are measured over time.
(4) Relaxation test - constant initial deformation is imposed and the reduction of load over time is measured.

When the transient high temperature effects are added, there are two more possible testing regimes:

(5) Transient creep test – the specimen is subjected to an initial load then the temperature is increased at a constant rate while the load is maintained at a constant level and deformations are measured.
(6) The applied load is varied throughout the test in order to maintain a constant level of strain as the temperature is increased at a constant rate.

For most materials, stress strain relationships at elevated temperatures can be obtained directly from the steady state tests at certain elevated temperatures or they can be derived from the results of transient tests.

Buchanan (2001), (from Anderburg (1988) and Schneider (1988)), states that the deformation of materials at elevated temperatures is usually described by assuming that the change in strain ($\Delta\varepsilon$) consists of four components.

$$\Delta\varepsilon=\varepsilon-\varepsilon_i=\varepsilon_\sigma(\sigma,T)+\varepsilon_{cr}(\sigma,T,\tau)+\varepsilon_{tr}(\sigma,T) \qquad \text{[Equation 4.8].}$$

where ε it the total strain at time t.

ε_i is the initial strain at time t = 0.

$\varepsilon_\sigma(\sigma,T)$ is the mechanical, or stress related strain, being a fraction of both the applied stresses and the temperature.

$\varepsilon_{th}(T)$ is the thermal strain being a function only of temperature, T.

$\varepsilon_{cr}(\sigma,T,\tau)$ is the creep strain, being additionally a function of time.

$\varepsilon_{tr}(\sigma,T)$ is the transient strain which only applies to concrete.

The stress-strain (σ–ε) relationship can be measured under stress rate or strain rate control. This relationship must be obtained under a high rate of loading or strain to avoid the influence of creep. Creep is important in ordinary carbon steel above 400°C. The influence of creep displaces the steel σ–ε diagram with a lower ultimate strength. The σ–ε curves can be used to establish compressive or tensile strength, modulus of elasticity and ultimate strain.

Stress strain relationships are not only required during the exposure phase of the fire but the decay phase as well due to structural members cooling in the decay phase and beyond, (Franssen 1990, El-Rimawi et al 1996).

Thermal Strain

The thermal strain (or thermal expansion) is measured on unloaded specimens in a transient test. Published literature suggests that there are only small deviations in thermal expansion for different steels and that is usually modelled linearly with temperature. The thermal expansion for siliceous concrete can also be approximated with a linear relationship. Thermal strain in heated members induces large forces throughout a structure especially where a cooler, more rigid

surrounding structure restrains these members. Thermal strain must be included in any analytical model for this reason.

Creep Strain

Creep is the long-term deformation of materials under constant load, which under ambient temperature conditions is only a problem where members have a very high permanent load. There is some recovery of creep deformation with the removal of load. Creep is an important phenomenon at elevated temperatures because creep can accelerate as load capacity reduces. This leads to secondary and tertiary creep. Acceleration of creep may lead to plastification and eventually runaway failure.

Relaxation is the reduction of stress in materials subjected to constant deformation over a long period of time.

The effect of creep strain in analytical models is not usually explicitly included because of its complexity and lack of sufficient input data. Anderburg (1988) reports that creep strain is unique for every type of steel. Creep strain is usually allowed for implicitly by using σ–ε relationships, which allow for the amount of creep that might usually be expected.

Transient Strain

Transient strain applies to the concrete model only. It is the strain related to the first time heating of the cement paste under load. Transient strain is often included in analytical models for predicting the behaviour of reinforced concrete structures exposed to fire.

Effect of the Strain Components.

A simplification to the relationship shown in Equation 2.8 has been made by Rotter et al (1999)). The last two terms have been ignored, thus:

$$\varepsilon_{total} = \varepsilon_{thermal} + \varepsilon_{mechanical} \qquad \text{[Equation 4.9].}$$

in which $\varepsilon_{mechanical} = \sigma$

$\varepsilon_{total} = \delta$

The total strains govern the deformed shape of the structure δ, through kinematic or compatibility considerations. The stresses in the structure σ (elastic or plastic) depend only on the mechanical strains $\varepsilon_{mechanical}$.

In structures where there is no resistance to thermal elongation the total strain is approximated by the thermal strain and all deflections (bowing or elongation) result only from thermal strain.

$$\varepsilon_{total} = \varepsilon_{thermal} \quad \text{and} \quad \varepsilon_{total} \rightarrow \delta \qquad \text{[Equation 4.10].}$$

In structures where the thermal strains are fully restrained without external loads $\varepsilon_{total} = 0$ as the thermal and mechanical strains are equal and opposite. Both may be very large resulting in high levels of plastification and high stresses.

$$0 = \varepsilon_{thermal} + \varepsilon_{mechanical} \quad \text{with} \quad \varepsilon_{mechanical} \rightarrow \sigma \qquad \text{[Equation 4.11].}$$

In real fire situations most structures have a complex mix of mechanical strains due to applied loading and mechanical strains due to restrained thermal expansion. The combination of these stresses may lead to extensive plastification. The deflections depend only on the total strains and thus may be quite small where restraint exists, but they are associated with extensive plastic straining. Where there is low or little restraint larger deflections may occur, but with a lesser demand for plastic straining and less degradation of the stiffness properties of the materials. These aspects of structural behaviour under fire conditions are quite counter-intuitive to those expected at ambient temperatures.

5 SUPPORT CONDITONS

5.1 Introduction

Four support conditions for the single span beam were analysed in two dimensions through the neutral axis of the section to investigate their effect on behaviour, stability and failure mechanisms for the composite beam. The four support conditions studied were a *pin–roller* case, a *pin–pin* case, a *fixed-fixed* case and a *fixed–slide* case, as illustrated later. While not all of these support conditions are typically used in construction, they make up an envelope of restraint conditions.

The four support conditions have been tested using the linear heat release rate curves as shown in Section 4.2.2 at 5°C per minute as well as 10 and 20°C per minute up to the point of failure (where the stiffness matrix turns negative). In later sections of this report these support conditions are investigated under exposure to the ISO 834 fire.

The displacement, axial force, bending moments and stresses have been investigated to find the significant reasons for the observed behaviour. Displacement, axial force and bending moment diagrams have been plotted individually against time while the steel flange stress diagrams have been plotted against time and compared with the thermally reduced EC3 Proportional Limit stress as well as the EC3 Yield Limit stress. Using the average temperature of the flanges from the *Thermal.out* SAFIR file and finding the comparative steel strength at that time gives plots for the thermally reduced EC3 Proportional Limit as well as the Yield strength from EC3 Table 3.1 (*Reduction factors for stress-strain relationship of steel at elevated temperatures*). The axial force has also been plotted against the critical buckling force to see whether the failure mechanism for the section is buckling. Local buckling of the section can not be included in this analysis, as beam elements are used where plane sections remain plane. A more complex and computationally demanding shell element model would have to be constructed for local buckling analysis.

In the *pin – pin* case and *pin – roller* case only the mid span results were reduced as the failure mechanism is expected to be a plastic hinge forming at the mid span. For the *fixed – fixed*

and *fixed – slide* mechanism, end of span data as well as the mid span data is shown as three plastic hinges are required for these failure mechanisms.

5.2 Pin – Pin Supports (5 ^{O}C per Minute).

Introduction

In this scenario the single bay composite section is tested using a linear heat release rate of 5°C per minute with a *Pin – Pin* end restraint condition, see Figure 5.2.1 for support schematic.

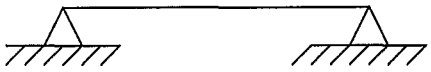

Figure 5.2.1 Support schematic for Pin-Pin case.

Under cold conditions with increasing load the expected failure mechanism for this support condition would be a plastic hinge forming at mid span.

Results

The results of the structural analysis show that the fire resistance of the one bay section is 9540 seconds (159 minutes) under two-dimensional analysis, (Figure 5.2.2). The failure mechanism is the bottom flange of the 610 UB 101 yielding in tension causing a plastic hinge at the mid span. The times for the bottom flange to reach the proportional limit, the yield limit and the failure mechanism are shown in Table 5.2.1.

Table 5.2.1 Behaviour time line of Pin-Pin supports at 5°C per minute.

	Behaviour	**Time**
(a)	Bottom flange reaches Proportional Limit	3960sec (66mins)
(b)	Bottom flange reaches Yield Limit	6540sec (109mins)
(c)	Failure mechanism	9540sec (159mins)

Figure 5.2.2 (d) shows that up to point (a) the composite beam shows elastic behaviour. There is an increase in axial force, displacement and thus an increased bending moment. The increase in compressive axial force starts to level off after 2700 seconds (45 mins) due to a loss in material strength, and displacements increase due to a loss in stiffness. The rate of increase in displacement ($\Delta\delta$) is greater than the rate of decrease in axial force (ΔP) thus the bending moment increases due to P - d effects, where $\Delta P < \Delta\delta$.

Figure 5.2.2 (d) shows that at point (a) the bottom flange stress equals the thermally reduced EC3 proportional limit stress. From point (a) to point (b) the composite section experiences plastification of the bottom flange. Figure 5.2.2 (a), (b) and (c) show that the compressive axial force levels off and then decreases due to the yielding. The displacements increase at a constant rate up to about 6300 seconds (105 mins) and then the slope of the displacement graph increases leading up to yielding of the bottom flange at point (b). The bending moment increases up to yielding of the bottom flange.

At point (b) in Figure 5.2.2 (d) the bottom flange stress equals the thermally reduced EC3 Yield stress at which point the plastic hinge forms at the mid span in the section. From point (b) onwards the bottom flange stress follows the Yield Limit envelope until collapse at point (c) after 9540 seconds. From point (b) to point (c) the axial force decreases to zero and then goes into tension. The tangent slope of the axial force continually decreases. The displacement increases at a constant rate and the bending moment decreases at a decreasing rate of change and reduces below its ambient load value. This is due to catenary action where the load is taken in tension rather than bending. Figure 5.2.2 (a) shows that the axial force goes into tension as the mid span displacement causes the beam to pull in on the supports.

Figure 5.2.2 (e) shows that the axial force never reaches the calculated critical buckling load so the section does not fail by buckling. The buckling load is calculated from Equation 2.2 put forward by Rotter et al (1999). Where the buckling load of the section is:

$$P_{cr} = \frac{\pi^2 EI}{l^2} = \pi^2 EA\left(\frac{r}{l}\right)^2.$$

For these calculations the section was broken down into three components, that being the top slab (Slab 1), the bottom slab (Slab 2) and the 610 UB 101. The reinforcing steel in the slab was ignored because of its minor influence on the buckling capacity. This is also conservative. The average temperatures, at each time step, of each component of the section, were found from the thermal SAFIR output files.

The second moment of area I for the section is determined by using the method outlined in Section 3.5.2 and finding the concrete stiffness ratio, n, at each time step as the Modulus of Elasticity of both the concrete and the steel reduce at varying rates with increasing temperature. In this way the effective width of the concrete relative to that of the steel can be found. The Modulus of Elasticity, E, is determined from the reduction factors published in the Eurocode (EC3: 1995) as described in Section 2.2.3 *EC3 1995 Properties at Elevated Temperatures.*. The effective length, l, is determined from the support conditions and is $1.0L$ for the *pin – pin* supports and $0.7L$ for the *fixed – fixed* supports where L is the length of the beam. Due to yielding during the fire the moment resistance at the ends of the span will decrease thus increasing the effective length. Therefore it is conservative to use an effective length of $1.0L$ for both the *pin – pin* and *fixed – fixed* cases. For the *pin – roller* and *fixed - slide* cases the critical buckling load was not calculated as there are no axial loads in these cases.

The above data was laid out in a *Microsoft Excel* spreadsheet and plotted against axial load data reduced from the structural SAFIR output files as shown below.

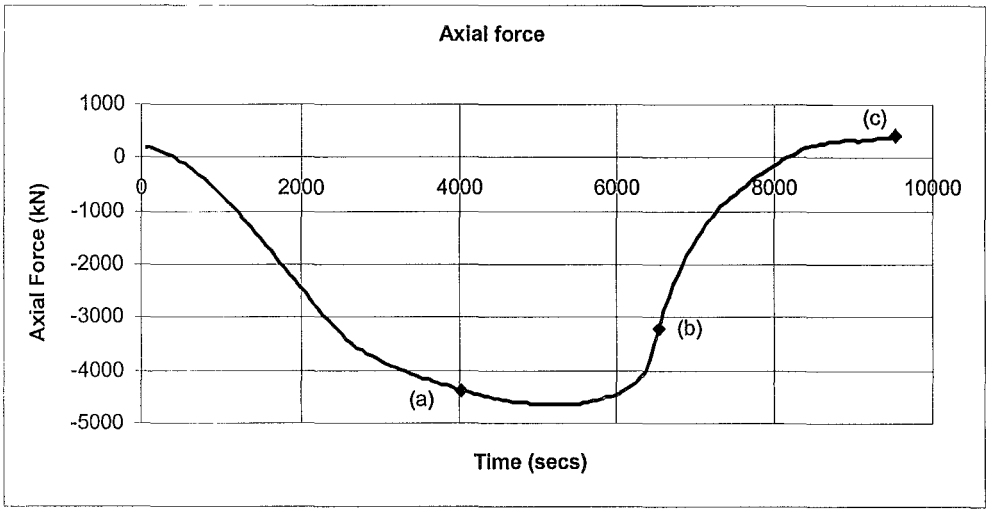

(a) Mid span axial force

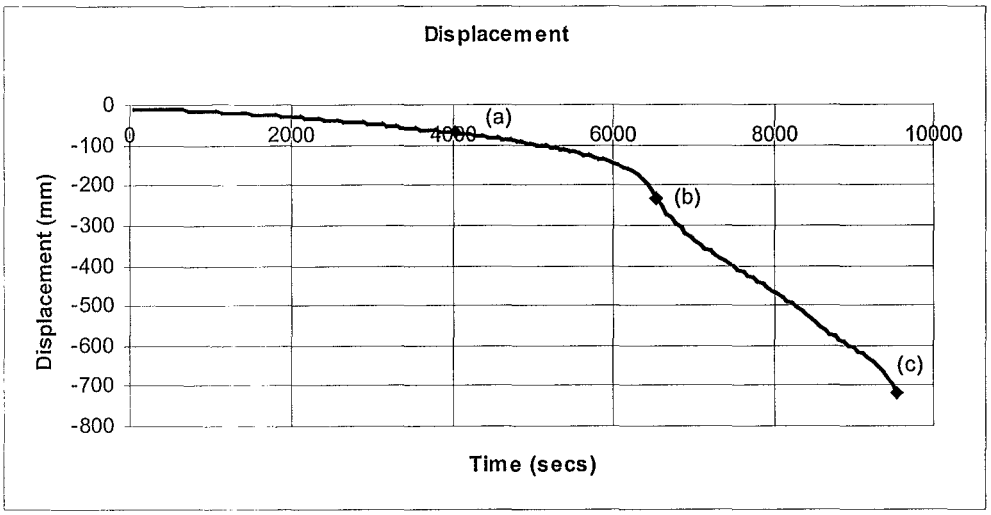

(b) Mid span displacement

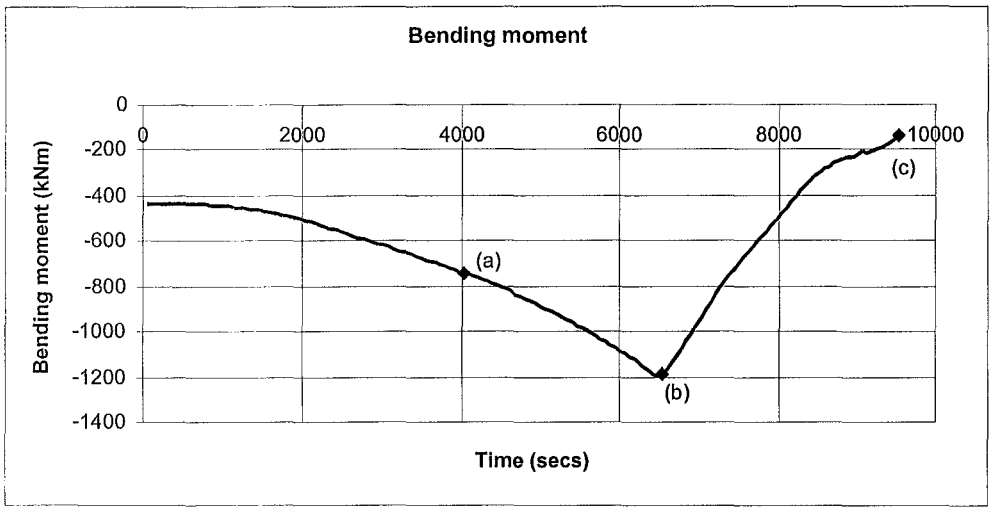

(c) Mid span bending moment

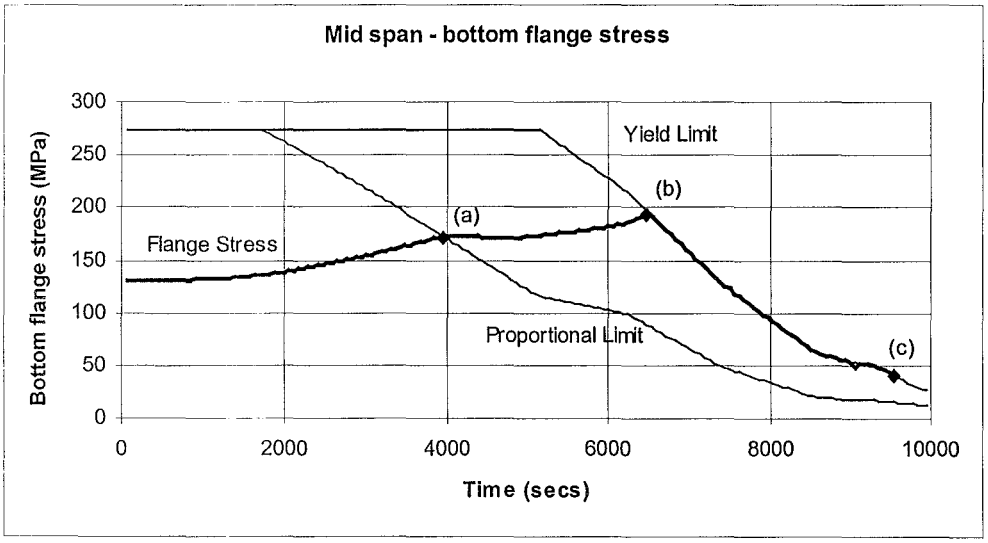

(d) Mid span bottom flange stress

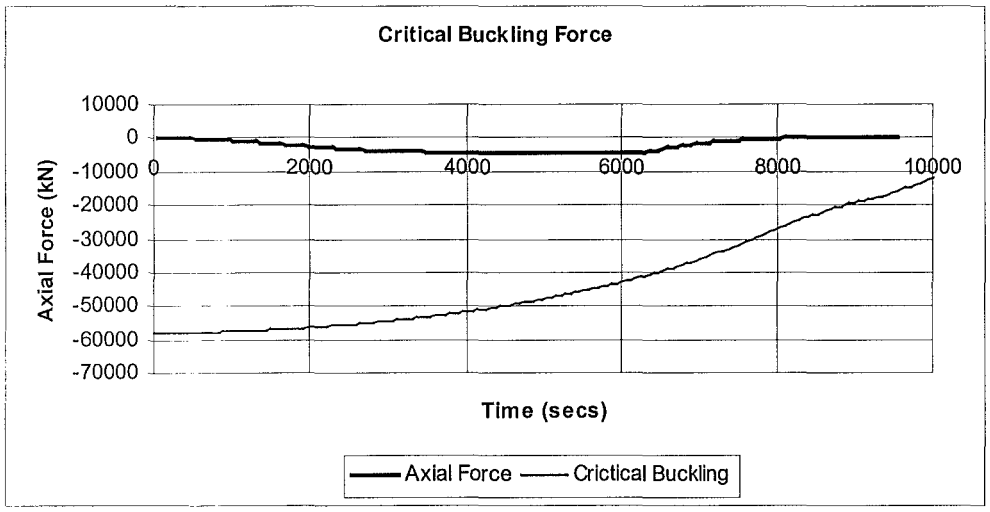

(e) Critical buckling force

Figure 5.2.2 Mid span results for Pin - Pin supports at 5°C per minute.

Figure 5.2.3 shows the shape of the bending moment diagram for the beam at six different time steps. The P-δ effects due to the axial restraint and displacement make the bending moment increase initially for the first four time steps shown below. As the beam yields, the axial force can not be sustained, and the P-δ moment decreases as $\Delta P > \Delta\delta$ for the last two time steps shown below. ΔP is the change in rate of axial force while $\Delta\delta$ is the change in rate of displacement. The last time step shows the effect of the catenary action where some of the load is being taken in tension rather than flexure.

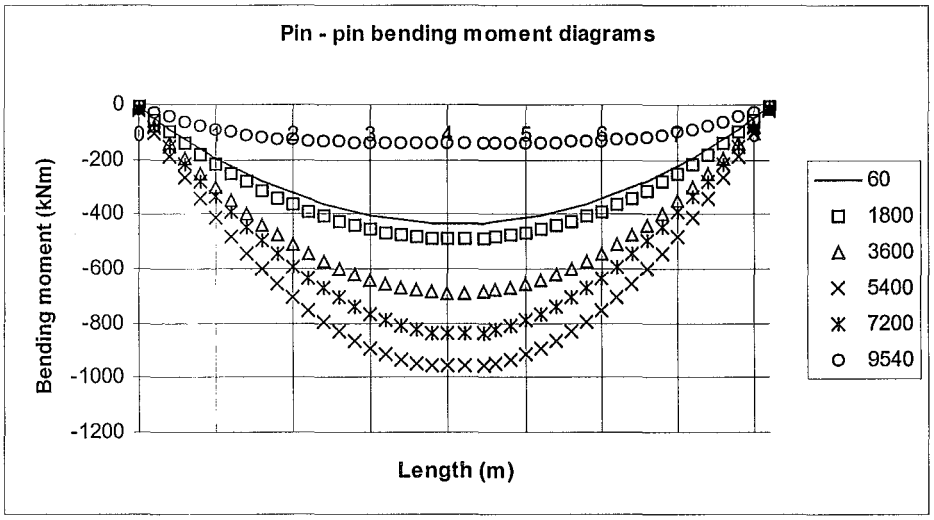

Figure 5.2.3 Pin - pin bending moment diagrams at 5°C per minute.

Summary

A plastic hinge formed at the centre of the span of the section causing a failure mechanism to be obtained as shown in Figure 5.2.4. The displacement increases throughout the fire. This is to be expected because the axial restraint counteracting the thermal elongation causes the section to deflect downwards. The entire length of the beam is under positive moment therefore the whole section is able to contribute to the moment capacity.

Runaway failure looks as though it might occur at point (b) when the bottom flange reaches the yield limit and the rate of deflection increases with a loss of stiffness in the section. At this point the axial force decreases significantly due to yielding, and redistribution of stress throughout the section allows the beam to last another 3000 seconds (50 minutes) prior to collapse due to catenary action. This behaviour was observed in the Cardington tests as explained in Section 4.2 *Real and test fire events in Composite Construction Buildings.*.

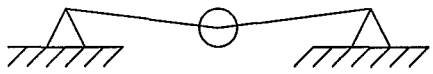

Figure 5.2.4 Failure mechanism for Pin - Pin case.

5.3 Pin – Roller Supports (5 ^{O}C per Minute).

Introduction

In this scenario a *Pin - Roller* support is used for the single bay composite section exposed to a rate of heating of 5°C per minute. Figure 5.3.1 shows the schematic for the *Pin – Roller* case.

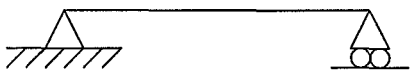

Figure 5.3.1 Support schematic for Pin - Roller case.

For this support condition the failure mechanism will be a plastic hinge forming at the mid span of the beam.

Results

Figure 5.3.2 shows the results of the structural analysis and that the fire resistance of the one bay section is 8280 seconds (138 minutes) under two-dimensional analysis. The failure mechanism is the bottom flange of the 610 UB 101 yielding causing a plastic hinge at mid span. The times for the bottom flange to reach the proportional limit, the yield stress, and the failure mechanism are shown in Table 5.3.1.

Table 5.3.1 Behaviour time line of Pin - Roller supports at 5°C per minute.

	Behaviour	**Time**
(a)	Bottom flange reaches Proportional Limit	3240sec (54mins)
(b)	Bottom flange reaches Yield Stress	7620sec (127mins)
(c)	Failure mechanism	8280sec (138mins)

Figure 5.3.2 (c) shows that up to point (a) the composite member displays elastic behaviour with very little vertical displacement due to the roller allowing for thermal elongation. There is no increase in bending moment because there is no axial restraint causing P-δ moments ie. $M=wl^2/8$. The bottom flange stress increases with displacement until it reaches the EC3 Proportional Yield stress.

Figure 5.3.2 (a) and (c) show that from point (a) to point (b) the section exhibits plastification and the mid span displacement increases. The bottom flange stress decreases while the bending moment stays constant. At point (b) the bottom flange stresses reaches the thermally reduced EC3 Yield stress. At this point the section is yielding and the displacements show runaway failure. The roller support is unable to offer any tension reaction. The member finally collapses 138 seconds (12 minutes) after the bottom flange reaches the yield limit.

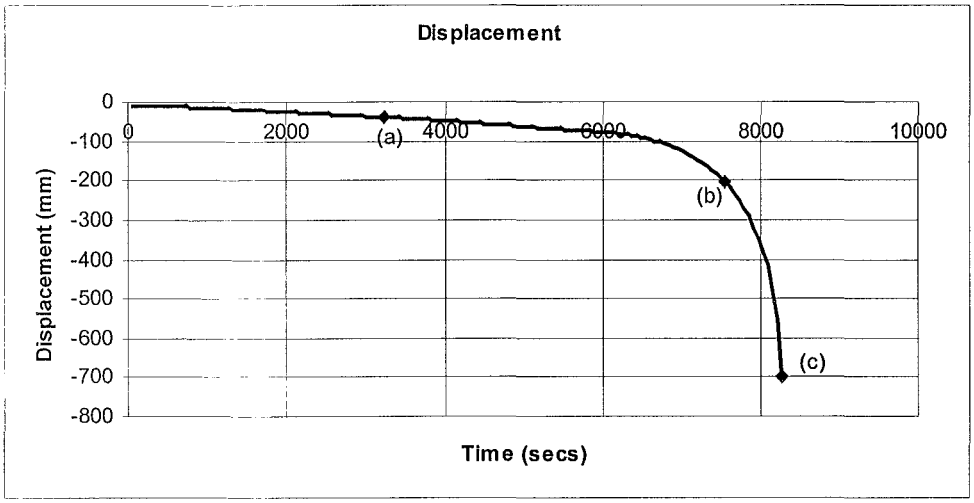

(a) Mid span displacement

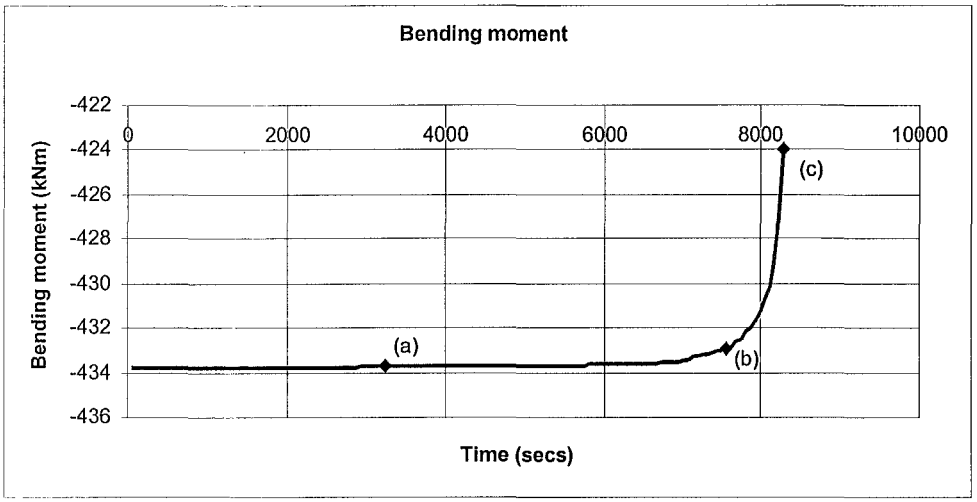

(b) Mid span bending moment

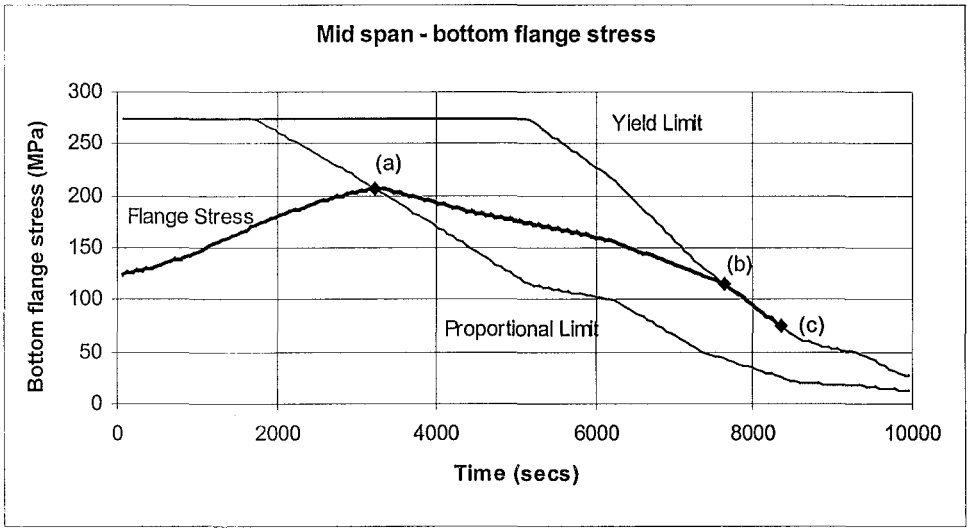

(c) Mid span bottom flange stress

Figure 5.3.2 Mid span results for Pin - Roller supports at 5^{0}C per minute.

Figure 5.3.3 shows that the bending moment stays consistently at the initial moment through out the fire life of the beam. This is expected, as there can be no P-δ amplification of the moment since there is no axial restraint. Near collapse the bending moment decreases slightly. This is due to a reduction in the length of the beam because of bending and the horizontal movement of the roller support. For a simply supported beam $M = wl^2/8$, therefore if l decreases M decreases.

The initial mid span deflection from the SAFIR analysis was 8.7mm after 60 seconds of heating. This compares reasonably well with the manually calculated deflection of 7.4mm in Section 3.10.3 *Simply Supported Deflection.*

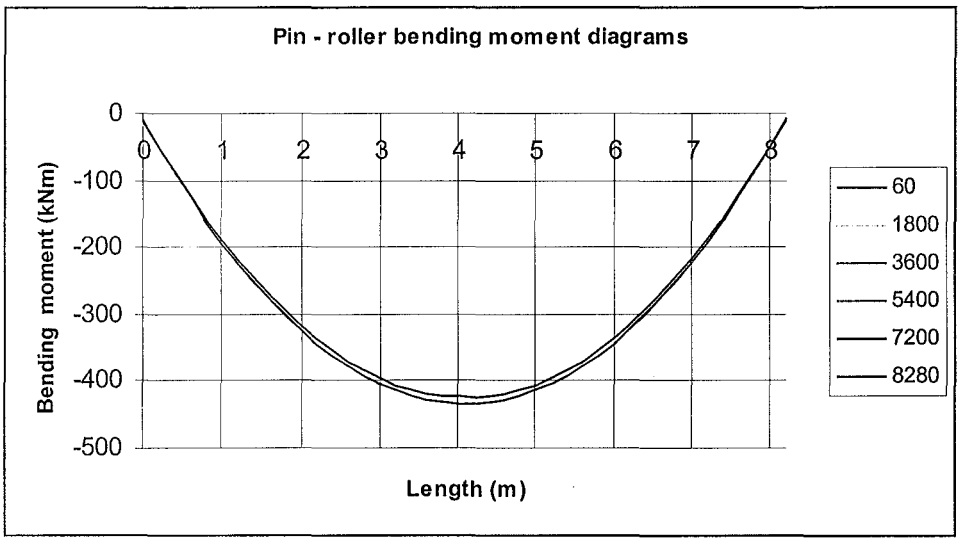

Figure 5.3.3 Pin - Roller bending moments diagrams at 5°C per minute.

Summary

Figure 5.3.4 shows the failure mechanism for the *Pin – Roller* two-dimensional analysis. A plastic hinge initiates in the bottom flange at the mid span of the beam. The tension failure of the bottom flange leads to the neutral axis moving up the section and failure occurring 12 minutes after the bottom flange reaches the yield limit.

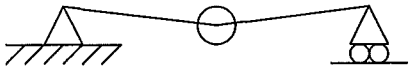

Figure 5.3.4 Failure mechanism for Pin - Roller case.

The displacements are fairly small throughout most of the fire life of the beam due to the roller allowing elongation. The beam maintains its shape until it is near collapse and then exhibits runaway failure.

5.4 Fixed – Fixed Supports (5 ^{O}C per Minute)

Introduction

In this scenario a *fixed - fixed* support is used for the single bay composite beam exposed to a thermal exposure of 5°C per minute. Figure 5.4.1 shows the support schematic for the *fixed – fixed* case.

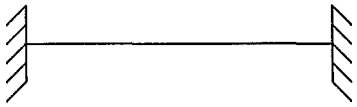

Figure 5.4.1 Support schematic for Fixed - Fixed case.

For this support condition it is expected that the failure mechanism will be three plastic hinges, one forming at each end of the span and one forming at the centre of the beam.

Results

Figure 5.4.2 and Figure 5.4.3 show the results of the thermal and structural analysis for the *fixed – fixed* support case. The fire resistance of the one bay section is 6960 seconds (116 minutes). The failure mechanism is three plastic hinges, two forming at the ends of the span and one forming at the mid span of the composite section as expected. A time line for the composite section

behaviour and for the plastic hinge formation is shown in Table 5.4.1 that relates to Figure 5.4.2 and Figure 5.4.3.

Table 5.4.1 Behaviour time line for Fixed - Fixed supports at 5°C per minute.

	Behaviour	**Time**
(a)	End of span bottom flange reaches the EC3 Proportional Limit stress.	1560sec (26mins)
(b)	Increase in rate of bending moment & displacement at the mid span	1620sec (27mins)
(c)	End of span top flange reaches the proportional limit stress.	2580sec (43mins)
(d)	Mid span top flange stress reaches proportional limit.	3240sec (54mins)
(e)	Decrease in rate of axial force. Increase in rate of bending moment & displacement at the mid span.	5100sec (85mins)
(f)	End of span top flange reaches minimum plastic stress. End of span bottom flange follows thermally reduced EC 3 yield limit.	5100sec (85mins)
(g)	End of span top flange reaches yield limit stress.	6840sec (114mins)
(h)	Failure mechanism achieved	6960sec (116mins)

Figure 5.4.3 (c) shows that up to point (a) the ends of the beam display elastic behaviour. Figure 5.4.3 (a) and (b) show that the axial force (which is reasonably uniform over the entire length of the section) increases, increasing the negative bending moment due to P-δ effects. Figure 5.4.3 (d) shows that at 1200 seconds (20 minutes) the entire steel section goes into compression due to thermal elongation being prevented by axial restraint. Figure 5.4.3 (e) shows that the reinforcing mesh at the end points is in tension due to negative moments. The top layer of the concrete slab has cracked in tension while the bottom layer of concrete shows little or no stress. At point (a) the end of span bottom flanges reach the non temperature affected EC3 Yield Limit, the bottom flanges follow the yield envelope until failure.

When the bottom flange reaches the proportional limit stress at the ends of the span, this in turn causes the mid span displacements and bending moments to increase after point (b) as shown in

Figure 5.4.2 (b), (c) and (d). Up to point (b) the mid span displacement is constant and the bending moment decreases due to increases in the end moments. Figure 5.4.2 (f) shows that the stress in the slab and the mesh stay fairly constant in compression under positive moment. Figure 5.4.2 (d) shows that the bottom flange of the 610 UB 101 goes into compression after 720 seconds (12 minutes).

Between points (a) and (c) in Figure 5.4.3 (e) the reinforcing mesh stress increases in tension while the bottom layer of concrete in the slab still exhibits no stress. Figure 5.4.3 (a), (b), (c) and (d) shows that the axial force increases and the negative bending moment decreases until it reaches zero at point (c) when the top flange at the ends of the span reach the EC3 Proportional Limit stress. The top flanges stay in the plastic region until point (g) where they reach the EC3 Yield stress and follow the yield envelope until failure.

Between points (b) and (d) in Figure 5.4.2 (a), (b) and (c) the mid span axial force and displacements increase at a relatively uniform rate leading to an increase in the positive bending moment. At point (d) in Figure 5.4.2 (e) the mid span top flange reaches the thermally reduced EC3 Proportional Limit stress but there is no detrimental effect on the rest of the beam at this time due to stress redistribution. Between points (b) and (e) in Figure 5.4.2 (a) and (d) the bottom flange displays effects of stress redistribution where the stress stays relatively constant (a slight decrease and then gradual increase) while the displacement increases at a uniform rate. Figure 5.4.2 (a) and (b) show that the axial force increases at a decreased rate between points (d) and (e) while the displacement increases at a uniform rate. The bending moment increases at a decreasing rate due to P-δ effects.

Between points (c) and (f) in Figure 5.4.3 the end of span behaviour is similar to that in the mid span because of the decreasing rate at which the axial force increases. The bending moment increases at a decreasing rate, due to yielding of the section. Figure 5.4.3 (e) shows that at point (c) the tension stress in the reinforcing mesh decreases and the bottom layer of concrete (Layer 11) goes into compression. This is because the end of span top flanges reaches the EC3 Proportional Limit causing a shift in the neutral axis. Figure 5.4.3 (d) shows that at point (f) the top flange reaches the minimum plastic stress in compression, this then increases until the yield limit stress is reached. After point (f) in Figure 5.4.3 (e), the mesh stress increases to yield in tension and the compression stress in bottom layer of concrete in the slab decreases slightly and then increases rapidly. The top layers of concrete do not contribute to the moment capacity as they have cracked in tension. Figure

5.4.3 (a) and (b) shows that there is a drop off in axial force but an increase in bending moment due to the increasing mid span displacement, where the rate of change in displacement is greater than the rate of change in axial force, $\Delta\delta > \Delta P$.

Figure 5.4.2 (a), (b) and (c) shows that after point (e) the axial force decreases due to yielding and the mid span displacement and bending moment increase at a greater rate of change. Increasing mid span displacement causes the third plastic hinge formation and the failure mechanism to be achieved at point (h).

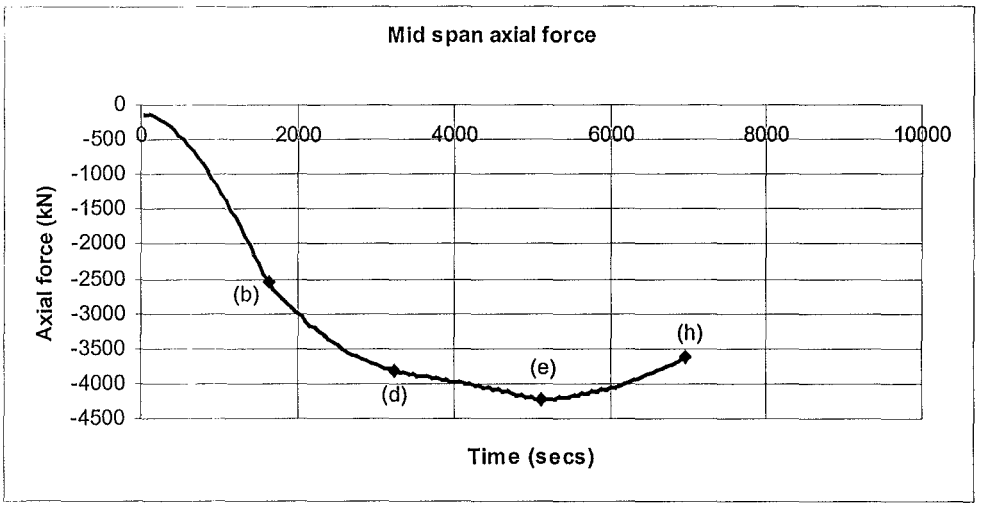

(a) Mid span axial force

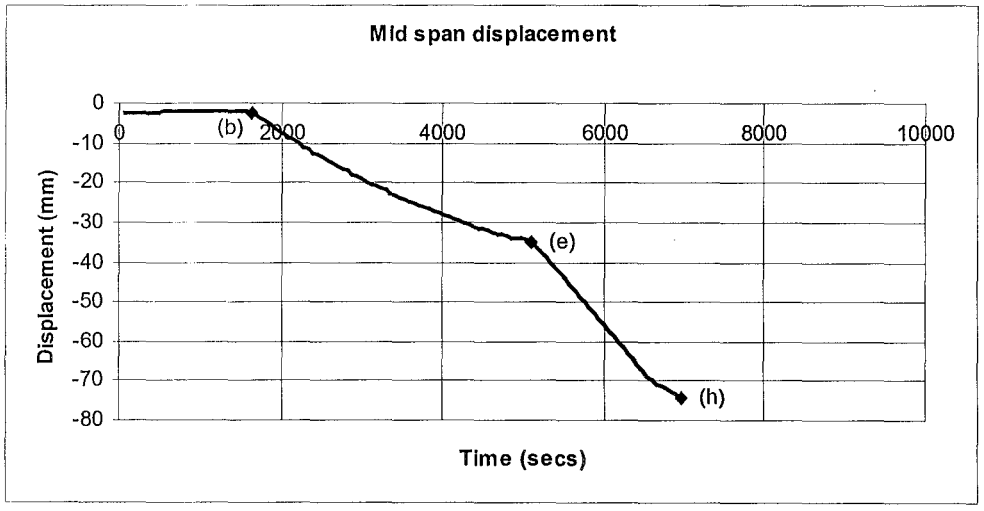

(b) Mid span displacement

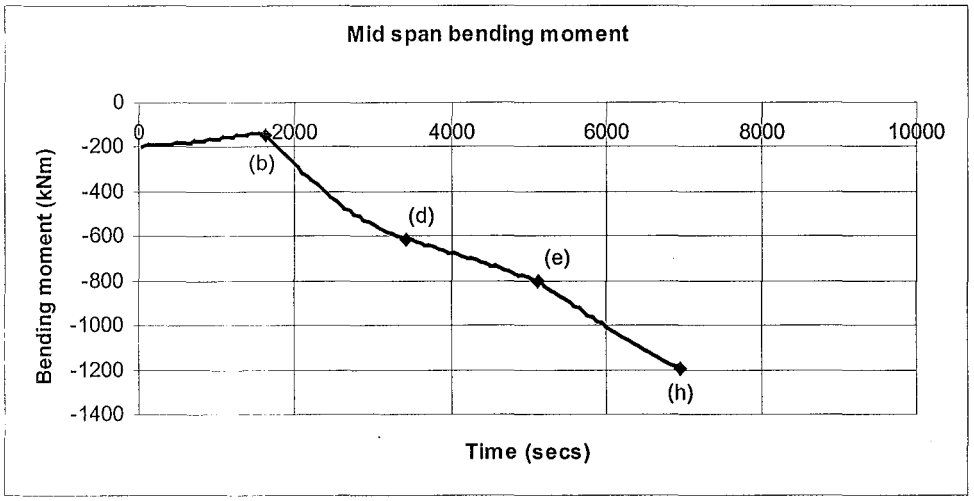

(c) Mid span bending moment

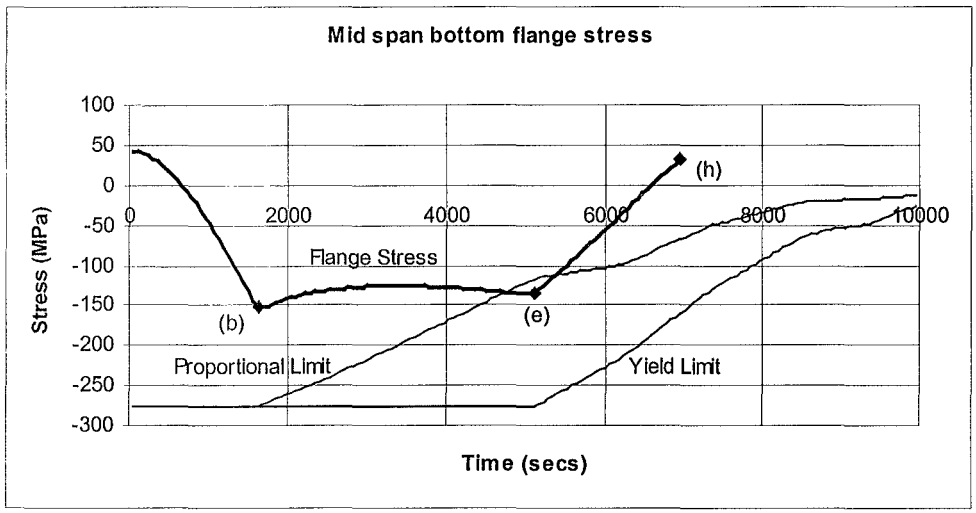

(d) Mid span bottom flange stress

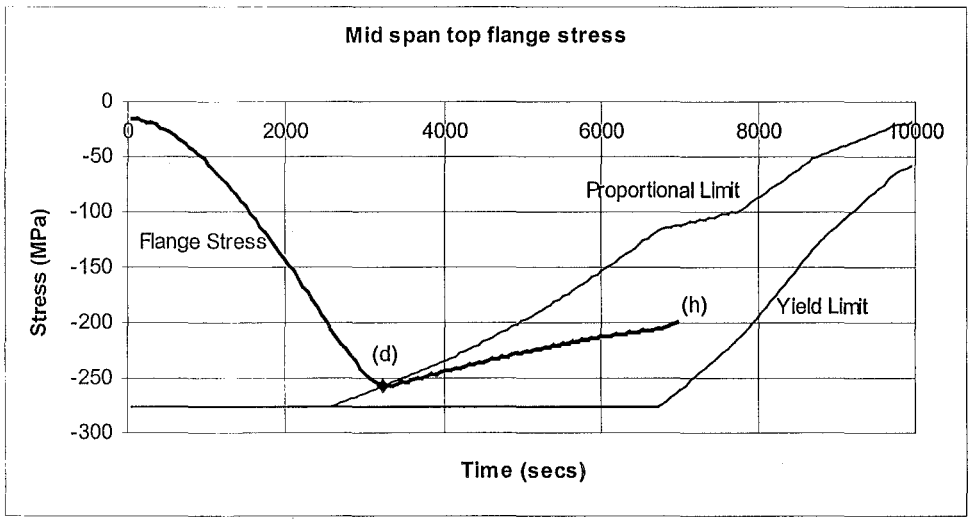

(e) Mid span top flange stress

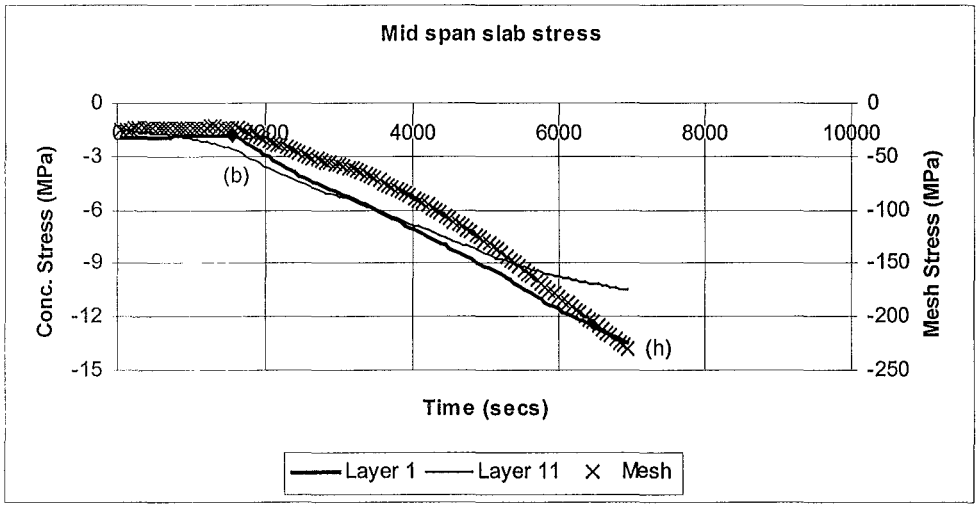

(f) Mid span concrete slab stress

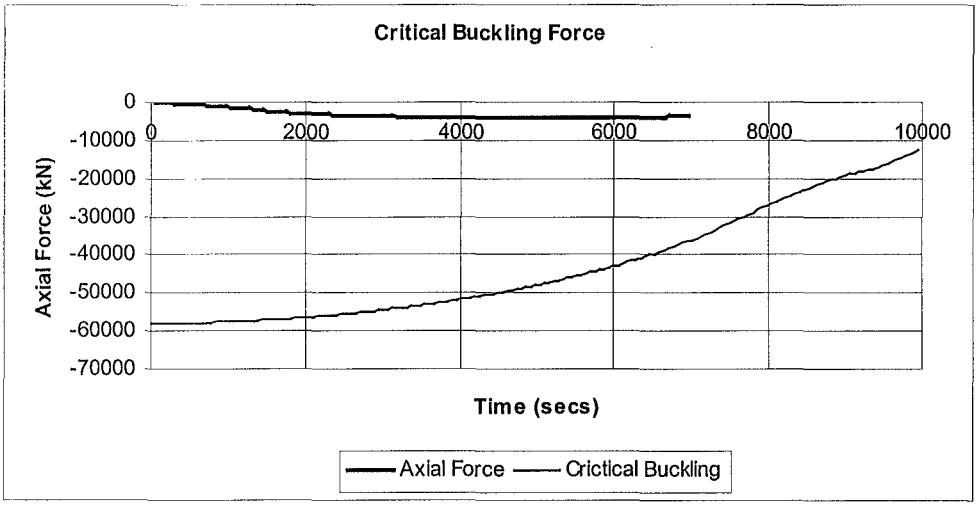

(g) Critical buckling

Figure 5.4.2 Mid span results for Fixed - Fixed supports at 5°C per minute.

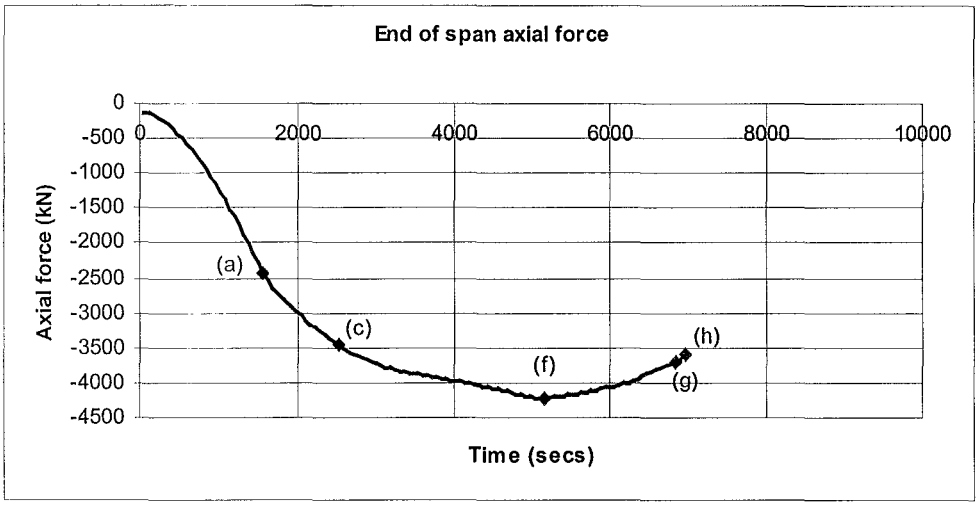

(a) End of span axial force

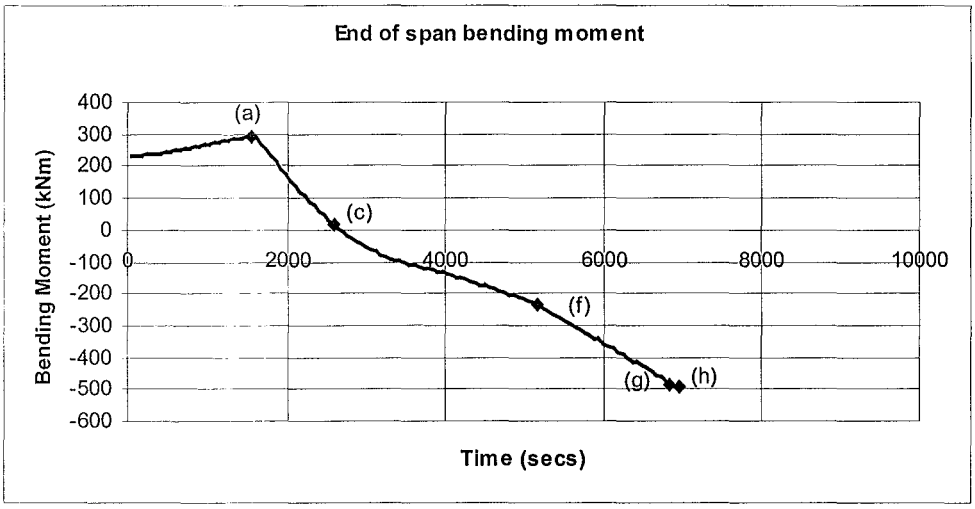

(b) End of span bending moment.

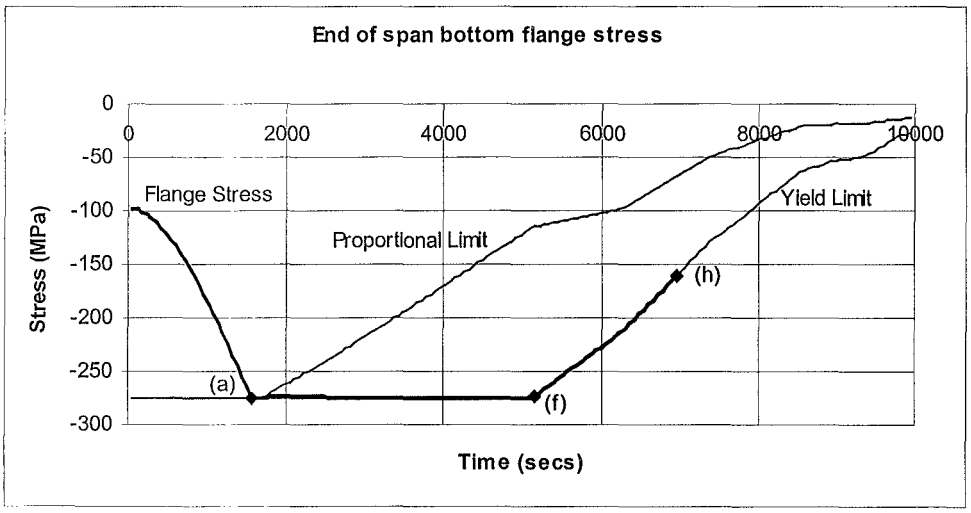

(c) End of span bottom flange stress

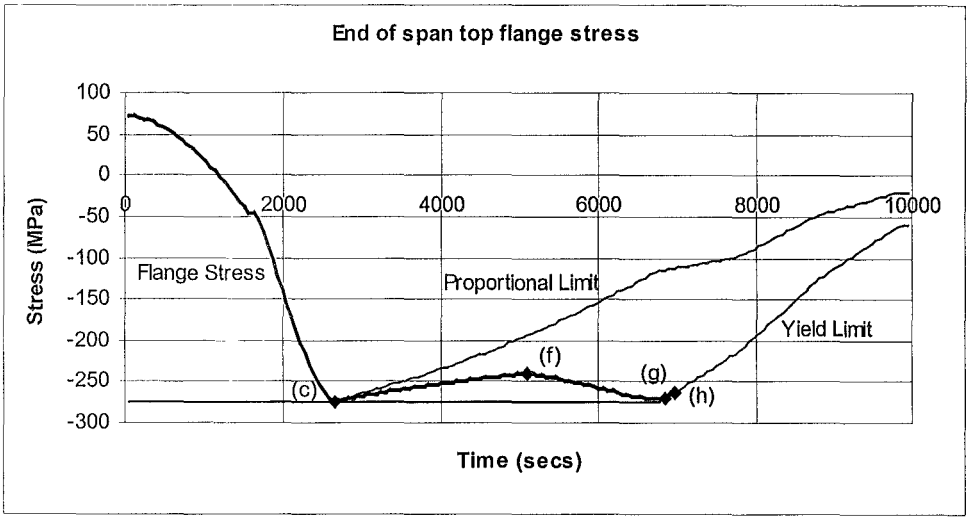

(d) End of span top flange stress

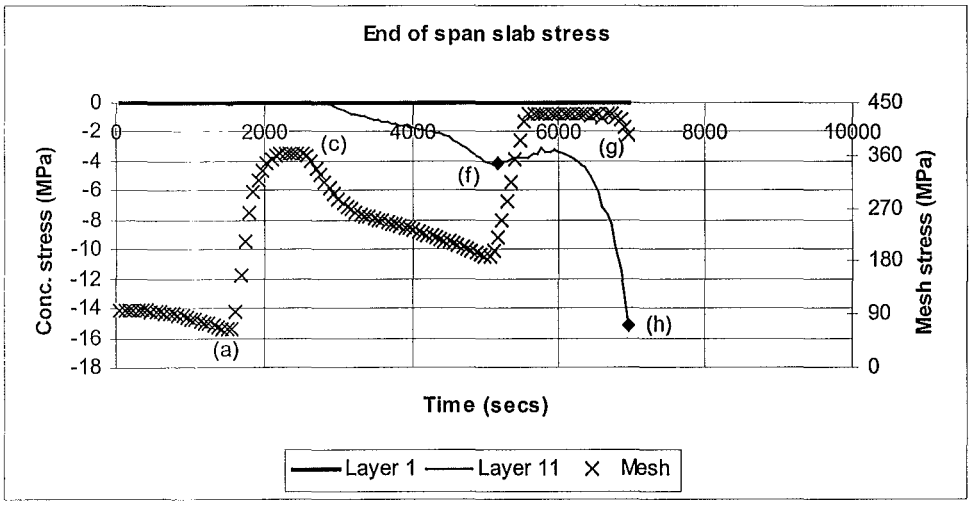

(e) End of span slab stress

Figure 5.4.3 End of span results for Fixed - Fixed supports at 5°C per minute.

Figure 5.4.2 (g) shows that the axial force doesn't reach the critical buckling load and therefore the section doesn't fail by buckling.

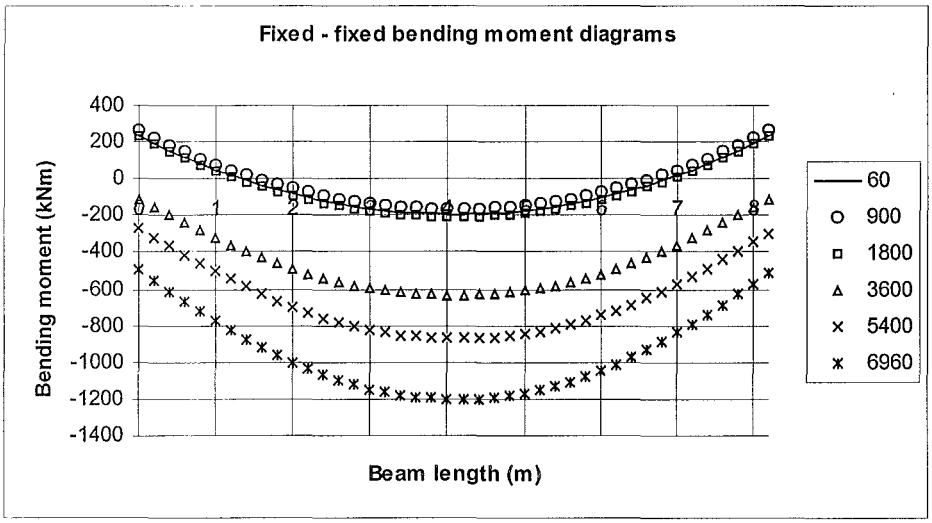

Figure 5.4.4 Fixed - Fixed bending moment diagrams at 5°C per minute.

Figure 5.4.4 shows that initially the bending moment stays relatively constant for the first three time steps. For the next three time steps the positive bending moment increases and the negative moment decreases until failure. The end of span moments turn positive due to plastic

hinging of the bottom and then top flanges of the 610 UB 101 as the concrete cracks early due to the thermally induced hogging at the ends of the span.

The curvature in the bending moment diagram increases during the fire because of P-δ amplification, initially from axial load and then displacement after yielding.

Summary

Figure 5.4.5 shows the failure mechanism for the *fixed – fixed* two-dimensional analysis. Plastic hinges initially form at the ends of the span due to compression and bending moment stresses in the bottom flange, 1(a) and 1(b), (Figure 5.4.5). The compression failure of the bottom flange leads to an increase in the mid span displacement increasing the mid span bending moment. The increasing axial force and loss of capacity in the bottom flange lead to yielding of the top flange at the ends of the span. This in turn leads to greater mid span displacement and the formation of the mid span plastic hinge, 2 in Figure 5.4.5. Load redistribution causes the stresses in the bottom flange to decrease while the stresses in the bottom layers of the slab and reinforcing mesh increase.

When the end of span bottom flange stress reaches the yield limit, the bending moment capacity at the ends of the span decreases due to plastic hinging. The compressive stresses due to thermal elongation are so high that the end of span top flange reaches the Proportional Limit stress when there is only a slight reduction due to temperature effects.

The increase in displacement at mid span and the high compressive axial forces cause the section to form the three plastic hinges, the expected failure mechanism. It is interesting to note and quite counter intuitive that this mechanism has the least resistance to fire. The high stresses at the ends of the beam cause the steel flanges to yield and the concrete slab doesn't contribute to the moment capacity as it is in tension.

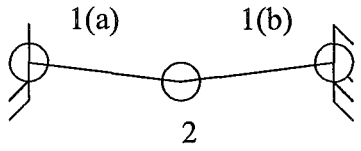

Figure 5.4.5 Failure mechanism for Fixed - Fixed case.

5.5 Fixed - Slide Supports (5 ^{O}C per Minute)

Introduction

In this scenario a *fixed - slide* support is used for the single bay composite beam exposed to a thermal load of 5°C per minute. Figure 5.5.1 shows the support schematic for the *fixed – slide* case.

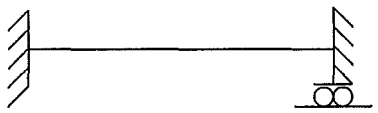

Figure 5.5.1 Support schematic for Fixed - Slide case.

For this support condition it is expected that the failure mechanism will be three plastic hinges, one forming at each end of the span and the third forming at the centre of the beam.

Results

Figure 5.5.2 and Figure 5.5.3 show the results of the thermal and structural analysis. The fire resistance of the one bay section is 8580 seconds (143 minutes) under two-dimensional analysis. The failure mechanism is the formation of three plastic hinges, two forming at the ends and one forming at the mid span of the composite section as expected. A time line for the composite section behaviour and for the plastic hinge formation which relates to Figure 5.5.2 and Figure 5.5.3 is shown in Table 5.5.1.

Table 5.5.1 Behaviour time line for Fixed - Slide supports at 5°C per minute.

	Behaviour	Time
(a)	Top layer of concrete slab cracks in tension at mid span.	1200sec (20mins)
(b)	End of span reinforcing mesh yields.	2400sec (40mins)
(c)	End of span top flange reaches proportional limit.	3060sec (51mins)
(d)	End of span bottom flange reaches proportional limit.	3360sec (56mins)
(e)	Mid span reinforcing mesh yields.	3540sec (59mins)
(f)	Maximum moment reached at end of span.	4080sec (68mins)
(g)	Bottom layer of concrete slab goes into compression mid span.	7140sec (119mins)
(h)	End of span bottom flange reaches yield limit.	7680sec (128mins)
(i)	Mid span bottom flange reaches the proportional limit.	7740sec (129mins)
(j)	Mid span top flange reaches the proportional limit.	8340sec (139mins)
(k)	Failure mechanism achieved.	8580sec (143mins)

Figure 5.5.2 (b) shows that from the initial stages of the fire the positive mid span bending moment decreases due to thermal bowing until approximately 1200 seconds when the mid span starts to hog and go into negative moment. Figure 5.5.2 (e) shows that the top of the concrete slab cracks under the tensile stress and the reinforcing mesh tensile stress increases. The bottom layer (Layer 11) of the slab also has tensile stress but does not reach the 0.5 MPa tensile stress capacity.

From point (a) to point (e) in Figure 5.5.2 (a) and (b) the mid span positive moment decreases and then goes into negative bending with no change in displacement. Figure 5.5.2 (c) and (d) show that the tensile stress in the top flange increases and the bottom flange of the steel beam goes into compression.

Figure 5.5.3 (a) shows that initially only the moments at the ends of the beam are affected. The negative moments increase due to thermal bowing. Figure 5.5.3 (d) shows that at point (b) the reinforcing mesh yields and the concrete cracks due to the tension stresses. Figure 5.5.3 (a) and (c) shows that between points (b) and (c) the negative bending moment increases and the top flange

reaches the thermally reduced EC3 Proportional Limit in tension forming the first plastic hinge. The bending moment increases up to point (d) where the stress increases in the bottom flange as shown in Figure 5.5.3 (b), until it also reaches the thermally reduced proportional limit and begins to yield. The stress stays constant until point (f) when the end of span moment decreases.

At point (e) in Figure 5.5.2 (c) and (e) the reinforcing mesh yields in tension at the mid span and the bottom flange compression stress reaches its maximum. Figure 5.5.2 (a) and (b) show that the tangent slope of the displacement starts to increase at the same time and shortly after this the mid span reaches its maximum moment. Figure 5.5.2 (d) shows that the top flange resists the moment increase in tension. The negative bending moment starts to decrease and at point (g) the bottom layer of the concrete slab goes into compression as the mid span is transferring back into positive moment.

From points (f) to (h) in Figure 5.5.3 (a), (b) and (c) the end of span bottom and top flange stress decreases because of yielding and the negative moment drops. At point (h) the bottom flange stress reaches the EC3 Yield Limit and follows the yield envelope down until failure at point (k).

Figure 5.5.2 (b) and (c) show that the mid span bottom flange reaches the thermally reduced EC3 Proportional Yield Limit stress at point (i) just after the transfer back into positive moment. Figure 5.5.2 (d) shows that at point (j) the top flange reaches the thermally reduced EC3 Proportional Limit stress as well. Figure 5.5.2 (b) and (e) show that the increase in positive moment is taken up by the increase in compressive stress in the slab and plastification in the flanges. Figure 5.5.2 (c) shows that the section fails when the bottom flange reaches the EC3 Yield limit and the third plastic hinge is formed after 8580 seconds. A runaway failure occurs due to the displacements causing the third plastic hinge to pull back in on the roller, which can not take tension forces.

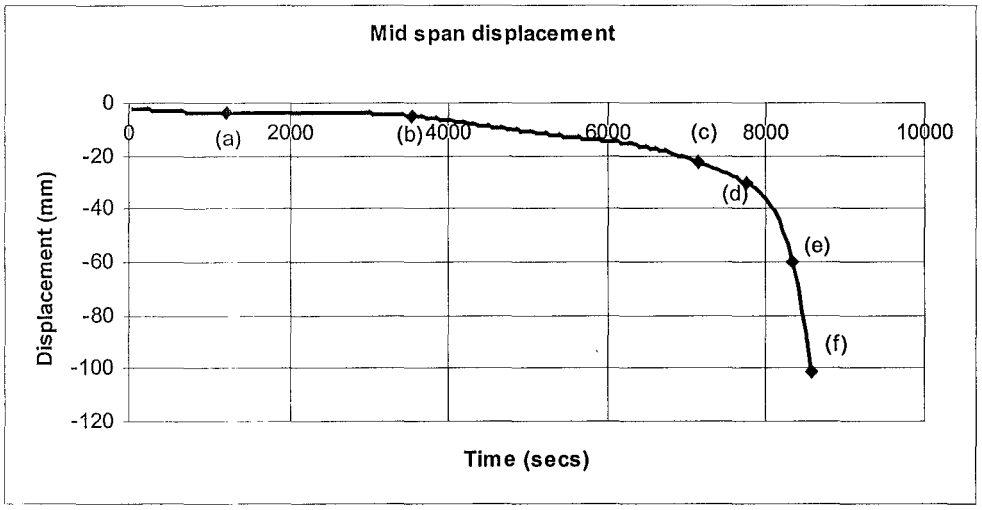

(a) Mid span displacement

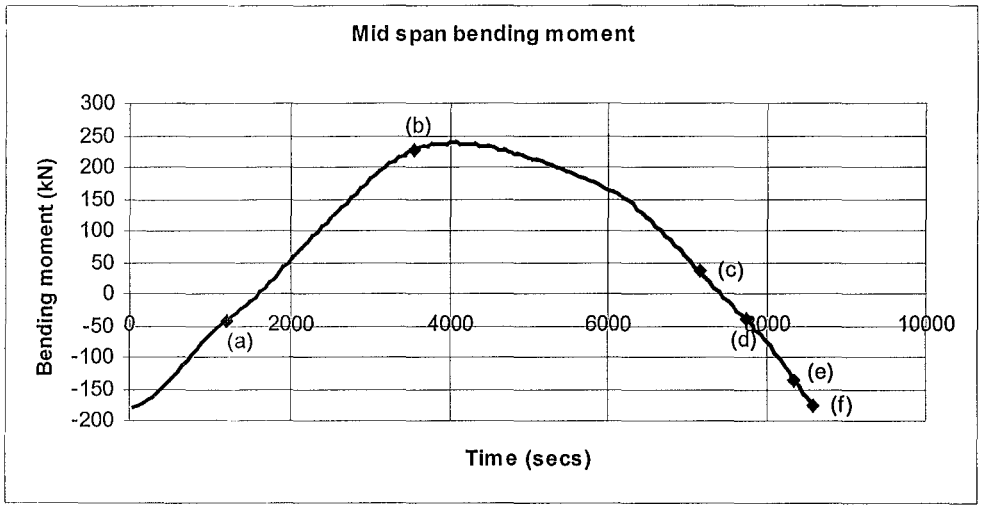

(b) Mid span bending moment

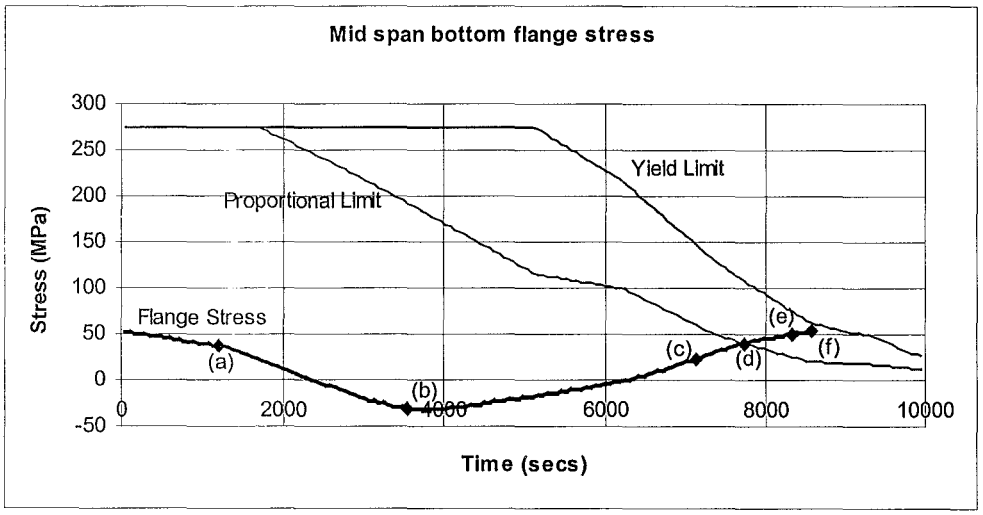

(c) Mid span bottom flange stress

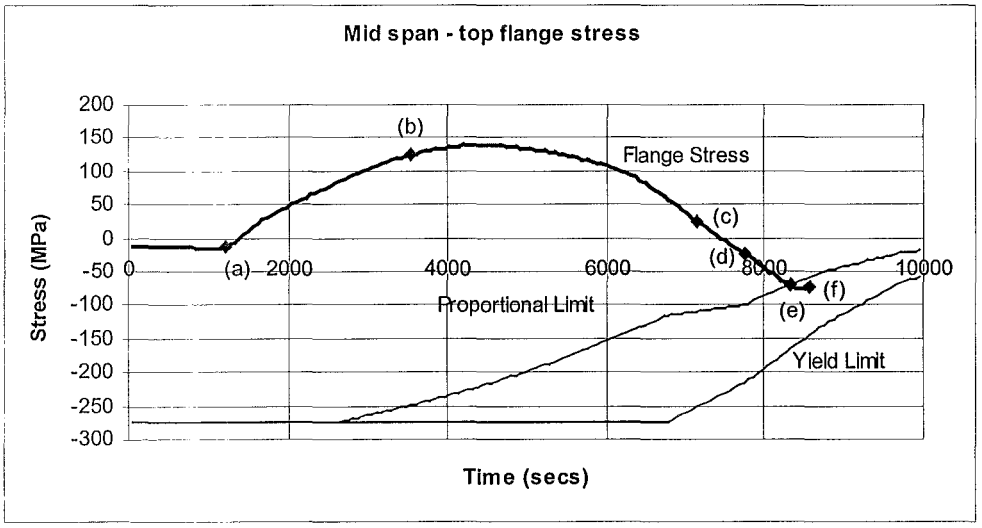

(d) Mid span top flange stress

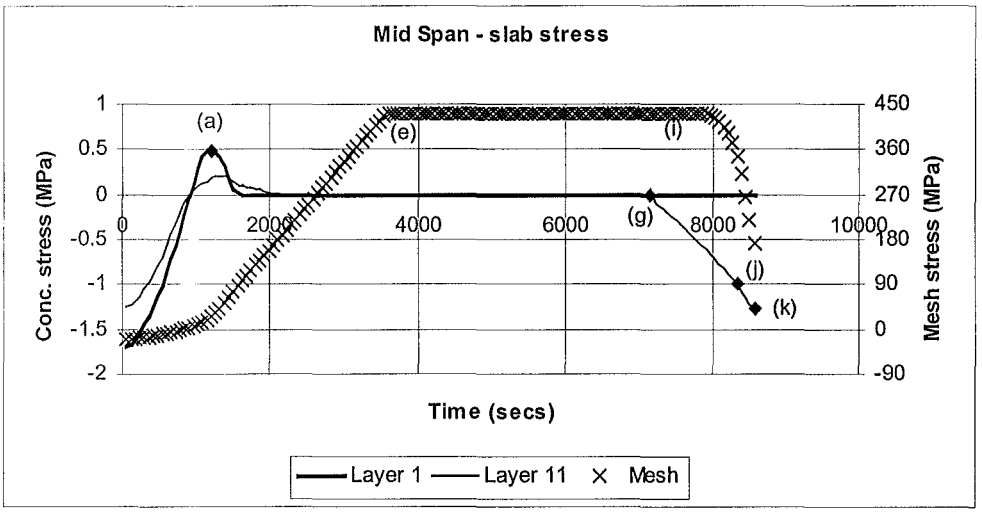

(e) Mid span slab stress

Figure 5.5.2 Mid span results for Fixed - Slide supports at 5°C per minute.

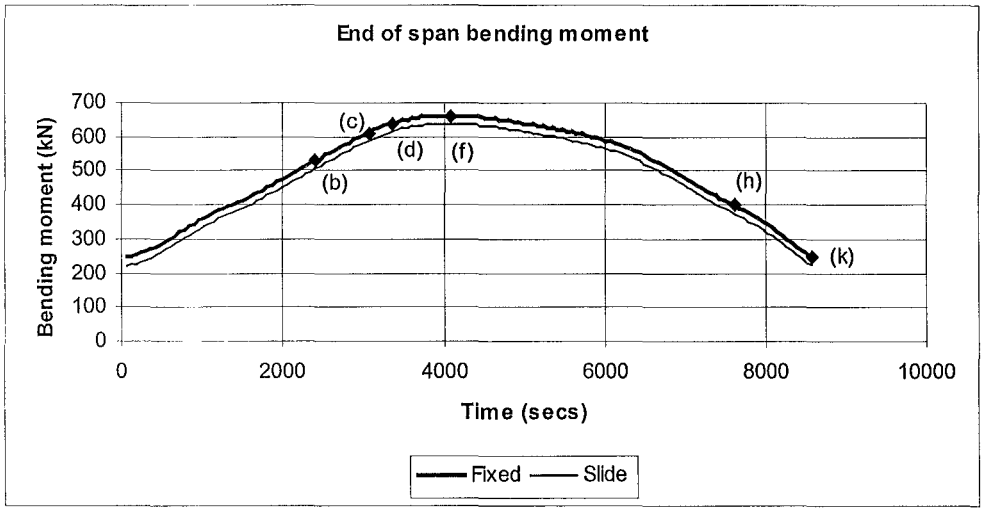

(a) End of span bending moment

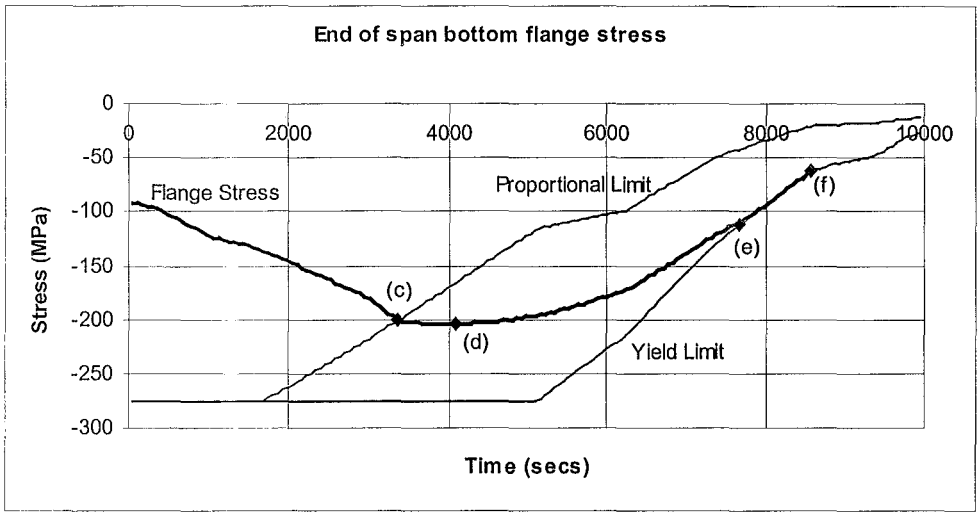

(b) End of span bottom flange stress

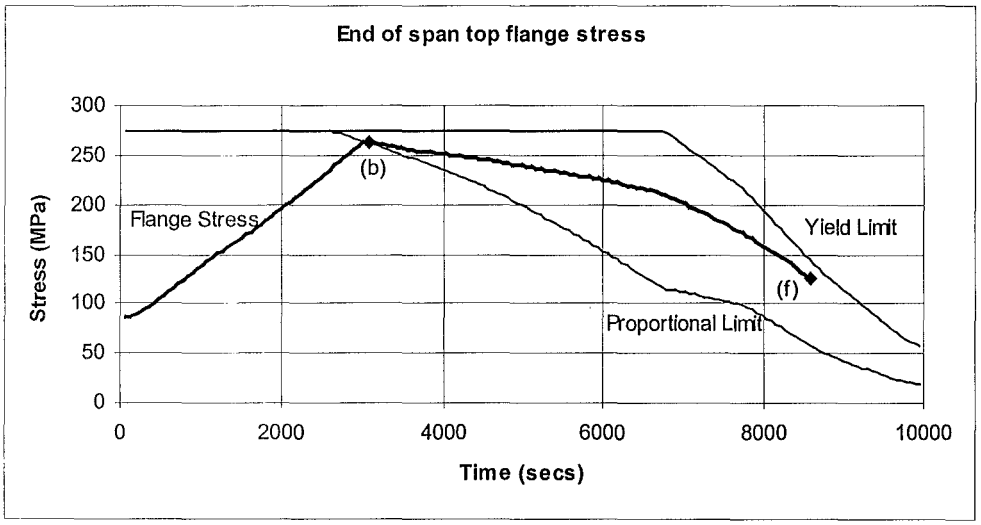

(c) End of span top flange stress

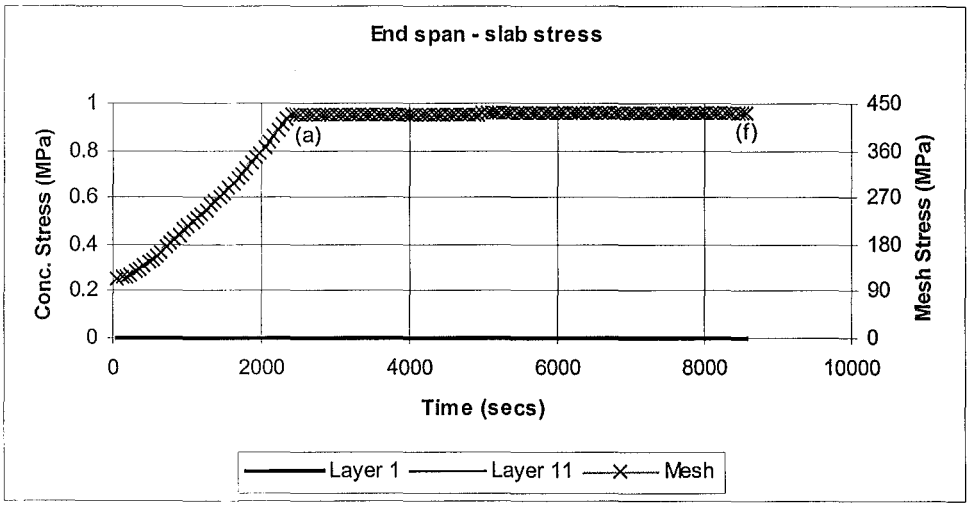

(d) End of span concrete slab stress

Figure 5.5.3 End of span results for Fixed - Slide supports at 5°C per minute.

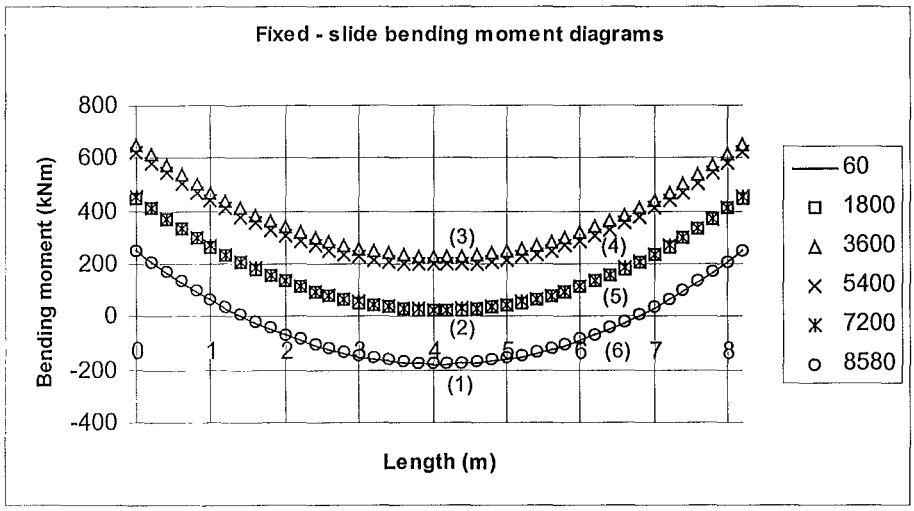

Figure 5.5.4 Fixed - Slide bending moment diagrams at 5°C per minute.

Figure 5.5.4 shows that the profile of the bending moment doesn't change through the duration of the fire, as there is no axial force to induce *P-δ* effects. The beam initially displays negative moments at the ends of the span and positive moment at the mid span. As the beam is heated, the negative moments at the end of the span increase and the mid span moments turn negative due to hogging caused by thermal bowing. Once the beam starts to yield and the plastic hinges form, the moment decreases. The mid span negative moment decreases and the then goes back into positive moment. The beam finally fails at approximately the same initial cold temperature moments.

Summary

Figure 5.5.5 shows the failure mechanism for the *fixed – slide* two-dimensional analysis. Plastic hinges initially form at the ends of the span due to tension stresses in the top flange and slab 1(a) and 1(b). The tension yield in the top flange causes compression yielding in the bottom flange forming the end of span plastic hinges. As the section heats up and is allowed to displace horizontally, due to elongation, a hogging moment is formed at the mid span where the initial displacements are fairly small. As the ends of the span form plastic hinges, and begin to yield, the hogging moment can not be sustained and the mid span displacement begins to increase. The mid span begins to sag and the beam is transferred back into positive moment. The bottom flange of steel section reaches the thermally reduced proportional limit first and then a short time after the top flange begins to yield forming the third plastic hinge, (2), shown in Figure 5.5.5, leading to a runaway failure.

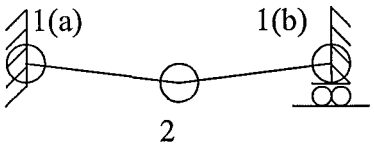

Figure 5.5.5 Failure mechanism for Fixed - Slide case.

5.6 Discussion.

The most significant finding in this section of the report is the relationship between the EC3 Proportional Limit stress and the EC3 Yield Limit stress with the change in displacement and axial force and therefore changes the bending moment due to P-δ effects.

Another significant finding is that the support restraint governs the displacement and fire resistance of the beam. These findings are detailed below.

5.6.1 Effects of EC3 Proportional and Yield limit stresses.

The relationship between the EC3 Proportional Limit and Yield Limit stresses with the displacement, axial force and bending moment is detailed below for each support case.

In the *pin – pin* support case when the bottom flange stress reaches the thermally reduced EC3 Proportional Limit the displacements increase due to yielding and a loss of stiffness in the section. At the same time the axial force decreases but the rate of change in the displacement is greater than the rate of change in axial force, therefore the bending moment increases due to P-δ effects. This trend in behaviour continues up to when the bottom flange stress reaches the thermally reduced EC3 Yield Stress, at which point the displacements increase and the axial force decreases. The rate of decrease in axial force is greater than the rate of increase in displacement causing a decrease in the bending moment. The loss of capacity in the section due to yielding causes a plastic hinge to form at the mid span and leads to failure.

In the *pin – roller* support case when the bottom flange reaches the EC3 Proportional Limit stress the mid span displacements increase, once again due to yielding and a loss in stiffness in the section. When the bottom flange stress approaches the EC3 Yield Limit, the beam displays a runaway failure. This is due to the increased displacements pulling in on the roller support and the roller not being able to provide any tensile resistance.

In the *fixed - fixed* support case, first yielding occurs when the end of span bottom flange reaches the ambient EC3 Yield Limit stress. This causes an increase in the displacement as well as the positive bending moment at mid span. The axial force increases but at a lower rate after first yield. The end of span top flange goes into compression and reaches the thermally reduced EC3 Proportional Limit stress with the increase in axial force and the loss in bottom flange capacity. As the displacements increase at the mid span the compression stress in the top flange increases until it also reaches the EC3 Proportional Limit stress. The mid span displacement increases with the bending moment up to failure, which occurs when the end of span top flange reaches the thermally reduced yield stress. After this point the mid span displacements increase forming the third plastic hinge and causing failure.

In the *fixed-slide* support case the end of span concrete cracks due to thermally enhanced negative moments. First yielding in the steel occurs when the end span top flange stress reaches the thermally reduced Proportional Limit stress in tension also due to the thermally enhanced negative moment. The compression stress in the bottom flange also increases up to the proportional limit stress. The times to yielding for this case are a lot longer than was found for the *fixed – fixed* case due to the lack of axial force. Mid span displacements do not increase until thermal bowing causes yielding in the reinforcing mesh. Significant increases in displacement do not occur until the mid span bottom flange reaches the thermally reduced EC3 Proportional Limit at which point a displacement runaway failure is observed.

The relationship between the EC3 Proportional and Yield Limit stress with the displacements, axial force and bending moment is well defined in the composite section behaviour. Yielding causes a loss in stiffness increasing displacements and decreasing axial force, which leads to more yielding and more displacements. The trigger for plastic hinging and composite section failure is the thermally reduced EC3 Proportional Limit stress except where axial restraint with moment restraint causes the EC3 Yield Limit to be achieved.

5.6.2 *Displacement Comparison*

Figure 5.6.1 shows the comparison in displacements between the four support conditions for the beam exposed to the 5°C per minute linear heating rate. The *fixed – fixed* and *fixed – slide* cases show the least displacement during the fire. This is because of the redundancy in forming the three plastic hinges. The non- moment resisting supports show the greatest displacement during the fire, because as the mid span yields there is no support at the end to redistribute the bending moment to. Axial restraint with moment restraint is detrimental to the fire resistance of the beam because of the high stresses in the steel. The other support conditions have a similar fire resistance but the *pin – pin* support case gives the best fire resistance due to thermal bowing and a positive bending moment allowing the concrete to contribute to the flexural strength.

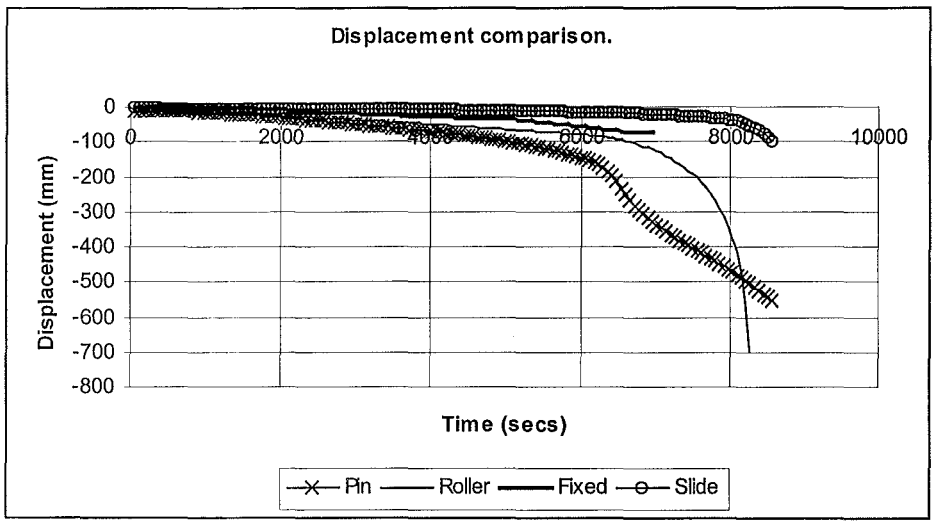

Figure 5.6.1 Displacement comparison for the four support conditions.

5.6.3 *Comparison of observed behaviour with real fire behaviour*

The *fixed – fixed* support case represents the Cardington test fire scenario the closest. The structural frame will provide axial restraint and the bolted connections in conjunction with the slab will provide moment resistance. The *fixed – fixed* SAFIR analysis shows early yielding at the ends of the span due to thermally induced bending stresses and axial force. In the Cardington fire tests it

was observed that local buckling occurred in the steel near the connections. Therefore the results from the SAFIR '*BEAM*' element analysis support the real fire event behaviour. As explained in Section 3.9 *FEM Structural Discretisation.* when finite element analysis is conducted with BEAM elements, plane sections remain plane, and local buckling can not be modelled. This behaviour is also observed to a lesser extent in the *fixed – slide* support case.

The *pined - pined* support case showed catenary action prior to collapse where the axial force turns tensile. Bailey et al (1999) believe that catenary action occurs in the section with tensile slab action providing the inherent fire resistance of the composite section at the later stages of the fire. A study into tensile slab action is not conducted in this report as it requires three dimensional finite element analysis. Note that during a fire the moment resisting connections may yield due to increasing stresses and thermal effects, therefore simply supported connections approximate real connections after yielding during a fire event.

5.7 Results for Higher Rates of Temperature Increase.

As stated in the introduction to this section of the report, heating rates of 10°C and 20°C per minute were also analysed using SAFIR. The collapse time for the four support conditions at the three heating rates are shown in Table 5.7.1.

Table 5.7.1 Collapse times for support conditions at 5, 10 and 20°C per minute.

TEMPERATURE INCREMENT	Pin –Pin Supports	Pin – Roller Supports	Fixed – Fixed Supports	Fixed – Slide Supports
5°C per minute	9540 sec	8280 sec	6960 sec	8580 sec
10°C per minute	4980 sec	4380 sec	3660 sec	4380 sec
20°C per minute	2580 sec	2340 sec	1920 sec	2280 sec

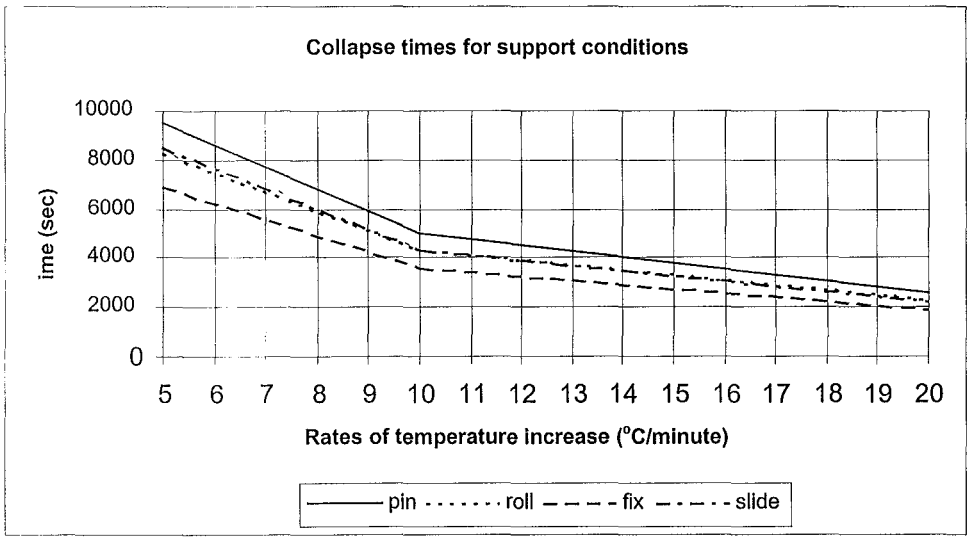

Figure 5.7.1 Collapse times for the four support conditions.

Figure 5.7.1 shows that as the heating rate increases, the times to collapse for the four support conditions converge. This suggests that for a very rapid fire growth all support conditions will have approximately the same resistance to fire. However for slower growing fires there will be a considerable difference in the fire resistance of the section. The non-axially restrained cases are very similar and diverge slightly at the smaller heating rates. The *pin – pin* support case shows the best fire resistance for all three linear heating rates, (Figure 5.7.1).

In comparing the different heating rates with the individual support conditions there is very similar behaviour albeit at a faster time of occurrence. Figure 5.7.2 to Figure 5.7.5 show that as the heating rate increases the fire resistance decreases but a similar pattern of displacements occur. This is the same for all four support cases which would suggest that beam behaviour is similar for slow to rapid linear fire growth but is dependent on end supports for modes of failure and behaviour. Section 7 *ISO 834 STANDARD FIRE* shows that under more severe thermal exposure beam behaviour changes.

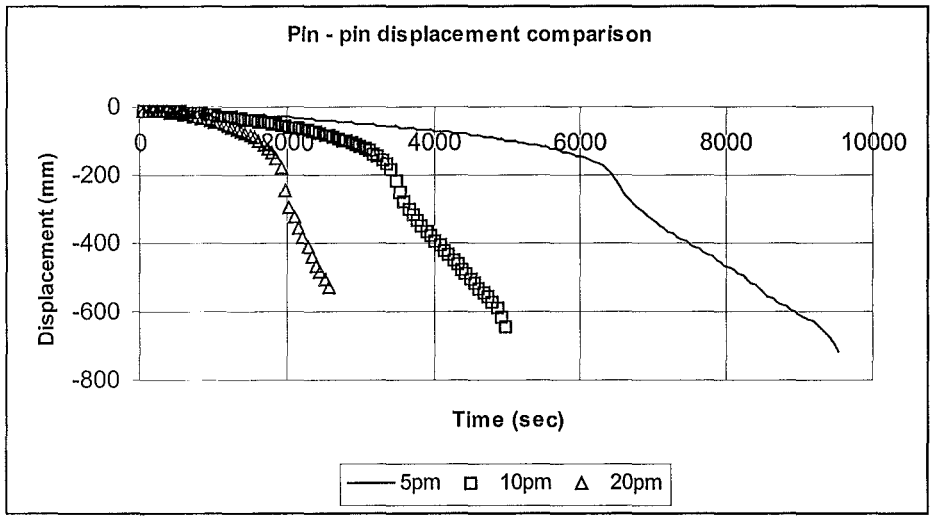

Figure 5.7.2 Comparison of Pin - Pin displacement at 5,10 and 20°C per minute.

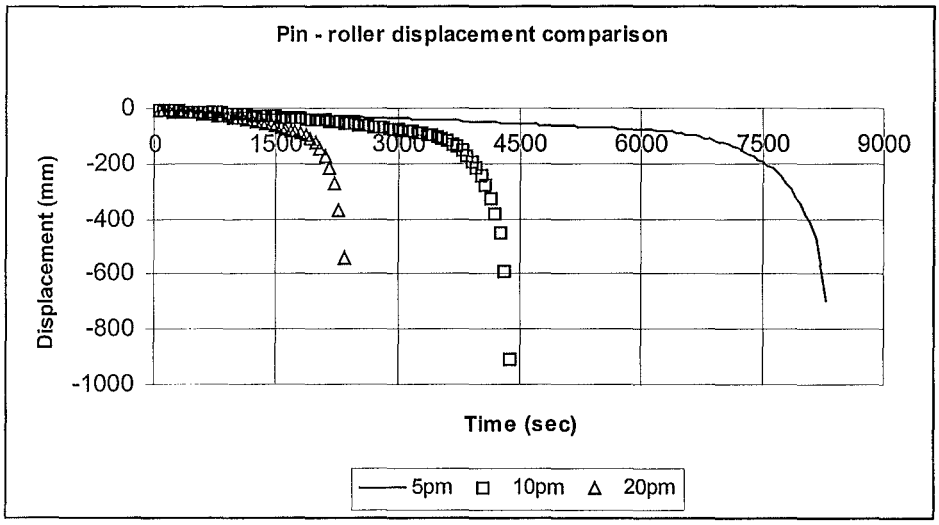

Figure 5.7.3 Comparison of Pin - Roller displacement at 5,10 and 20°C per minute.

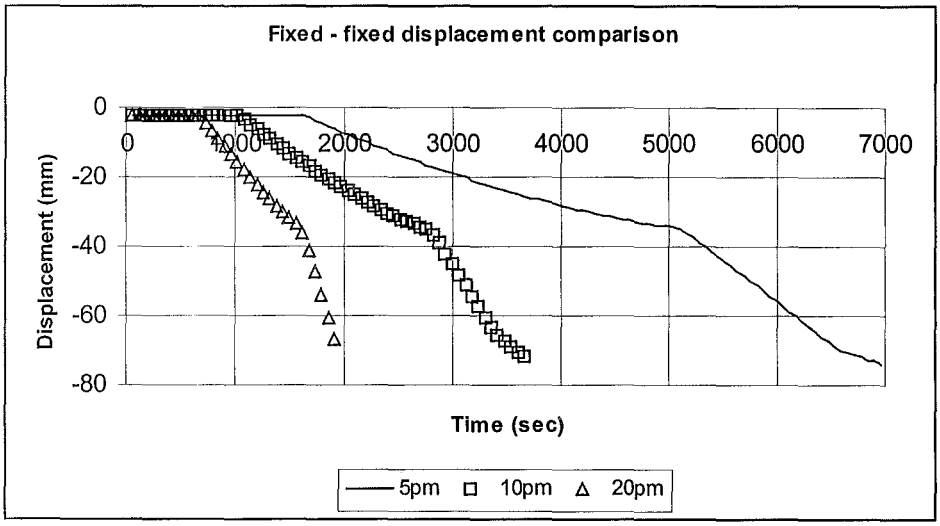

Figure 5.7.4 Comparison of Fixed - Fixed displacements at 5,10 and 20°C per minute.

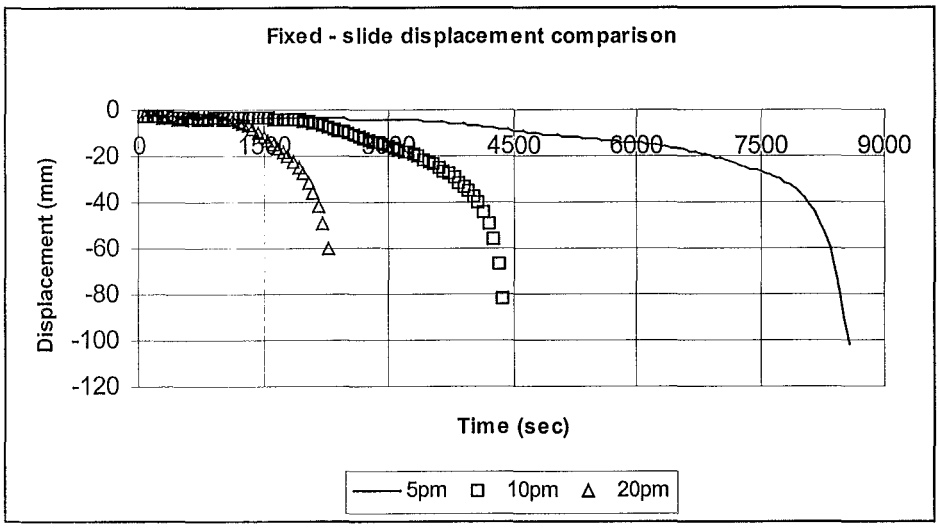

Figure 5.7.5 Comparison of Fixed - Slide displacements at 5,10 and 20°C per minute.

5.8 Conclusions

All four support conditions showed their expected failure mechanisms. The moment resisting end supports failed with three plastic hinges while the simply supported cases failed with one plastic hinge.

The fire resistance for the four support cases varied. The *pin – pin* support case lasted the longest at 159 minutes prior to collapse while the *fixed - slide* case lasted the second longest at 143 minutes. The *pin - roller* case lasted 138 minutes and the *fixed – fixed* case showed the least resistance to failure collapsing after 116 minutes. These results are counter intuitive to structural behaviour at cold temperatures, as it would be expected that the *fixed – fixed* support case would have more redundancy in forming the three plastic hinges.

The *fixed – fixed* support case fails due to the compression force and bending moment causing large stresses in the flanges at the ends of the beam. The bottom flanges of the 610 UB 101 at the ends of the span are unable to maintain the stress even prior to the thermal degradation in strength of the steel. The top flanges soon follow causing the first two hinges of the failure mechanism. The third plastic hinge is formed at the mid span of the beam due to increased deflection caused by the end of span plastic hinges.

The *pin – pin* support case has the best fire resistance even though there is axial restraint causing thermal bowing and high initial deflection. This means that even though the stresses are high at the mid span, because of the positive moments, the concrete slab is able to contribute to the moment capacity of the section. The bottom flange of the 610 UB 101 yields due to the thermal degradation in steel strength but there is sufficient redistribution of stress to allow the beam to survive a significantly longer period.

For the two non-axially restrained cases the low stresses in the flanges means better fire resistance. The *fixed - slide* supports have better fire resistance because of the redundancy required in forming the three plastic hinges. The negative end moments cause high stress and failure in the *fixed - slide* case where as large displacement causes failure in the *pin – roller* case.

In all four support cases, when the steel stress reaches the EC3 Proportional Limit stress and the EC3 Yield Limit stress, the behaviour in the displacements and axial forces change. In the axially restrained cases this causes changes in the bending moment due to P-δ effects. In the non-axially restrained cases the displacements are affected. Yielding also causes moment redistribution in the moment resisting connections. The relationship is that once the EC3 Proportional Limit or Yield Limit stress is achieved, yielding causes displacements and increased moments which in turn cause more yielding.

The same behaviour was observed for the two other temperature increments of 10°C per minute and 20°C per minute. Intuitively the only difference is that the collapse occurs more quickly. As the heating rate increases, the collapse times for the four supports converge, meaning that in very rapid fire growth all four support cases would be expected to have a similar fire resistance.

6 AXIAL SPRINGS

6.1 Introduction

In this section of the report further analysis is carried out to investigate support conditions on beam behaviour and fire resistance using an axial spring. This support case lies between the *pin – roller* support and the *pin – pin* support cases, and depending on the stiffness of the spring, tends towards either case. The model simulates beam behaviour between columns where the columns act as axial springs to restrain the composite beam with varying rigidity, depending upon the stiffness of the columns.

The system is modelled in SAFIR by placing a non-yielding truss element axial spring between a *pin* support and a *roller* support as shown in Figure 6.1.1. The standard composite section is placed between a *pin* support and the *roller* support on the left-hand side of the system while the spring is placed on the right hand side of the system between the *roller* and a *pin* support.

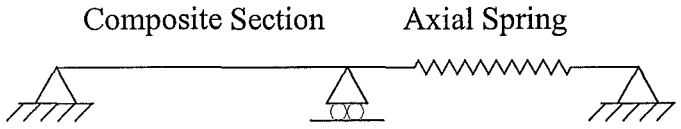

Figure 6.1.1 Support schematic for axial spring.

The non-yielding axial spring was provided by evaluating the maximum axial force encountered from the *pin – pin* support case in the previous section of this report and using a sufficiently strong steel truss element. The maximum axial force encountered was 4.51MN and the spring yield strength at ambient temperatures is 13.51MN for a 200mm diameter solid steel section with a yield strength of 430MPa. The spring is not heated and remains at ambient temperature throughout the simulations.

The spring stiffness is modified using the stiffness modulus *AE/L* relative to that of the composite section and a series of simulations are run to test performance using the SAFIR finite element package. The stiffness modulus (***K***) of the composite section is calculated by altering the relative material areas using the ratio of the modulus of elasticity (***n***) for steel, compared to that of

concrete as shown in Section 3.5.2 *Manual Calculation.* The relative stiffness (***k***) of the spring was determined and entered into SAFIR by modifying the tangent modulus of the steel spring as shown in Table 6.1.1. The area of the spring remained constant for all of the simulations and a standard length of 1m was also used.

Table 6.1.1 Elastic modulus for relative spring stiffness of steel spring.

Relative Stiffness	Elastic Modulus (GPa)
0% (Pin – Roller)	As simulated previously
2%	0.57E9
6%	1.70E9
10%	2.84E9
20%	5.67E9
25%	7.09E9
26%	7.37E9
30%	8.51E9
50%	14.18E9
70%	19.85E9
90%	25.52E9
100%	28.35E9
∞ (Pin – Pin)	As simulated previously

The same linear heating rate was used for the thermal exposure in this set of simulations as was used in the previous section, that being 5°C per minute, 10°C per minute and 20°C per minute as shown in Figure 3.4.1. The composite section was heated uniformly while the spring remained at ambient temperature.

Two groups of springs have been labelled as soft springs and stiff springs due to variations in the observed behaviour. The soft springs have a relative stiffness up to and including 25% relative stiffness of the composite section, whereas the stiff springs have a relative stiffness greater than 25% of the composite section under a linear heating rate of 5°C per minute.

The displacement, axial force, bending moments and stresses versus time have again been obtained to find the significant reasons for the observed behaviour. Displacement, axial force and bending moment diagrams have been plotted individually against time whereas the steel flange stress graphs have been plotted against time and compared with the thermally reduced EC3 Proportional Limit and the EC3 Yield Limit.

Only the mid span results were required as the failure mechanism will be a plastic hinge forming at the mid span of the beam for the varying spring stiffness.

6.2 Soft Spring Behaviour (5^{0}C per Minute)

Introduction

The relative stiffness of the soft springs ranges between the *pin – roller* support case (0% relative stiffness) and 25% stiffness. Under cold conditions as well as thermal and gravity loading the failure mechanism will be a plastic hinge forming at centre of the span.

Results

Figure 6.2.1 shows the results of the structural analysis. The failure mechanism is a plastic hinge forming at the mid span for all of the soft spring and *pin - roller* support simulations. Table 6.2.1 shows the beam fire resistance times and deformations prior to failure for the soft spring cases. With axial restraint the composite section fire resistance increases by approximately 20 minutes over that of the *pin - roller* support case. For the soft springs (2% to 25% relative stiffness) collapse occurs at approximately 158 minutes. Increasing the soft spring stiffness doesn't alter the beams fire resistance. The displacement just prior to collapse (when the stiffness matrix is not positive) decreases as the spring stiffness increases, but is still greater than that achieved for the *pin – roller* support case. A time line for the composite section behaviour which relates to Figure 6.2.1 is shown in Table 6.2.2.

Table 6.2.1 Time to failure and displacement of soft springs.

Spring Stiffness	Time to failure	Displacement prior to collapse.
0% (pin – roller)	8280 secs (138 mins)	696 (mm)
2%	9420 secs (157 mins)	956 (mm)
4%	9480 secs (158 mins)	883 (mm)
6%	9600 secs (160 mins)	877 (mm)
8%	9480 secs (158 mins)	816 (mm)
10%	9540 secs (159 mins)	821 (mm)
20%	9540 secs (159 mins)	799 (mm)
25%	9420 secs (157 mins)	751 (mm)

Table 6.2.2 Behaviour time line of soft spring supports at 5°C per minute.

	Behaviour	Time (Approx)
(a)	Bottom flange reaches EC3 Proportional Limit	3180 secs (53 mins)
(b)	Top flange reaches EC3 Proportional Limit	4380 secs (73 mins)
(c)	Axial force decreases – Displacement increases	6300 secs (105 mins)
(d)	Bottom flange reaches EC3 Yield Limit. Top flange compression stress decreases. Displacements increase.	7380 secs (123 mins)
(e)	Bending moment decreases	7620 secs (127 mins)
(f)	Section goes into tension. Rate of displacement change decreases. Max tension stress in top flange	8280 secs (138 mins)
(g)	Failure mechanism achieved.	9480 secs (158 mins)

Up to point (a) in Figure 6.2.1 (a), (b) and (c) the composite section displays elastic behaviour with the displacement increasing slightly and the axial force increasing, leading to an increase in bending moment due to P-δ effects. The initial displacement for all of the soft springs cases is similar, but as expected axial force increases as spring stiffness increases; therefore the bending moment increases as spring stiffness increases. Figure 6.2.1 (d) and (e) show that the stress in the bottom flange of the steel section increases in tension and the top flange stress increases in compression due to thermal bowing.

At point (a) in Figure 6.2.1(d) the bottom flange tension stress reaches the thermally reduced EC3 Proportional Limit stress and then displays plastic behaviour. As the spring stiffness increases it takes longer for the bottom flange to reach the EC3 Proportional Limit. This is due to axial force compression stresses counteracting the tension stress associated with bending in the bottom flange of the steel section. The difference in the time taken for the bottom flange to reach the proportional limit is only slight, as the displacement is slightly greater for the stiffer springs due to thermal bowing.

From point (a) to point (b) in Figure 6.2.1 (e) the compression stress increases in the top flange where at point (b) the thermally reduced EC3 Proportional Limit stress is achieved. Intuitively, as the spring stiffness increases, the time for the top flange stress to reach the proportional limit decreases, due to the increased axial force compression stresses. As the spring stiffness tends towards 0% the top flange compression stress decreases, leading to a longer elastic behaviour duration. This is due to decreased thermal bowing effects where the beam is able to elongate.

Figure 6.2.1 (a), (b) and (c) show that at point (c) the rate of increase in axial force decreases due to concrete crushing and yielding of the steel section. The rate of displacement increase is greater than the rate of axial force decrease, leading to an increase in the bending moment. This behaviour continues up to point (d).

Figure 6.2.1 (d) shows that at point (d) the bottom flange stress reaches the EC3 Yield Limit stress and follows the yield envelope until failure. Figure 6.2.1 (e) shows that yielding in the bottom flange causes a transfer in tension stress through the web and into the top flange of the steel section. Figure 6.2.1 (a), (b) and (c) show that the displacements increase rapidly and the axial force decreases, leading to a drop off in the bending moment at point (e). The displacement increases at this point with increasing spring stiffness due to the larger stresses causing yielding. Figure 6.2.1 (c) shows that the bending moments coincide and decrease at the same rate for the range of soft springs. This suggests that the rate of increase for displacement is directly proportional to the rate of decrease in axial stress. The function ***Te'*** (P-δ effect) from $M=wl^2/8 + Te'$ is approximately equal for all soft springs as $wl^2/8$ does not change significantly with the small change in length (l) of the beam where l is the length of the beam.

Figure 6.2.1 (b) shows that at point (f) the composite section goes into tension due to the formation of the plastic hinge at the mid span. Figure 6.2.1 (a), (b) and (c) show that at point (f) the displacements, axial force and bending moments are equal for all of the soft springs. Figure 6.2.1 (e) shows that at point (f) the top flange reaches its maximum tensile stress and shortly after approaches the thermally reduced EC3 Yield stress and follows the yield envelope until failure. The flange stresses in this report are average stresses over the entire flange. For this reason parts of the flange will be fully yielding but the average stress will only approach the Yield stress. Figure 6.2.1 (a), (b) and (c) show that after point (f) the beam displays a reduction in length below the initial length l. This is highlighted by a reduction in mid span moment where $M = wl^2/8$ and as l decreases, M also decreases. The axial spring gives tension restraint to the composite section and there is a decrease in the rate of displacement for all springs. The rate of displacement decreases as the spring stiffness increases. This is due to the softer spring providing less tensile restraint, decreasing l. The *pin - roller* support has a runaway failure at point (f), as the roller isn't able to restrain tensile forces. As the composite section decreases in length, the mid span displacement increases, leading to failure approximately 20 minutes later at point (g).

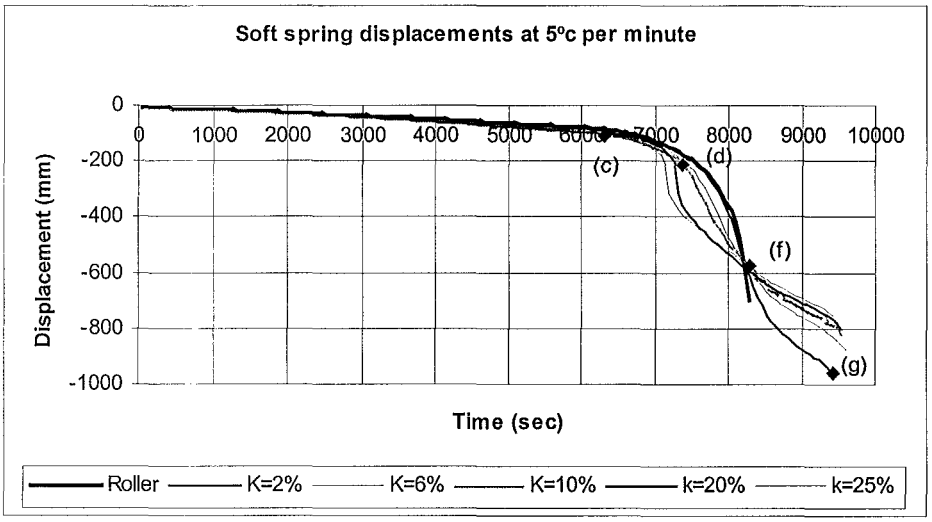

(a) Displacements

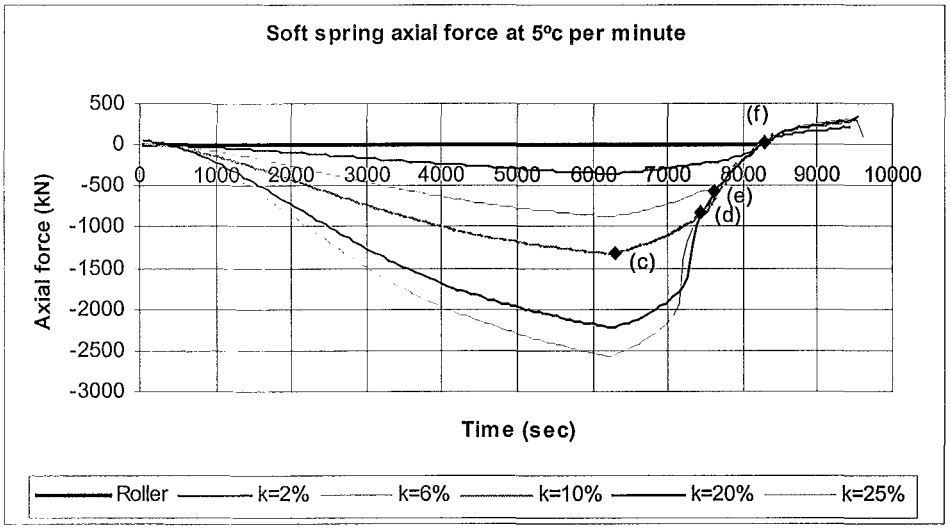

(b) Axial force

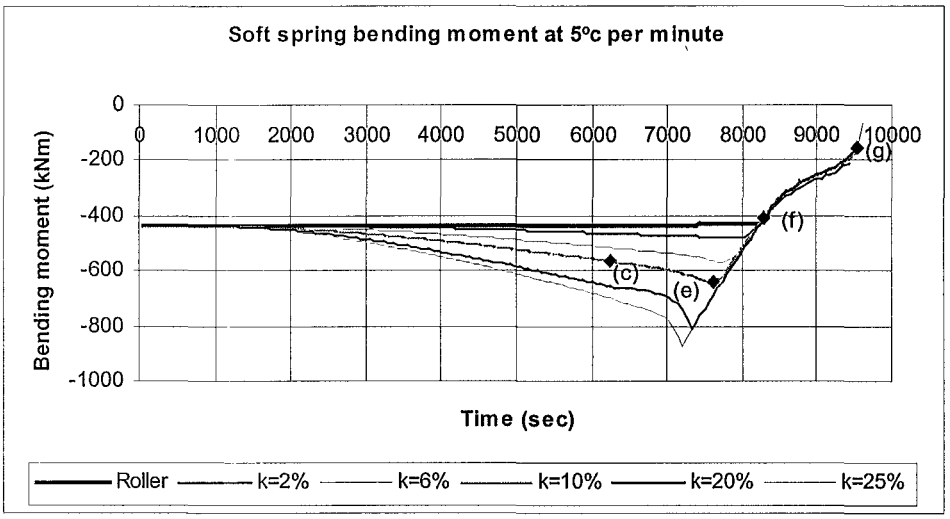

(c) Bending Moment

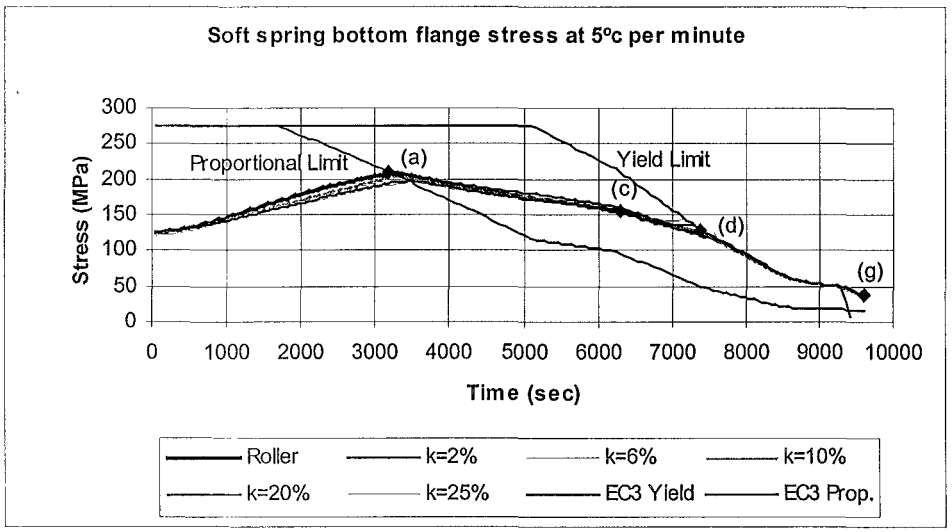

(d) Bottom flange stress

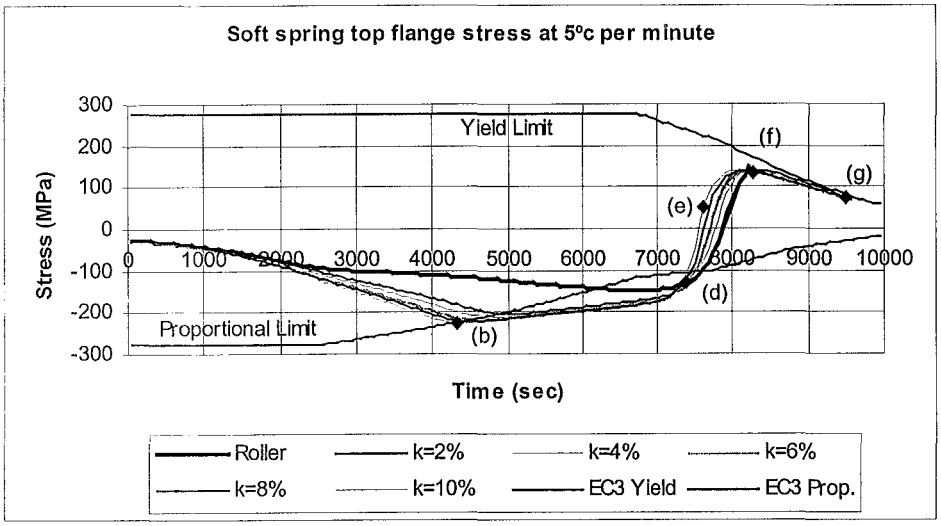

(e) Top flange stress

Figure 6.2.1 Mid span results for soft springs at 5°C per minute.

Figure 6.2.2 shows that the P-δ effects due to the axial restraint and displacement make the curvature of the bending moment increase initially for the first five time steps. As the section yields the axial force can't be sustained and the *P-δ* moment decreases where the rate of change in axial force is greater than the rate of change in displacement ($\Delta P > \Delta\delta$). The two last time steps show that the bending moment decreases below $wl^2/8$ where the section length decreases, due to displacements causing tensile stresses in the spring. This phenomenon is common for the range of soft springs.

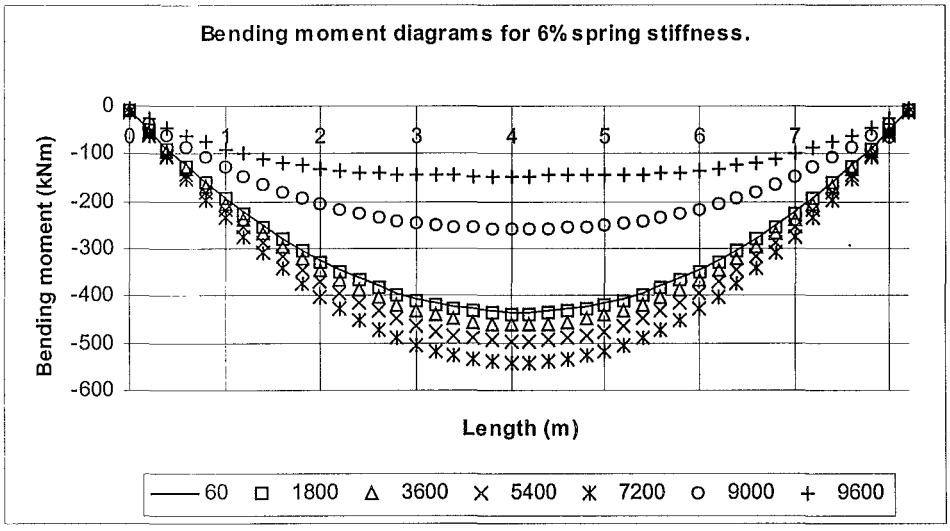

Figure 6.2.2 Bending moment diagrams for 6% relative spring stiffness at 5°C per minute.

Summary

The results show that with a soft spring, the time to failure of the composite section increases over that of the *pin - roller* case, but this is independent of spring stiffness as the time to collapse for the springs is relatively similar. Collapse of the system is once again through a plastic hinge forming at the centre of the beam.

Initially the displacement of the composite section with varying spring stiffness is similar, but the axial force increases with spring stiffness leading to an increase in bending moment due to P-δ effects. The higher axial forces associated with the stiffer springs increases the elastic life of the bottom flange of the steel section because of the tension failure associated with this part of the section. The top flanges take longer to yield due to the composite compressive action of the slab. As the spring stiffness increases, the duration to top flange yielding decreases because of the increased axial force.

Once the bottom flange reaches the yield envelope there is a sudden redistribution in tension stress through the web and into the top flange of the steel section. The displacements increase rapidly and increase with spring stiffness. The axial force decreases at a quicker rate than the increasing displacement, causing the mid span bending moment to decrease. The decrease in the rate of bending moment is similar for all spring stiffness and is fairly linear, suggesting that the function of ***Te*** (P-δ effect) for all soft springs is constant. That is, that the increase in displacement is directly proportional to the decrease in axial force at the formation of a plastic hinge for the range of soft springs.

When the plastic hinge forms the beam goes into tension and the length, ***l,*** decreases causing the bending moment to decrease below the gravity loading moment. In the *pin – roller* case the roller can't restrain the tension stresses and there is a quick runaway failure.

Compared to the *pin – roller* case the inclusion of an axial spring leads to an increase in initial displacements, axial forces and bending moments due to *P-δ* effects, but is better for the fire resistance of the beam.

6.3 Stiff Spring Behaviour (5°C per Minute)

Introduction

The relative stiffness (k) of the stiff springs range between 26% and ∞ (*pin – pin* supports). Under cold conditions as well as thermal and gravity loading the expected failure mechanism is a plastic hinge forming at mid span.

Results

Figure 6.3.1 shows that the failure mechanism for the *pin – pin* supports is a plastic hinge forming at the mid span. Figure 6.3.1 (c) shows that failure mechanism for the 26% through 100% relative spring stiffness is undefined. Failure occurs prior to the change in P–δ effect where the rate of change in axial force decrease becomes greater than the rate of change in displacement increase, as was observed in the soft spring cases. Table 6.3.1 shows that above 25% relative spring stiffness the time to failure of the composite section decreases dramatically and decreases with an increase in spring stiffness. As the spring stiffness approaches infinity (*pin – pin* supports) the time to failure increases to that found for the soft springs. The displacement at collapse also decreases dramatically above 25% but is relatively constant for 30% through 100% relative spring stiffness. The displacement at collapse for the *pin – pin* case matches the trend set by the soft springs. A time line for the stiff spring behaviour that relates to Figure 6.3.1 is shown in Table 6.3.2.

Table 6.3.1 Time to failure and displacement of stiff springs.

Spring Stiffness	Time to failure	Displacement at collapse.
25%	9420 secs (157 mins)	751 (mm)
26%	7200 secs (120 mins)	343 (mm)
30%	7260 secs (121 mins)	136 (mm)
50%	6840 secs (114 mins)	125 (mm)
70%	6600 secs (110 mins)	128 (mm)
90%	6480 secs (108 mins)	130 (mm)
100%	6420 secs (107 mins)	131 (mm)
∞ (Pin - pin)	9540 secs (159 mins)	718 (mm)

Table 6.3.2 Behaviour time line of stiff spring supports at 5°C per minute.

	Behaviour	Time range
(a)	Top flange reaches EC3 proportional limit.	2760 secs to 3600 secs (46 mins to 60 mins)
(b)	Bottom flange reaches EC3 proportional limit	3600 secs to 3960 secs (60 mins to 66 mins)
(c)	Crushing strength of concrete reached in top layer of slab. Axial force decreases.	5280 secs to 6240 secs (88 secs to 104 mins)
(d)	Crushing stress of concrete reached in bottom layer of slab. Top flange compression stress decreases rapidly. Displacement increases rapidly. Stress in slab decreases.	6240 secs to 6430 secs (104mins to 107mins)
(e)	$P - d$ effects decrease the bending moment and stiff spring simulations end.	6420 secs to 7260 secs (107mins to 121mins)
(f)	Bottom flange reaches yield limit and follows envelope until failure. Bending moment decreases.	6480 secs (108 mins)
(g)	Top flange stress is tensile. Displacements decrease	6720 secs (112 mins)
(h)	Composite section goes into tension.	8160 secs (136 mins)
(i)	Failure mechanism achieved.	9540 secs (159 mins)

Up to point (a) Figure 6.3.1 (a), (b) and (c) the composite section displays elastic behaviour. The displacements increase slowly at a uniform rate. The axial force increases quickly and increases with relative spring stiffness, thus bending moment increases with spring stiffness as was observed for the soft spring cases. Figure 6.3.1 (e) shows that for the stiffer springs, the stress in the top flange of the section reaches the thermally reduced EC3 Proportional Limit in compression first at point (a), unlike the soft springs where the bottom flange reached the proportional limit first. The stress in the top flange increases with spring stiffness whereas the stress in the bottom flange decreases with spring stiffness due to the increased axial force counteracting the tensile bending stress. Note that the stiff spring range does not include the 25% relative spring stiffness, this plot has been included

on these graphs to show the variation between stiff and soft spring behaviour. For a relative spring stiffness of 26% the top flange and the bottom flange of the steel section reach the thermally reduced EC3 Proportional Limit at approximately the same time. This seems to be the cross over point between soft and stiff spring behaviour for this composite section.

Figure 6.3.1 (a), (b) and (c) show that between points (a) and (b) the axial force and bending moment both increase while the displacements stay relatively uniform, despite the varying spring stiffness. Figure 6.3.1 (e), (f) and (g) show that between point (a) and (d) the compression stress in the slab increases due to bending while the stress in the top flange decreases due yielding. Figure 6.3.1 (d) shows that the stress in the bottom flange still increases in tension up to point (b) where it reaches the thermally reduced EC3 Proportional Limit stress. After this point is reached the bottom flange stress decreases at a varying rate, the stiffer the spring the less the decrease in stress due to the higher axial forces. Figure 6.3.1 (e) shows that between point (a) and (d) the top flange displays plastic behaviour and the compression stress decreases at a relatively uniform rate despite spring stiffness.

Figure 6.3.1 (b), (f) and (g) show that at point (c) the axial force starts to decrease due to crushing in the top layer of the concrete slab. Figure 6.3.1 (a), (b) and (c) show that at point (c), even though the axial force decreases, the bending moment still increases as the rate of change in displacement is greater than the rate of change in axial force.

At point (d) in Figure 6.3.1 (d), (f) and (g) the entire concrete slab has reached the thermally reduced EC2 crushing stress while the bottom flange of the 610 UB 101 reaches the EC3 Yield Limit stress. There is an upward shift in the neutral axis and the compression stress in the top flange decreases as shown in Figure 6.3.1 (e). The top flange goes into tension due to the loss in capacity of the bottom flange. Figure 6.3.1 (a), (b) and (c) shows that between points (d) and (f) the displacements increase rapidly due to yielding but the decrease in axial force is greater, causing the bending moment to begin to decrease, as was observed in the soft spring behaviour. For the 26% through 100% relative spring stiffness, the failure mechanism is obtained during this period at point (e). This failure mechanism is attributed to the SAFIR model itself, rather than any natural phenomenon. It is believed that the actual stiff spring behaviour will range between the 25% relative spring stiffness and the *pin – pin* support case which form the boundaries of the stiff spring behaviour.

Figure 6.3.1 (a) and (e) shows that at point (g) the top flange goes into tension and there is a decrease in the rate of increase in displacement, as was observed in the soft spring cases. Figure 6.3.1 (b) and (e) shows that at point (h) the composite section goes into tension and the maximum tensile stress is achieved in the top flange. The section yields and fails 23 minutes later at point (i).

Figure 6.3.1 (b) and (c) show that at point (h) the bending moment decreases below its gravity load value. At this point the beam is showing catenary action as the length, l, between the supports can not decrease. This means that some of the gravity load is being taken in tension rather than flexure.

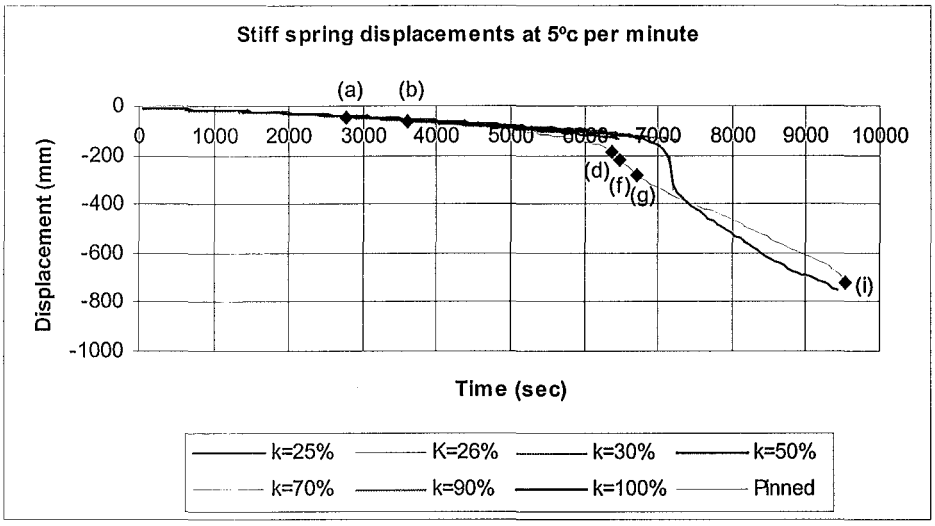

(a) Displacements

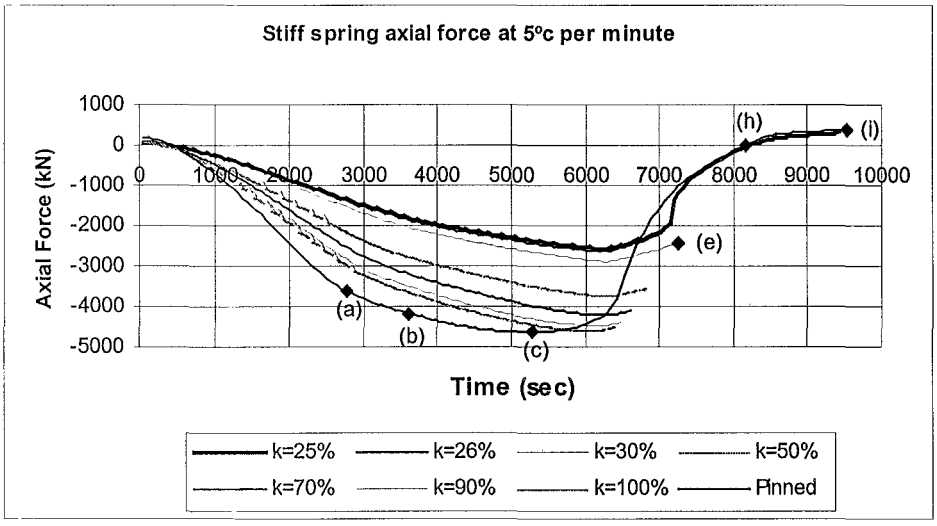

(b) Axial force

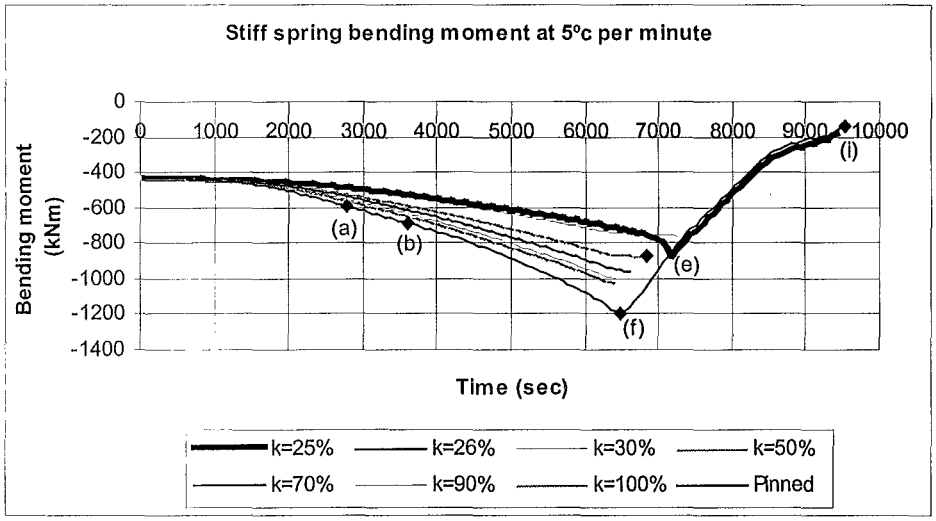

(c) Bending moment

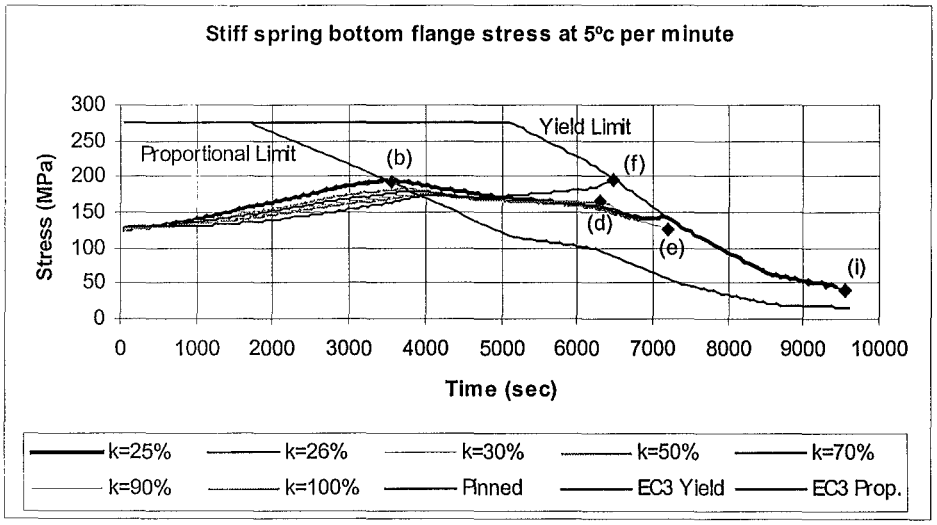

(d) Bottom flange stress

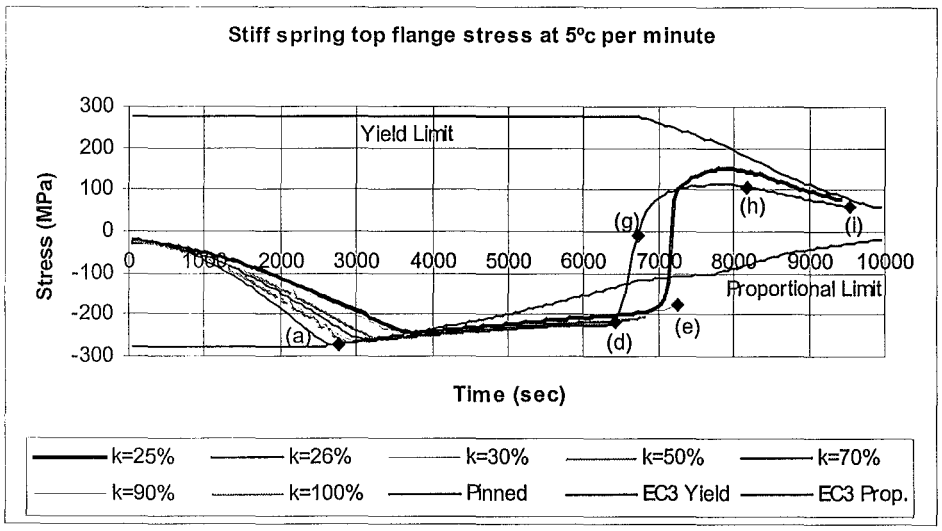

(e) Top flange stress

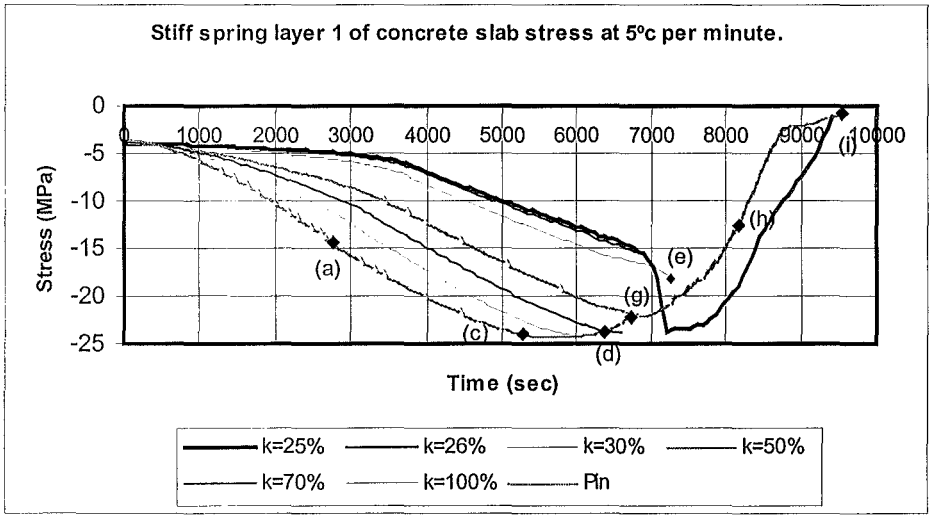

(f) Slab Stress - Layer 1 (top) of concrete slab.

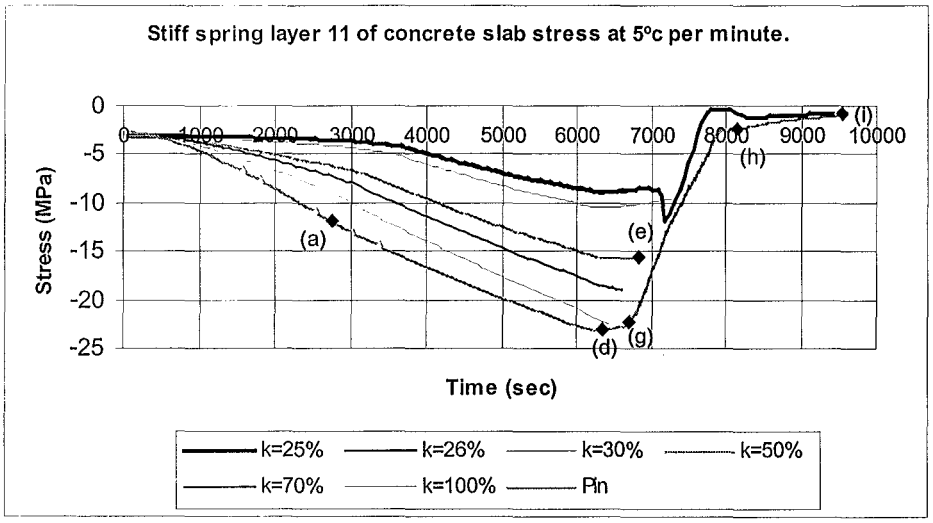

(g) Slab stress – Layer 11 (bottom) of concrete slab.

Figure 6.3.1 Mid span results for stiff springs at 5°C per minute.

Figure 6.3.2 show that the P-δ effects due to the axial restraint and displacement make the curvature of the bending moment increase for the first five time steps. The composite section fails prior to the decrease in bending moment. This behaviour was observed for all stiff spring cases with the exception of the *Pin – Pin* support case, where the bending moment decreases due to yielding and a decrease in the axial force.

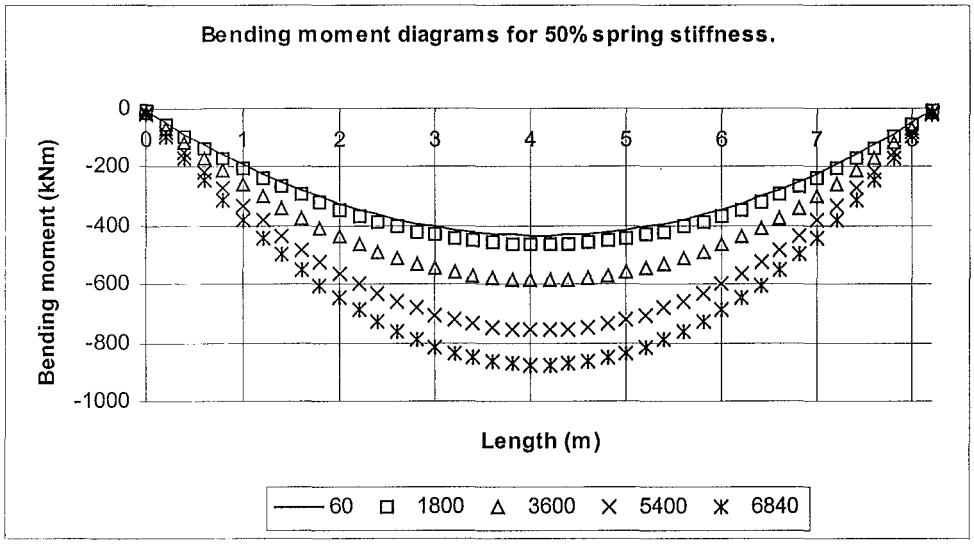

Figure 6.3.2 Bending moment diagrams for 6% relative spring stiffness at 5°C per Minute.

Summary

The results show that with a stiff spring, the time to failure of the composite section is very short in comparison to that of the *pin - pin* support case. Collapse of the system is undefined, as the steel section doesn't reach the yield limit. The failure mechanism for the stiff springs is attributed to numerical error in the running of the model. The extra terms in the stiffness matrix associated with the stiffer springs seem to cause instability in the resolution of the matrix calculations. A 1000% relative spring stiffness simulation was also run but not included in the results. The results of this simulation displayed an even shorter beam fire resistance. Therefore as the *pin – pin* support condition is approached with stiff springs, the fire resistance decreases which is shown to be untrue by the *pin–pin* support case.

At a relative spring stiffness of 26% the top flange of the steel beam reaches the thermally reduced EC3 Proportional Limit stress in compression first, unlike the soft spring case where the bottom flange reaches the proportional limit in tension first. The higher axial restraint of the stiff spring system increases the axial force developed in the member, leading to higher stresses in the top flange. The concrete slab takes up the required compression stresses and the stress in the bottom flange increases until reaching the thermally reduced EC3 Proportional Limit. Once the entire steel section has reached the proportional limit, the stresses in the top and bottom flange decrease with the decrease in axial force due to crushing in the concrete.

In the 26% to 100% relative spring stiffness cases, the top and bottom flanges show a constant decrease in stress after the thermally reduced EC3 Proportional Limit stress is reached. As spring stiffness increases the observed behaviour approaches that of the *pin – pin* support case where the concrete slab reaches the thermally reduced EC2 crushing stress. Unlike the *pin – pin* support case, the stiff spring simulations end prior to the decrease in axial force and bending moment.

For the *pin – pin* support case the displacements increase because of the crushing of the concrete and the plastic behaviour of the steel section. The axial force decreases and the bending moment increases, as the rate of change in the displacement is greater than the rate of change in axial force. Once the bottom flange reaches the thermally reduced EC3 Yield Limit, the compression stress in the top flange decreases. This is due to an upward shift in the neutral axis, as the top flange has to take the tension stresses. The top flange approaches the EC3 Yield Limit in tension. Once the entire steel section reaches the yield limit the beam goes into tension pulling back on the supports. The supports are fixed and therefore due to the decreased flexural capacity of the section, load is taken in tension and the beam displays catenary action. Collapse of the system occurs 23 minutes later. Apart for the catenary action, this behaviour was observed in the soft spring cases.

6.4 Effect of Changing the Rates of Temperature Increase.

Introduction

Included in this section of the report are the results of simulations run with the higher heating rates of 10°C per minute and 20°C per minute. The simulations were run with a relative spring stiffness of 6% and 50%. These springs were selected as the 6% relative stiffness lies within the range for the soft springs while the 50% relative spring stiffness lies within the range for the stiff springs for the 5°C per minute heating rate. The displacements, axial force and bending moments have been plotted and used to compare the composite section behaviour under varying thermal exposure with varying relative spring stiffness.

Results

Figure 6.4.1 and Figure 6.4.2 show the results at higher rates for heating for the composite section with a 6% and a 50% relative stiffness axial spring. Table 6.4.1 shows the collapse times for the *pin – roller*, 6% relative spring stiffness, 50% relative spring stiffness and *pin – pin* support conditions at the three heating rates.

Table 6.4.1 Collapse times for varying axial stiffness at 5, 10, 20°C per minute.

Rate of Heating.	Pin – Roller Supports	6% Relative spring stiffness	50% Relative spring stiffness	Pin –Pin Supports
5°C per minute	8280 sec	9600 sec	6840 sec	9540 sec
10°C per minute	4380 sec	4860 sec	3600 sec	4980 sec
20°C per minute	2340 sec	2760 sec	2820 sec	2580 sec

Table 6.4.1 shows that as the heating rate increases the fire resistance of the beam decreases, which is the intuitive solution. The stiff spring behaviour figures contained within the table may be inaccurate due to the problems associated with the numerical stability with these simulations.

Figure 6.4.1 shows that for a soft spring, of 6% relative stiffness, the pattern of the displacements, axial force and bending moments for the higher rates of heating matches that of the initial 5°C per minute case, albeit at a faster rate of occurrence. As the heating rate increases the maximum axial force decreases. The lower axial force is attributed to higher thermal gradients throughout the section, causing lower average temperatures and less thermal elongation. This will also reduce the effects of thermal bowing, therefore the displacement at maximum moment decreases as the rate of heating increases. As the heating rate increases the maximum mid span bending moment decreases due to the decrease in axial force and displacement reducing the P-δ effects.

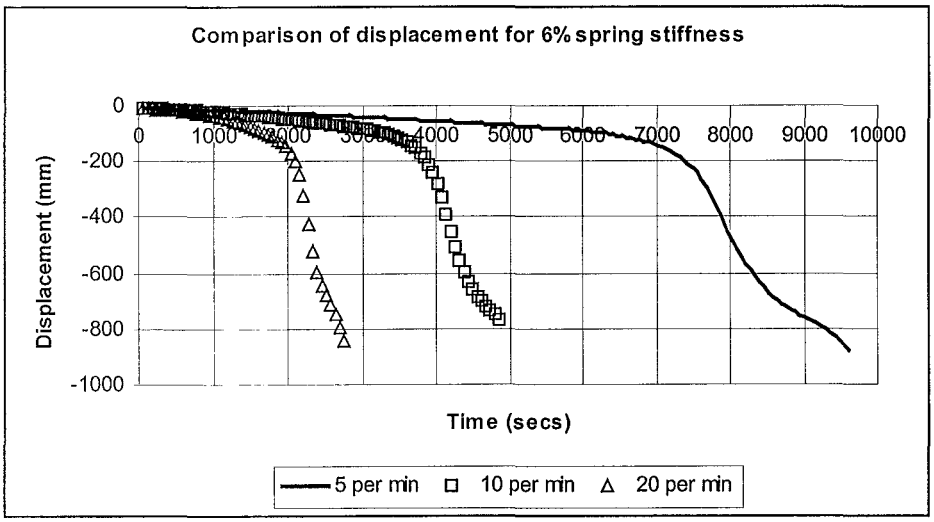

(a) Displacements

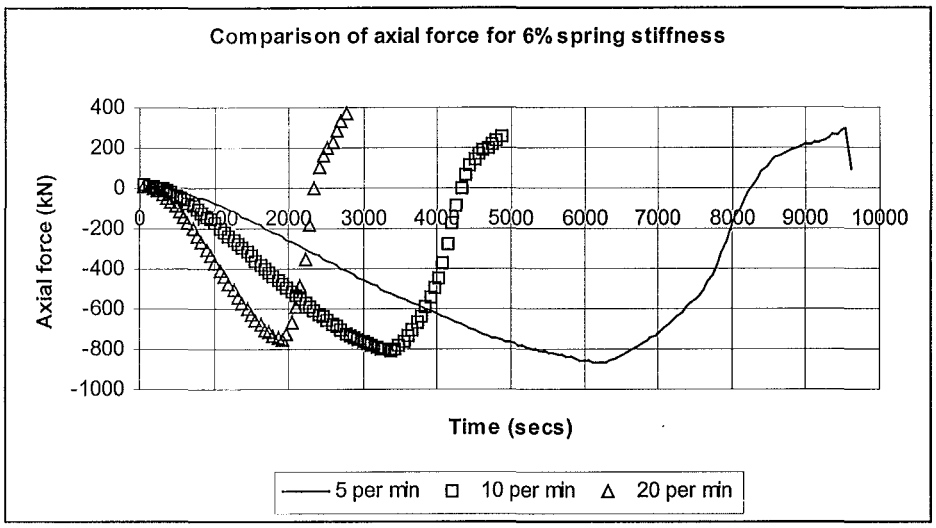

(b) Axial force

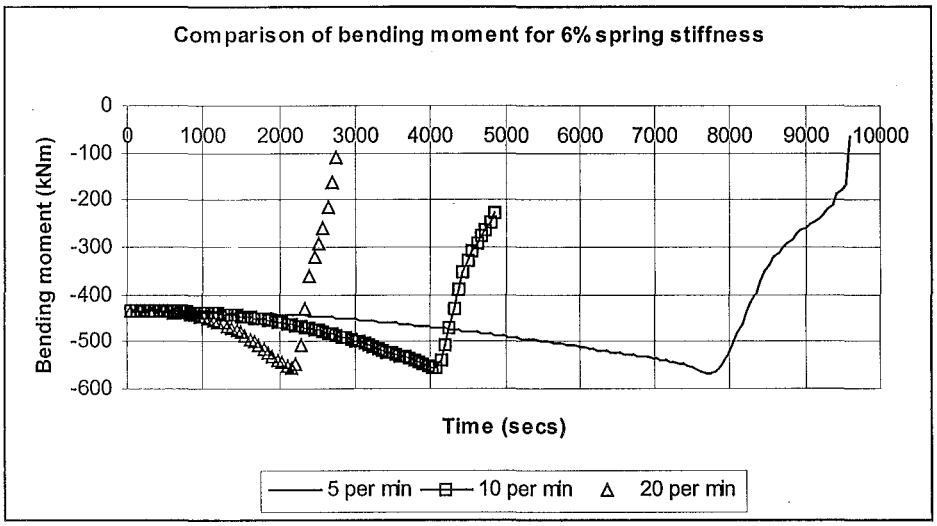

(c) Bending moment

Figure 6.4.1 Comparison of heating rates for 6% spring stiffness.

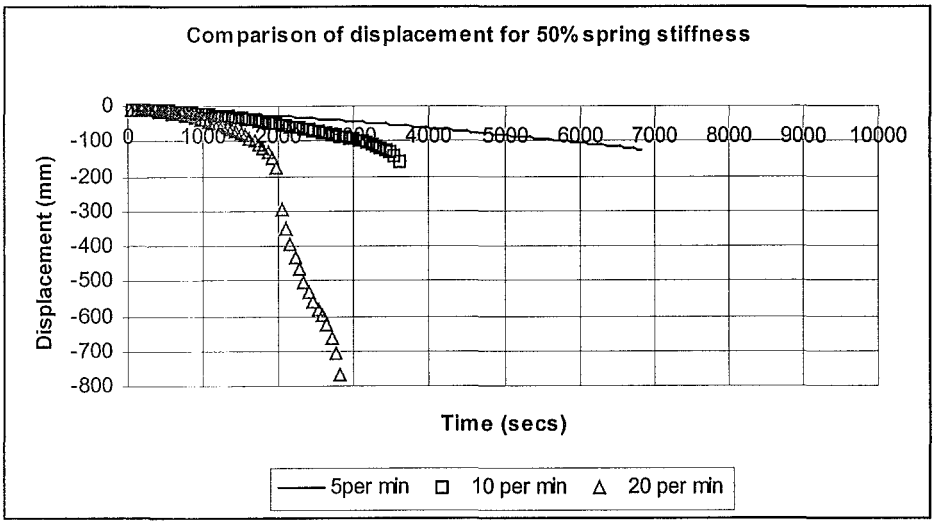

(a) Displacements

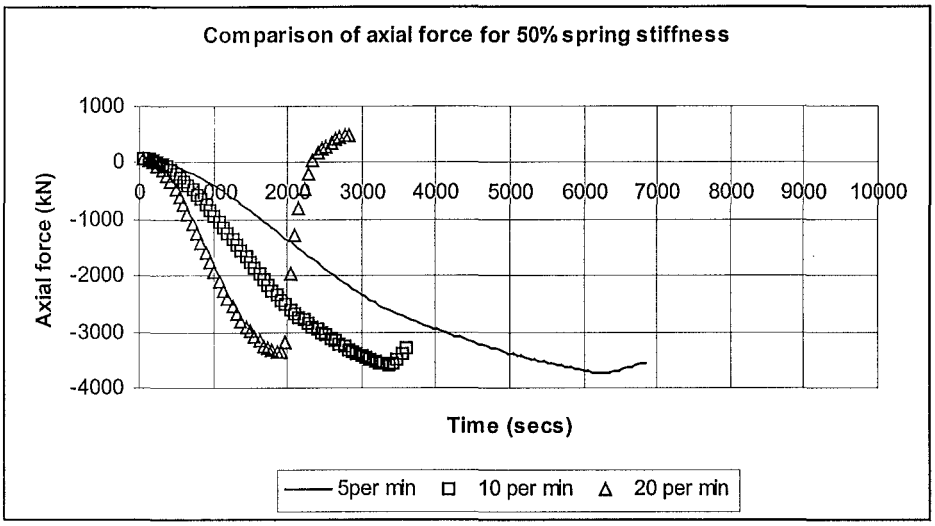

(b) Axial force

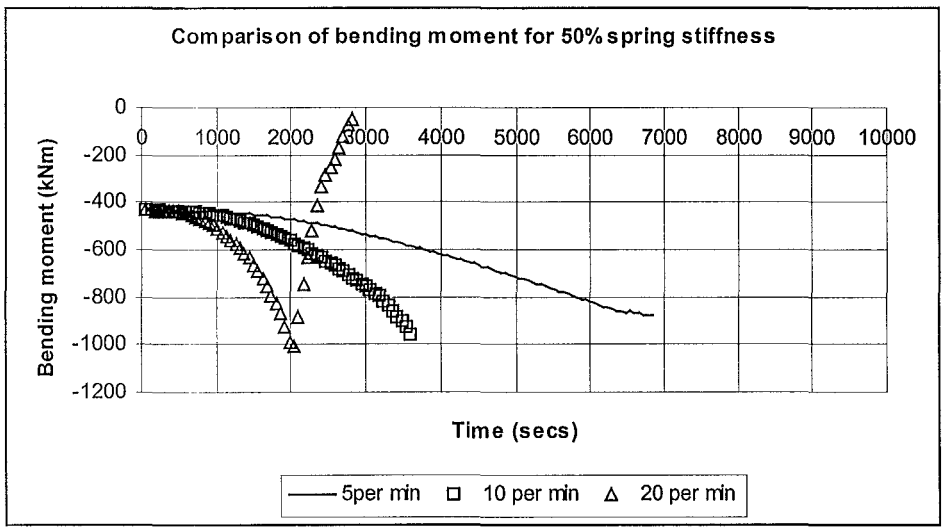

(c) Bending moment

Figure 6.4.2 Comparison of heating rates for 50% spring stiffness.

Figure 6.4.2 shows that for the relative spring stiffness of 50% the displacements, axial force and bending moments for the higher heating rates are similar to that of the initial 5°C per minute case. The exception is the 20°C per minute heating rate, which initially follows the stiff spring behaviour and then follows the soft spring behaviour with a decreasing bending moment.

Again, as the heating rate increases, the maximum axial force decreases. This again suggests that as the heating rate increases there are greater temperature differentials in the section causing lower average section temperatures and smaller thermal elongation.

Figure 6.4.3 and Figure 6.4.4 show that the decrease in axial force associated with the lower average section temperatures decrease to the point where, for the 20°C per minute heating rate the bottom flange of the section reaches the EC3 Proportional Limit stress prior to the top flange. This is the cross over point between the stiff and soft spring behaviour. This simulation then follows the soft spring behaviour as described previously.

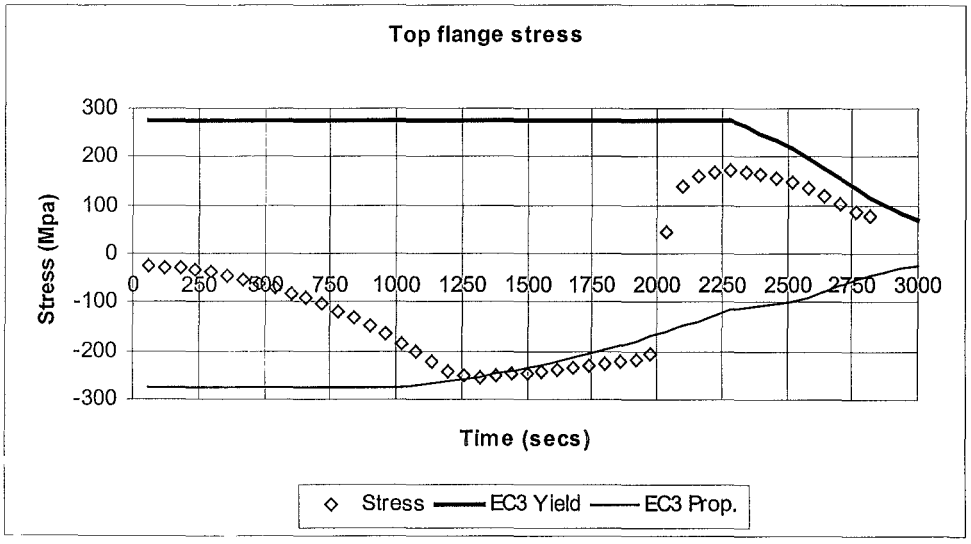

Figure 6.4.3 Top flange stress at 50% relative spring stiffness (20°C /min).

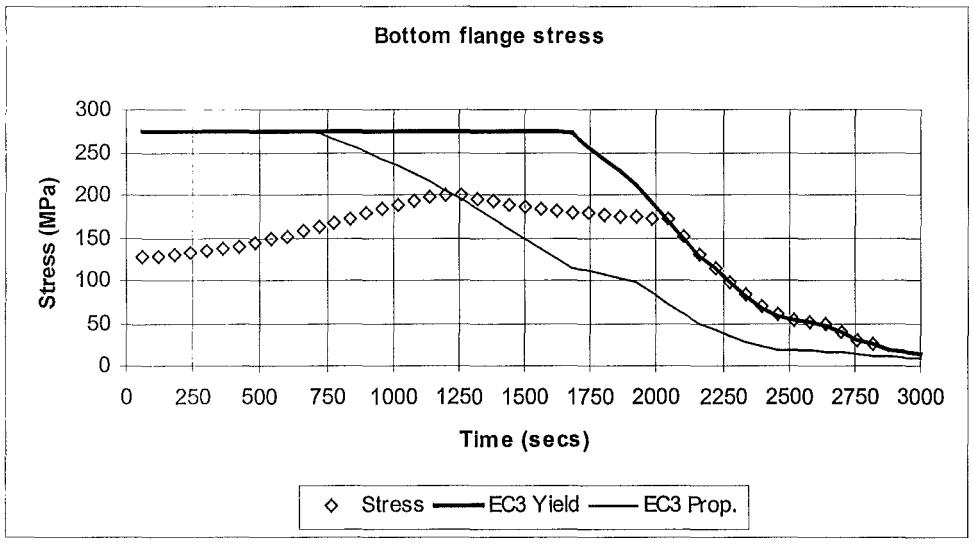

Figure 6.4.4 Bottom flange stress at 50% relative spring stiffness (20°C /min).

Figure 6.4.5 shows that as the heating rate increases, the time to failure of the four axial spring systems (*pin – roller*, *soft spring*, *stiff spring* and *pin – pin* cases) converge. This means that at rapid temperature increases the axial spring stiffness becomes irrelevant for simple beam bending conditions. Note that the 50% relative spring stiffness time to failure falls outside the *pin – pin* and *pin – roller* axial spring boundaries. As noted previously this is due to numerical instability in the SAFIR simulations.

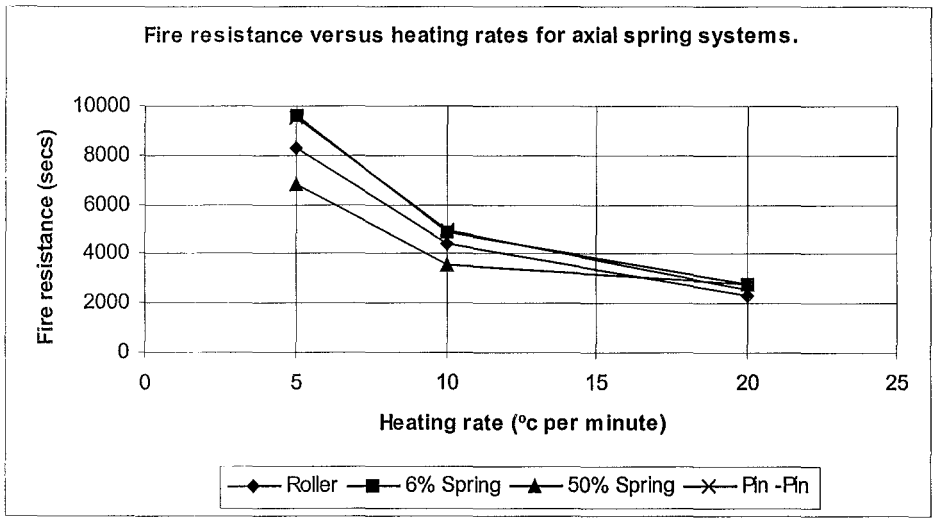

Figure 6.4.5 Fire resistance versus heating rates for axial spring systems.

Summary

The effect of increasing the rate of heating affects the behaviour of the axial spring system. The more rapid the fire growth, the less axial force there is developed in the axial spring system due to lower average section temperatures caused by increasing temperature differentials. There is a decrease in the rate of displacement due to a decrease in the effects of thermal bowing with the decreased axial force. Therefore, because of the decrease in displacement and axial force, the maximum bending moments decrease with increased temperature increments. The increase in heating rate intuitively causes a decreased fire resistance for the beam. As the heating rate increases, the time to failure of the axial spring systems converge. Therefore the time to failure of the system is independent of axial support conditions in rapid growing fires for simple beam bending.

6.5 Conclusions

The failure mechanism for the composite section with a non-yielding axial spring under uniform heating with a linear heating rate, is a plastic hinge forming at the centre of the beam. The spring stiffness ranges between 0% stiffness for the *pin - roller* case and approaches infinity with the *pin – pin* support case.

The fire resistance of the composite section with an axial spring increases over that of the *pin - roller* case. The fire resistance for the varying spring stiffnesses is relatively similar, including the *pin – pin* support case, and is independent of spring stiffness. The fire resistance of the stiff spring cases identified in this section of the report was a lot shorter than that of the soft springs cases due to numerical instability in SAFIR as opposed to a natural phenomenon. It is believed that without this numerical error the stiff spring behaviour would show soft spring behaviour. The numerical error theory is supported with the 1000% relative stiffness simulation where the time to failure of the system was a lot less than even the 100% relative spring stiffness. As the spring stiffness approaches infinity the beam behaviour should approach that of the *pin – pin* case. The *pin – pin* support case shows stiff spring behaviour (the top flange reaching the thermally reduced EC3 Proportional Limit first) but has a time to failure and behaviour similar to that of the soft springs. The displacement at collapse decreases with spring stiffness.

Initially the displacement of the composite section with varying spring stiffness is uniform but the axial force increases with spring stiffness leading to an increase in bending moment through P-δ effects. The higher axial forces associated with the higher spring stiffness increases the elastic life of the bottom flange of the steel section. This is due to the compressive axial forces counteracting the tensile bending stresses associated with this part of the section. As the spring stiffness increases the time for the top flange to reach the thermally reduced EC3 Proportional Limit stress decreases due to the increased compressive stresses caused by axial force. Above 25% relative spring stiffness, with a heating rate of 5°C per minute, the top flange reaches the thermally reduced EC3 Proportional Limit first (stiff spring behaviour) for this composite section. With higher heating rates the average section temperature decreases due to higher thermal gradients. The thermal elongation of the section therefore decreases and the axial forces developed in the section also decrease. With increased rates of heating, the bottom flange reaches the thermally reduced EC3 Proportional Limit prior to the top flange at higher spring stiffness.

When the bottom flange reaches the EC3 Yield Limit, the bending moment capacity of the section decreases. There is a sudden shift in top flange stress due to the neutral axis shifting up as the top flange takes up the tensile stress capacity lost in the bottom flange. The composite section goes into tension once the plastic hinge has been formed at the mid span. The bending moment decreases below the gravity load level due to a decrease in, $\boldsymbol{l}$, the length of the beam. The displacements decrease with increasing spring stiffness at this point as the stiffer springs are able to resist the tensile forces. The *pin – roller* support case has a runaway failure as the roller is unable to provide any axial restraint.

When the bottom flange reaches the thermally reduced EC3 Yield Limit and the bending moment decreases, the moments for the varying springs coincide, suggesting that the decrease in axial force is directly proportional to the increase in displacement, independent of spring stiffness.

As the heating rate increases the fire resistance converges, independent of the spring stiffness. For rapid fire growth the axial spring stiffness is irrelevant for simple beam bending.

7 ISO 834 STANDARD FIRE

7.1 Introduction

Simulations for the composite section in an ISO 834 standard fire have been included in this report as this is the internationally recognised standard fire test. The same four support conditions used in the linear heating rate cases have been utilised as they provide an envelope of end restraint for two-dimensional finite element analysis.

The ISO 834 standard fire is shown in Figure 3.4.2 and is a rapid growing, non-linear fire that will subject the composite section to a much more rigorous initial fire growth than was provided by the linear heating rate cases. The beam is subjected to the fire until failure (negative stiffness matrix).

The displacements, axial force, bending moments and stresses have been reduced from the SAFIR output to find significant reasons for the observed behaviour. Displacement, axial force and bending moment diagrams have been plotted individually against time, but the steel flange average stress diagrams have been plotted against time and compared with the thermally reduced EC3 Proportional and Yield Limit stresses. Using the average temperature of the flanges from the thermal SAFIR, file and finding the comparative steel strength at that time, gives plots for the thermally reduced EC3 Proportional Limit as well as the Yield strength from EC3 Table 3.1 (*Reduction factors for stress-strain relationship of steel at elevated temperatures*). Centre line stresses have also been compared with the EC3 Proportional Limit stress and EC3 Yield stress at times where the behaviour of the beam changes rapidly.

Mid span and end of span results were plotted for the *fixed – fixed* and *fixed - slide* supports whereas only the mid span results were plotted for the *pin – pin* and *pin – roller* supports. The reason for this is the failure mechanism for the simply supported cases will be a plastic hinge at the mid span and for the moment resisting cases the formation of three plastic hinges.

7.2 Pin – Pin Supports (ISO 834 fire)

Introduction

For this simulation the composite section is tested until failure in an ISO 834 fire with *pin – pin* end restraints. Figure 3.4.4 shows the three-sided thermal boundary that was used in this simulation. See Figure 5.2.1 for support schematic.

Results

Figure 7.2.1 and Figure 7.2.2 show the results of the structural analysis. The fire resistance of the one bay section in an ISO 834 standard fire, two-dimensional simulation, is 660 seconds with a displacement prior to collapse of 53mm. The failure mechanism for the standard fire is a lot more complicated than for the linear heating rates explained in previous sections of this report. The failure mechanism is not fully understood but is believed to be a plastic hinge at the mid span formed by yielding in the web under axial loading combined with yielding in the top flange due to axial force and bending. Table 7.2.1 shows the postulated behaviour time line for the composite section with *pin – pin* supports that relates to Figure 7.2.1.

Table 7.2.1 Behaviour time line of Pin - Pin supports in ISO 834 fire.

	Behaviour	**Time**
(a)	Part of the web in the steel beam reaches the EC3 Proportional Limit.	160 secs
(b)	The top flange and the entire web reach the proportional limit.	380 secs
(c)	Part of the bottom flange reaches the proportional limit. The axial force decreases due to a loss of stiffness in the steel.	500 secs
(d)	More of bottom flange reaches the proportional limit. Rapid decrease in axial force.	560 secs
(e)	Failure mechanism achieved.	660 secs

Figure 7.2.1 (a), (b) and (c) show that up to point (a) the section shows elastic behaviour. Initially there is very little deflection but the axial force increases rapidly due to the elongation caused by the large thermal exposure induced from the standard fire. The axial load is

predominantly from the steel section because of the thermal lag associated with the concrete. The increase in axial force and slight increase in displacement lead to an increase in bending moment from P-δ effects. Figure 7.2.1 (d) and (e) show that the top flange compression stress increases and the tension stress in the bottom flange decreases and goes into compression with the increase in axial force. The entire section quickly goes into compression due to the large compressive stresses associated with the thermal elongation.

Figure 7.2.2 (b) shows that at point (a) in Figure 7.2.1 the top part of the web in the 610 UB 101 begins to reach the thermally reduced EC3 Proportional Limit. Figure 7.2.1 (b) shows that as the web yields at the support height (line of thrust) the axial force plateaus and the unyielding parts of the section take up more of the axial force. Figure 7.2.1 (a) shows that at point (a) the displacements increase because of the decrease in section stiffness. Figure 7.2.1 (c) shows that the increased displacement causes an amplification of the bending moment due to P-δ effects. Figure 7.2.1 (e) shows that the bottom flange compressive stress plateaus due increased axial force stresses counteracting increased bending stresses. Figure 7.2.1 (d) shows an increase in the compressive stress in the top flange. This is due to the increased bending stress from the displacements

Figure 7.2.1 (f) shows that after point (a) there is a decrease in the average compressive stress in the bottom layer of the concrete slab. This decrease in average stress is due to a degradation of material properties in the very thinly discretised bottom layer of concrete. The degradation in the concrete properties is due to the severe thermal exposure. The top flange stress increases, taking the compressive stresses lost in the bottom layer of the slab.

At point (b) in Figure 7.2.1 (d) the top flange stress reaches the thermally reduced EC3 Proportional Limit. Figure 7.2.2 (c) shows that at the same time the entire web has reached the proportional limit. Figure 7.2.1 (a), (b) and (c) shows that after point (b) the displacements continue to increase at a uniform rate and the axial force is still constant, leading to an increasing bending moment. Figure 7.2.1 (d) and (e) show that after point (b) the top flange stress begins to decrease slightly with yielding and the bottom flange stress stays relatively constant. Figure 7.2.1 (f) shows that the compression stress in the top of the slab increases due to bending and the loss of strength in the top flange. The stress in the bottom of the slab stays constant due to an increasing loss in strength. Figure 7.2.1 (e) shows that the stress in the bottom flange stays constant due to an increase

in bending stress (in tension) counteracted by the need for the bottom flange to take more of the axial force lost by the yielding steel in the web.

At point (c) in Figure 7.2.1 (a), (b) and (c) there is a drop off in axial force as the steel section losses stiffness. This is due to a decrease in the elastic modulus caused by the thermal exposure. The displacements increase due to the decrease in stiffness. The bending moment still increases, as the rate of change in displacement is greater than the rate of change in axial force, $\Delta\delta > \Delta P$. Figure 7.2.1 (e) shows that there is a decrease in stress in the bottom flange due to parts of the bottom flange reaching the proportional limit. Figure 7.2.1 (e) and Figure 7.2.2 (c) shows that the average stress in the flange doesn't reach the proportional limit. The parts of the flange most affected by the thermal exposure, namely the tips of the flanges, will however reach the proportional limit more quickly than the area close to the web where the mass of steel in this area acts as a heat sink. Figure 7.2.1 (f) shows that the stress in the top layer of the concrete slab still increases due to bending.

Figure 7.2.1 (e) shows that at (d) more of the bottom flange reaches the proportional limit and the compression stress decreases further with the decrease in axial force and increase in bending stress. Figure 7.2.1 (a), (b) and (c) shows that as the axial force decreases the displacements increase with yielding at a more rapid rate and the bending moment increases. Figure 7.2.2 (e) shows that by this stage most of the steel section has reached the thermally reduced EC3 Proportional Limit.

Leading up to failure at point (e), Figure 7.2.1 (a), (b) and (c) show that the axial force decreases and the rate of increase in displacement decreases. This leads to the bending moment staying constant. Figure 7.2.2 (e) and (f) show that the compressive stress in the whole of the composite section decreases due to yielding, causing a reduction in axial force. The failure mechanism itself is not evident, as none of the components have reached their respective yield limits. There isn't a runaway failure with displacements leading to the conclusion that failure must be sudden as the steel section approaches the yield limit. It is postulated that as the web reaches the thermally reduced EC3 Yield Limit stress, increased bending will cause the bottom flange to yield. The neutral axis will suddenly move up and the top flange will yield in tension. The concrete slab will quickly fail due to cracking as the top flange yields.

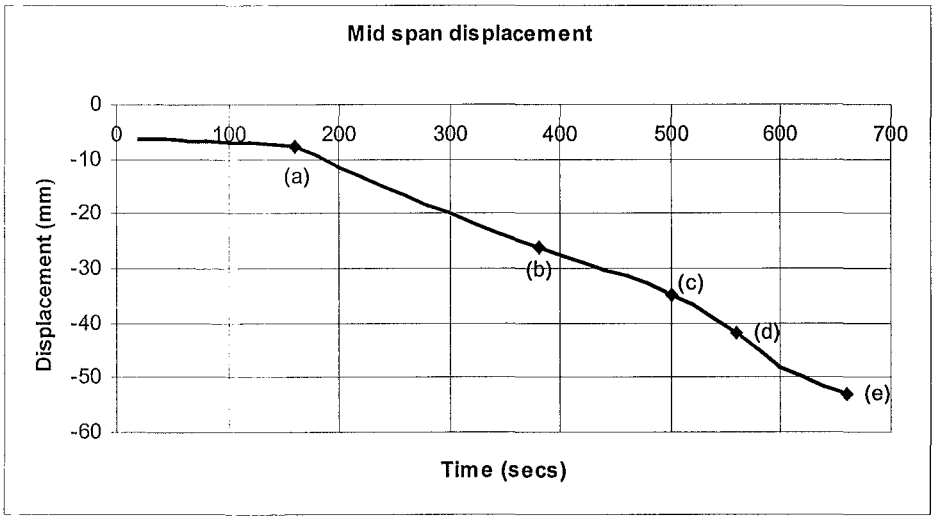

(a) Displacement

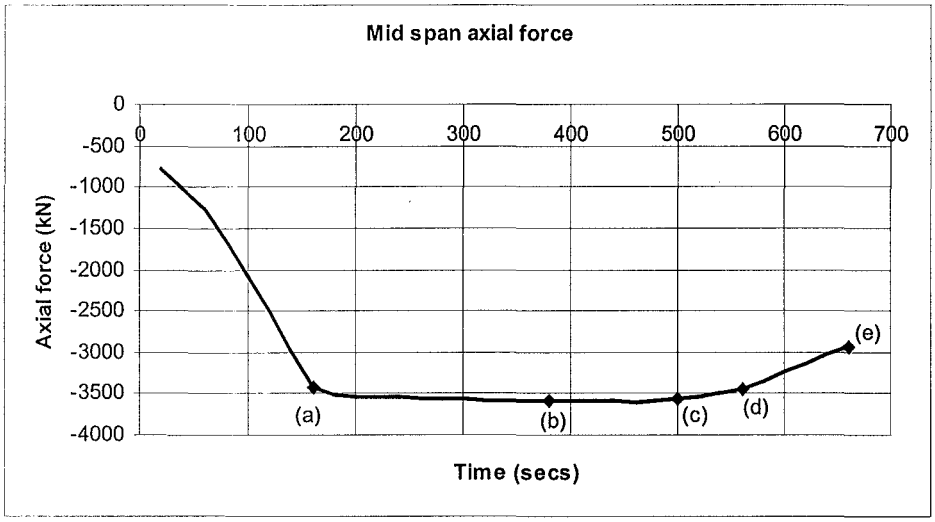

(b) Axial Force

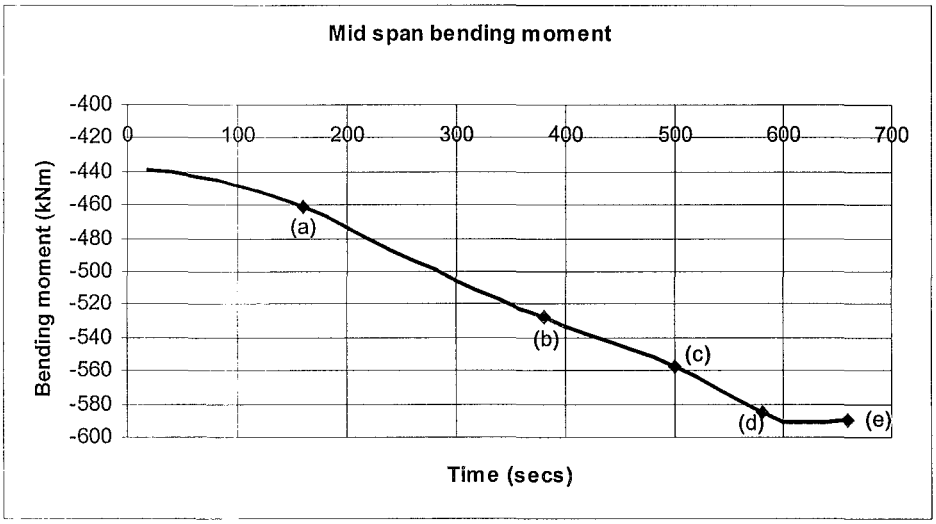

(c) Bending moment

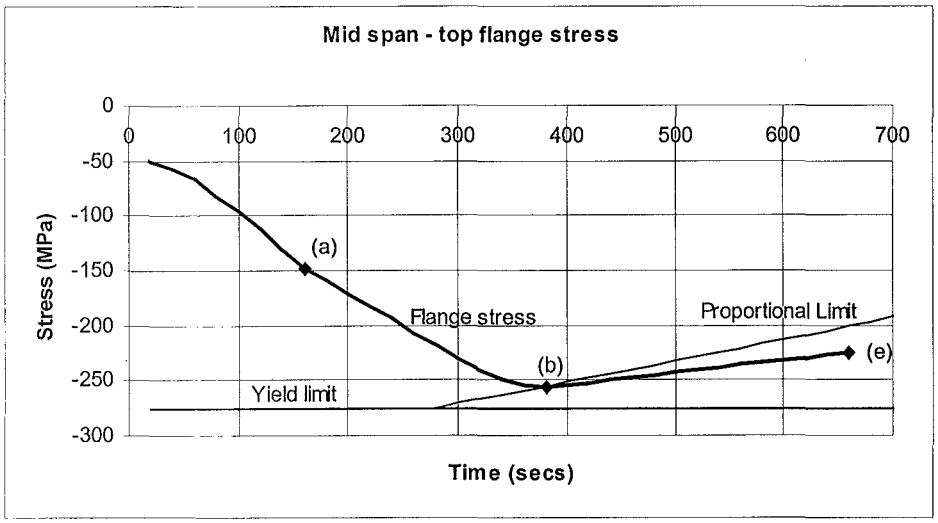

(d) Top flange stress

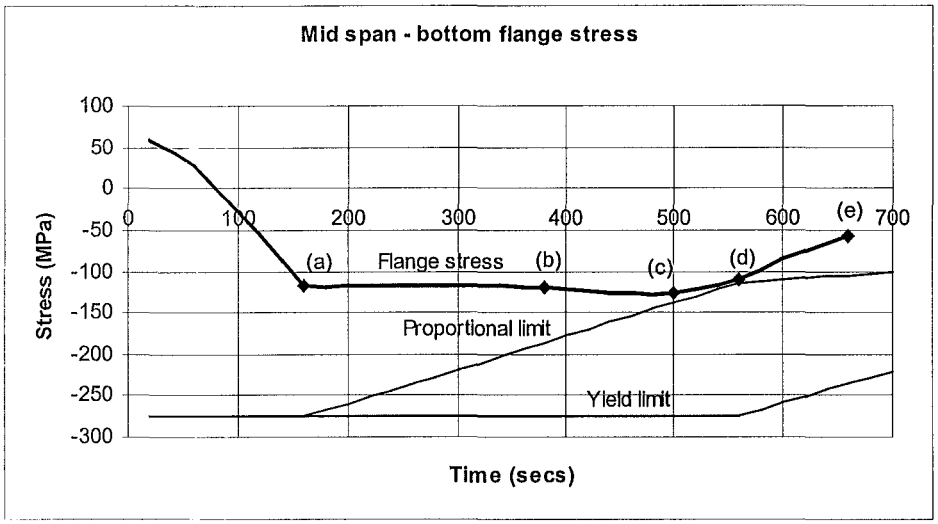

(e) Bottom flange stress.

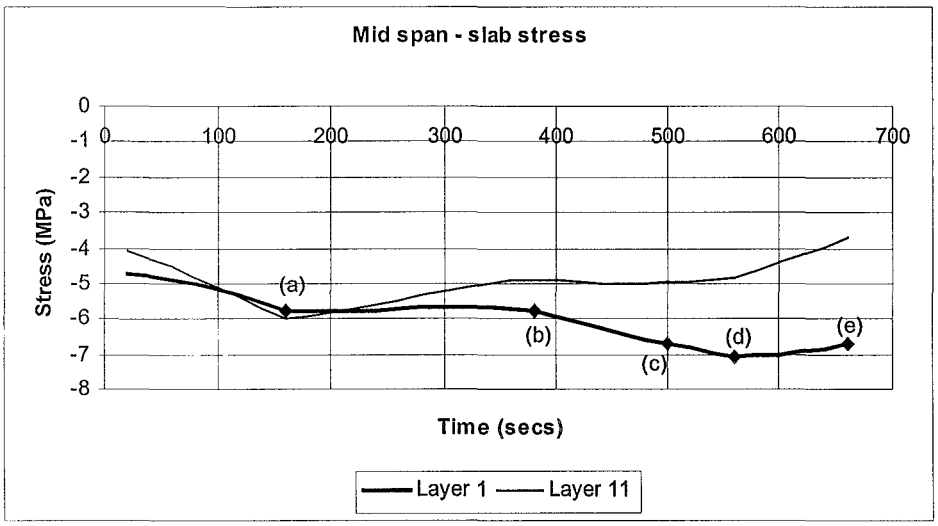

(f) Concrete stress

Figure 7.2.1 Mid span results for Pin - Pin supports in ISO 834 fire.

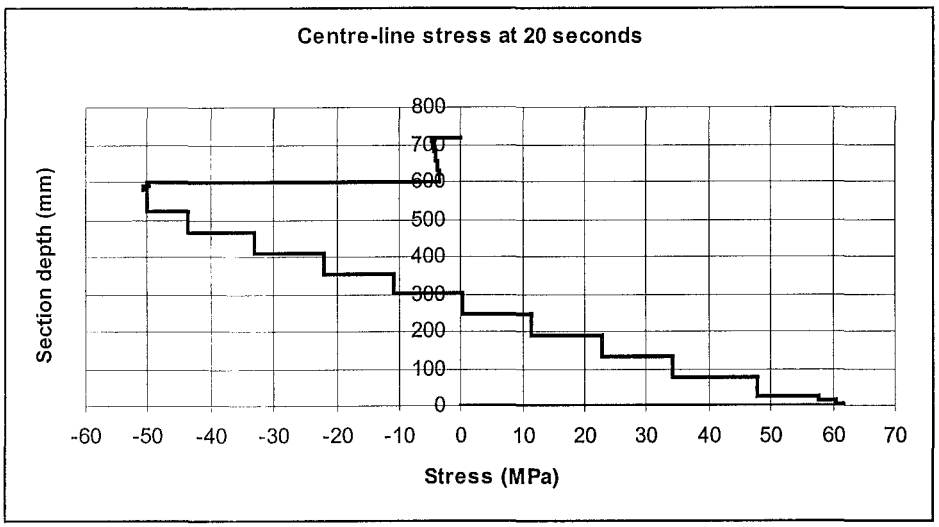

(a) Centre line stress at 20 seconds.

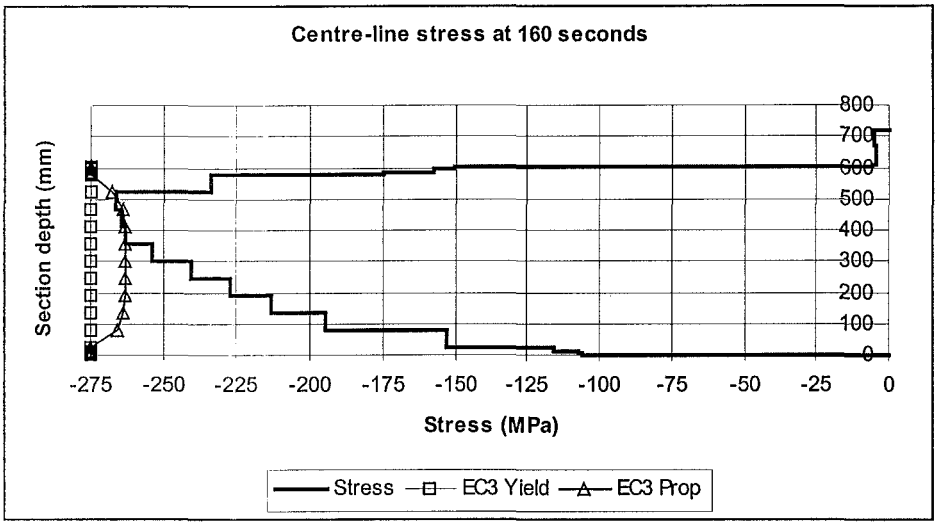

(b) Centre line stress at 160 seconds, point (a).

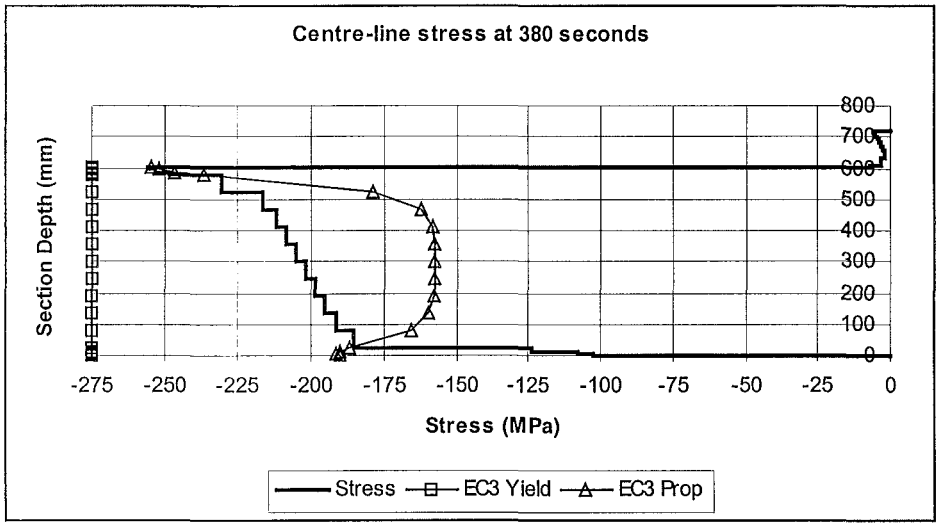

(c) Centre line stress at 380 seconds, point (b).

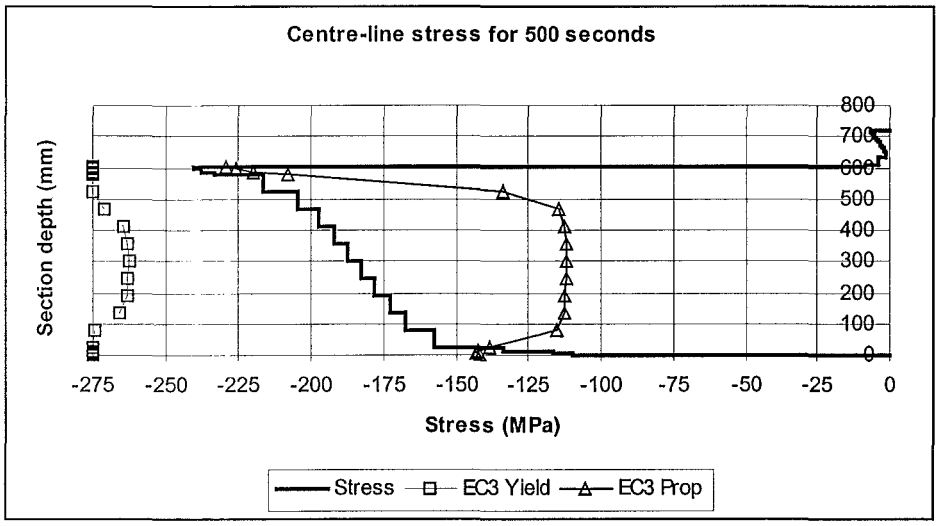

(d) Centre line stress at 500 seconds, point (c).

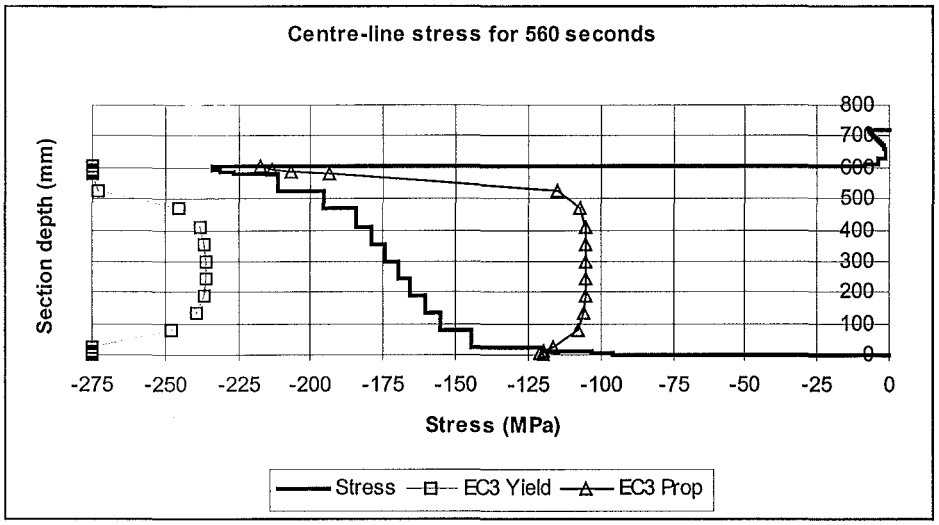

(e) Centre line stress at 560seconds, point (d).

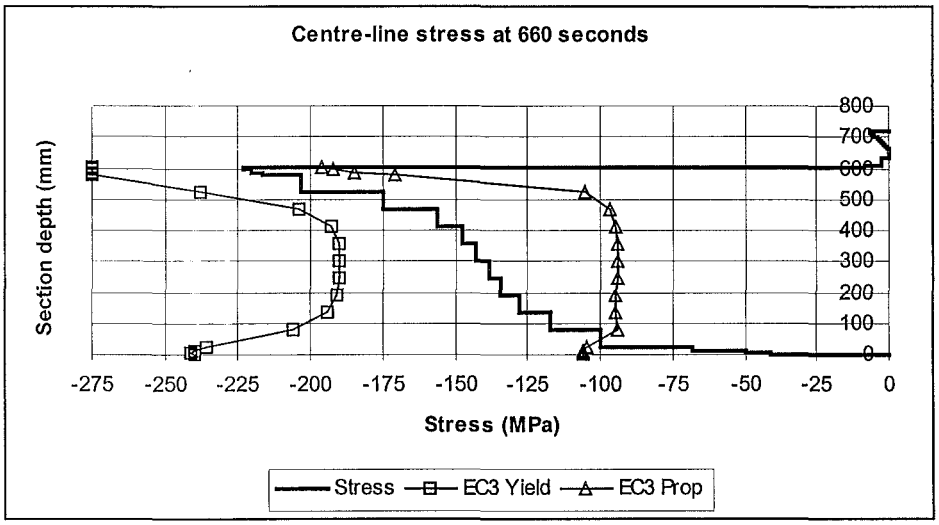

(f) Centre line stress at 660 seconds, point (e).

Figure 7.2.2 Mid span centre line stress for Pin - Pin supports in ISO 834 fire.

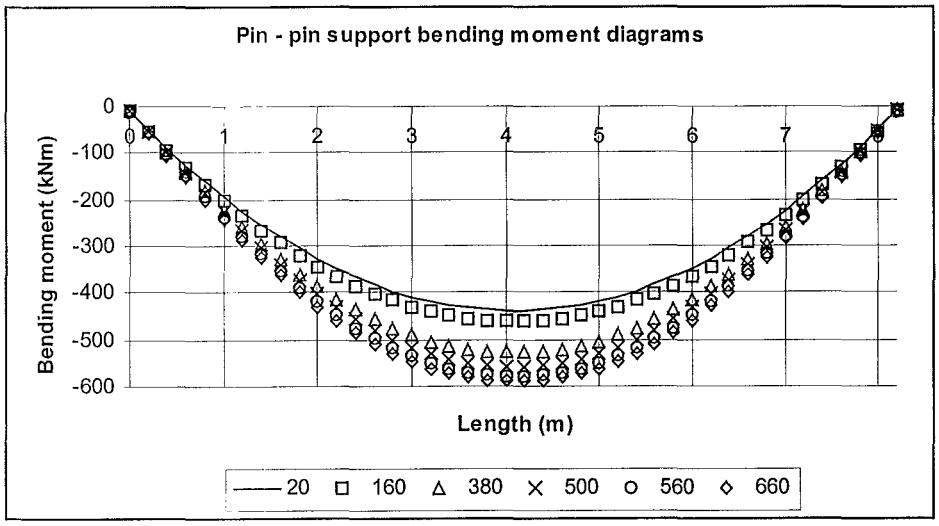

Figure 7.2.3 Pin - pin support bending moment diagrams in ISO 834 fire.

Figure 7.2.3 shows that P-δ effects due to the displacement and axial force amplify the bending moment. The bending moment increases until failure and there is no reduction in bending moment as was shown in the linear heating rate cases.

Summary.

As stated at the start of the results, the failure mechanism for the composite beam in a standard fire is far more complicated than found in the previous investigations carried out in this report. Due to the severity of the fire growth the web reaches the thermally reduced EC3 Proportional Limit before the flanges. This is due to the slenderness of this component and the fact that the high axial force induced from the thermal exposure causes compression that counteracts the bending stress in the bottom flange. Figure 7.2.4 shows the yielding that occurs in the web as the top and bottom flanges elongate, causing crushing of the web. The top flange of the section heats up more slowly than the bottom flanges due to the top of the flange being shielded by the concrete, and the fact that the concrete acts as a heat sink. Therefore the yielding will move down the web reasonably quickly. Even with greater bending and compressive stresses it takes considerably longer for the top flange to reach the thermally reduced EC3 proportional limit stress compared to the web.

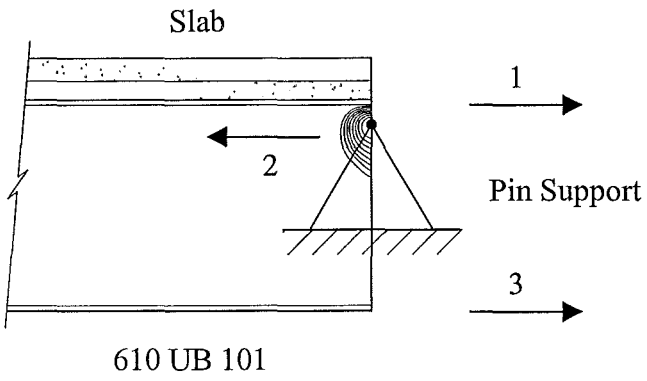

Figure 7.2.4 Web yielding diagram

where: 1 is the top flange elongation force.

2 is the web crushing.

3 is the bottom flange elongation force.

The low thermal conductivity of the concrete will mean that this component of the composite section will induce only a small axial load. Therefore yielding in the steel section will lead to a decrease in the thermally induced axial force.

The stresses in the slab are not near the crushing strength of the concrete and are driven by bending rather than axial load. The bottom layer (Layer 11) of the slab, because it has been finely discretised in the model, may however reach the thermally reduced crushing strength at the extremities of the profile (beyond Slab 2) because of the insulating properties of the concrete. This would explain the decrease and subsequent plateau in the average stress in the bottom layer of concrete after 160 seconds.

It is believed that shortly after 660 seconds the top flange and the web reach the thermally reduced EC3 Yield Limit stress causing the bottom flange to yield in bending because of the reduced axial force. The top flange will reach the thermally reduced Yield stress in tension due to a shift in the neutral axis and the concrete will fail quickly due to tension forces causing cracking.

7.3 Pin – Roller Supports (ISO 834 fire)

Introduction.

For this simulation, the composite section is tested in an ISO 834 fire with *pin – roller* end restraints. The standard three sided thermal boundary has been used in this simulation. Refer to Figure 5.3.1 for support schematic for the *pin – roller* case.

Results

The results of the structural analysis are shown in Figure 7.3.1 and Figure 7.3.2. The fire resistance of the one bay section in a standard fire two-dimensional simulation is 1160 seconds with a displacement of 640mm. The failure mechanism for the standard fire case is similar to that of the linear heating rate case. Initially the bottom flange of the 610 UB 101 yields inducing more yielding through the section, forming a plastic hinge at the mid span. Table 7.3.1 which relates to Figure 7.3.1 shows the times for the bottom flange to reach the thermally reduced EC3 Proportional Limit stress, the EC3 Yield Limit stress and the failure mechanism are shown in Table 7.3.1.

Table 7.3.1 Behaviour time line for Pin - Roller supports in ISO 834 fire.

	Behaviour	**Time**
(a)	The bottom flange reaches the thermally reduced EC3 Proportional Limit stress.	280 secs
(b)	The top flange approaches the thermally reduced EC3 Proportional Limit stress.	840 secs
(c)	The bottom flange reaches the thermally reduced EC3 yield Limit stress.	940 secs
(d)	The top flange goes from compression into tension.	1020 secs
(e)	The failure mechanism is achieved.	1160 secs

Up to point (a) in Figure 7.3.1 (c) and (d) the entire section behaves elastically as it heats and the stresses increase. Figure 7.3.1 (a) shows that the increase in displacements is only slight, as the beam is able to elongate without any axial resistance because of the roller support. There is no axial force in the system and therefore no amplification of bending moments due to P-δ effects. Figure

7.3.1 (c) and (e) show that the bottom flange tension stress increases due to bending and the stress in the top of the concrete slab goes from compression into tension as the beam elongates rather than deflecting down. This is due to the effects of thermal bowing.

At point (a) in Figure 7.3.1 (e) the average bottom flange stress reaches the thermally reduced EC3 Proportional Limit stress. Figure 7.3.2 (b) shows that part of the web has also reached the proportional limit stress at point (a). Figure 7.3.1(f) shows that the top layer of concrete (Layer 1) reaches its maximum tensile stress of 0.5 MPa.

Figure 7.3.1 (a) shows that between points (a) and (b) the displacement increases more rapidly due to the loss of stiffness in the steel section. This is caused by a decrease in the modulus of elasticity with temperature. Figure 7.3.1 (d) shows that the tensile stress in the bottom flange decreases as it softens, showing plastic behaviour. The stress in the top flange increases in compression due to bending but this is counteracted by an upward shift in the neutral axis. Figure 7.3.2 (b) and (c) shows that the neutral axis shifts up between points (a) and (b). This allows the stress in the concrete to remain relatively constant while more of the web shifts into tension.

At point (b) in Figure 7.3.1 (d) the average flange stress approaches the EC3 Proportional Limit. The most thermally affected parts of the top flange reach the proportional limit. This is not shown in Figure 7.3.2 (c) as this is a plot of the centre line stress where the root fillet and mass of steel act as a heat sink. The tips of the flanges will be affected as they receive the most energy from the fire from three sided heating. Figure 7.3.1(f) shows that as the top flange begins to yield, the top layer of concrete (Layer 1) takes up the required compression stresses.

Figure 7.3.1 (a) shows that between points (b) and (c) the displacement increases more rapidly, again due to a loss in stiffness in the steel section. Figure 7.3.2 (d) shows that more of the web goes into tension to compensate for the loss in capacity of the bottom flange, ie an upward shift in the neutral axis. Figure 7.3.1 (c) shows that the top flange compression stress decreases due to the neutral axis shift. Figure 7.3.1 (b) shows that the bending moment begins to decrease as the length of the beam decreases due to the displacements causing the roller to move in. At point (c) in Figure 7.3.1(e) and Figure 7.3.2 (d), the bottom flange and some of the web stresses reach the thermally reduced EC3 Yield Limit. The yield envelope is followed until failure.

Between points (c) and (d) the behaviour is similar to that between points (b) and (c). Figure 7.3.2 (e) and Figure 7.3.1 (a) show that more of the web goes into tension due to the increased displacements. Figure 7.3.1 (e) shows that the higher compression stresses the top layer of the concrete are attributed to the increased displacements, and that the stresses in the bottom layer of the slab do not change dramatically due to their close proximity to the neutral axis. Figure 7.3.1 (b) shows that the bending moment still decreases as the length, *l*, decreases with displacement.

At point (d) in Figure 7.3.1(d) and Figure 7.3.2(e) the top flange of the UB 610 101 goes into tension as more of the web reaches the thermally reduced EC3 Proportional limit and EC3 Yield Limit in tension. At this point failure begins to occur more rapidly as the plastic hinge is forming. The steel section loses stiffness due to the reduction in elastic modulus with thermal exposure. This causes a runaway failure in displacement as shown in Figure 7.3.1 (a). The bending moment decreases more rapidly as the displacement increases, reducing the length of the beam.

Up to 1160 seconds, the displacements increase with the runaway failure. At this point the entire steel section has reached the EC3 Yield Limit as shown in Figure 7.3.2(f), and there is no resistance to bending except from the slab. Figure 7.3.1(f) shows that approaching 1160 seconds the compression stress in the slab reaches the crushing stress and the slab yields quickly. The *timeprint* (output interval) for this particular simulation was 20 seconds so failure could occur at any time between 1160 and 1180 seconds. This is why full yielding is not readily visible on the graphs.

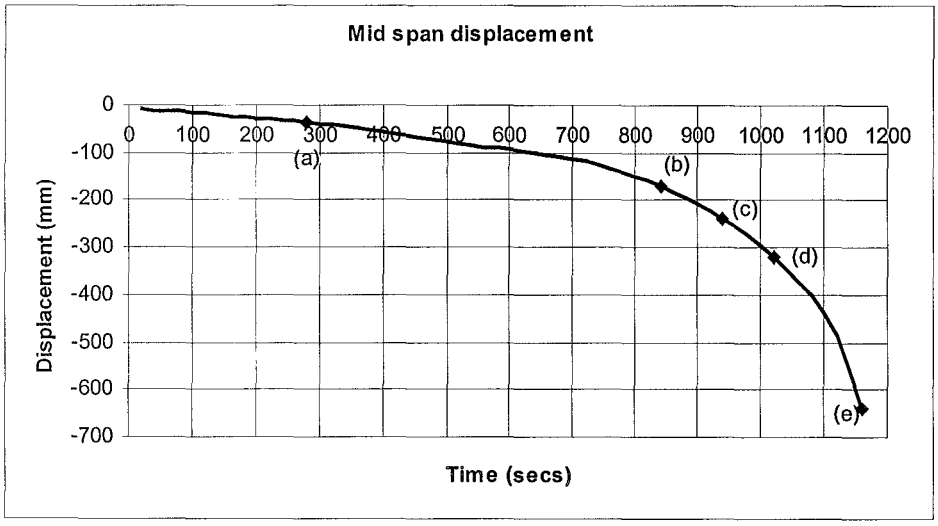

(a) Displacement.

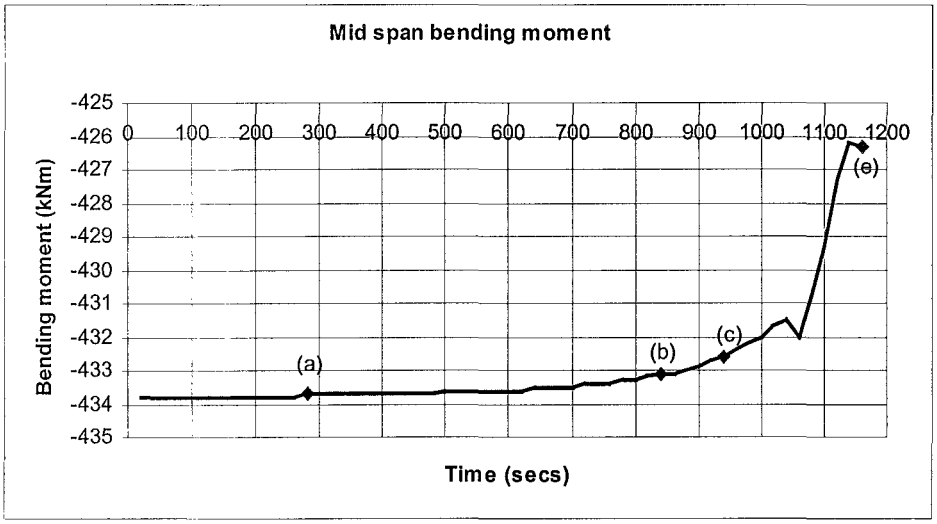

(b) Bending moment.

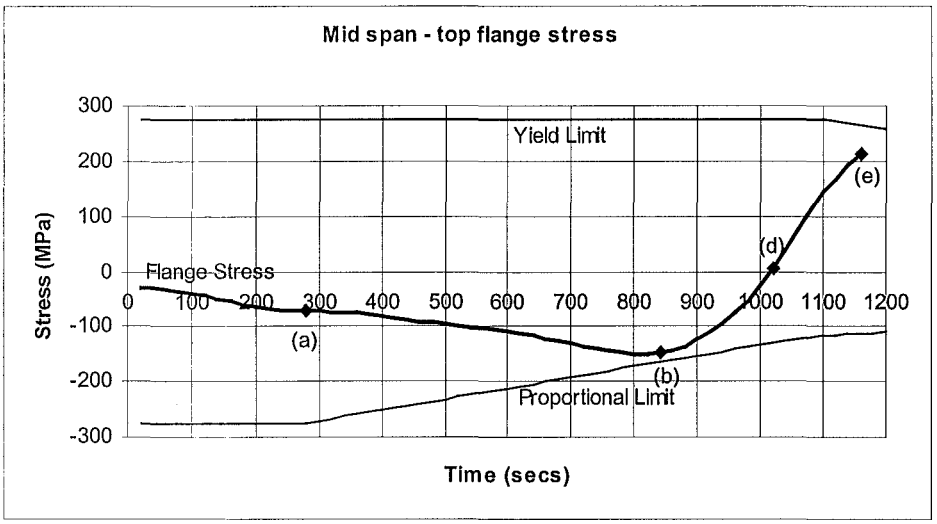

(c) Top flange stress.

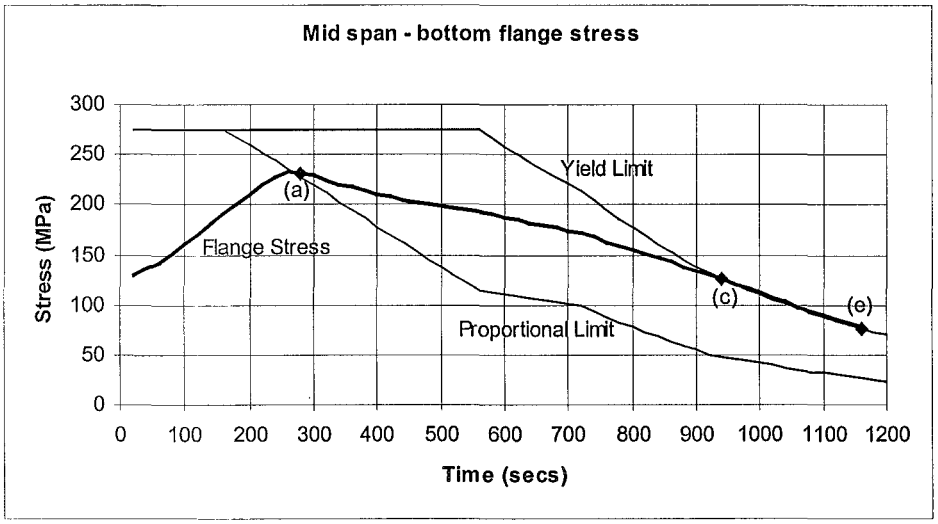

(d) Bottom flange stress.

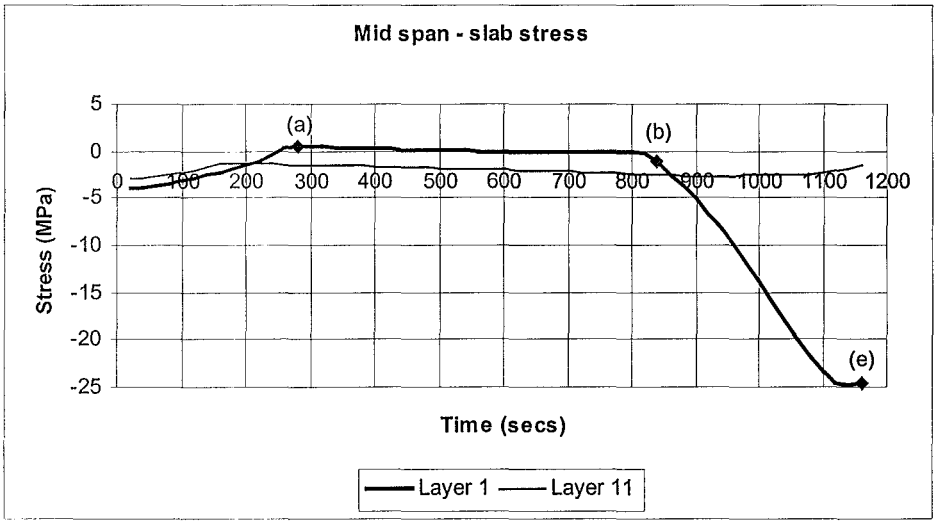

(e) Concrete stress.

Figure 7.3.1 Mid span results for Pin - Roller supports in ISO 834 fire.

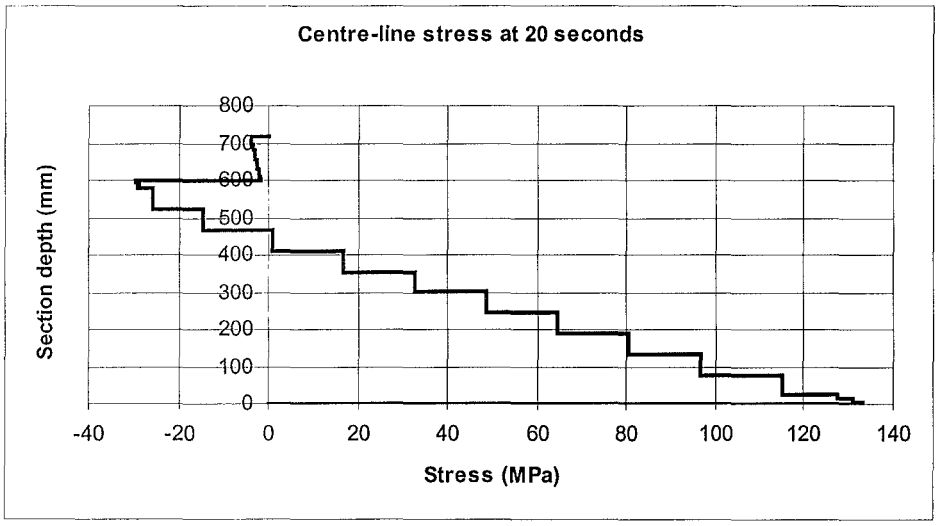

(a) Centre line stress at 20 seconds.

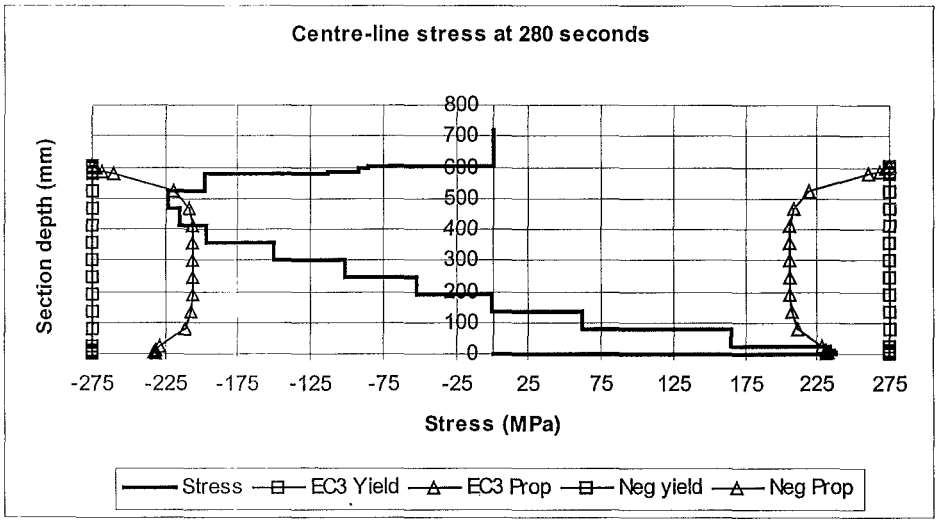

(b) Centre line stress at 280 seconds, point (a).

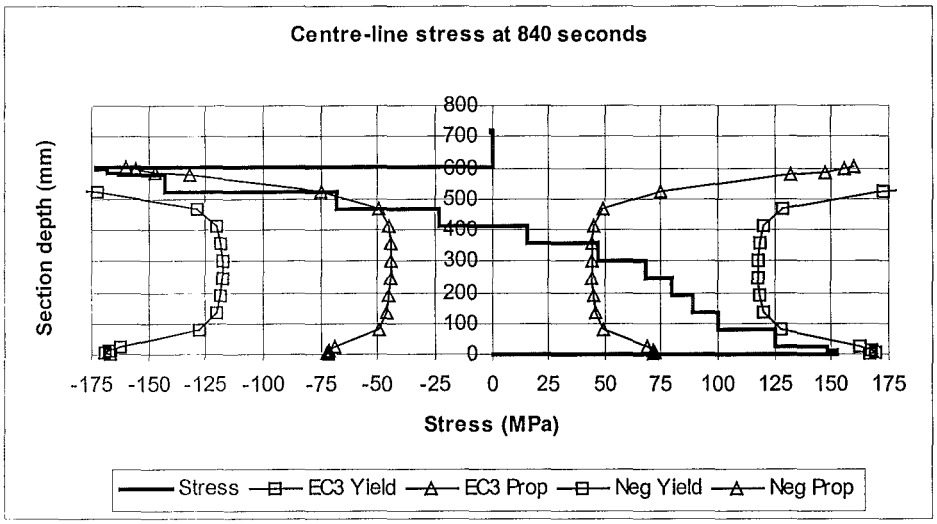

(c) Centre line stress at 840 seconds, point (b).

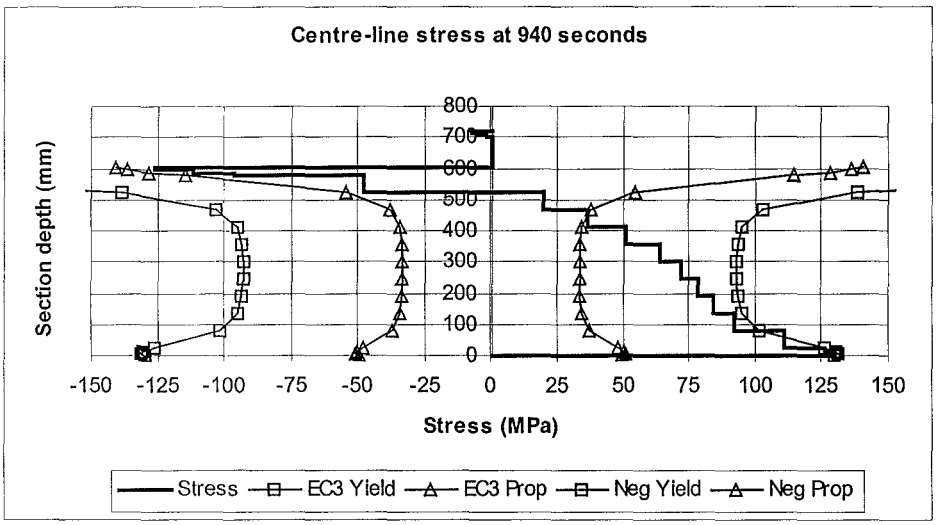

(d) Centre line stress at 940 seconds, point (c).

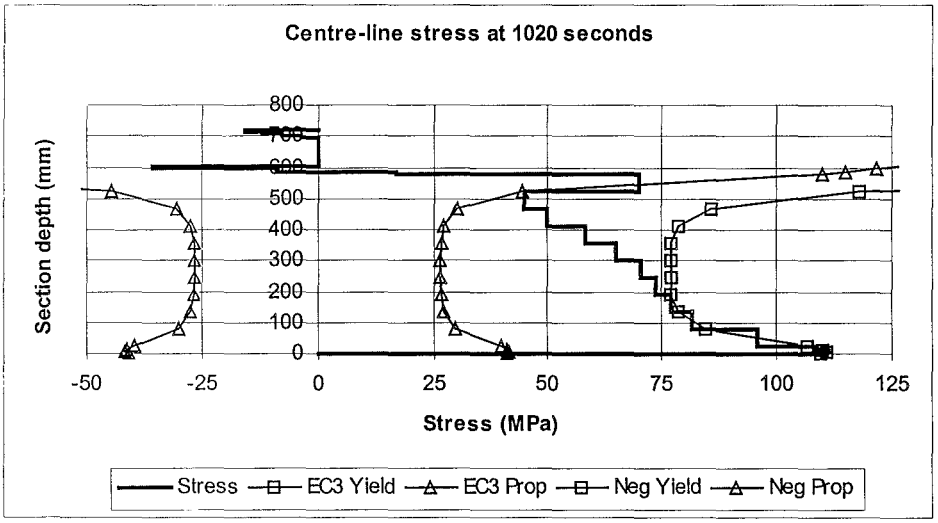

(e) Centre line stress at 1020 seconds, point (d).

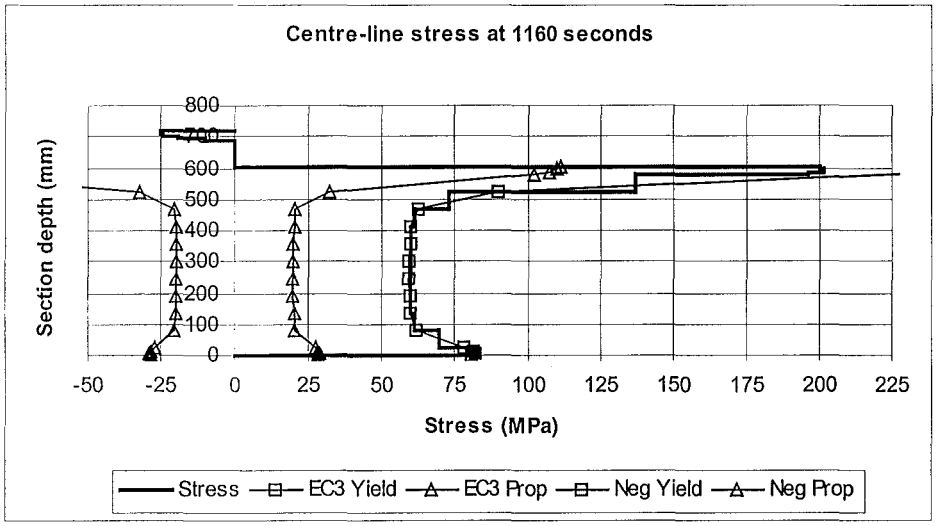

(f) Centre line stress at 1160 seconds, point (e).

Figure 7.3.2 Mid span centre line stress for Pin - Roller supports in ISO 834 fire.

Figure 7.3.3 shows that the change in bending moment diagram with time is very small. This is because there is no axial restraint to cause P-δ effects that amplify the bending moment. Near failure the bending moment decreases due to a decrease in length, l, of the beam. This is caused by the mid span displacements pulling the roller in. The change in bending moment is almost negligible.

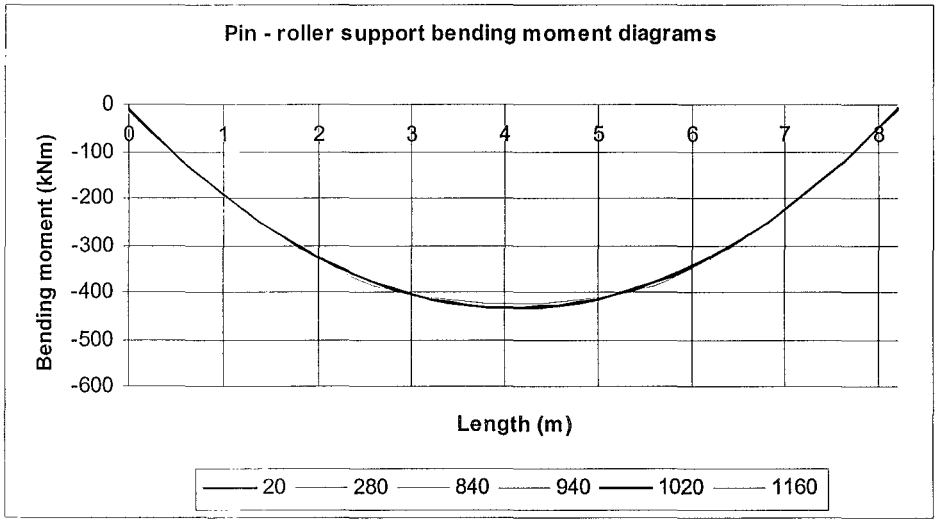

Figure 7.3.3 Pin – Roller supports bending moment diagrams in ISO 834 fire.

Summary

The failure mechanism exhibited in this simulation is very similar to the failure exhibited in the slower linear heating rate case of 5°C per minute. That is, the bottom flange and part of the web of the 610 UB 101 reaches the thermally reduced EC3 Proportional Limit causing a loss in stiffness leading to the formation of a plastic hinge mid span.

As the bottom flange yields, more of the steel section goes into tension and there is an upward shift in the neutral axis. Due to increasing thermal load and stress, more of the steel section yields with very little effect on the slab. When most of the steel section goes into tension, the slab starts to show compression stresses in the top layers. At failure, all of the steel section has reached the EC3 Yield Limit and the slab is unable to take the required load in bending. Concrete cracking occurs leading to rapid failure. There is a runaway failure due to the roller being unable to resist the tension forces induced by the increase in displacement.

7.4 Fixed – Fixed Supports (ISO 834 fire).

Introduction

For this simulation the composite section is tested in an ISO 834 fire *with fixed – fixed* end restraints. The standard three sided thermal boundary has been used in this simulation. Refer to Figure 5.4.1 for the support schematic for the fixed – fixed case.

Results

The results of the structural analysis are shown in Figure 7.4.1, Figure 7.4.2, Figure 7.4.3 and Figure 7.4.4. The fire resistance of the one bay section in a standard fire two-dimensional simulation is 760 seconds with a mid span displacement of 70mm. The failure mechanism is three plastic hinges, two forming at the ends of the span and one forming at the mid span of the composite section. Table 7.4.1, which relates to Figure 7.4.1, Figure 7.4.2, Figure 7.4.3 and Figure 7.4.4, shows a time line for the observed composite section behaviour and formation of the plastic hinges.

Table 7.4.1 Behaviour time line for Fixed - Fixed supports in ISO 834 fire.

	Behaviour	Time
(a)	Axial force increases at an increased rate due to thermal exposure. All top layer end of span concrete is cracked.	60 secs
(b)	End of span bottom flange reaches the EC3 Yield Limit.	140 secs
(c)	End of span top flange reaches the EC3 Proportional Limit.	320 secs
(d)	Mid span top flange reaches the EC3 Proportional Limit.	380 secs
(e)	Mid span bottom flange approaches the EC3 Proportional Limit.	480 secs
(f)	Failure mechanism achieved.	760 secs

Up to point (a) in Figure 7.4.3 (e) the concrete fails in tension at the ends of the span and shows no or little stress. Figure 7.4.3 (a) shows that at point (a) the rate of increase in axial force increases, this is due to the temperature increase in the steel section. As previously stated in this section, due to the rapid fire growth, the steel section will drive the axial force through thermal elongation. There will be a thermal lag in the elongation of the slab because of its mass and thermal properties.

Figure 7.4.3 (b) shows that from the start of the simulation up to point (b) the negative bending moment at the end of the span increases. This is due to the increase in axial force with thermal elongation causing hogging with P-δ effects. Figure 7.4.3 (c) shows that the top flange stress decreases in tension and then moves into compression at around 120 seconds. Figure 7.4.3 (d) shows the bottom flange stress increases in compression. Figure 7.4.4 (a) (b) and (c) show the transition in the bottom flange and web from tension into compression at the ends of the span during the initial stages of the simulation. The transition from tension stress into compression stress is due to the increased axial forces.

Up to point (b) in Figure 7.4.1 (c) the mid span positive bending moment decreases as the negative moment increases at the ends of the span. Figure 7.4.1 (a) shows that there is little displacement at mid span due to the thermal bowing. Figure 7.4.1 (d) and (e) shows that the top flange stress increases in compression and the bottom flange tension stress decreases and moves into compression. Figure 7.4.1 (f) shows that the slab stress stays constant in the top layer (Layer 1) while the bottom layer (Layer 11) compression stress increases due to the thermal bowing. The top

slab stress stays constant because of the increase in axial force counteracting the tension stress caused by the thermal bowing. Figure 7.4.2 (a) and (b) show the stress distribution along the centre line of the section at the mid span of the beam during the initial stages of the simulation.

At point (b) in Figure 7.4.3 (d) and Figure 7.4.4 (c) the bottom flange stress reaches the EC3 Yield Limit and the bottom of the web reaches the thermally reduced EC3 Proportional Limit in compression. The stresses due to thermal elongation cause a compression failure in the bottom flange before the material properties are thermally reduced. This, with the loss in concrete strength, causes the formation of the first plastic hinges at the ends of the span as shown in Figure 7.4.3 (b) at point (b) where there is a decrease in moment. Yielding in the bottom flange causes the steel section to soften and thus deflections increase near the supports. Figure 7.4.1 (a) and (c) show that the positive bending moment at the mid span therefore increases with the formation of the end of span plastic hinges causing the mid span displacements to increase. Figure 7.4.1 (b) shows that the axial force increases linearly. Figure 7.4.1 (e) shows that the mid span bottom flange compression stress decreases slightly as the beam deflects. This is due to tension stresses from bending counteracted by the increasing compression stresses from the axial force. Figure 7.4.1 (f) shows that there is an increase in the compression stresses in the top layer of concrete (Layer 1) while the stresses in the bottom layer of concrete increase uniformly.

At point (c) in Figure 7.4.3 (c) the end of span top flange stresses reach the thermally reduced EC3 Proportional Limit. Figure 7.4.4 (d) shows that at this stage the entire steel section has reached the proportional limit. Figure 7.4.3 (b) shows that the end of span bending moment rate of change decreases and then plateaus. This is duplicated by the mid span bending moment.

At point (d) in Figure 7.4.1 (d) and Figure 7.4.2 (d) the mid span top flange stress increases in compression until it reaches the EC3 Proportional Limit. Figure 7.4.1 (a), (b) and (c) show that the rate of mid span bending moment increase decreases with the axial force due to P-δ effects while the displacements increase uniformly. Figure 7.4.2 (d) shows that at this point most of the steel section has reached the proportional limit and only the bottom flange is still in the elastic range. Figure 7.4.1 (f) shows that the slab stresses increase in compression due to increased bending stress. At point (d) in Figure 7.4.3 (b) the end of span bending moment goes from being negative to being positive due to a loss in capacity of the steel.

After 480 seconds at point (e) in Figure 7.4.1 (e) the average mid span bottom flange stress approaches the EC3 Proportional Limit. Some of the bottom flange reaches the proportional limit due to higher temperatures at the tips of the flange. Figure 7.4.2 (e) shows that at this point nearly all of the steel section has reached the proportional limit. Figure 7.4.1 (a), (b) and (c) shows that the displacements increase and the axial force decreases due to a loss in steel stiffness. The rate of increase in displacement is greater than the decrease in axial force, and the bending moment increases with P-δ effects. Figure 7.4.1 (e) shows that as the axial force decreases, the stresses in the bottom flange decrease. Figure 7.4.1 (f) shows that compression stresses in the slab increase uniformly.

Leading up to failure between 760 and 780 seconds the end of span positive bending moments increase with the bending moment at the mid span. Figure 7.4.3 (c) and Figure 7.4.4 (e) show that the end of span top flange stress increases slightly but most of the steel section has reached the EC3 Yield Limit. Figure 7.4.1 (e) and Figure 7.4.2 (f) shows that the mid span bottom flange stress approaches tension and fails at this point with the formation of the third plastic hinge due to the web reaching the yield limit. At this point no load can be redistributed anywhere else in the section. The stresses will increase quickly at mid span and the whole of the steel section will reach the thermally reduced EC3 Yield Limit stress. The concrete slab is unable to withstand the load in flexure and fails.

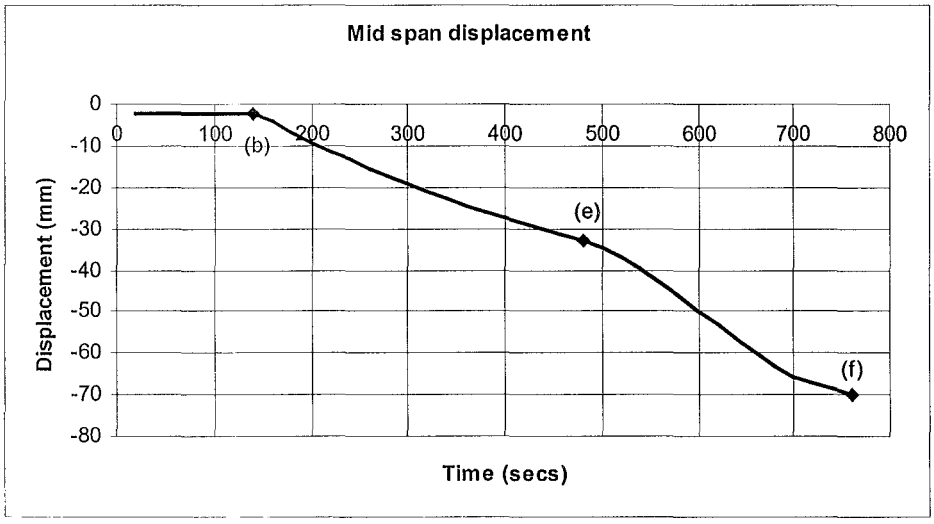

(a) Displacements.

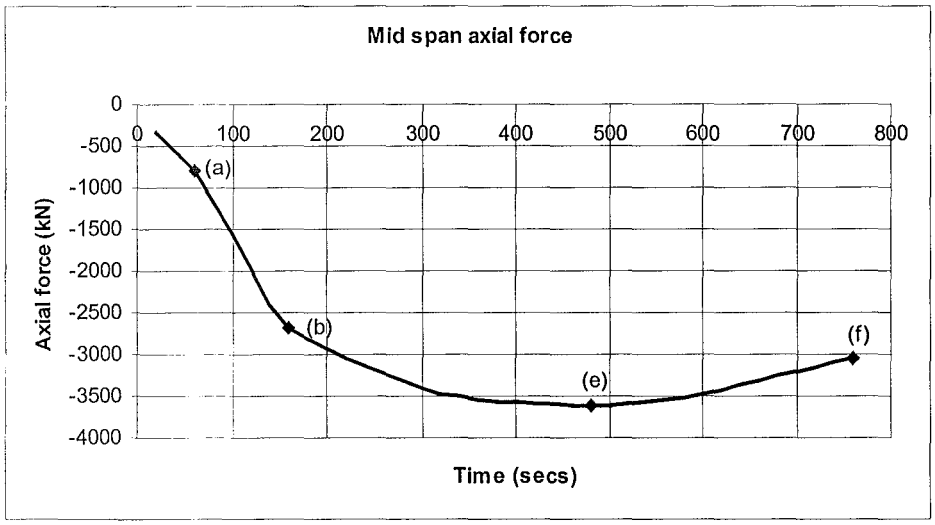

(b) Axial force.

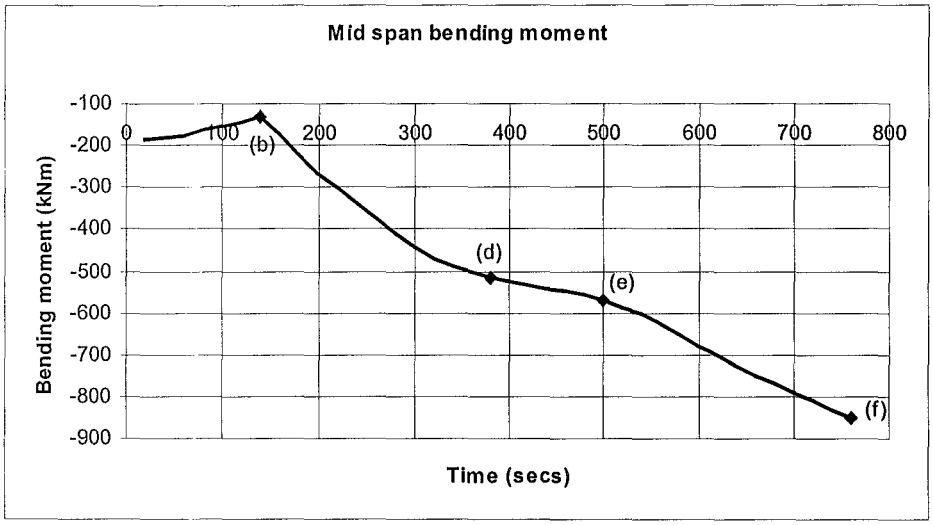

(c) Bending moment.

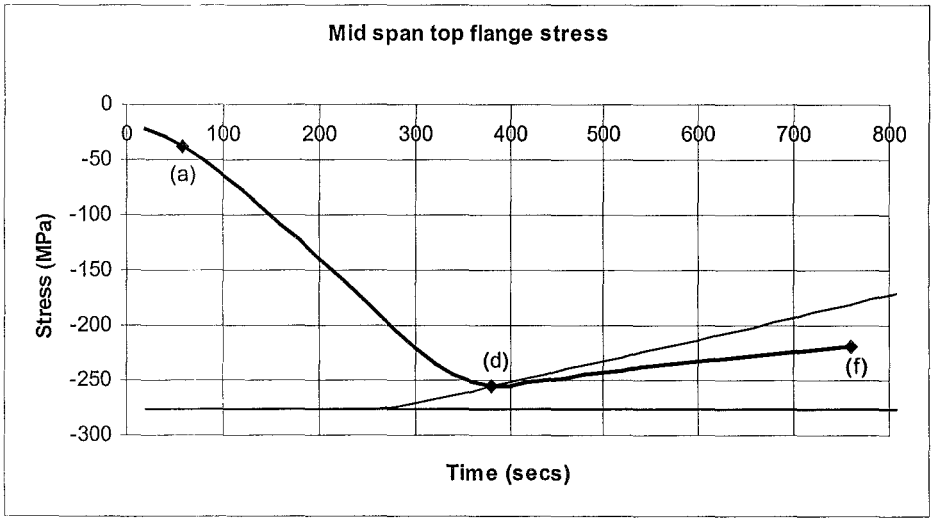

(d) Top flange stress.

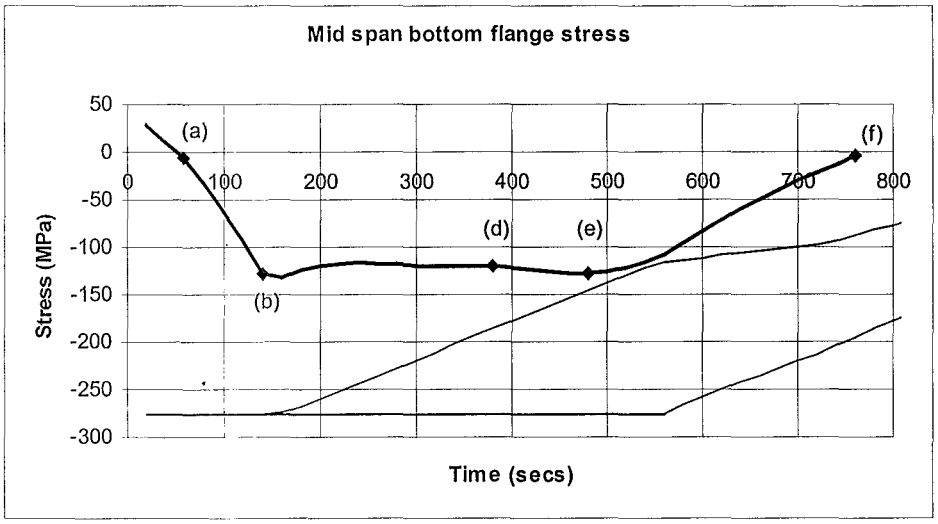

(e) Bottom flange stress.

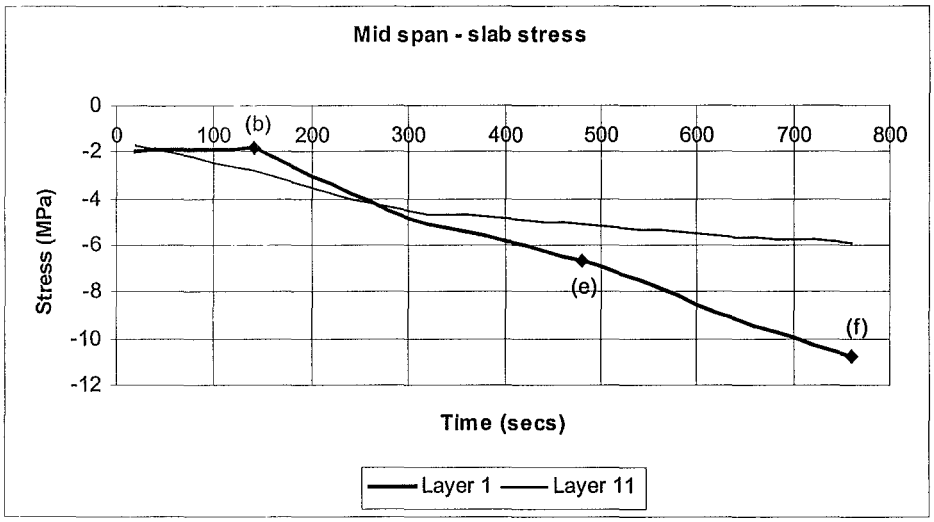

(f) Concrete stress.

Figure 7.4.1 Mid span results for Fixed - Fixed supports in ISO 834 fire.

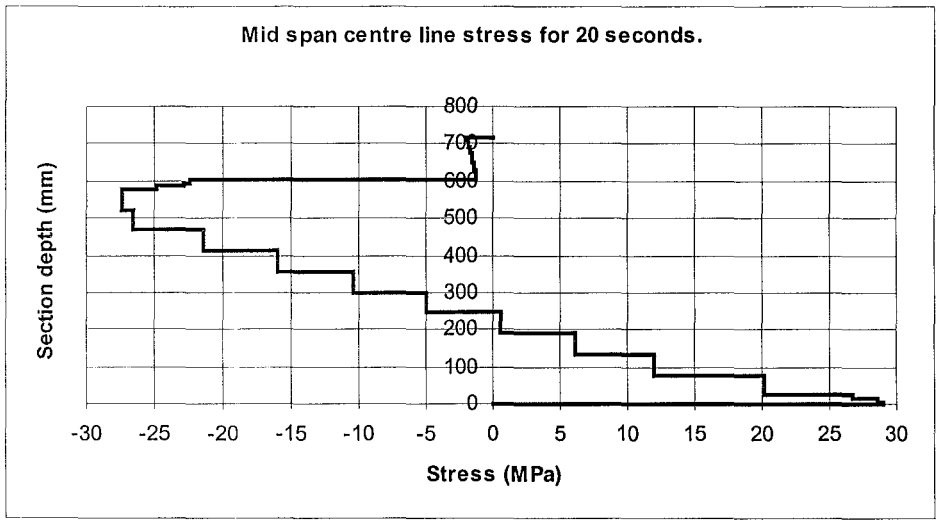

(a) Mid span centre line stress at 20 seconds.

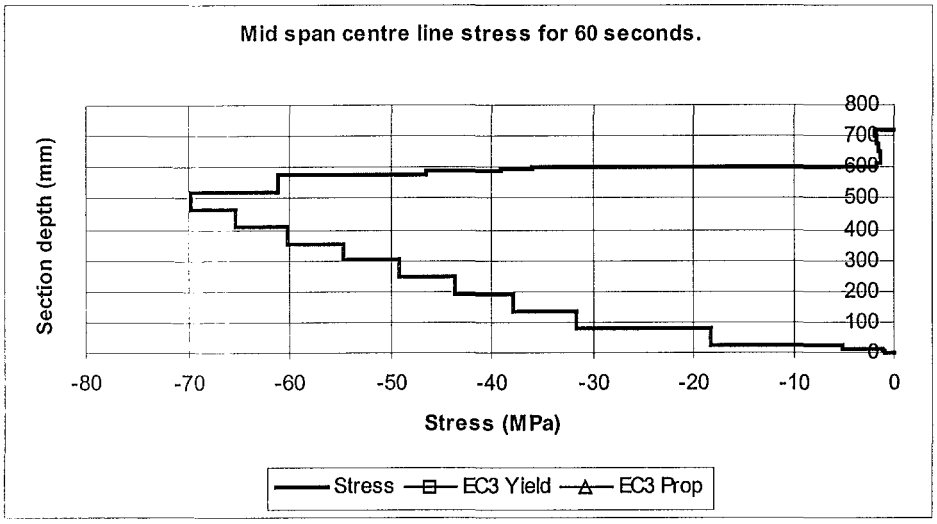

(b) Mid span centre line stress at 60 seconds, point (a).

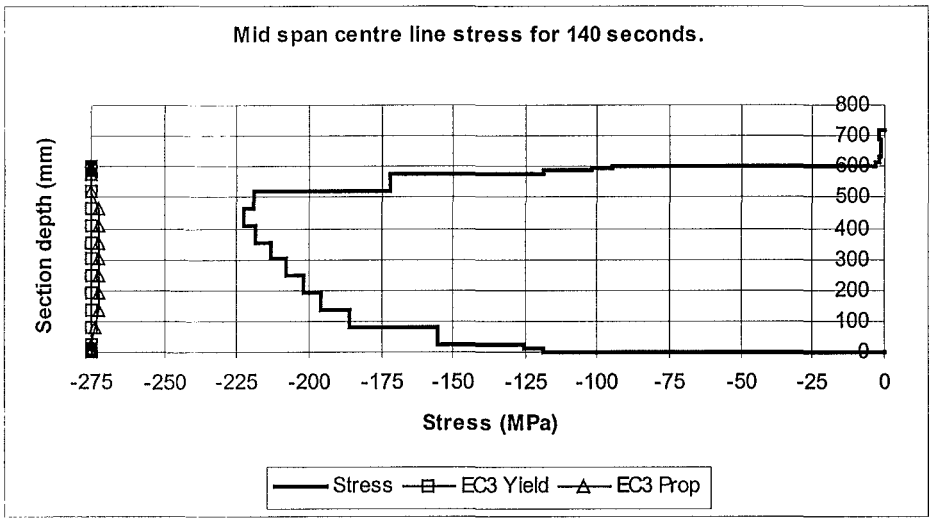

(c) Mid span centre line stress at 140 seconds, point (b).

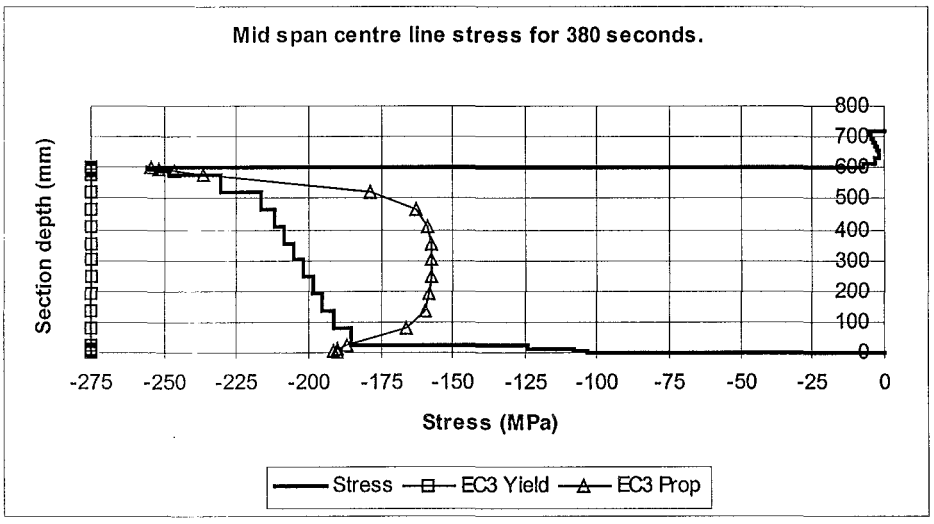

(d) Mid span centre line stress at 380 seconds, point (d).

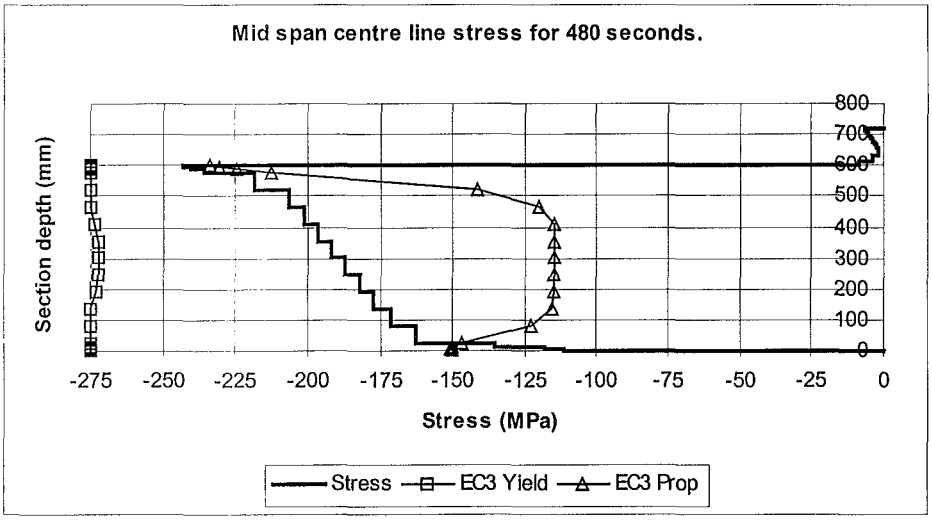

(e) Mid span centre line stress at 480 seconds, point (e).

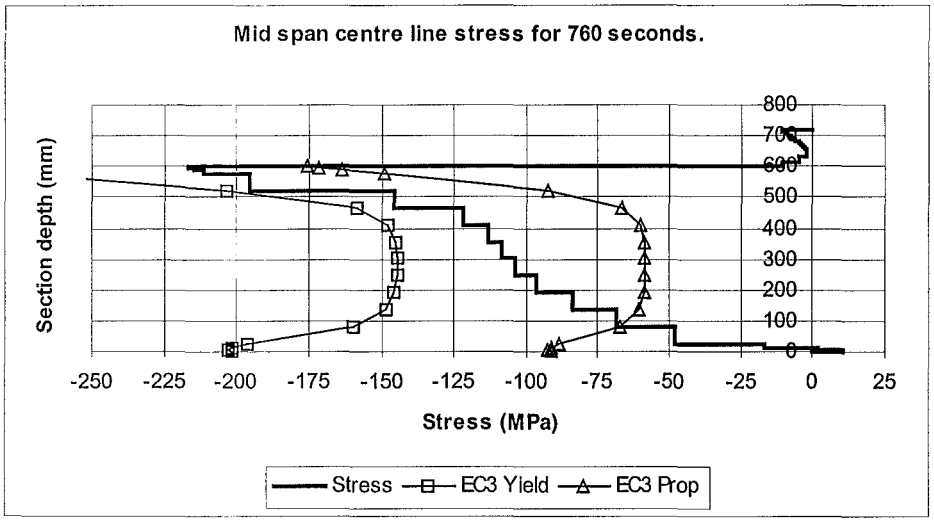

(f) Mid span centre line stress at 760 seconds, point (f).

Figure 7.4.2 Mid span centre line stress for Fixed - Fixed supports in ISO 834 fire.

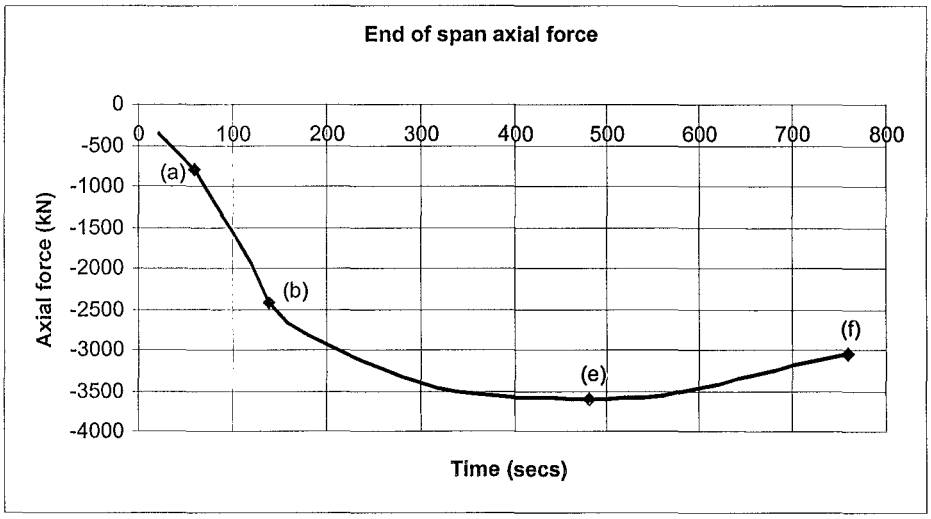

(a) Axial force.

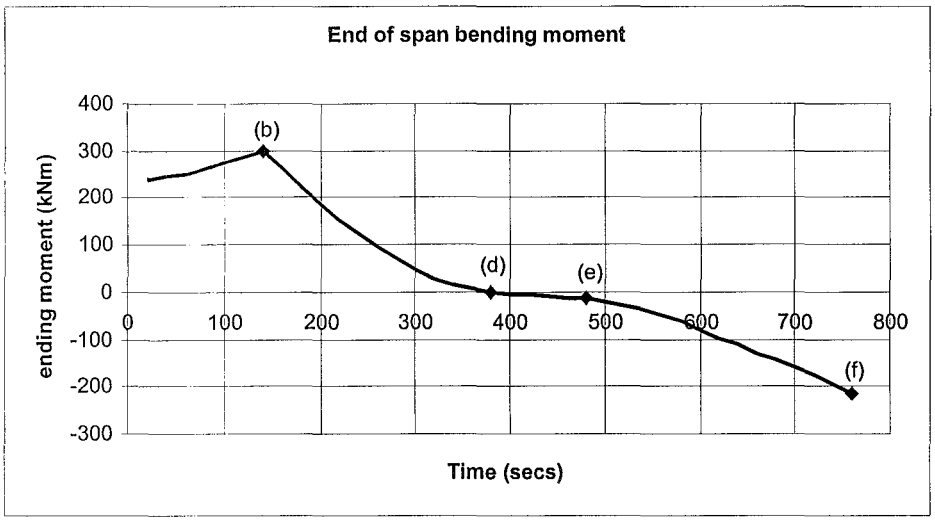

(b) Bending moment.

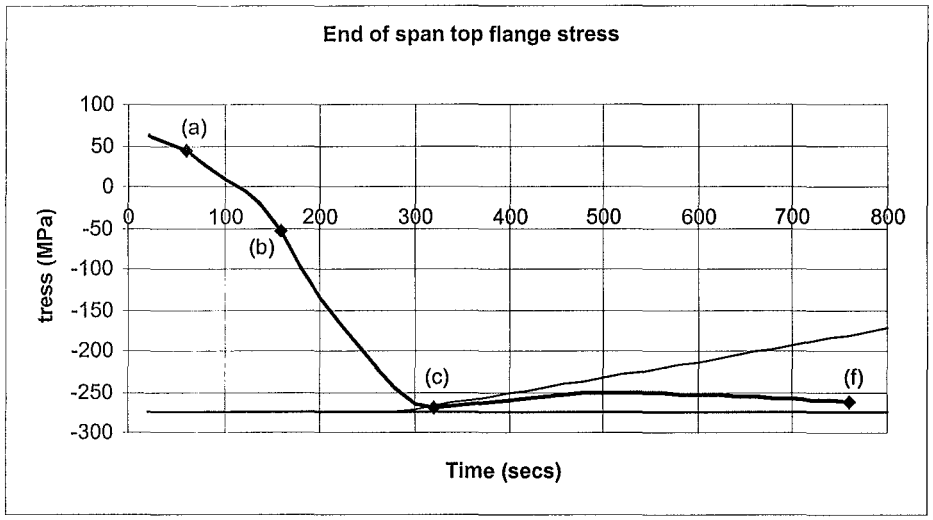

(c) Top flange stress.

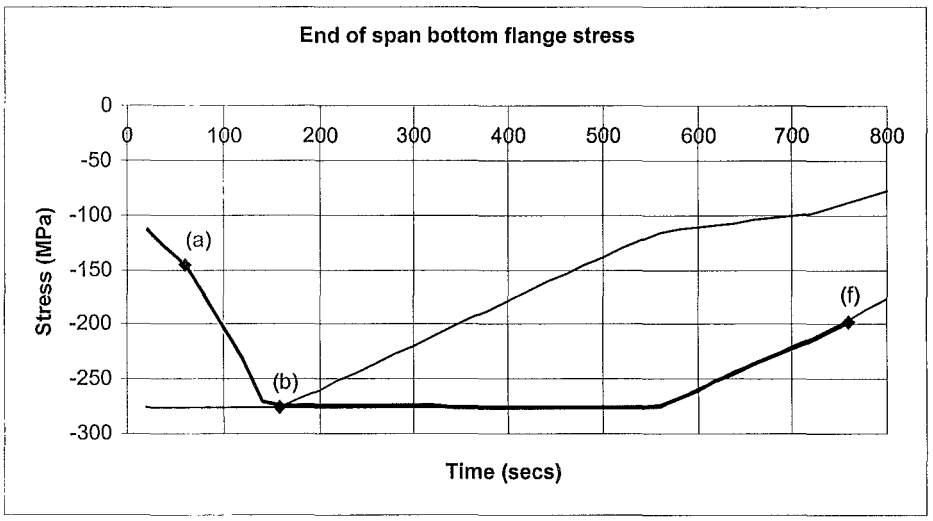

(d) Bottom flange stress.

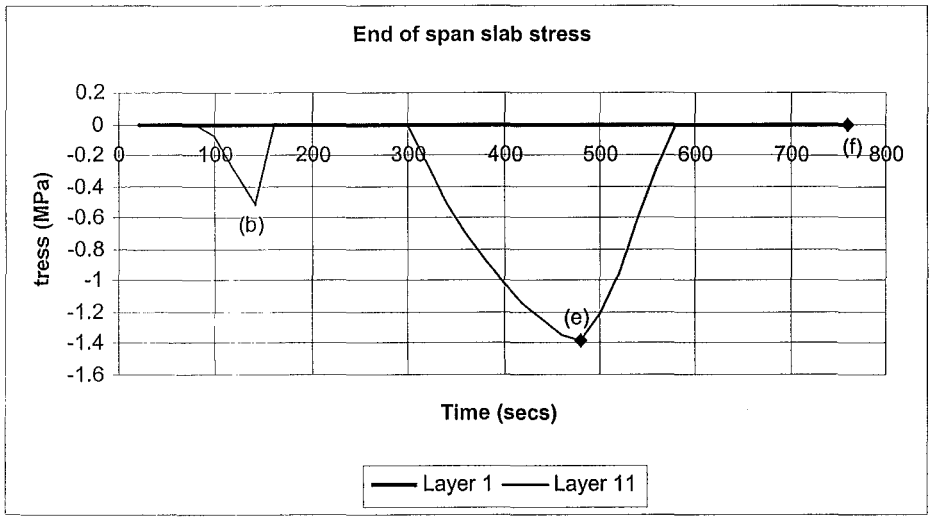

(e) Concrete slab stress.

Figure 7.4.3 End of span results for Fixed - Fixed supports in ISO 834 fire.

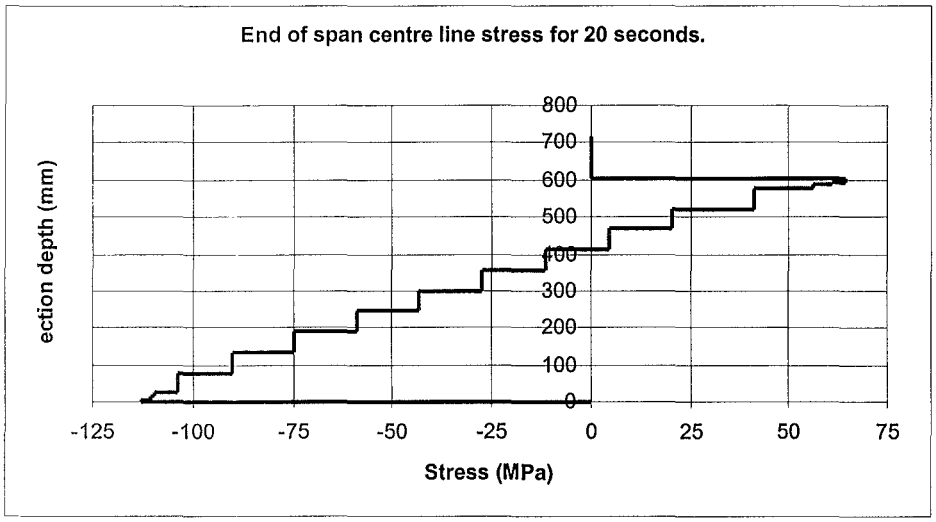

(a) End of span centre line stress at 20 seconds.

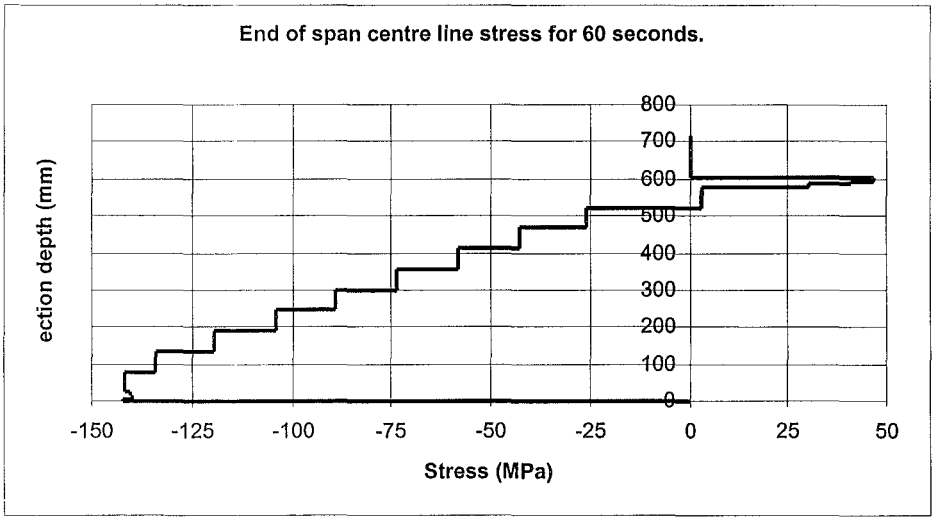

(b) End of span centre line stress at 60 seconds, point (a).

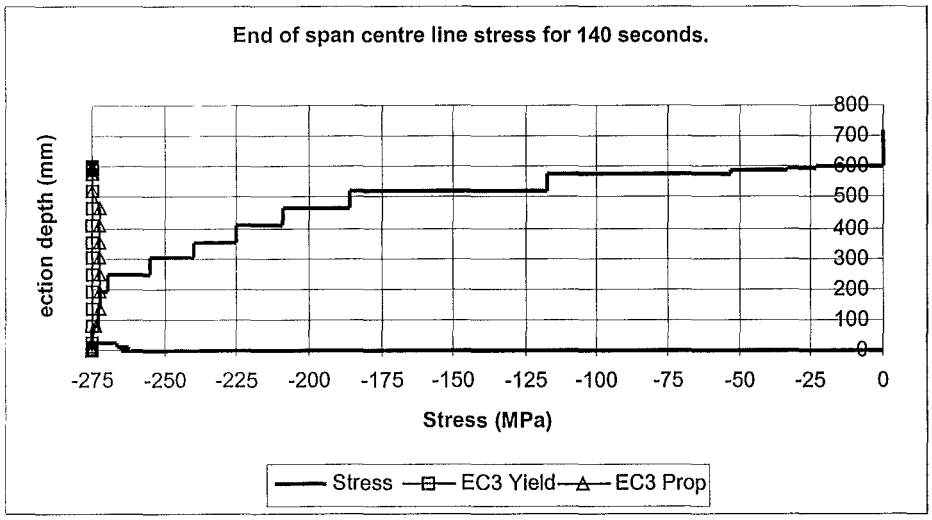

(c) End of span centre line stress at 140 seconds, point (b).

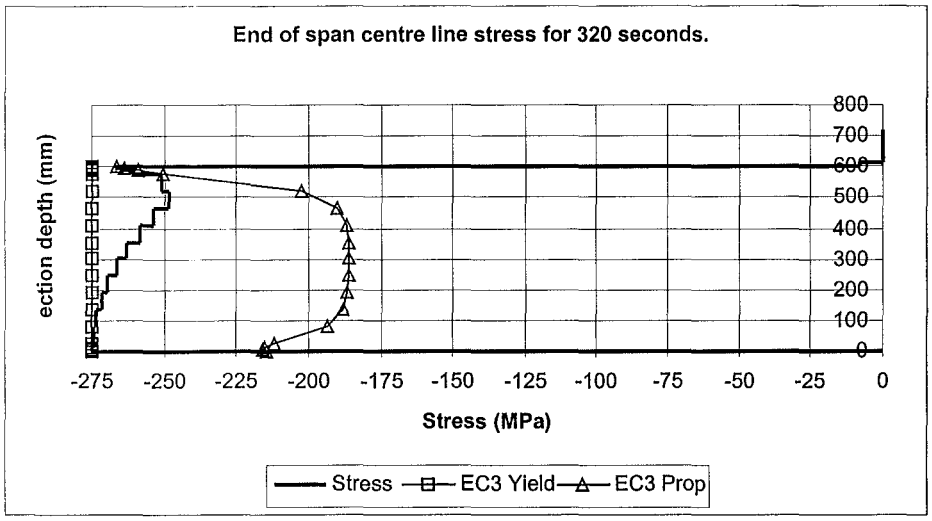

(d) End of span centre line stress at 320 seconds, point (c).

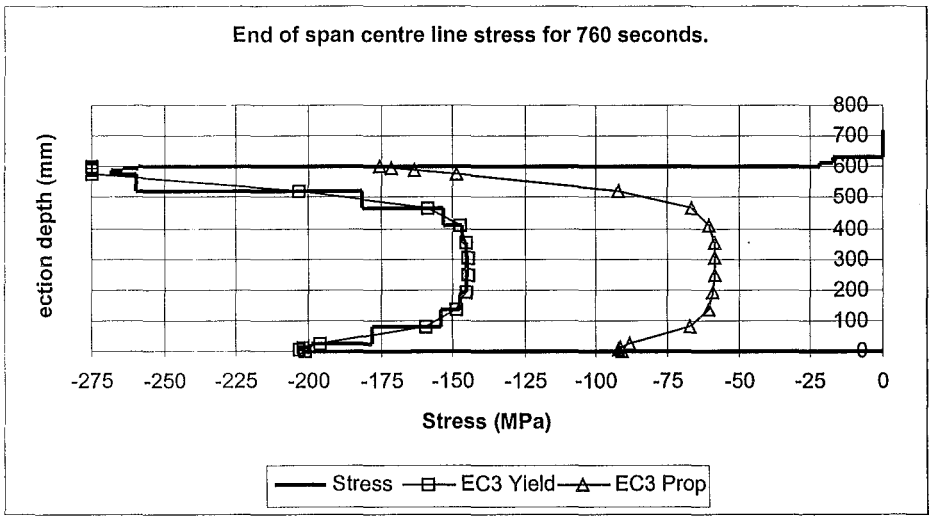

(e) End of span centre line stress at 760 seconds, point (f).

Figure 7.4.4 End of span centre line stress for Fixed - Fixed supports in ISO 834 fire.

Figure 7.4.5 shows the bending moment diagram for the beam with *fixed – fixed* supports in an ISO 834 fire. For the first three time steps the negative bending moment at the ends of the spans increases decreasing the mid span positive moment. Once the end of the span bottom flange stresses reach the EC3 Yield Limit the end of span negative bending moments decrease causing the mid span negative moment to increase. The mid span moment then goes into positive moment and is followed by the end of span moment. This trend occurs throughout the rest of the time steps. The curvature in the bending moment diagram increases during the fire because of P-δ effects, initially from axial load and then displacement after yielding.

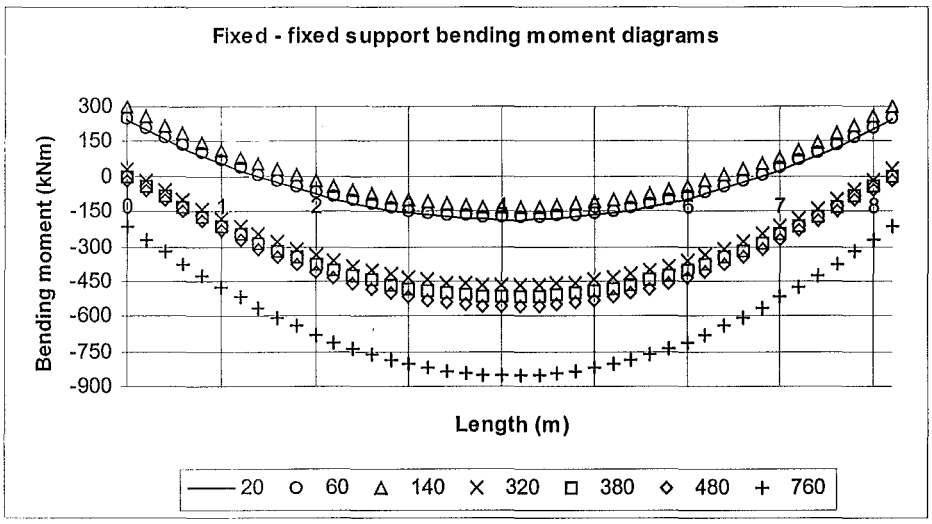

Figure 7.4.5 Fixed - Fixed supports bending moment diagrams in ISO 834 fire.

Summary

The results show that the failure mechanism for the *fixed – fixed* support case is three plastic hinges. The first two forming at the ends of the span while the third one forms in at the centre of the span.

The high compression forces due to thermal axial loading and negative bending cause sufficient stress in the end of span bottom flanges to yield prior to there being any loss due to temperature in the steel properties. The concrete at the ends of the span fails in tension almost immediately. The top flanges in the ends of the span reach the thermally reduced proportional limit

compression stress next. The steel properties in the top flange have not significantly reduced by this stage.

The loss in the end of span capacity leads to mid span displacement causing the top flange to reach the thermally reduced proportional limit compression stress. The top flange reaches the proportional limit first due to the compression forces cancelling out the tension forces induced in the bottom flange by bending. Once all the other components of the steel have reached the proportional limit the tips of the flanges in the bottom flange approach the proportional limit. This causes a decrease in axial force but increased displacements. The rate of change in displacement is greater than the rate of change in axial force and so the bending moment increases. At the early stages the bending moment is governed by axial force. At the formation of the third plastic hinge the bending moment is governed by the displacement due to yielding.

Once the mid span web reaches the thermally reduced yield limit the third plastic hinge has been formed and the failure is rapid, within twenty seconds. The steel section losses capacity at mid span as it is unable to redistribute load elsewhere. The concrete slab is unable to take the load in flexure.

7.5 Fixed – Slide supports (ISO 834 fire).

Introduction

For this simulation the composite section is tested in an ISO 834 fire *with fixed – slide* end restraints. The standard three sided thermal boundary has been used in this simulation. See Figure 5.5.1 for support schematic.

Results

The results of the structural analysis are shown in Figure 7.5.2, Figure 7.5.3, Figure 7.5.4 and Figure 7.5.5. The fire resistance of the one bay section in a standard fire two-dimensional simulation is 1180 seconds with a mid span displacement of 98mm. The failure mechanism is three plastic hinges, two forming at the ends of the span and one forming at the centre of the span of the beam.

Table 7.5.1 relates to Figure 7.5.2, Figure 7.5.3, Figure 7.5.4 and Figure 7.5.5 and shows a time line for the observed behaviour and plastic hinge formation.

Table 7.5.1 Behaviour time line for Fixed - Slide supports in ISO 834 fire.

	Behaviour	**Time**
(a)	Mid span top flange and bottom flange in tension.	100 secs
(b)	End of span top flange stress reaches the EC3 Yield Limit.	260 secs
(c)	End of span bottom flange stress reaches the EC3 Proportional Limit.	360 secs
(d)	Maximum end of span and mid span bending moment achieved.	460 secs
(e)	Mid span bottom flange goes into tension. Mid span concrete goes into compression.	720 secs
(f)	End of span bottom flange reaches the EC3 Yield Limit.	820
(g)	Mid span bottom flange stress reaches the EC3 Proportional Limit.	980
(h)	Failure mechanism achieved.	1180 secs

Figure 7.5.2 (b) and Figure 7.5.4 (a) show that during the initial stages of the fire the end of span negative moment increases and the mid span positive moment decreases due to hogging induced from thermal bowing. Figure 7.5.2 (e) shows that at point (a) the concrete slab cracks due to tensile stress. The bottom of the concrete slab goes into tension as well but does not reach the maximum 0.5 MPa tensile strength. Figure 7.5.4 (d) shows that the concrete at the ends of the span cracks due to tension almost immediately due to the large hogging moments induced from the thermal bowing.

Up to point (a) in Figure 7.5.2 (c) and (d) the top and bottom flange stresses are constant. At point (a) the mid span bottom flange tension stress decreases and the top flange compression stress decreases until shortly after it goes into tension. This is also due to thermal bowing. As the section heats up it is able to freely expand due to the roller. Figure 7.5.2 (a) and (b) show that there is no mid span displacement and the negative moment increases due to thermal bowing until the steel looses sufficient stiffness at point (d).

At the ends of the span up to point (b) in Figure 7.5.4 (b) and (c) and Figure 7.5.5 (a) the steel section displays elastic behaviour with compression in the bottom flange and tension in the top flange. Figure 7.5.4 (b) and Figure 7.5.5 (b) show that at point (c) the end of span top flange stress reaches the EC3 Proportional Limit in tension prior to the steel strength properties being thermally reduced. Figure 7.5.4 (a) shows that between points (b) and (c) the negative bending moment increases even though the top flange stress decreases due to yielding. Figure 7.5.4 (c) and Figure **7.5.5** (c) show that the bottom flange stress increases in compression until it reaches the thermally reduced EC3 Proportional Limit. At this point most of the web is still in the elastic range. For obvious reasons the end of span displacements have not been plotted and the axial force is zero due to the roller.

At the mid span between points (a) and (d) in Figure 7.5.2 (b) and (d) show that the negative bending moment increases while the bottom flange stays in tension but approaches compression. The top flange tension stress increases until point (d) in Figure 7.5.2 (c) Figure 7.5.3 (d) when parts of the web reach the thermally reduced EC3 Proportional Limit. The stress in the top flange is constant at this point. Figure 7.5.2 (e) shows that the concrete is not taking any load but the bottom layer of the slab has not cracked under the tensile stress. At point (b) in Figure 7.5.2 (a) and Figure **7.5.4** (b) the displacements begin to increase due to yielding in the top flange at the end of the span.

At point (d) in Figure 7.5.2 (b) and Figure 7.5.4 (a) the maximum negative bending moment is obtained at both the ends of the span and mid span locations. It is intuitive that these bending moments peak at the same time, as there are no axial forces to cause P-δ effects and variations in moment ratio.

Between points (c) and (f) in Figure 7.5.4 (c) the end of span bottom flange stress increases slightly in tension and then begins to decrease with yielding. Figure 7.5.4 (b) shows that the top flange stress continues to decrease. At point (f) in Figure 7.5.4 (c) Figure 7.5.5 (e) the bottom flange stress reaches the thermally reduced EC3 Yield Limit stress and follows the yield envelope until failure. This is the formation of the first two plastic hinges. Figure 7.5.5 (c), (d) and (e) show that the top and bottom flange stress stays relatively constant while more of the web moves into compression and reaches the EC3 Proportional Limit.

Figure 7.5.2 (c) and (d) shows that at the mid span between points (d) and (e), the bottom flange stress goes into compression while the tension stress in the top flange decreases. Figure 7.5.2 (a) and (b) show that the displacements increase and the bending moment decreases due to a loss in section capacity from yielding at the ends of the span. Figure 7.5.2 (d) and (e) shows that at point (e) the bottom flange goes back into tension and the bottom of the slab displays compression. At this point the effect of the gravity loading is greater than the effect of thermal bowing. This is due to a loss of stiffness in the steel. This is emphasised by the increase in the rate of displacement shown in Figure 7.5.2 (a). Figure 7.5.4 (d) shows that most of the web is in compression while the flanges are in tension. Figure 7.5.1 shows this unusual stress distribution is due to bending stresses putting the bottom flange into tension while thermal bowing dominates the web and top flange behaviour. The web is in compression due to the addition of these stresses. Note that the stresses in Figure 7.5.1 are diagrammatic rather than actual calculated stresses due to the difficulties in calculating the plastic stresses experienced by the web.

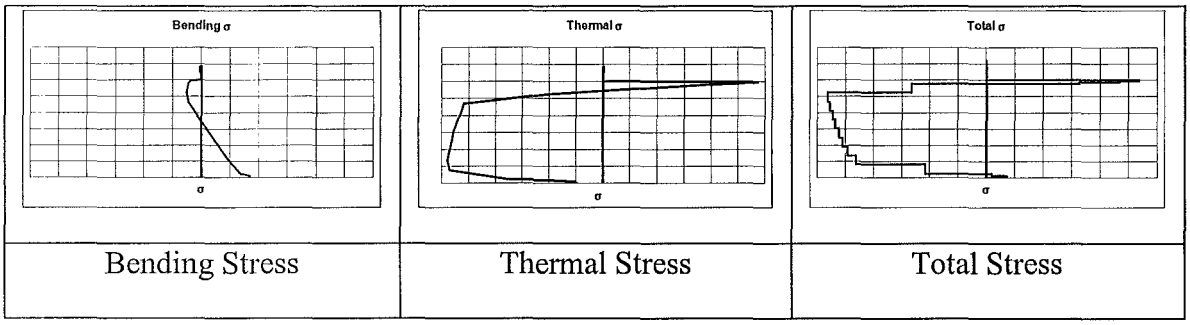

Figure 7.5.1 Stress distribution at the end of the span at 460 seconds, point (d).

At point (g) in Figure 7.5.2 (d) the mid span average bottom flange stress reaches the thermally reduced EC3 Proportional Limit stress in tension. This is the formation of the third plastic hinge. Figure 7.5.2 (b) and (c) shows that the bending moment returns to being positive and the top flange stress goes back into compression. Figure 7.5.2 (e) shows that the compression stress increases in the bottom layer (Layer 11) of the slab as the top layer (Layer 1) has cracked from the earlier tensile stress. Figure 7.5.3 (e) shows that most of the web and bottom flange has reached the thermally reduced Proportional Limit and that part of the web has reached the Yield Limit. After 980 seconds the displacements increase quickly due to the loss in stiffness from the thermally reduced elastic modulus.

Figure 7.5.5 (f) shows that, at approaching failure between 1180 and 1200 seconds the entire end of span steel section has fully yielded. Figure 7.5.2 (b) and Figure 7.5.4 (a) show that the bending moment at the end of the span as well as the mid span approaches the ambient gravity load bending moment. Figure 7.5.3 (f) shows that at the mid span the average bottom flange stress approaches the yield limit. Once this point is reached all thermal effects are finished and the gravity load forces a runaway failure. The roller is unable to retain the tension force caused by the displacements at mid span.

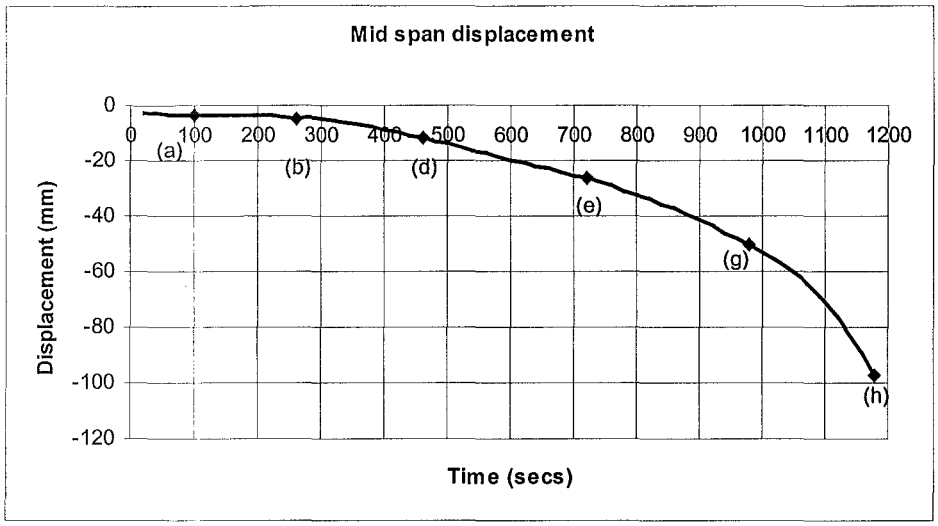

(a) Displacements.

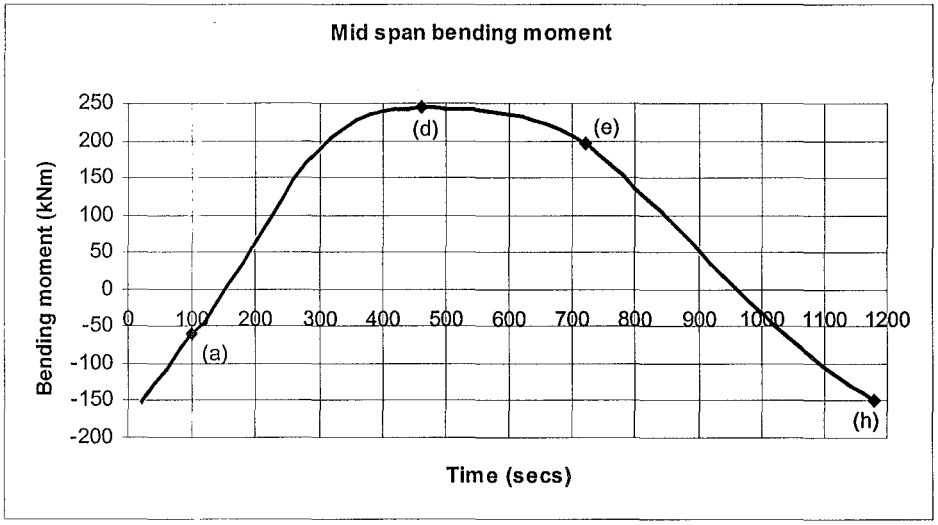

(b) Bending moment.

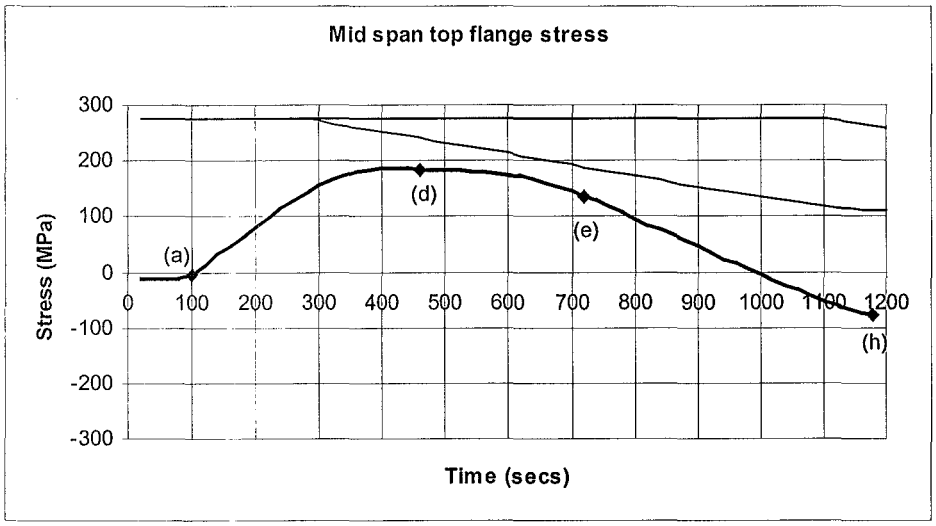

(c) Top flange stress.

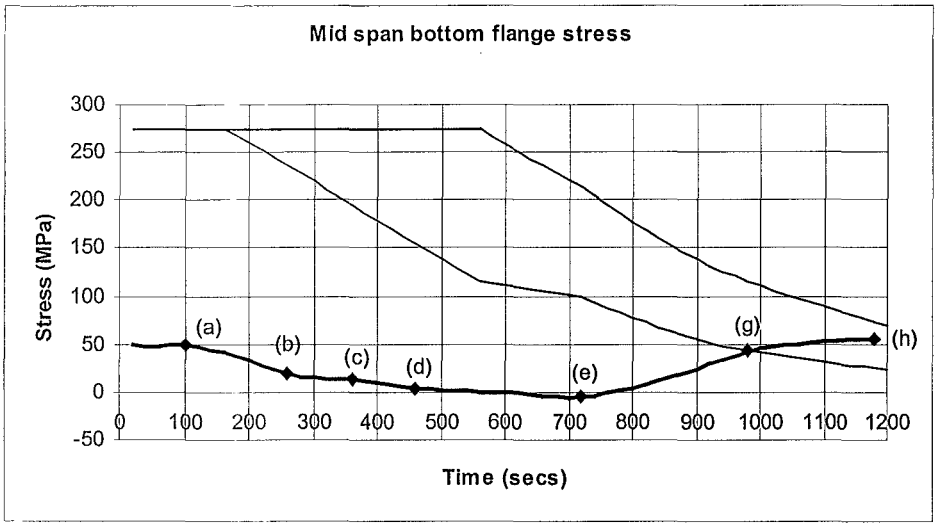

(d) Bottom flange stress.

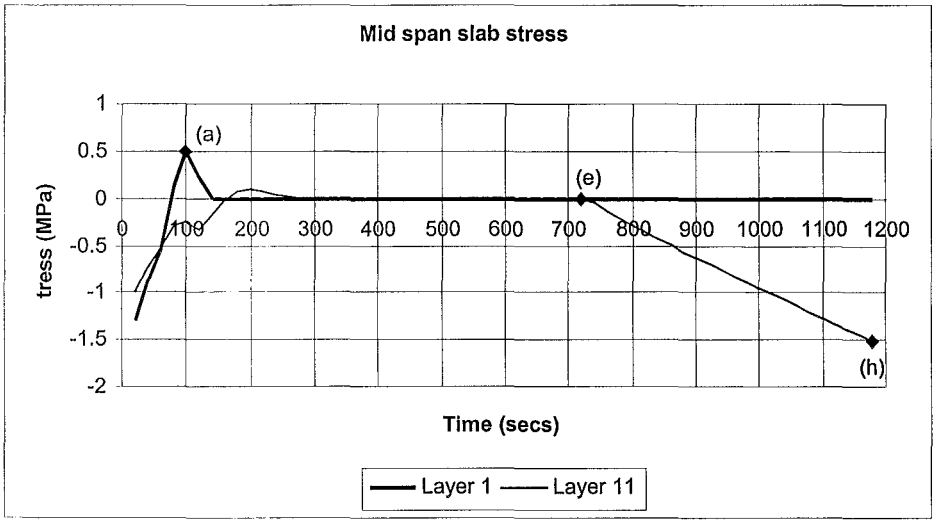

(e)Concrete slab stress.

Figure 7.5.2 Mid span results for Fixed - Slide supports in ISO 834 fire.

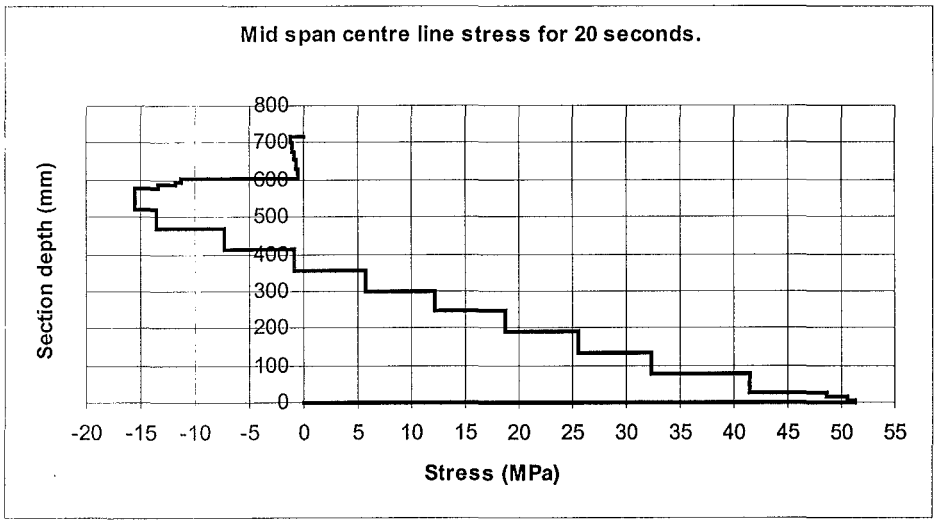

(a) Mid span centre line stress at 20 seconds.

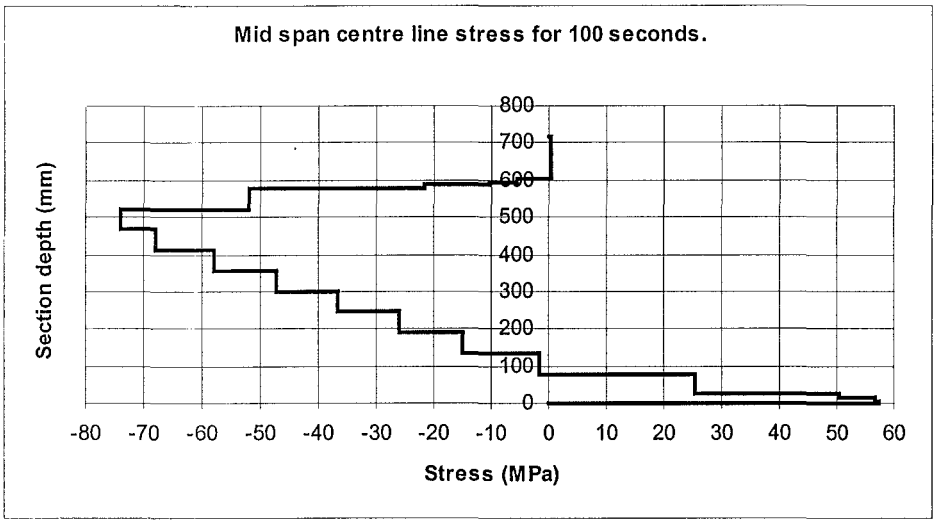

(b) Mid span centre line stress at 100 seconds, point (a).

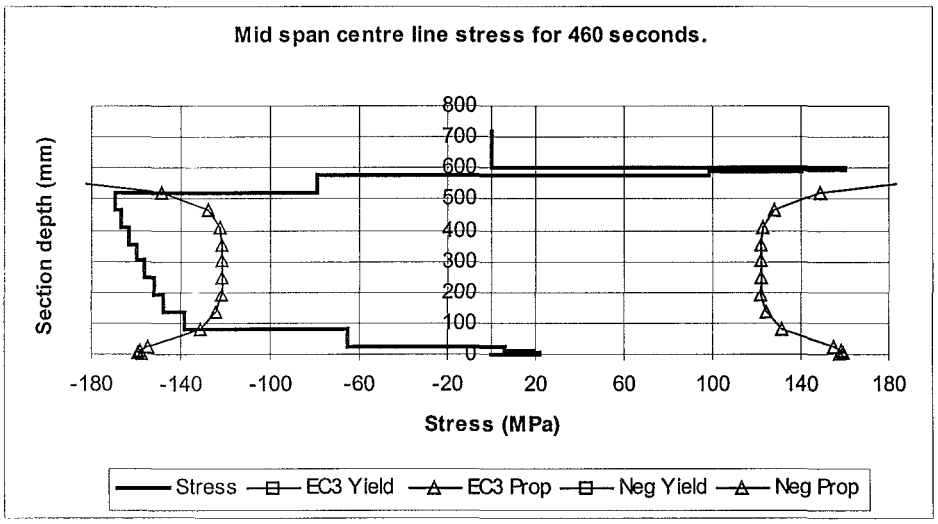

(c) Mid span centre line stress at 460 seconds, point (d).

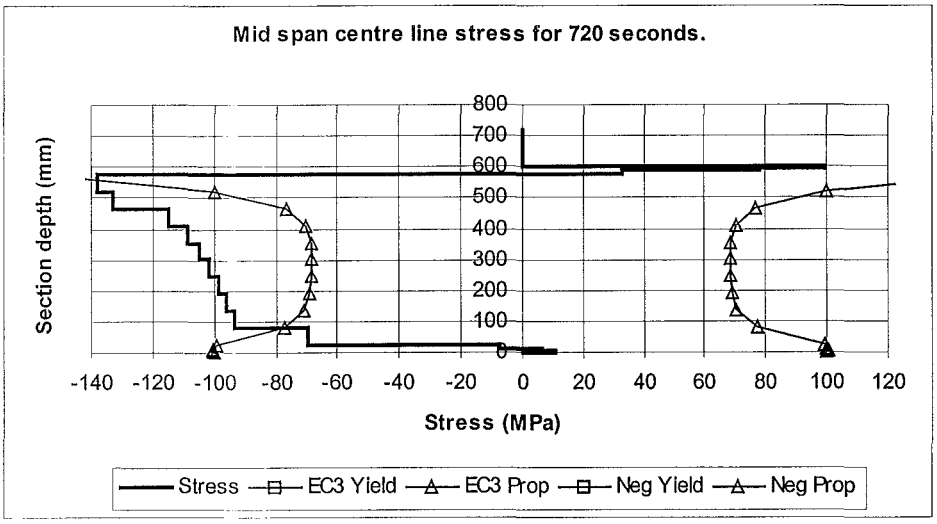

(d) Mid span centre line stress at 720 seconds, point (e).

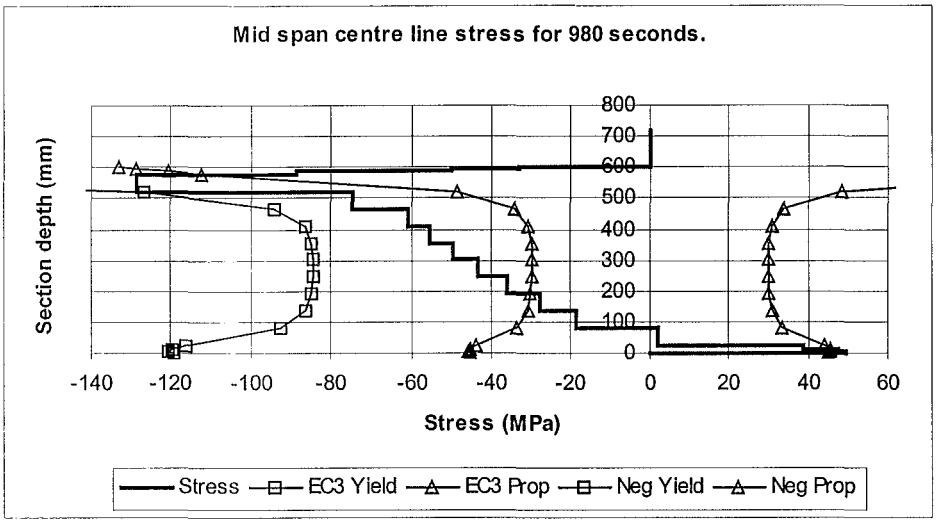

(e) Mid span centre line stress at 980 seconds, point (g).

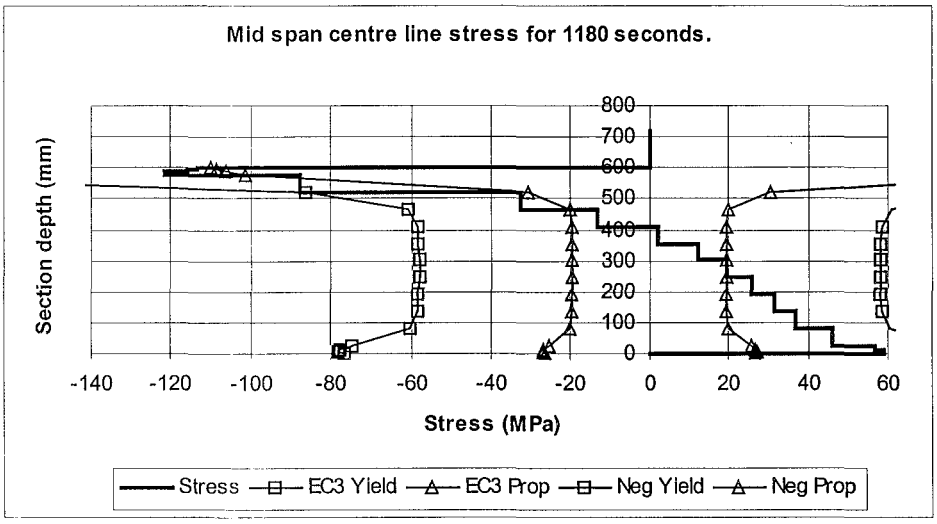

(f) Mid span centre line stress at 1180 seconds, point (h).

Figure 7.5.3 Mid span centre line stress for Fixed - Slide supports in ISO 834 fire.

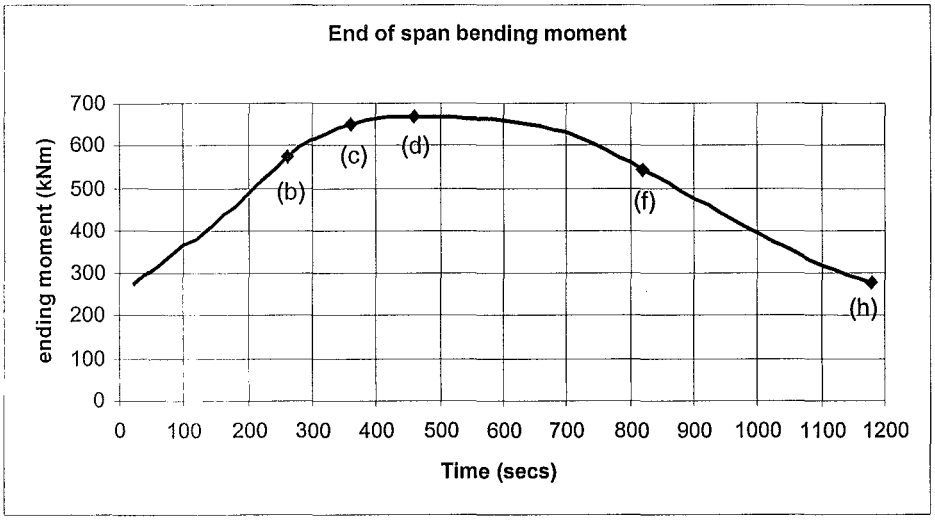

(a) Bending moment.

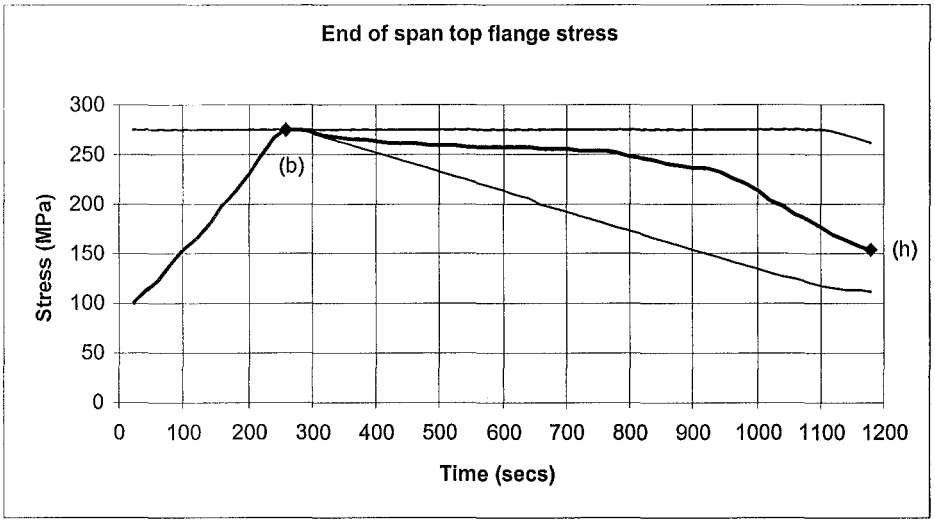

(b) Top flange stress.

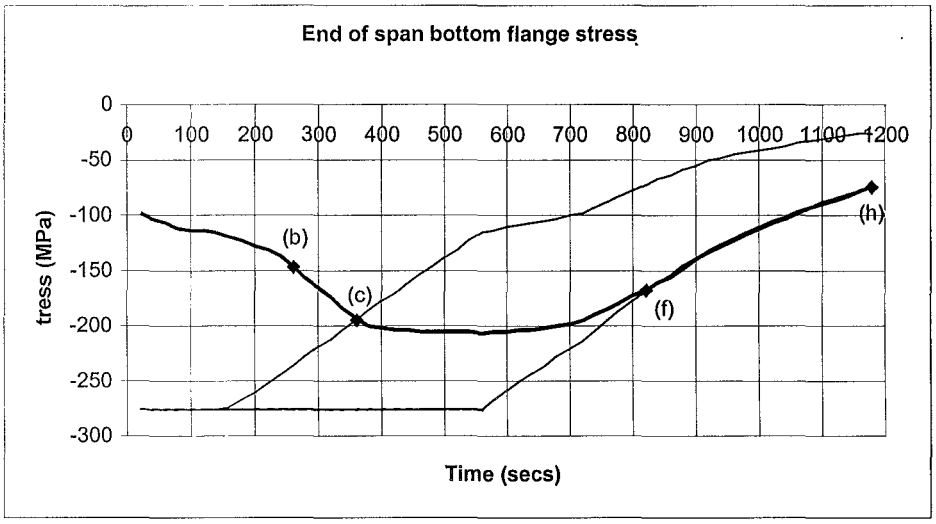

(c) Bottom flange stress.

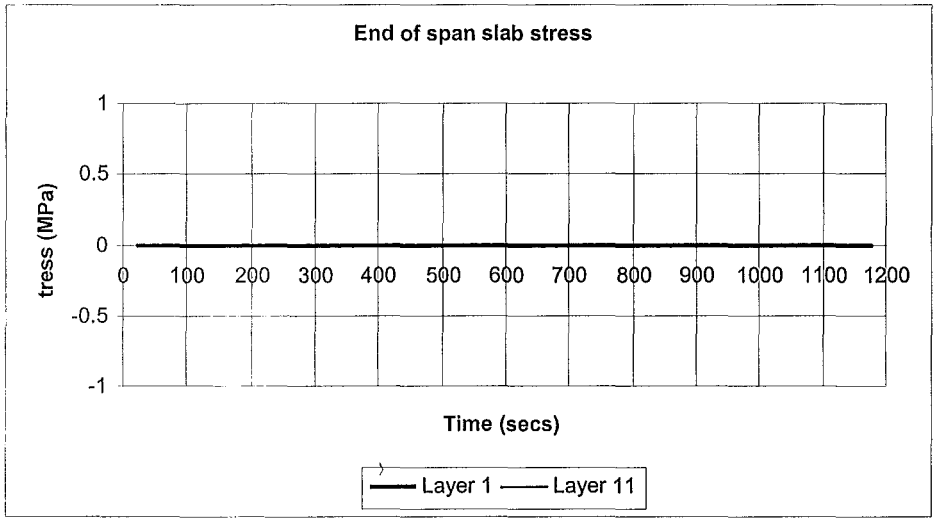

(d) Concrete slab stress.

Figure 7.5.4 End of span results for Fixed - Slide supports in ISO 834 fire.

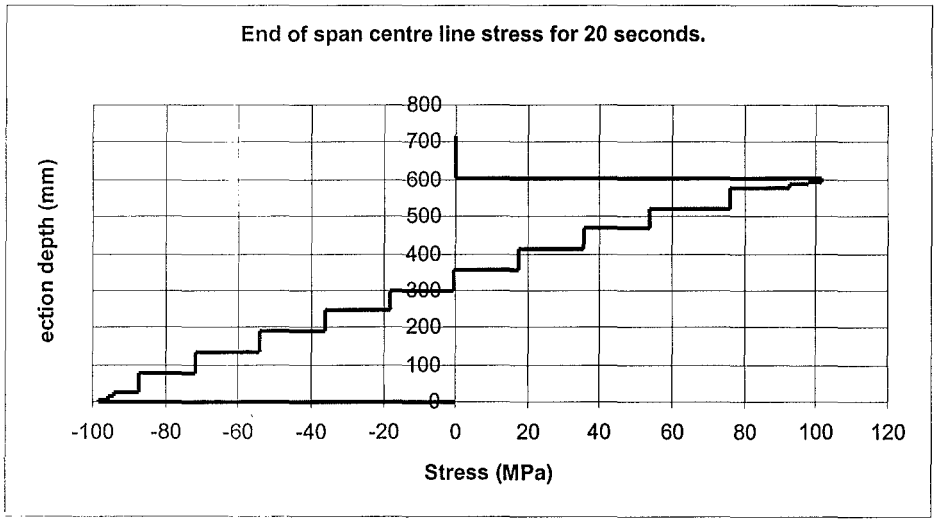

(a) End of span centre line stress at 20 seconds.

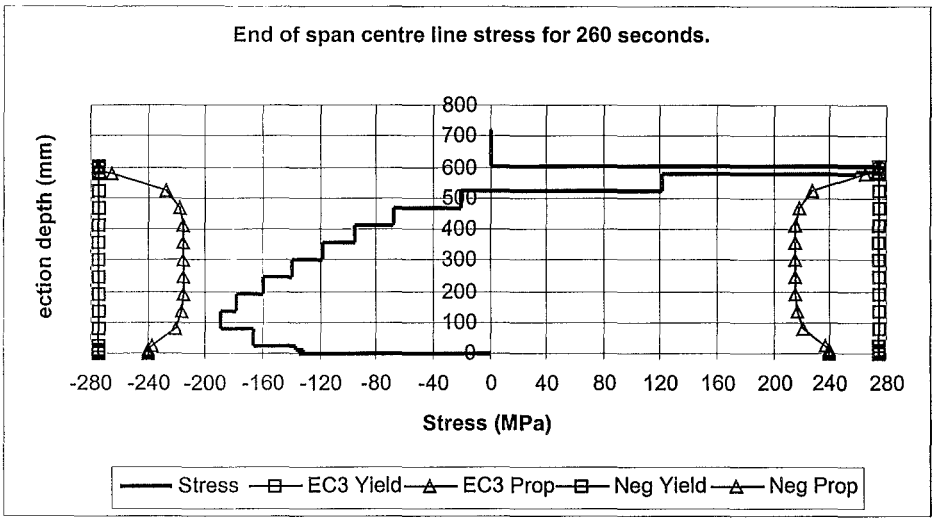

(b) End of span centre line stress at 260 seconds, point (b).

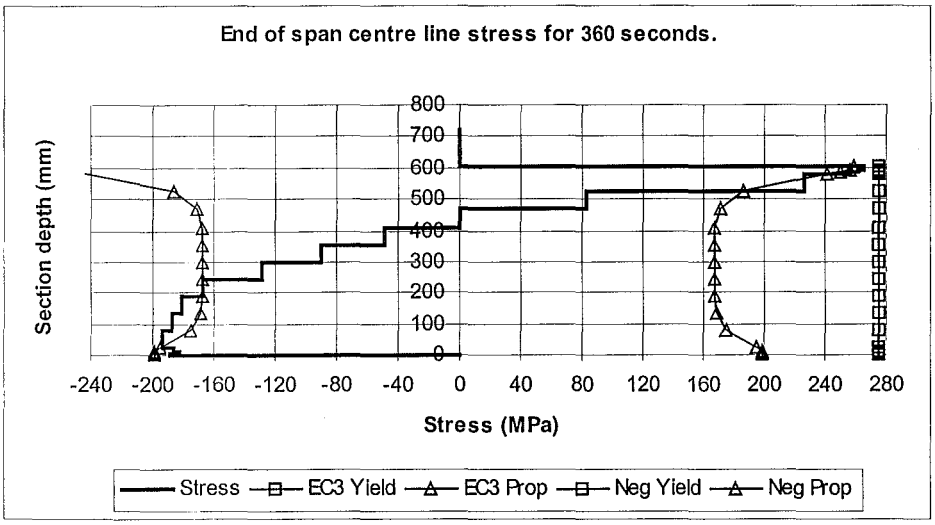

(c) End of span centre line stress at 360 seconds, point (c).

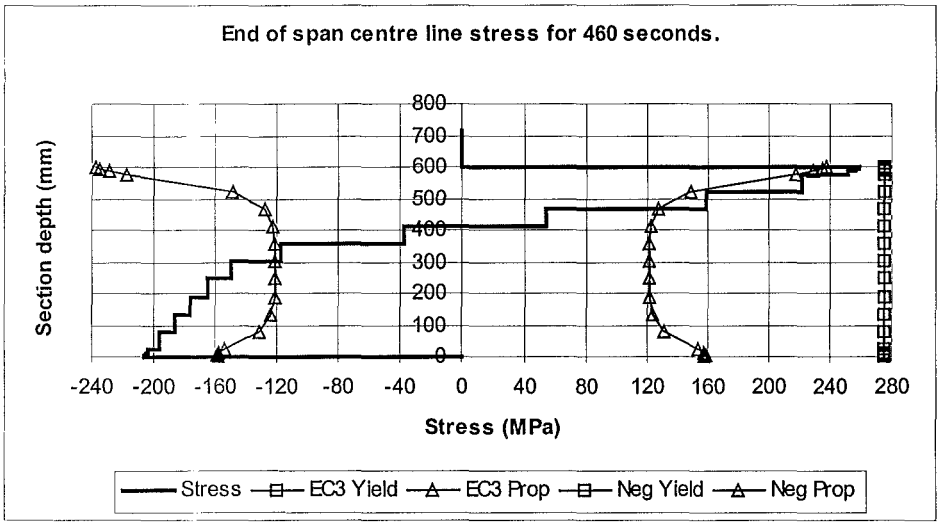

(d) End of span centre line stress at 460 seconds, point (d).

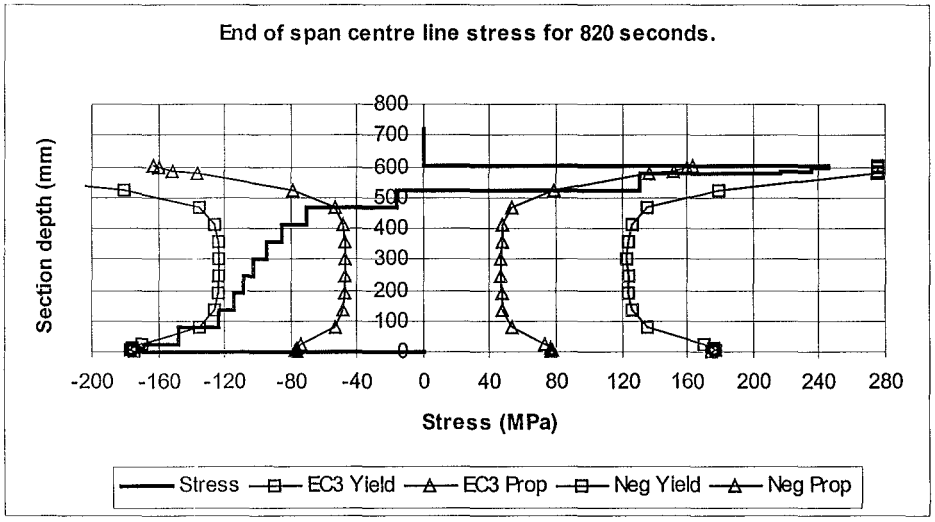

(e) End of span centre line stress at 820 seconds, point (f).

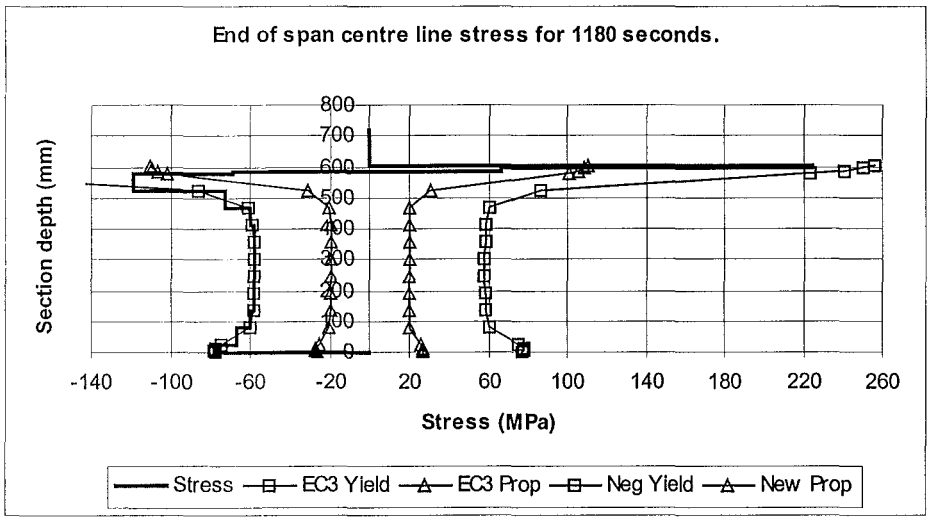

(f) End of span centre line stress at 1180 seconds, point (h).

Figure 7.5.5 End of span centre line stress for Fixed - Slide supports in ISO 834 fire.

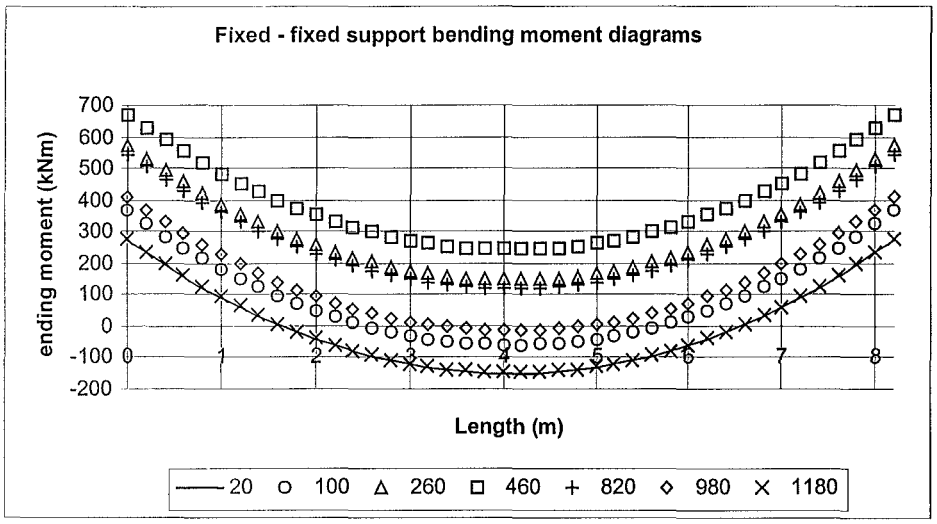

Figure 7.5.6 Fixed - Slide supports bending moment along the beam length vs. time.

Figure 7.5.6 shows that the profile of the bending moment doesn't change through the duration of the fire, as there is no axial force to induce P-δ effects as was found in the linear heating rate cases. The beam initially displays negative moments at the ends of the span and positive moment the mid span. As the beam is heated the negative moments at the ends of the span increase and the mid span moments turn negative due to hogging caused by thermal bowing at time steps 3 and 4. Once the beam starts to yield and the plastic hinges form at the ends of the span the moment

decreases. The mid span negative moment decreases and the then goes back into positive moment at time step 6. The beam finally fails at approximately the same initial cold temperature moments.

Summary.

As previously stated the failure mechanism for the *fixed – slide* two dimensional analysis is three plastic hinges. The first two plastic hinges form at the ends due to thermally enhanced tension stresses in the top flange. The bottom flange then reaches the EC3 Proportional Limit in compression. As was found for the linear heating rate case, as the section heats up it is allowed to displace horizontally. Due to thermal effects a hogging moment forms over the length of the beam. The initial mid span displacements is very small until yielding occurs at the ends of the span. The hogging moment can not be sustained and the mid span displacements increase. The mid span then transfers back into positive moment. The bottom flange reaches the thermally reduced EC3 Proportional Limit in tension. Due to the mid span displacement, the mid span moment decreases. The roller support is unable to restrain the tensile forces caused by the displacements and therefore the length of the beam, l, reduces. The bending moment therefore reduces as $M = wl^2/16$ where the three plastic hinge moments are equal. The increase in displacement causes a runaway failure.

7.6 Displacement comparison.

Figure 7.6.1 shows the comparison in displacement for the four support conditions in an ISO 834 fire scenario. As was found in the linear heating rate case, lack of axial restraint is good for the fire resistance of the beam. The axially restrained cases (*pin – pin* and *fixed – fixed* supports) have the least mid span displacement and resistance to fire due to the effects of the rapid thermal exposure. The rapid thermal exposure causes very high axial loads due to the axial restraint on the beam. The beam fails under these two support conditions before displacements are able to develop.

For the non-axially restrained cases the *fixed - slide* case has the best resistance to the ISO 834 and the second highest displacement at the point of failure due to the three plastic hinges needing to be formed. The *pin – roller* has the next best resistance to the ISO 834 fire and the highest displacement at failure because the beam carries the gravity load in plane bending without axial forces and the concrete is able to act compositely with the steel to provide full flexural

capacity. In the moment resisting cases the concrete can not withstand the tensile forces caused by thermal bowing inducing hogging over the beam and fails due to cracking.

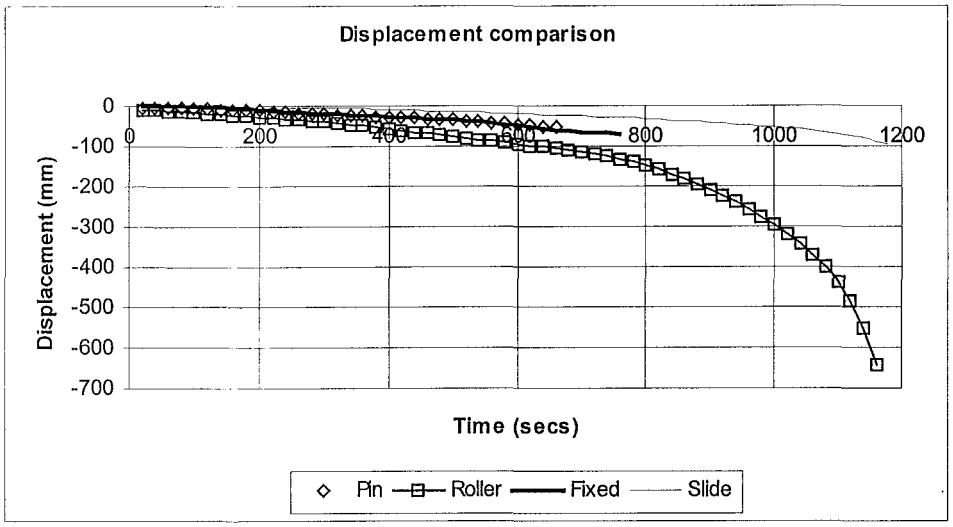

Figure 7.6.1 Displacement comparison for the four support conditions in an ISO 834 fire.

7.7 Fire temperature versus displacement comparisons.

The ISO 834 displacement results obtained for the four support conditions have been compared with those obtained for the linear heating rate cases. Figure 7.7.1 shows that in all four support cases the same behaviour is obtained albeit at a higher fire temperatures. This is due to a lag in the heating rate of the materials. For low heating rates the average temperatures in the materials will be far more uniform with the fire temperature. In more severe thermal exposure, due to the conductivity properties of the materials, the exposed faces will heat up far more quickly but it will take longer for the average section temperature to increase to the fire temperature. The ISO 834 fire temperature increases rapidly early on but as it progresses, its rate of temperature rise decreases. As the rate of temperature rise decreases the average steel temperature approaches the fire temperature as shown in Figure 7.7.2.

In the *pin – pin* support case the ISO 834 fire results show that the mechanism is not able to achieve the same displacements as for the linear heating rate cases. This is due to the high axial forces induced from the rapid temperature increase and the associated web failure. In the linear heating rate results for the *pin-pin* supports, flange yielding governed and led to a slow mid span

plastic hinge failure. While not fully understood, it is believed that in the ISO 834 fire the web yields leading to rapid plastic hinge formation at the centre of the beam.

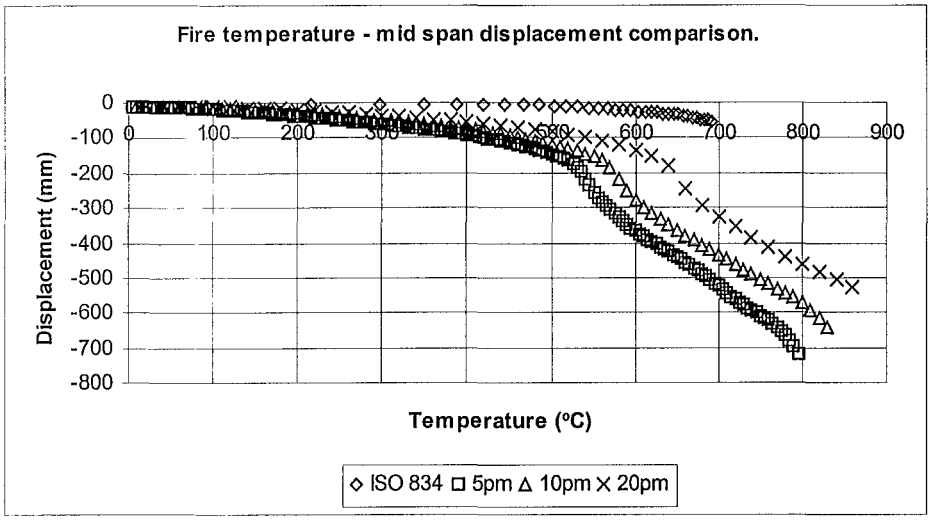

(a) Pin – pin supports.

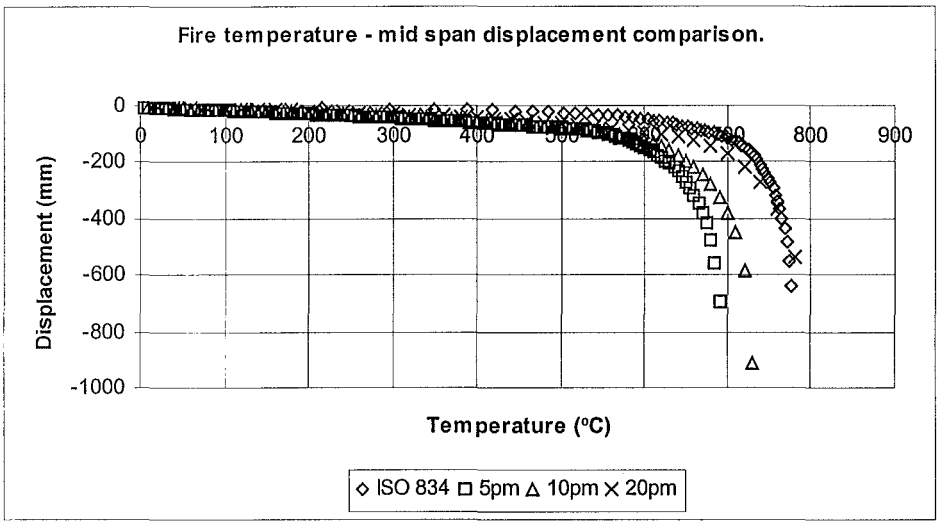

(b) Pin – roller supports.

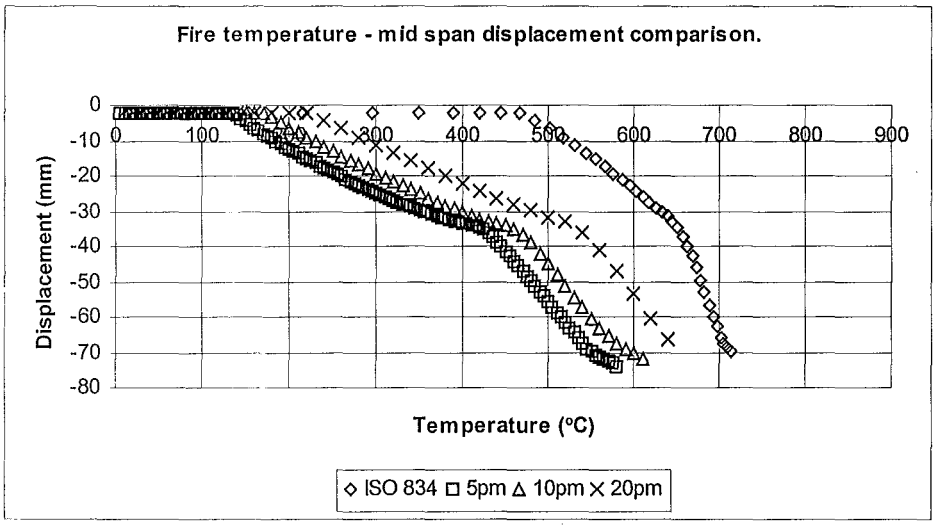

(c) Fixed – fixed supports.

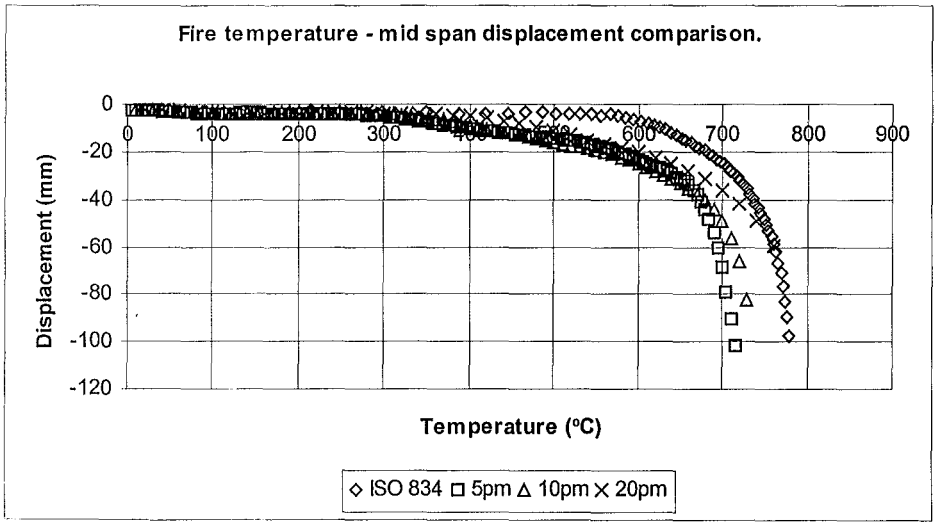

(d) Fixed – slide supports.

Figure 7.7.1 Fire temperature vs displacement comparison for ISO 834 & linear heating rates.

Figure 7.7.2 shows the results of the spreadsheet method for calculating the average steel temperature as shown in Buchanan 2001 (from Milke and Hill, 1996, based on Gamble, 1989). The results show that as the rate of fire growth increases there is a greater lag in the steel temperature. This is due to the thermal properties of the material. Although not as slow as concrete there is some thermal lag attributed to the conductivity of the steel. See Appendix B for formulae and calculations.

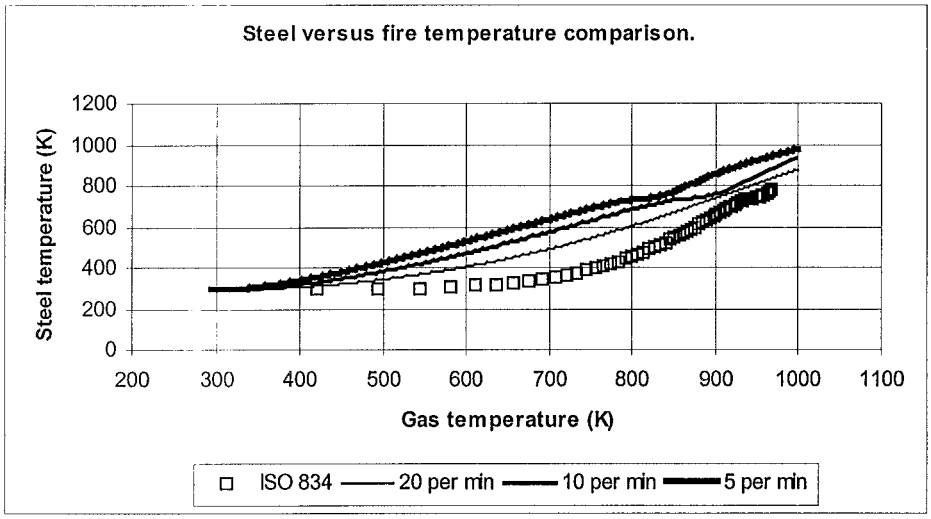

Figure 7.7.2 Steel temperature versus fire temperature (Spreadsheet method).

7.8 Conclusions.

As with the linear heating rate cases the failure mechanisms for the four support cases were as expected. The moment resisting support cases failed with three plastic hinges while the simply supported cases failed with one plastic hinge at mid span.

The composite section behaved very poorly in the more severe standard fire only surviving a maximum of 1180seconds, (20 minutes) for the *fixed – slide* case. The behaviour in the standard fire tests were very similar to those in the linear heating rate cases except that the fire temperature at which the behaviour occurred was a lot higher for the standard fire. This is due to a thermal lag in the average temperature of the section due to the conductivity of the material. The exposed faces of the steel and concrete sections approach the fire temperatures but the average steel temperature would initially be a lot lower. As the fire duration proceeds the rate of change in fire temperature decreases and the steel and gas temperatures become much more uniform. The composite sections' resistance to the standard fire is very short. There is a substantial difference in observed behaviour for the standard fire case compared to the more uniform linear heating rate fires with respect to fire temperature versus beam behaviour.

The fire resistance of the four support cases can be put into two groups, the first '*with axial restraint*', and the second '*without axial restraint*'. The *pin – pin* and *fixed – fixed* cases, (those with

axial restraint) had the least resistance to the standard fire, that being 660 seconds and 760 seconds respectively. This is due to the high axial loads developed because of the severity of the temperature increase in conjunction with web yielding at the support height for the *pin – pin* case. The *pin – roller* and *fixed – slide* cases had better resistance to the standard fire, that being 1160 and 1180 seconds respectively. The failure mechanisms for these systems were the same as for those found for the linear heating rate cases.

Table 7.8.1 shows the displacements at failure for the four support cases in a standard fire as well as the linear heating rate cases. The *pin - roller*, *fixed - fixed* and *fixed - slide* cases all give displacements in the same order of magnitude which reinforces that beam behaviour is pretty much independent of fire severity. For the *pin – pin* case however the displacements at failure in the standard fire show that failure occurs suddenly due to the high axial forces developed in the steel causing web failure. This leads to a rapid failure with little displacement.

Table 7.8.1 Mid span displacements at failure.

	Pin - Pin	**Pin – Roller**	**Fixed - Fixed**	**Fixed - Slide**
5°C / minute	-718 (mm)	-696 (mm)	-74 (mm)	-101 (mm)
10°C / minute	-644 (mm)	-912 (mm)	-72 (mm)	-82 (mm)
20°C / minute	-528 (mm)	-538 (mm)	-66 (mm)	-60 (mm)
ISO 834 fire	-53 (mm)	-640 (mm)	-70 (mm)	-98 (mm)

In the *pin – pin* case the severity of the fire causes high axial load and degradation of material properties. Parts of the web reach the EC3 proportional limit followed closely by the top flange. The axial force pushes the bottom flange into compression over riding the tension forces due to bending. This gives the bottom flange greater fire resistance. This is counter-intuitive, as it would be expected that the bottom flange would yield more quickly due to its four-sided heating.

In the *pin – roller* case failure is obtained in exactly the same manner as for the linear heating rate case. The bottom flange reaches the proportional limit in tension and the plastic hinge forms as the bottom flange approaches yield. The top flange takes the tensile stress and a runaway failure occurs due to the roller not being able to restrain the tensile forces caused by the mid span displacement.

In the *fixed – fixed* case the failure mechanism was similar to that found for the linear heating rate case. Plastic hinges formed at the ends of the span, initially through the top flange and then through the bottom flange. In the linear heating rate case, the ends of spans top flanges yield triggering yielding in the top flange at mid span. The reason for this is the higher compression stresses in the bottom flange at the end of the span due to axial force. The end of span yielding causes displacements at mid span but due to the axial force the bottom flange stress stays in compression until failure.

In the *fixed - slide* case the formation of three plastic hinges with no axial restraint allows for greater fire resistance. Thermal bowing and elongation cause hogging moments over the whole length of the beam. The concrete cracks at the ends of the span almost immediately and the top flange stress reaches the EC3 Proportional Limit in tension because of the hogging moment. The bottom flange then reaches the proportional limit in compression. This behaviour is identical (but in a different time frame) to that found in the linear heating rate case. The formation of the two plastic hinges at the ends of the span lead to the displacements and yielding at the mid span. Collapse is due to a plastic hinge forming at the mid span causing a runaway failure.

As with the linear heating rate cases, the trigger for the plastic hinges to form in the ISO 834 fire is the steel reaching the EC3 Proportional Limit causing yielding, load redistribution and displacements. Though stress can be maintained in the Proportional Limit state for considerable lengths of fire resistance, inevitably as the steel section heats up and stresses increase due to thermally induced axial loads and thermal and gravity load bending, the steel stresses reach the EC3 Yield Limit. With moment resisting supports the concrete at the ends of the spans has a very short fire resistance because of the enhancement of negative moments from thermal bowing. The mid span concrete may also suffer cracking from thermal bowing leaving the slab virtually useless to carry load, especially in the fixed - slide case.

8 COOLING PHASE BEHAVIOUR

8.1 Introduction.

In this section of the report the behaviour of the composite section in the cooling phase will be investigated. In the cooling phase, or decay phase, of the fire it is expected that the composite section will restore some of the strength lost during the growth phase. The growth model for this fire is the ISO 834 Standard fire up to 600 seconds where the gas temperature is approximately 678°C. The decay rate for the fire is 625°C per hour which leaves a total fire duration of 4393 seconds (73.2 minutes). See Section 3.4.3 *ISO 834 Standard Fire.* for the fire growth model used.

As was found in the previous section of this report, the resistance of the composite section to the standard fire isn't particularly good in comparison to the linear heating rates. It must be remembered that this report only covers single bay two-dimensional analysis and thus doesn't take into consideration the effects of the tension membrane action of the concrete slab or load redistribution to redundant areas of the structure. If the fire growth ends before beam failure then it is expected that the composite section will be able to restore some of its loss of strength and displacement but this is dependent on the temperatures of the composite section. The steel will cool very quickly in comparison to the concrete slab which is expected to keep increasing in temperature well after the growth phase of the fire has finished because of its insulating properties. The increase in temperature of the slab will mean that the top flange of the steel section may experience an increase in temperature through conduction. This will further affect the stiffness and strength characteristics of the steel.

As has been adopted in the previous simulations of this report, four standard support cases have been used for investigating beam behaviour. The displacements, axial force, bending moments and stresses have been reduced from the SAFIR output to determine the significant reasons for the observed behaviour. The reduction and presentation of these beam behaviour characteristics are similar to those presented in the previous sections of this report. For a detailed description of the presentation of these results see Section 6.1 *Introduction.*

Note that for up to 600 seconds the section behaviour will be the same for all four support cases as that discussed in Section 7 *ISO 834 STANDARD FIRE.* The results obtained and discussed

in this section only cover those time steps above 600 seconds. The SAFIR output time print for these results is not as fine in this analysis ie 60 seconds as opposed to 20 seconds. This is due to the demands of data management. Therefore the plots in this section are coarser in comparison to Section 7 *ISO 834 STANDARD FIRE.*

The simulations in this section have only been run for a duration of 7200 seconds. For some of the simulations contained in this section the beams are still showing the effects of heating and haven't returned to ambient temperatures. For a fuller explanation, further simulations would be required but due to time constraints and problems associated with running simulations past 7200 seconds, it has not been possible to include them in this report.

8.2 Temperature Characteristics of the Section.

To fully understand the behaviour of the section in the cooling phase of the fire an investigation into the average section temperatures needed to be conducted as shown in Figure 8.2.1. Table 8.2.1 shows the times that the components of the composite section reach their respective maximum temperatures.

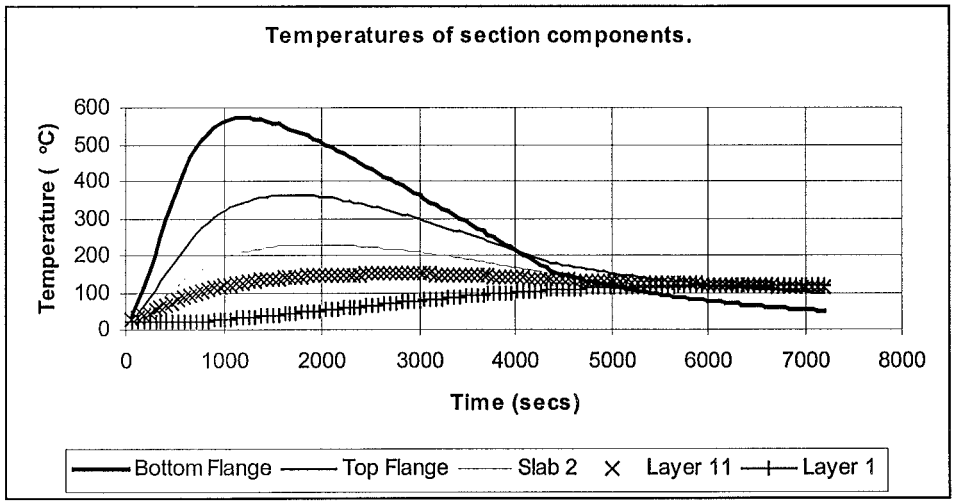

Figure 8.2.1 Average temperatures of section components versus time.

Table 8.2.1 Time to reach the maximum average temperatures for composite section components.

Component	Time
Bottom flange	1200 secs
Top flange	1680 secs
Slab 2	1920 secs
Slab 1 – Layer 11	2760 secs
Slab 1 – Layer 1	6600 secs

All of the components of the section show an increase in their respective average temperatures after the growth phase of the fire has finished. As expected the bottom flange of the steel section shows the highest temperatures in the growth phase of the fire. The top flange of the steel section also displays high temperatures in the growth phase but cools considerably slower than the bottom flange and at approximately 4140 seconds the bottom flange becomes cooler than the top flange.

Slab 2, the discretisation of the deck profile, shows the third highest temperatures due to its thermal boundary to area ratio being larger than that of Slab 1. The bottom layer of the main slab (Layer 11) has 50% of its boundary protected from the fire by Slab 2 and therefore has a lower average temperature than Slab 2. Layer 1 of the main slab shows the slowest temperature increase.

The components with the lowest temperature profile also have the longest time to reach their peak temperature. Layer 1 at the top of the main slab doesn't begin cooling until 6600 seconds (110 minutes). The bottom of the main slab has cooled but not considerably and this is the same for slab 2. This causes the reduction in cooling of the top flange. This means that although the bottom flange properties are more detrimentally affected, the duration of the degradation is not as long as the top flange. The top flange temperature is fairly uniform and similar to that of Slab 1 and Slab 2 at the end of the simulation.

8.3 Pin – Pin Supports (ISO 834 fire with cooling).

Introduction.

For this simulation the composite section has been subjected to a 600 second ISO 834 fire with a cooling phase. The section is supported with *pin – pin* end supports. Refer to Figure 5.2.1 for the *pin-pin* support schematic.

In Section *7.2 Pin – Pin Supports (ISO 834 fire)* it was determined that the failure mechanism for the composite section with *pin – pin* supports was achieved in 660 seconds. Therefore the growth phase of the fire ends 60 seconds prior to the failure mechanism.

Results

The results of the structural analysis are shown in Figure 8.3.1. The fire resistance of the one bay section in a standard fire with a cooling phase is 660 seconds, exactly the same as shown in Section 7.2 *Pin – Pin Supports (ISO 834 fire).*

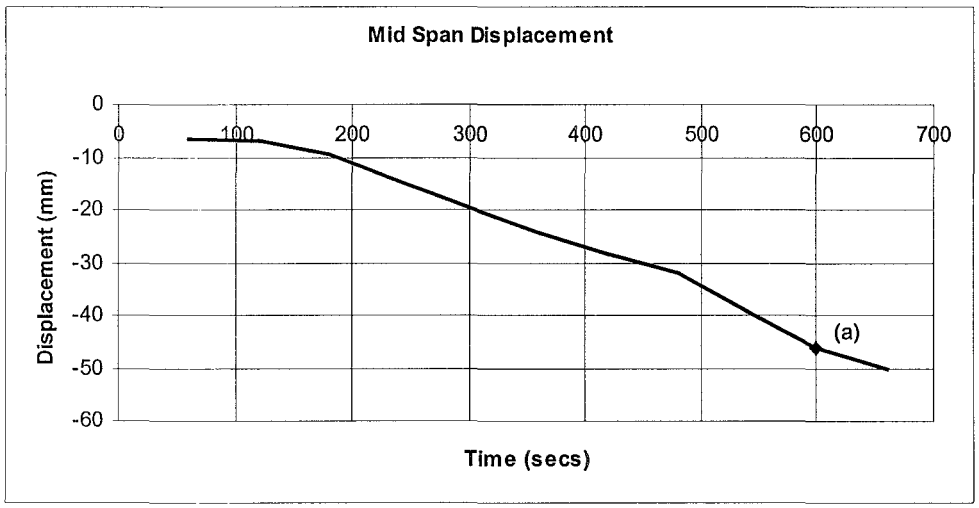

(a) Displacement

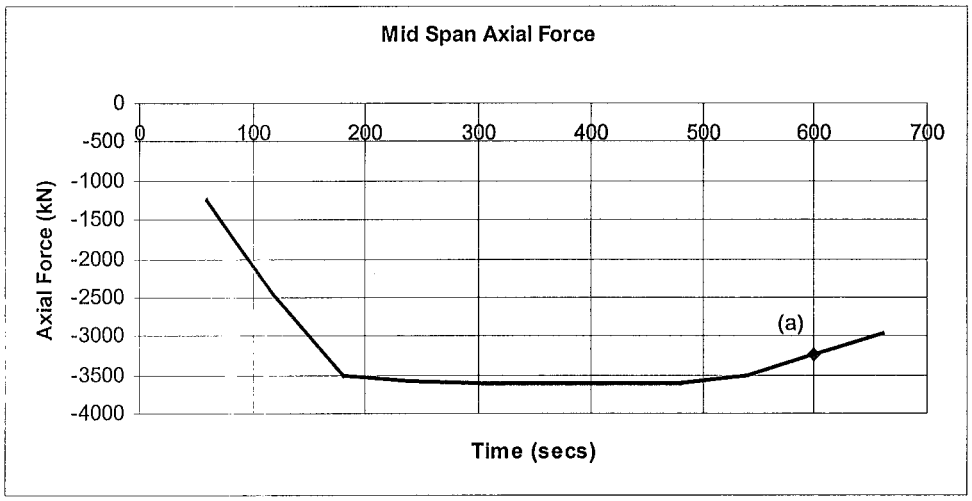

(b) Axial force

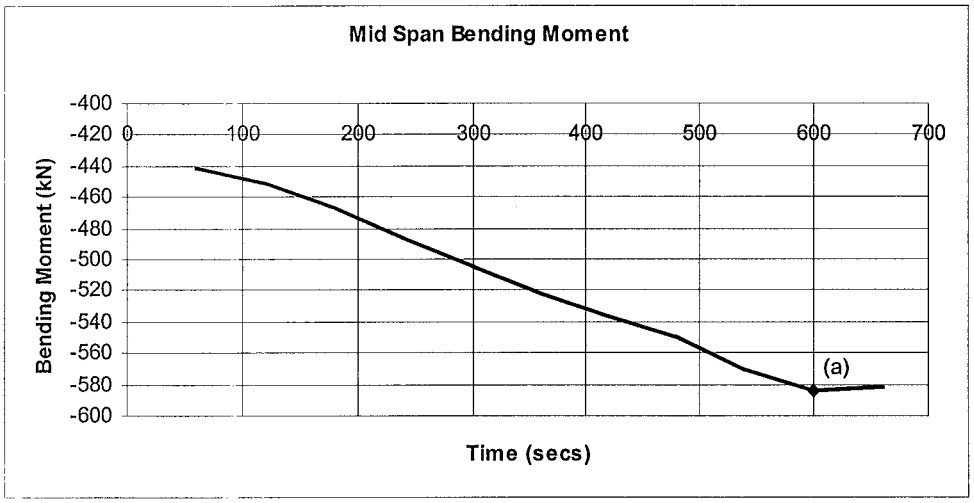

(c) Bending moment.

Figure 8.3.1 Mid span results for Pin - Pin supports in ISO 834 fire with cooling phase.

Note that '*(a)*' in the plots depicts the end of the growth phase at 600 seconds.

Summary.

The effect of ending the growth phase after 600 seconds makes no difference to the time taken to reaching the failure mechanism. The temperatures in all components of the composite section are still increasing and while there will be a slight increase in the time to failure of the section, the failure mechanism has already been achieved. The increasing axial force and bending will cause the bottom flange, and hence the rest of the section, to quickly yield.

8.4 Pin – Roller Supports (ISO 834 fire with cooling).

Introduction.

For this simulation the composite section has been subjected to a 600 second ISO 834 fire with a cooling phase. The section is supported with *pin – roller* end supports. Refer to Figure 5.3.1 for support schematic.

In Section 7.3 *Pin – Roller Supports (ISO 834 fire)* it was determined that the failure mechanism for the composite section with *pin – roller* supports was achieved in 1160 seconds. Therefore the growth phase of the fire ends 560 seconds prior to failure.

For results up to 600 seconds see section 7.3 *Pin – Roller Supports (ISO 834 fire).*

Results.

Figure 8.4.1 shows the results of the structural analysis in which the composite section is able to survive the 600 second growth phase of the ISO 834 fire with a cooling phase. There was a permanent deformation of 62mm at the end of the simulation. The behaviour time line which relates to Figure 8.4.1 for the composite section with *pin – roller* supports is shown in Table 8.4.1.

Table 8.4.1 Behaviour time line of Pin - Roller supports in ISO 834 fire with cooling phase.

	Behaviour	**Time**
(a)	Growth phase of fire ends.	600 secs
(b)	Top flange stress reaches the thermally reduced EC3 Proportional Limit stress.	780 secs
(c)	Maximum mid span displacement.	1140 secs
(d)	Bottom flange stress decreases below the thermally reduced EC3 Proportional Limit stress.	1860 secs
(e)	Top flange stress decreases below the thermally reduced EC3 Proportional Limit stress.	2580 secs
(f)	Top flange goes into tension and there is a change in the rate of displacement.	4380 secs

Up to point (a) in Figure 8.4.1 the composite beam behaviour is exactly as explained in Section 7.3. After point (a) the cooling phase of the fire occurs. As previously explained the average temperatures in the steel and concrete components of the section are still increasing at this stage. Therefore the strength and stiffness properties of the materials continue to decrease.

At point (b) in Figure 8.4.1 (b) the mid span top flange stress reaches the thermally reduced EC3 Proportional Limit stress. At this point the compression stress in the top flange begins to decrease and then remains relatively constant until it reduces below the EC3 Proportional Limit stress at point (e). During the yielding period the reduction in compression stress in the top flange is taken by an increase in stress in the concrete.

Figure 8.4.1 (a) shows that the displacements increase up to point (c), which is when the average bottom flange temperature becomes constant, (Figure 8.2.1). At this stage both the top flange and the bottom flange of the section have reached the proportional limit, but the temperature in the bottom flange and the web are decreasing. Therefore recovery of stiffness in the steel section will begin to occur, causing a recovery of the displacement. The top flange temperature is still increasing but the slab is taking the required compression stresses as shown in Figure 8.4.1 (d).

As the section begins to cool and the displacement decreases with the recovery of stiffness in the steel section, the tension stress in the bottom flange decreases. Figure 8.4.1 (b), (c) and (d), show that the compression stress in the top flange decreases at point (d) at which time the compression stress in the concrete slab increases and the bottom flange stress decreases below the EC3 Proportional Limit stress.

Figure 8.4.1 (b) shows that at point (f) the top flange stress becomes tensile. The bottom flange stress has already become compressive at this stage. The reason for the change in stress sign between the top and bottom flange is due to the rate of cooling. The bottom flange cools faster than the top flange due to the thermal mass of the concrete still heating the top flange. As the bottom flange cools it will reduce in length. At approximately 4140 seconds the top flange temperature is higher than the bottom flange and therefore the top flange will have a higher thermal strain than the bottom flange due to thermal elongation. This change in strain causes bowing in the opposite direction, causing the stress in the flanges to change signs.

The tension in the top flange is attributed to the effects of thermal bowing being greater than the effects of the bending stress. The bending stress of this element will not be significant, due to its close proximity to the neutral axis. The thermal bowing component of stress in the bottom flange is significant as the bottom flange is further from the neutral axis causing tensile bending stress but the bottom flange is in compression. Note that at 7200 seconds the tensile stress in the top flange is approximately double that of the compression stress in the bottom flange. This emphasises the effects of the bending stress on the bottom flange in relation to the thermal effects in the top flange.

Figure 8.4.1 (d) shows that as the top flange is in tension, the concrete slab is in compression. This is attributed to the bending stress in the slab being greater than the tensile stress associated with the thermal bowing strains.

Figure 8.4.1 (a), (b), (c) and (d) show that at point (f) the rate of compression stress increase in the slab decreases along with the rate of displacement recovery. The rate of tension stress increase in the top flange decreases, and the rate of compression stress increase in the bottom flange decreases. This behaviour is associated with a decrease in thermal bowing due to the section cooling. This behaviour continues until the end of the simulation at 7200 seconds (120 minutes).

The simulation ended prior to the temperatures in the composite section returning to ambient. There will be very little change in displacement after 7200 seconds as the material temperatures at this time are not high enough to reduce the EC2 or EC3 Modulus of Elasticity. The bottom flange stress will revert back into tension and the top flange and slab will revert back into compression once the slab has cooled and there is no thermal bowing. There is very little change in bending moment and axial force which is the expected behaviour with *pin – roller* supports.

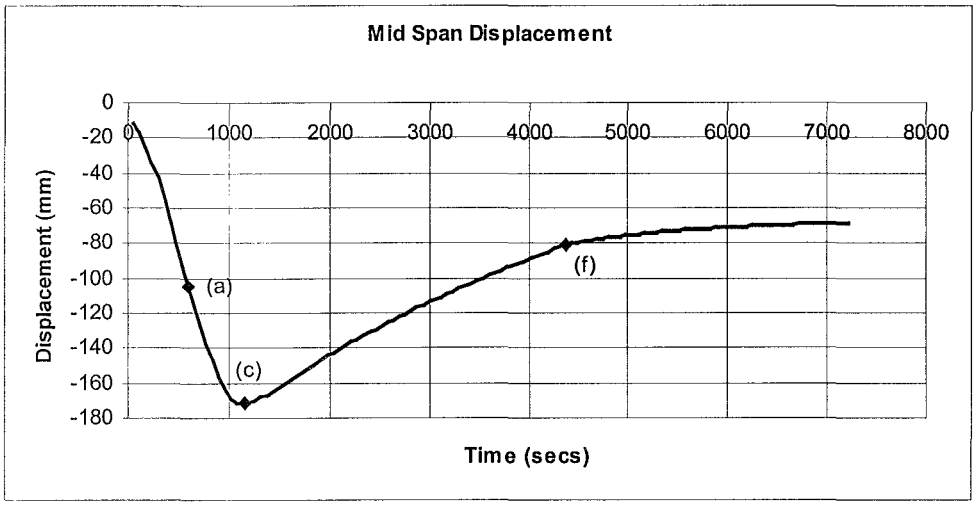

(a) Displacement.

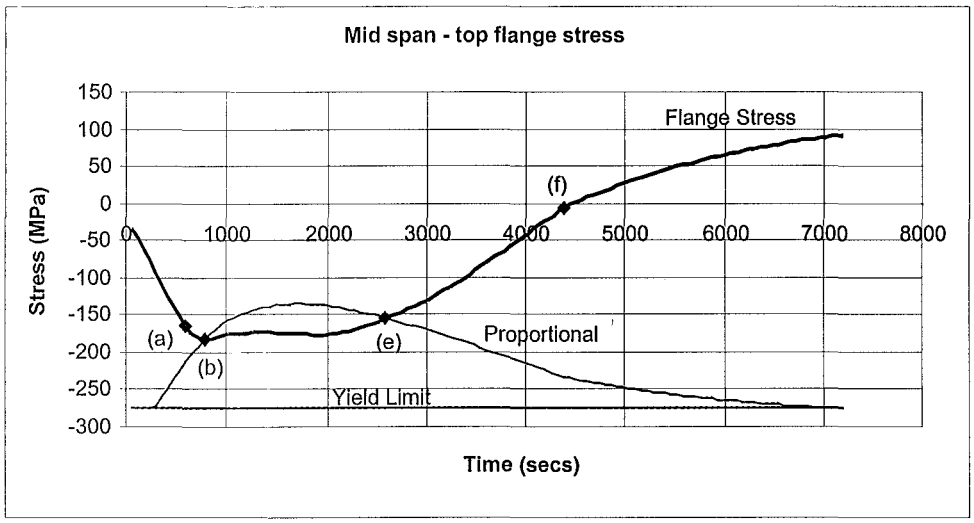

(b) Top flange stress.

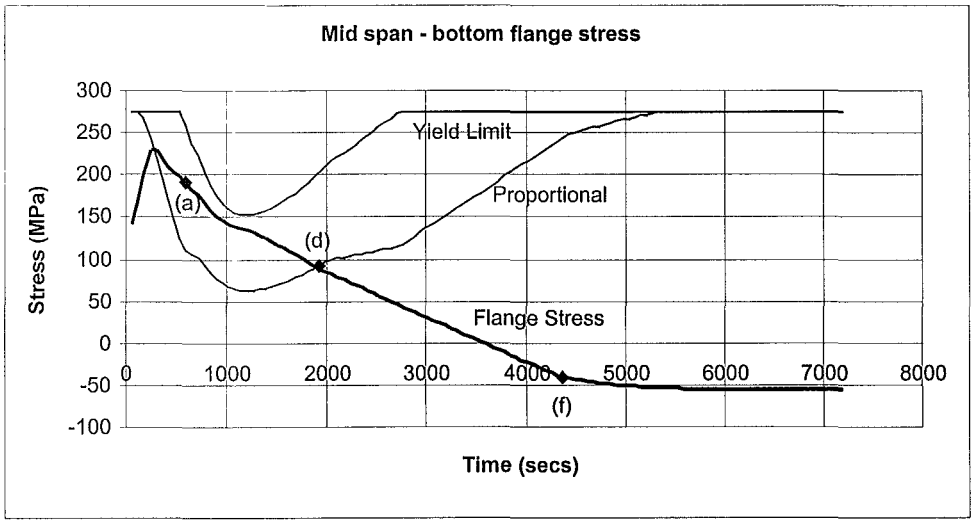

(c) Bottom flange stress.

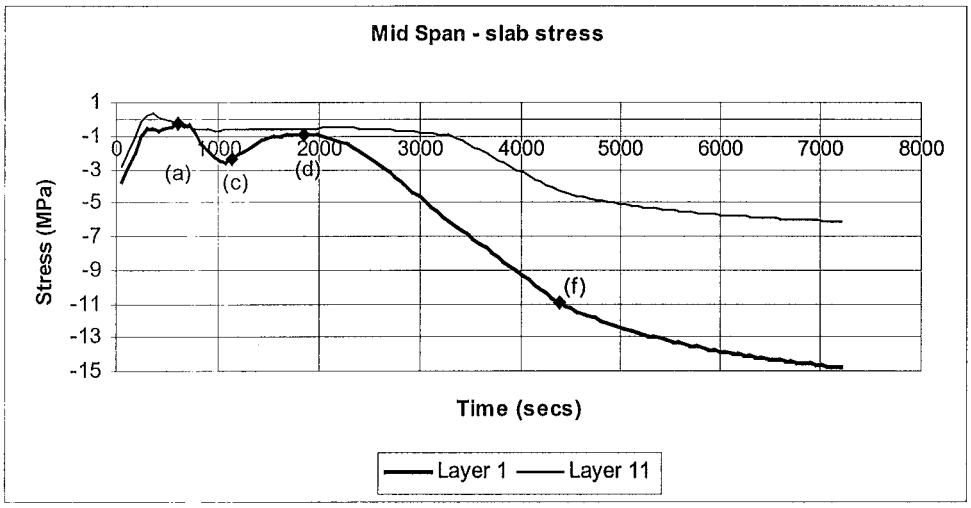

(d) Slab stress.

Figure 8.4.1 Mid span results for Pin - Roller supports in ISO 834 fire with cooling phase.

Summary.

The results show that during the growth phase of the fire the composite section displaces and yields. The compression stress in the top flange increases and the tension stress in the bottom flange increases due to deformation caused by thermal bowing and a loss in stiffness of the steel section. Once these components of the cross section reach the thermally reduced EC3 Proportional Limit stress, their respective stresses decrease due to yielding and then drop below the proportional limit stress during the cooling phase of the fire.

Due to the concrete temperature the top flange cools a lot slower than the bottom flange. This causes thermal bowing in the cooling phase. The direction of the thermal bowing in the cooling phase is opposite to that observed in the growth phase of the fire. This enhances the displacement recovery along with the increase in steel stiffness. As the section cools and the effects of the thermal bowing decrease, the rates at which displacement recovery takes place decreases. This causes a decrease in the rate of stress increase in the top flange, the bottom flange and the concrete slab, up to the end of the simulation. It is believed that after 7200 seconds the bottom flange stress will return back to tension and the top flange stress will become compressive with a decrease in thermal bowing with cooling.

At the end of the simulation there was a permanent deformation of 62 mm.

8.5 Fixed – Fixed Supports (ISO 834 fire with cooling)

Introduction.

For this simulation the composite section has been subjected to a 600 second ISO 834 fire with a cooling phase. The section is supported with moment resisting *fixed – fixed* end supports. See Figure 5.4.1 for support schematic.

In Section 7.4 *Fixed – Fixed Supports (ISO 834 fire).* it was determined that the failure mechanism for the composite section with *fixed – fixed* supports was achieved in 780 seconds. Therefore the growth phase of the fire ends 180 seconds prior to the failure mechanism.

Results.

The results of the structural analysis are shown in Figure 8.5.1 and Figure 8.5.2. The fire resistance of the one bay section in a standard fire with a cooling phase is 780 seconds, as per Section 7.4 *Fixed – Fixed Supports (ISO 834 fire).*

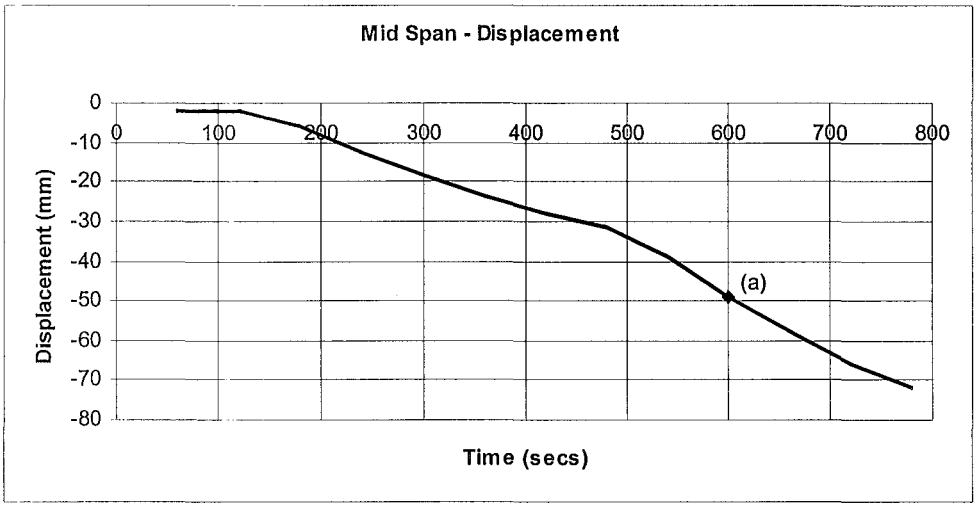

(a) Displacement.

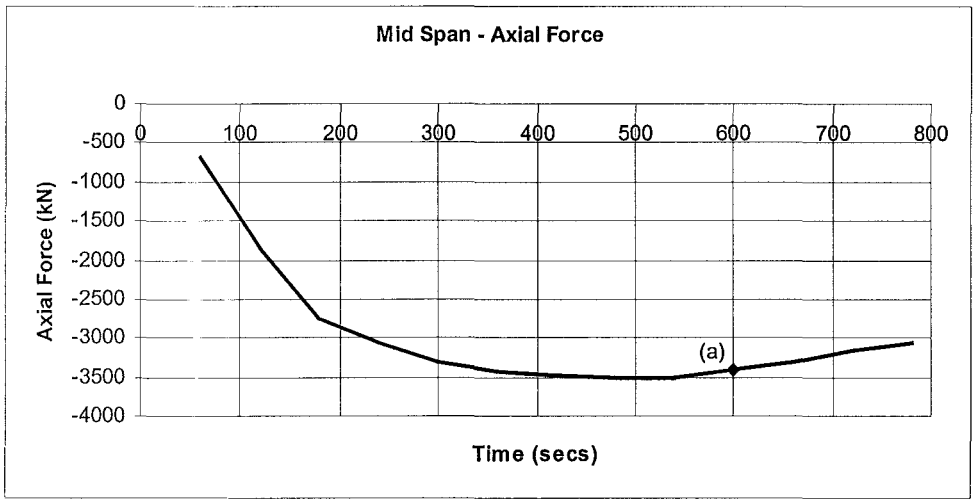

(b) Axial force.

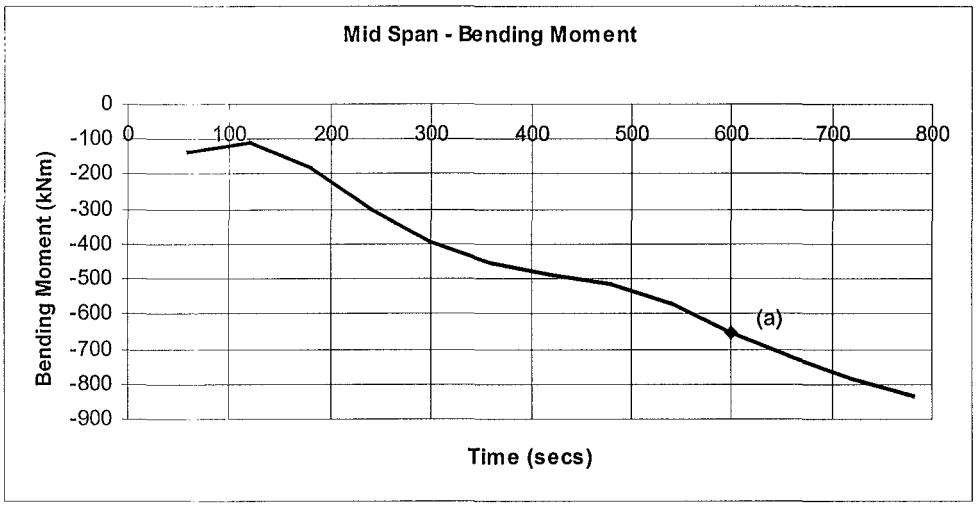

(c) Bending moment.

Figure 8.5.1 Mid span results for Fixed - Fixed supports in ISO 834 fire with cooling phase.

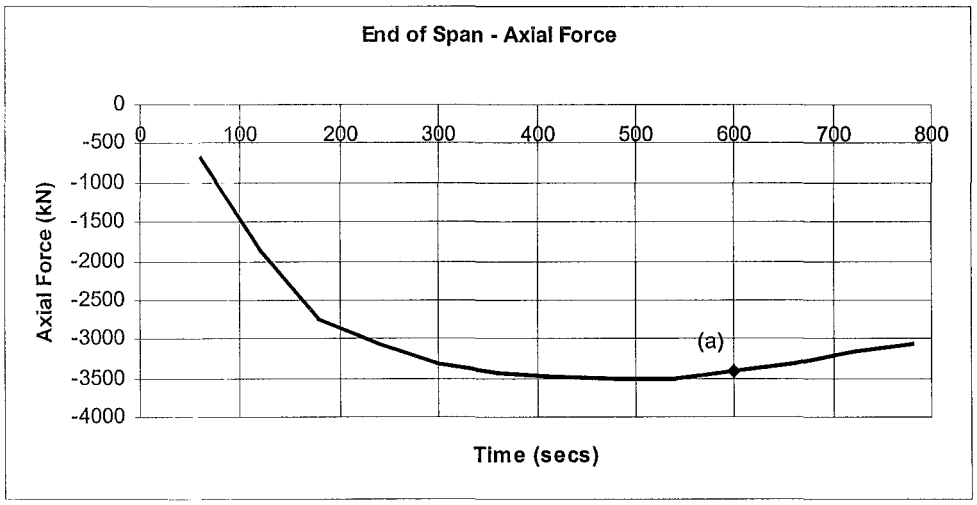

(a) Axial force.

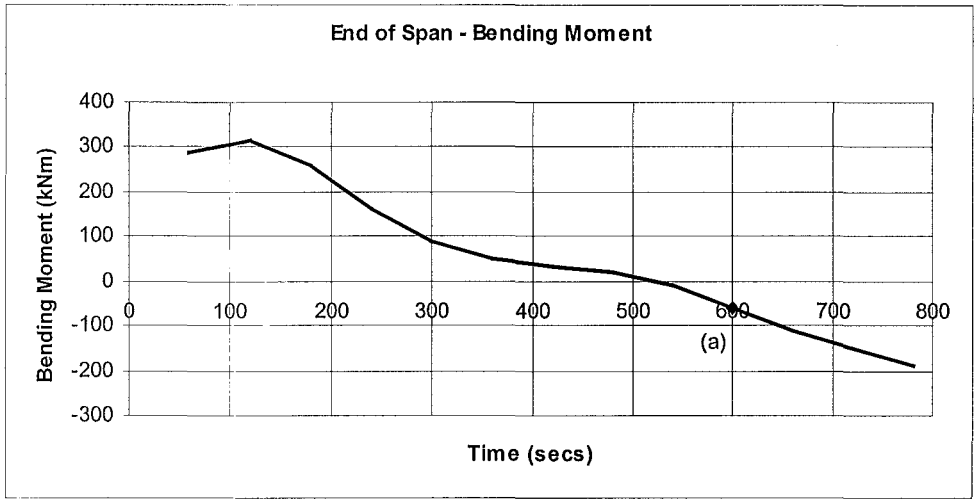

(b) Bending moment.

Figure 8.5.2 End of span results for Fixed - Fixed supports in ISO 834 fire with cooling phase.

Note that *(a)* in the plots depicts the end of the growth phase at 600 seconds.

Summary.

The effect of ending the growth phase after 600 seconds makes no difference to the time taken to reach the failure mechanism for the *fixed – fixed* case. The temperatures in all components of the composite section are still increasing and while there will be a slight increase in the time to failure of the section, the failure mechanism has already been achieved. The increasing axial force and bending will cause the section to fail quickly.

8.6 Fixed – Slide Supports (ISO 834 fire with cooling)

Introduction.

For this simulation the composite section has been subjected to a 600 second ISO 834 fire with a cooling phase. The section is supported with moment resisting *fixed – slide* end supports. See Figure 5.5.1 for support schematic.

In Section 7.5 *Fixed – Slide supports (ISO 834 fire).* it was determined that the failure mechanism for the composite section with *fixed – slide* supports was achieved in 1180 seconds. Therefore the growth phase of the fire ends 580 seconds prior to the failure mechanism. For results up to 600 seconds see Section 7.5 *Fixed – Slide supports* (ISO 834 fire).

Results.

Figure 8.6.1 and Figure 8.6.2 show the mid and end of span results of the structural analysis in which the composite section is able to survive the 600 second growth phase of the ISO 834 fire with a cooling phase. There was a permanent deformation of 15.3 mm at the end of the simulation. The behaviour time line which relates to Figure 8.6.1 and Figure 8.6.2 for the composite section with *fixed - slide* supports is shown in Table 8.6.1.

Table 8.6.1 Behaviour time line of Fixed - Slide supports in ISO 834 fire with cooling phase.

	Behaviour	**Time**
(a)	Growth phase of fire ends.	600 secs
(b)	Maximum mid span displacement.	1200 secs
(c)	End of span top flange stress decreases below the thermally reduced EC3 Proportional Limit stress.	1560 secs
(d)	End of span bottom flange stress decreases below the thermally reduced EC3 Proportional Limit stress.	2100 secs
(e)	Mid span top flange stress reaches the thermally reduced EC3 Proportional Limit stress.	2400 secs
(f)	Top layer of concrete goes into compression.	3120 secs
(g)	Rate of increase in compression stress in the bottom layer of concrete continues. Mid span top flange stress drops below the EC3 Proportional Limit stress.	3780 secs
(h)	End of span top flange stress reaches the EC3 Proportional Limit stress in compression. Mid span displacement recovery decreases.	4440 secs

Figure 8.6.1and Figure 8.6.2 show that up to point (a) the composite beam behaviour is exactly as explained as for the ISO 834 fire behaviour in the previous section of this report. After point (a) the cooling phase of the fire begins. As detailed in Section 8.2 *Temperature Characteristics of the Section.* the average temperatures in the steel and concrete components of the composite section are still increasing at this stage. Therefore the strength and stiffness properties of the materials continue to decrease.

Figure 8.6.1 (a) shows that between points (a) and (b) the mid span displacement continues to increase due to the increasing temperature and loss in stiffness of the section. Figure 8.2.1 shows that at 1200 seconds (which relates to point (b) in Figure 8.6.1) the bottom flange has reached its maximum temperature and is beginning to cool, thus contracting and increasing in stiffness, there is a recovery of the displacement. Figure 8.6.1 (b) shows that the mid span negative bending moment decreases at a constant rate until point (c) where it goes into positive bending. The tangent slope of the rate of decrease in negative bending moment is the same as that for the positive bending. There is no enhancement of the bending moment from P- δ effects due to the roller support.

Figure 8.6.2 (a) shows that the end of span bending moment decreases after point (a) as the plastic hinges form at the ends of the span due to the steel section yielding and the concrete cracking as explained in Section 7.5 *Fixed – Slide supports* (ISO 834 fire). The bending moment decreases in negative bending until approximately point (f) where it goes into positive bending. Once again the slope of negative bending moment decrease is equal to the slope of positive bending moment increase. The mid span bending moments are dominated by the end of span moments. Initially, due to thermal bowing, the end of span negative moments increase making the mid span go into negative bending. Once the plastic hinges form at the ends of the span, there is a reduction in end of span moment capacity. Therefore the end of span moments decreases. The mid span moment decreases in negative bending and then goes into positive bending.

Figure 8.6.3 shows that up to approximately point (b) the roller is being pushed out by thermal elongation. Once the bottom flange and the rest of the steel starts to cool, the roller is then pulled back in even though the concrete section is still increasing in temperature. As the steel contracts the concrete is trying to elongate causing thermal bowing leading to a recovery of the displacements. Therefore due to thermal strains in the concrete the concrete does not develop compression stresses until approximately 3200 seconds even though the top flange is already in compression at this time.

Figure 8.6.2 (b) shows that after the plastic hinges have formed in the end of span top flange, the tension stress decreases below the thermally reduced EC3 Proportional Limit, and then at approximately point (e) goes into compression. Figure 8.6.2 (c) shows that at the same time the end of span bottom flange stress decreases in compression and at point (d) falls below the thermally

reduced EC3 Proportional Limit stress. At point (g) the bottom flange goes into tension. Due to the concrete cracking, the steel section provides the only flexural resistance at the ends of the span.

Yielding at the ends of the span causes a change in the signs of the stresses in the top and bottom flanges at the ends of the span. The stresses now resemble those at the mid span of a simply supported beam where the top flange is in compression and the bottom flange is in tension.

Figure 8.6.1 (c) shows that at point (e) the top flange reaches the EC3 Proportional Limit stress in compression and remains yielding until point (g). Figure 8.6.1 (e) shows that at point (f) the mid span concrete starts to go into compression to compensate for the yielding steel. After point (g) the top flange stress decreases as it returns to the elastic range. Figure 8.6.1 (a) shows that at point (f) the concrete goes into compression due to cooling reducing the thermal bowing. There is a upward shift in the neutral axis and the displacements recover at a much faster rate, as the concrete is able to contribute to taking bending stress making the section much stiffer.

Figure 8.6.1 (c), (d) and (e) show that as more of the bending moment is redistributed to the mid span due to yielding at the ends of the span, the tension stress in the bottom flange increases. The compression stress in the top flange decreases while the compression stress in the concrete increases.

Figure 8.6.2 (b) shows that between points (e) and (f) the compression stress in the top flange increases at a uniform rate with the bending moment. At point (h) the top flange compression stress reaches the EC3 Proportional Limit stress. As the section looses capacity the rate of increase in positive bending moment decreases. Figure 8.6.1 (a), (b), (d) and (e) show that, the end of span yielding affects the mid span bending moment, and with it the increase in displacement recovery, the bottom flange tension stress and the concrete compression stress.

This behaviour occurs up to the end of the simulation at 7200. At this point the mid span and end of span bottom flange stress, as well as the end of span top flange stress, approach the EC3 Yield stress.

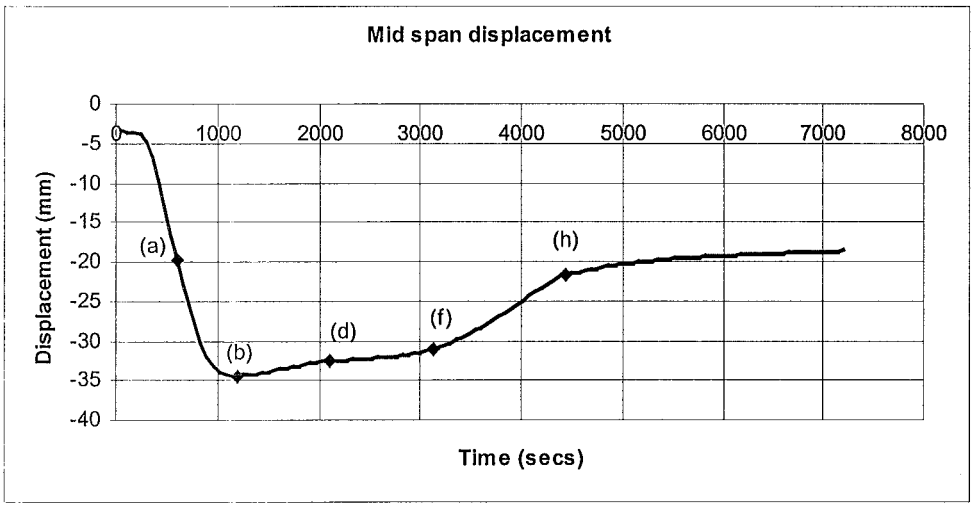

(a) Displacement.

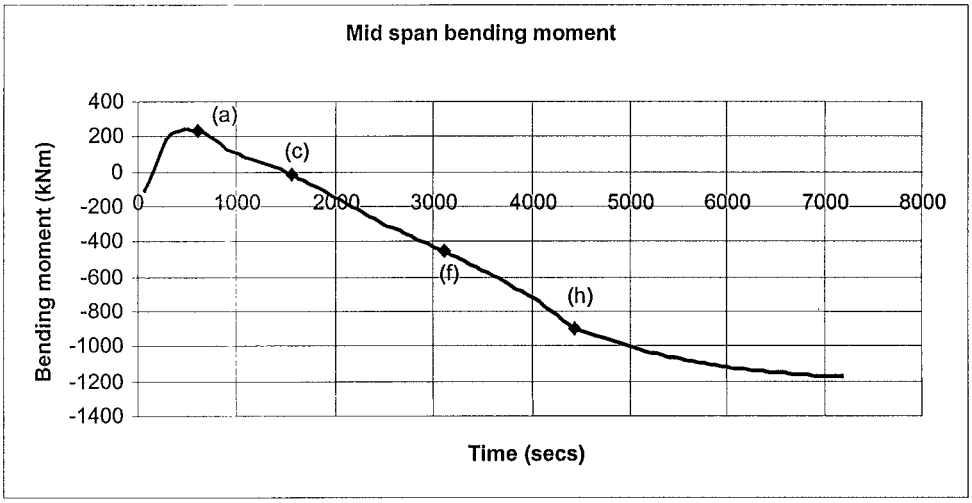

(b) Bending moment.

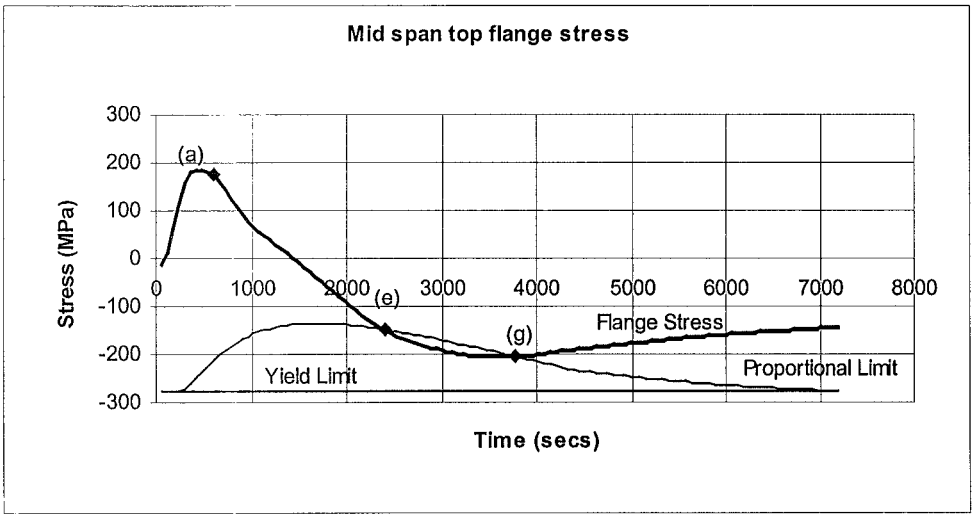

(c) Top flange stress.

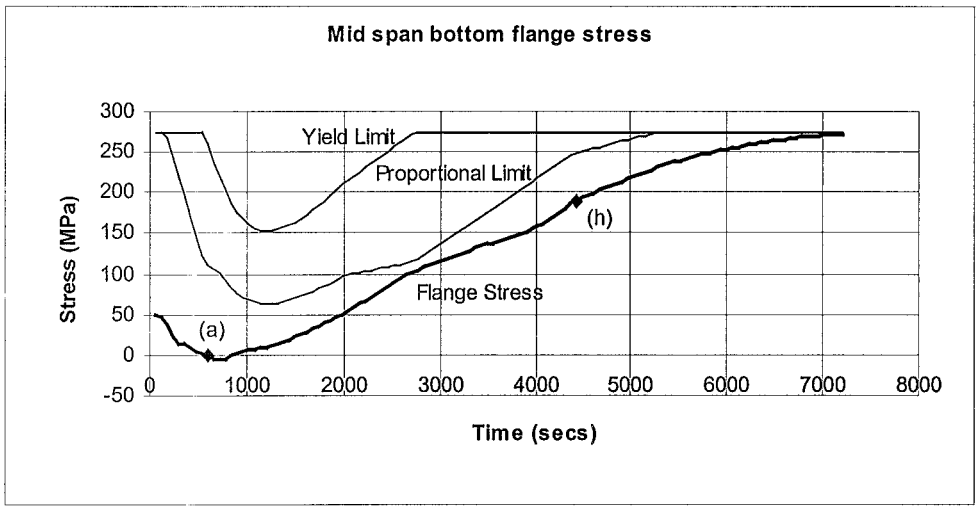

(d) Bottom flange stress.

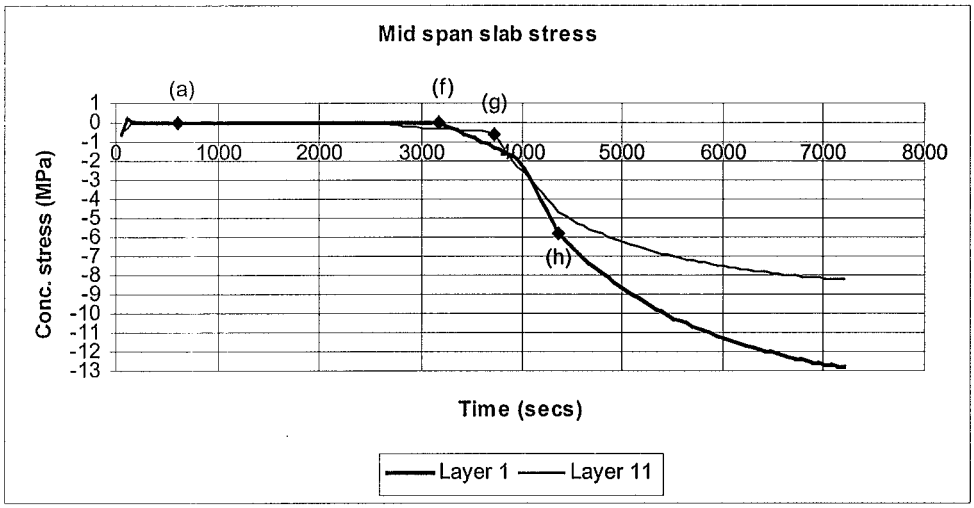

(e) Concrete slab stress.

Figure 8.6.1 Mid span results for Fixed - Slide supports in ISO 834 fire with cooling phase.

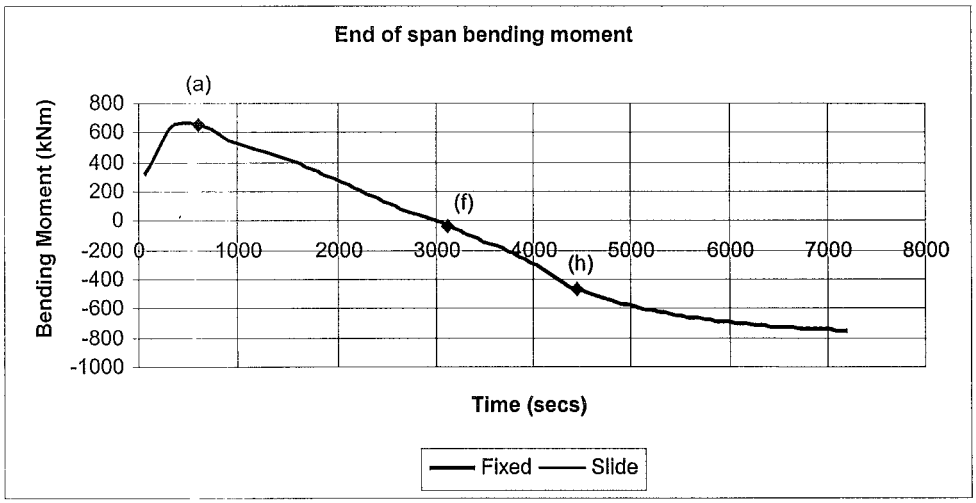

(a) Bending moment.

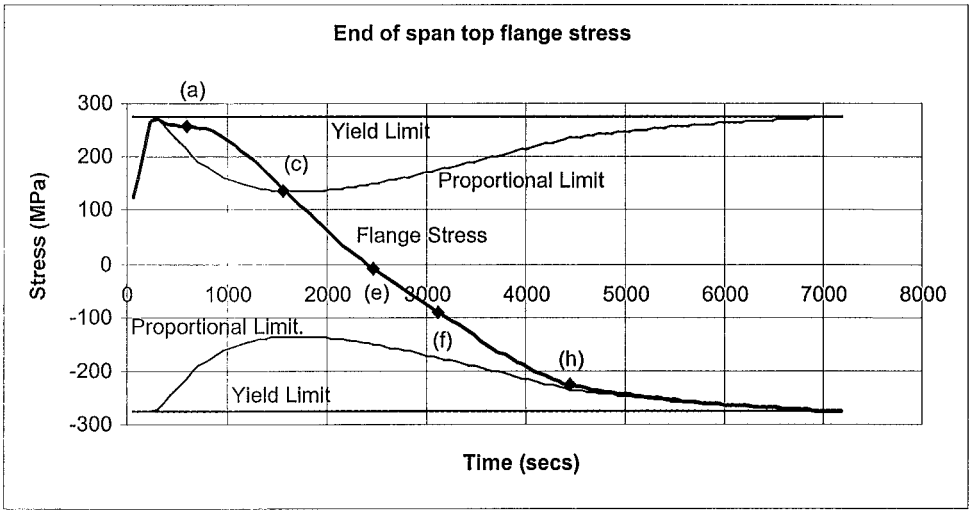

(b) Top flange stress.

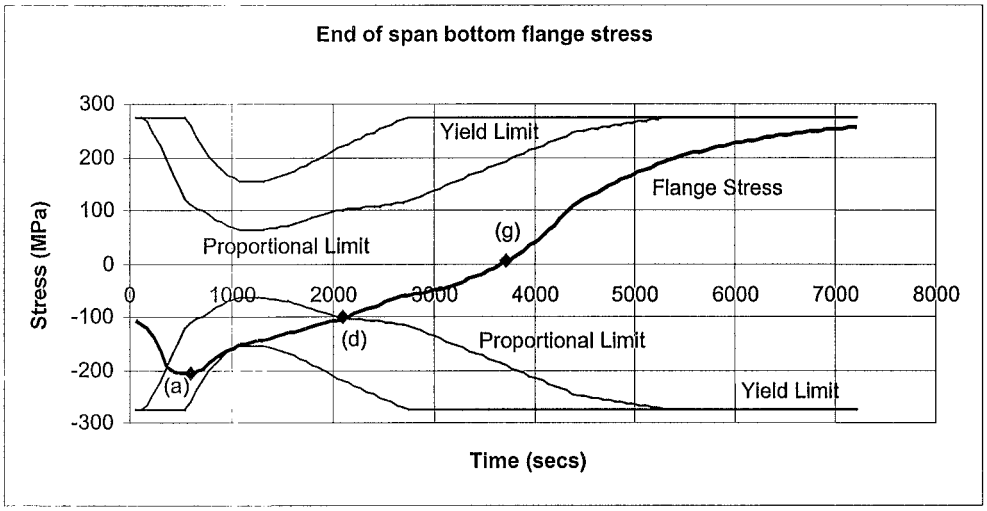

(c) Bottom flange stress.

Figure 8.6.2 End of span results for Fixed - Slide supports in ISO 834 fire with cooling phase.

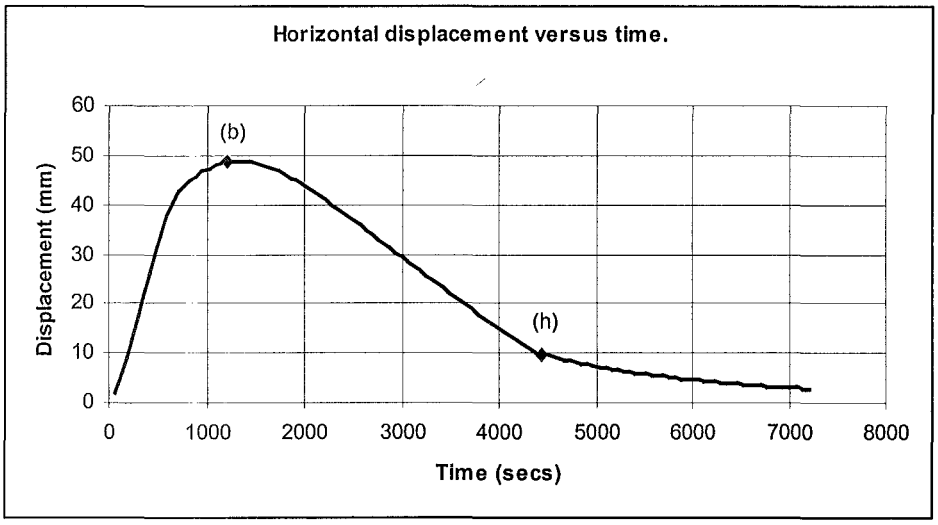

Figure 8.6.3 Slide horizontal displacement in ISO 834 fire with cooling.

Figure 8.6.4 shows the bending moment diagrams of the beam versus time. Initially the mid span bending moment behaviour follows the thermally enhanced negative end of span bending moment up to 1200 seconds. At 1200 seconds plastic hinges form at the ends of the span and the bending moment decreases with the loss in section capacity. The mid span negative moment decreases and then goes into positive bending at 1560 seconds. The end of span negative bending moment decreases until 3120 seconds where it goes into positive bending as well. Both the mid span and end of span positive moment increase at the same rate until the end of the simulation.

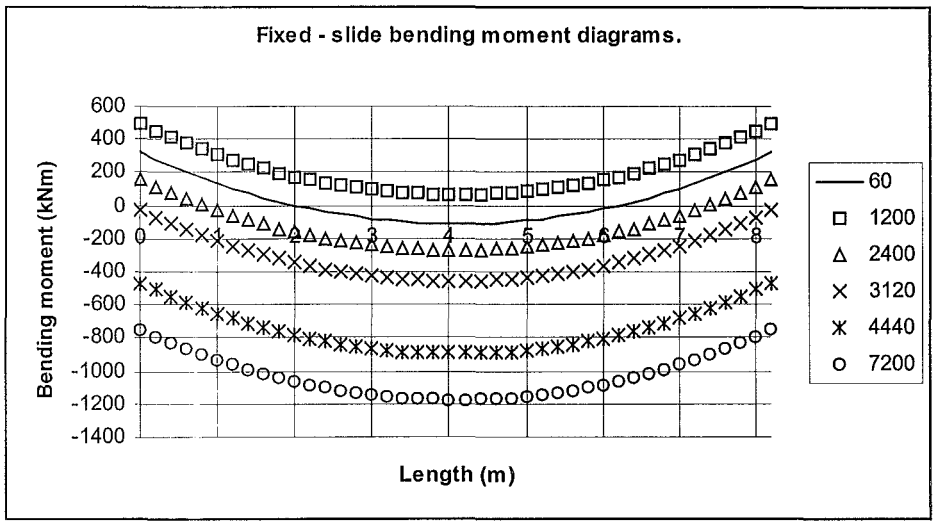

Figure 8.6.4 Fixed - slide bending moment diagrams in ISO 834 fire with cooling.

Summary.

During the initial stage of the cooling phase of the fire, the section temperatures increase and the mid span displacement continues to increase due to plastic hinging at the ends of the span, and a loss in stiffness in the section. As the bottom flange begins to cool and regain stiffness there is a recovery in the displacements. Thermal bowing in the opposite direction to that of the growth phase of the fire enhances the displacement recovery.

Initially the thermally enhanced negative end of span moments increase causing the mid span moments to turn negative as well. The end of span and mid span negative moments then decrease due to the plastic hinging at the ends of the span. The negative moment decrease continues and the beam goes into positive bending along the entire length of the beam. The increase in positive bending moment leads to an increase in tension stress in the bottom flange at both the ends of the span as well as the centre of the span. The top flanges show compressive stresses. The increase of these stresses is uniform with that of the bending moments. The mid span top flange stress reaches the thermally reduced EC3 Proportional Limit stress for a short period, upon cooling, and the concrete slab taking the compression stresses, reduces below the proportional limit. The mid span top flange stress then continues to decrease.

Once the section cools sufficiently and the cooling phase thermal bowing effects decrease, the slab exhibits compression stresses. This enhances the stiffness of the section, and the rate of displacement recovery increases until the end of span top flange stress reaches the EC3 Proportional Limit stress in compression, and follows it until the end of the simulation. Once yielding occurs, the rate of displacement recovery decreases, as well as the rates of stress increase in the slab, top flange and bottom flange at the mid span, as well as the ends of the span. This behaviour is observed until the end of the simulation at 7200 seconds, where the end of span top flange stress and bottom flange stress as well as the mid span bottom flange stress approach the yield limit. There was a permanent deformation of 15mm.

8.7 Conclusion.

The investigation into the temperature characteristics of the section show that even after the growth phase of the fire has ended all the components of the section increase in temperature for at least another 600 seconds. The bottom flange of the section reaches the highest temperatures and is more severely affected, while the top flange temperature is lower but cools more slowly. The top flange temperature becomes uniform with the slab temperature and because of the concretes thermal properties, stays at elevated temperatures a lot longer. The temperature differentials in the section cause thermal bowing opposite to the direction of the thermal bowing experienced in the growth phase of the fire. This thermal bowing enhances displacement recovery.

The results for the axially restrained support cases (*pin – pin* case and the *fixed - fixed* case) show that there is no beneficial effect in ending the growth phase just prior to reaching the failure mechanism. The temperatures in all components of the composite section are still increasing and while there will be a slight increase in the time to failure of the section, due to slightly cooler temperatures, the failure mechanism has already been achieved. As was found in Section 7 *ISO 834 STANDARD FIRE* the stresses, due to both axial restraint and bending, cause rapid and unpreventable failure even if the growth phase of the fire is relatively short. Not included in the results of this section was an investigation into growth rate times required for beams with axially restraining support conditions to survive an ISO 834 fire with a cooling phase. The longest ISO 834 fire growth rate the *pin – pin* and *fixed – fixed* support cases could resist was 380 seconds. This highlights the fact that under rapidly growing fires axial restraint is bad for the fire resistance of a composite beam in two dimensional analysis.

The results for the *pin – roller* support condition show that during the cooling phase of the fire some of the displacements are recovered due to thermal bowing, as well as the section cooling and increasing in stiffness. The steel reaching the proportional limit is also a catalyst for yielding, causing decreasing compressive stresses in the top flange, while the concrete slab takes up the required compression stresses. As the section cools and the steel stress decreases below the EC3 Proportional Limit stress, thermal bowing causes the stresses in the top and bottom flanges to change signs. The top flange goes into tension, while the bottom flange goes into compression. The concrete slab continues to increase in compression. The concrete compressive stress is governed by bending, while steel stresses are governed by thermal bowing. As the section cools, and the effects

of the thermal bowing decrease, the rate at which displacement recovery takes place decreases. This affects the top flange stress, the bottom flange stress and the concrete slab stress, up to the end of the simulation At the end of the simulation there was a permanent deformation of 62 mm.

The results for the *fixed – slide* case show that, as the bottom flange begins to cool and regain stiffness, there is a recovery in the displacements. Once again the cooling phase thermal bowing enhances the displacement recovery. Plastic hinging at the ends of the span leads to a decrease in the end of span and mid span moments. The moments then turn positive and increase, increasing the stresses in the concrete slab and the 610 UB 101. The mid span top flange stress reaches the EC3 Proportional Limit stress for a short period until it cools sufficiently to drop below the proportional limit, and then decreases slightly. This has little effect on the rest of the section. Once the section cools sufficiently, the thermal bowing effects decrease and the slab exhibits an increase in compression stresses. With this, there is an increase in section stiffness, and the rate of displacement recovery increases. Due to bending stresses, the end of span top flange stress reaches the EC3 Proportional Limit stress in compression and follows it until the end of the simulation. Once yielding occurs, the displacement recovery, as well as the slab, top flange and bottom flange stresses are affected at the mid span and the ends of the span. There is a reduction in both the stresses as well as the displacement recovery. This behaviour is observed until the end of the simulation. There was a permanent deformation of 15mm.

The support cases with no axial restraint provide better fire resistance to the beam in an ISO 834 fire growth with cooling phase. Thermal bowing, caused by temperature differentials as well as an increased stiffness during the cooling phase, assist in the displacement recovery. Thermal strains in the concrete cause the concrete slab to exhibit no or little stresses until sufficient cooling occurs in the slab. Once sufficient cooling has occurred, the slab stress is dominated by bending stresses, while the steel stress is dominated by thermal bowing. The thermally reduced EC3 Proportional Limit stress acts as a catalyst to beam behaviour causing yielding and redistribution of moment. The moment resisting connection endures less permanent deformation due to three plastic hinges requiring to be formed, where as the simply supported case shows greater permanent deformation as it begins to form its only plastic hinge early on in the ISO 834 fire.

9 PROBLEMS

In the SAFIR analysis carried out in this report several problems occurred that should be made apparent to any person wanting to replicate these simulations. It has to be noted that SAFIR is a finite element model, which in itself has inherent problems. Of most importance is the selection of the correct model and approach in describing the model. The higher the degree of accuracy in the model the higher the precision of the results but this comes at a computational cost.

The greatest problem associated with this program is in the reduction of element stresses. At present the SAFIR post-processor DIAMOND 2001, Franssen et al (2000), will reduce axial force, displacement and bending moment data from the structural analysis. When reducing stresses this user recommends that the *Structural.out* file be input into *Microsoft Excel* using the fixed width delimitation option. In this manner element numbers may be separated into separate columns from the stresses. If the first two columns in the *worksheet* are left clear then "*IF – THEN – ELSE*" logic statements may be used to select the required stresses at each time step. Between the required stresses *FALSE* statements help in with data manipulation. In the other free column an "*IF – THEN – ELSE*" statement may be used to insert the time step value at each selected stress. By copying the first two columns (of which this user found may contain up to 60,000 lines of data for some analysis) and then inserting them into a new *worksheet* using the *Paste Special – Values* options the data may be manipulated using the *Data Sort* option. This procedure may only be used for a single element stress or summation of element stresses ie top or bottom average flange stresses.

In the Axial Spring analysis the simulations finished prior to the expected result, (due to a negative stiffness matrix), as was demonstrated by the boundary condition results. It is assumed that this was caused by a numerical error associated with the extra spring terms in the stiffness matrix compounding with each time step to form an instability. The instability seemed to occur for the simulations where the top and bottom flanges of the steel section reach the proportional limit at approximately the same time step. To rectify this problem it is suggested that the boundary conditions be investigated. This problem also changes with thermal exposure therefore simulations may be run at various fire growth rates to see if the required results can be approximated.

10 CONCLUSIONS

10.1 Introduction

This report was conducted to investigate the behaviour of composite steel – concrete beams in fire using a two dimensional thermal and structural finite element program, SAFIR. The 610 UB 101 steel beam with a 120mm thick composite concrete slab was analysed with four support conditions in three linear rates of heating as well as the ISO 834 standard fire and ISO 834 standard fire with cooling phase. The composite beam was also tested using axial springs and the three linear heating rates to find the beam behaviour between the *pin – pin* and *pin – roller* support cases.

In order that finite element models be used to reliably design structures to withstand elevated temperatures, analytical models must be able to accurately predict behaviour observed in real fire events. For this reason the second objective of this report was to compare the observed behaviour obtained from the SAFIR modelling with the behaviour observed in the Broadgate Phase 8, Churchill Plaza and BRE Cardington test facility fire events.

10.2 General Conclusions

All four support conditions showed their expected failure mechanisms under gravity load and elevated temperatures. The moment resisting end supports failed with three plastic hinges while the simply supported cases failed with one plastic hinge at the centre of the span.

The fire resistance for the four support cases varied. In the linear rate cases the *pin – pin* support case has the best fire resistance. The fixed slide case had the second best fire resistance while the *pin - roller* had the third best fire resistance. The *fixed – fixed* support case had the least fire resistance. These results are counter intuitive to structural behaviour at ambient temperatures, as it would be expected that the *fixed – fixed* support case would have more redundancy in forming the three plastic hinges. This trend in results was followed for all three linear heating rates and as the heating rate increased the fire resistance decreased. As the heating rate increases the fire resistance times for the four support conditions converge and may converge to a point where fire resistance is independent of end support conditions.

In the ISO 834 fire scenario the composite section fire resistance was not as good as for the linear heating rate cases. This was expected due to the greater rate of fire growth in the ISO 834 fire. The behaviour in the standard fire tests were very similar to those in the linear heating rate test for most support cases except that the fire temperature at which the behaviour occurred was a lot higher for the standard fire. This was due to a thermal lag in the average temperature of the section due to the conductivity of the material.

In the ISO fire with a cooling phase, the investigation into the temperature characteristics of the section show that even after the growth phase of the fire has ended all the components of the section increase in temperature for at least another 600 seconds. The temperature differentials in the section cause thermal bowing in the cooling phase opposite to the direction of the thermal bowing experienced in the growth phase of the fire. The cooling phase thermal bowing enhances displacement recovery.

10.3 Influence of EC3 Proportional and Yield Limit Stress

In all four support cases, for all fire growth models, when the steel stress reaches the EC3 Proportional Limit stress and the EC3 Yield Limit stress the behaviour in the displacements and axial forces change. In the axially restrained cases this causes changes in the bending moment due to P-δ effects as well as moment redistribution. The relationship is that once the EC3 Proportional Limit or Yield Limit stress is achieved, yielding causes displacements and increased moments which in turn causes more yielding.

10.4 Pin – Pin End Supports

In the linear heating rate cases the *pin – pin* supports had the best fire resistance even though there is axial restraint causing thermal bowing and high initial deflection. This means that even though the stresses are high at the mid span, because of the positive moments, the concrete slab is able to contribute to the moment capacity of the section. The bottom flange of the 610 UB 101 yields due to the thermal degradation in steel strength but there is sufficient redistribution of stress to allow the beam to survive a significantly longer period.

In the ISO 834 fire the severity of the fire causes high axial load and rapid degradation of material properties which leads to the *pin – pin* support case having the least fire resistance. Parts of the web reach the EC3 proportional limit followed closely by the top flange. The web yielding causes the composite section to fail with a much smaller displacement than was found for the linear heating rate cases.

The effect of ending the growth phase of the ISO 834 fire after 600 seconds makes no difference to the time taken to reach the failure mechanism.

Near failure, the *pin – pin* support case shows catenary action where the steel beam takes some of the load in tension where the flexural capacity of the beam has been lost. This is believed to occur in real fire events especially in conjunction with the tensile membrane action of the concrete slab.

10.5 Pin – Roller End Supports

In the *pin – roller* case failure is obtained when the bottom flange reaches the proportional limit in tension and the plastic hinge forms as the bottom flange approaches yield. The top flange takes the tensile stress and a runaway failure occurs due to the roller not being able to restrain the tensile forces caused by the mid span displacements. This failure mechanism occurred for both the ISO 834 fire as well as the linear heating rate cases.

In the ISO 834 fire with cooling phase case the effect of ending the growth phase at 600 seconds causes some of the displacements to be recovered due to thermal bowing and increasing material stiffness. As the section cools and the steel stress decreases below the proportional limit, thermal bowing causes the stresses in the top and bottom flanges to change signs. The concrete compressive stress is governed by bending while steel stresses are governed by thermal bowing. As the effects of the thermal bowing decrease, the rates at which displacement recovery take place decrease.

10.6 Fixed – Fixed End Supports

The *fixed – fixed* support case fails due to the thermally induced compression forces and negative bending moments causing large stresses in the flanges at the ends of the beam. In the linear heating rate cases the bottom flanges of the 610 UB 101 at the ends of the span are unable to maintain the stress even prior to the thermal degradation in strength of the steel. The top flanges soon follow causing the first two hinges of the failure mechanism. In the ISO 834 fire the top flange yields quickly followed by the bottom flange. This behaviour is consistent with the behaviour observed at the Cardington Test Facility where local buckling occurred in the bottom flange near the supports. Local buckling was not modelled in this report, as shell element modelling is required for this analysis.

The third plastic hinge is formed at the mid span of the beam due to increased deflection caused by the end of span plastic hinges.

The effect of ending the growth phase of the ISO 834 fire after 600 seconds makes no difference to the time taken to reach the failure mechanism.

10.7 Fixed – Slide End Supports

In the *fixed - slide* case the formation of three plastic hinges with no axial restraint allows for greater fire resistance. Thermal bowing and elongation cause hogging moments over the whole length of the beam. The concrete cracks at the ends of the span almost immediately and the top flange stress reaches the EC3 Proportional Limit in tension because of the hogging moment. The bottom flange then reaches the proportional limit in compression. This behaviour is identical (but in a different time frame) for both the linear heating rates as well as the ISO 834 fire. The formation of the two plastic hinges at the ends of the span lead to the displacements and yielding at the mid span. Collapse is due to a plastic hinge forming at the mid span causing a runaway failure.

In the ISO 834 fire with cooling phase the *fixed – slide* case shows that as the bottom flange begins to cool and regain stiffness there is a recovery in the displacements. Cooling phase thermal bowing enhances the displacement recovery. Due to the redundancy of the *fixed – slide* case the permanent deformation is not as high compared to the *pin – pin* support case. Once the section cools

sufficiently the thermal bowing effects decrease and the slab exhibits an increase in compression stresses. With this there is an increase in section stiffness and the rate of displacement recovery increases. Yielding during the cooling phase causes the rate displacement recovery to decrease.

10.8 Axial Springs

The failure mechanism for the composite section with a non-yielding axial spring under uniform heating with a linear heating rate is a plastic hinge forming at the centre of the beam. The spring stiffness ranges between 0% stiffness for the *pin - roller* case and approaches infinity with the *pin – pin* support case. The fire resistance of the composite section with an axial spring increases over that of the *pin - roller* case. The fire resistance for the varying spring stiffnesses is relatively similar, including the *pin – pin* support case, and is independent of spring stiffness.

The behaviour observed in the axial spring cases was similar to that of the *pin – pin* support case. As axial spring stiffness increases the axial forces increase and the displacements are more pronounced leading to an increase of bending moment due to P-δ effects. The bottom flange of the 610 UB 101 yields and the top flange goes into tension under simple bending. Once the top flange yields the concrete slab is unable to sustain the gravity load under flexure.

When the bottom flange reaches the thermally reduced EC3 Yield Limit and the bending moment decreases, the moments for the varying springs coincide suggesting that the decrease in axial force is directly proportional to the increase in displacement, independent of spring stiffness.

As the heating rate increases the fire resistance converges, independent of the spring stiffness. For rapid fire growth the axial spring stiffness is irrelevant for simple beam bending.

Numerical error in the finite element modelling caused the simulations of a set of axial spring cases to be a lot shorter than expected. The numerical error seems to occur when the top flange of the 610 UB 101 reaches the EC3 Proportional Limit stress prior to the bottom flange. When the bottom flange reaches the EC3 Proportional Limit stress first good results are obtained. In the *pin – pin* support case the top flange reaches the thermally reduced EC3 Proportional Limit first

but has a time to failure and behaviour similar to that of the cases where the bottom flange yields first.

10.9 Axial Restraint

For the two non-axially restrained cases the low stresses in the flanges means better fire resistance. The *fixed - slide* supports have better fire resistance because of the redundancy required in forming the three plastic hinges. The negative end moments cause high stress and failure in the *fixed - slide* case where as large displacement causes failure in the *pin – roller* case.

When axial restraint is introduced into the supports high axial loads cause compressive stresses in the steel section but this is dependent on the heating rate. For the linear heating rate cases, axial restraint causes thermal bowing in the *pin – pin* support case leading to prolonged fire resistance. In the ISO 834 fire scenario due to the thermal exposure the axial restraint causes web yielding and rapid failure for this support case.

In the ISO 834 fire with a cooling phase there was no effect in ending the growth phase at 600 seconds for the axially restrained cases as the failure mechanism has already been achieved. The support cases with no axial restraint provide better fire resistance to the beam during the fire growth rate and cooling phase. Thermal bowing caused by temperature differentials as well as an increased stiffness during the cooling phase assist in the displacement recovery.

10.10 Moment Resisting Connections

With moment resisting supports the concrete at the ends of the spans has a very short fire resistance because of the enhancement of negative moments from thermal bowing. The mid span concrete may also suffer cracking from thermal bowing leaving the slab virtually useless to carry load, especially in the fixed - slide case.

In conjunction with axial force, moment resisting connections cause very high compressive stresses in the steel section. This behaviour is consistent with the behaviour observed at the Cardington Test Facility where local buckling occurred in the bottom flange near the supports.

10.11 Future Research

It is recommended that future research should include:

- A study into the effects of changing the support height
- Analysis of partial moment resisting connections to simulate beam-column joint connections
- Analysis of axial restraint on moment resisting connections – between the *fixed- fixed* and *fixed – slide* case
- The effects of unsymmetrical and partial loading
- The effect of continuity of the composite section where 3 spans should be investigated with thermal exposure to the centre span, an end span and a centre and end span combination
- 2-D frame analysis for a single storey of the building
- 3-D shell and beam element analysis including the effects of tensile membrane action and frame redundancy.
- Experimental verification of analytical results

11 REFERENCES

Bailey C et al, 1999, *The Behaviour of Multi-Story Steel Framed Buildings in Fire*, British Steel plc, Swinden Technology Centre, Moorgate, United Kingdom.

Buchanan A.H., 2001, *Structural Design for Fire Safety*, University of Canterbury, Christchurch, New Zealand.

CIB, 1986. Design Guide – Structural Fire Safety, CIB-W14. Fire Safety Journal. Vol. 10, No. 2, pp 75-138.

EC1, 1994. Eurocode 1: Basis of Design and Design Actions on Structures. Part 2-2: Actions on Structures Exposed to Fire. ENV 1991-2-2: European Committee for Standardisation, Brussels.

EC2, 1993. Eurocode 2: Design of Concrete Structures. ENV 1992-1-2: General Rules – Structural Fire Design. European Committee for Standardisation, Brussels.

EC3, 1995. Eurocode 3: Design of Steel Structures. ENV 1993-1-2: General Rules – Structural Fire Design. European Committee for Standardisation, Brussels.

EC4, 1994. Eurocode 4: Design of Composite Steel and Concrete Structures. ENV 1993-1-2: General Rules – Structural Fire Design. European Committee for Standardisation, Brussels.

El-Rimawi, J.A. Burgess, I.W. and Plank, R.J. 1996. The Treatment of Strain Reversal in Structural Members During the Cooling Phase of a Fire. Journal of Constructional Steel Research. Vol 37, No 2, pp 115-135.

Franssen J.M, Kodur V.K.R, Mason J, 2000. Users Manual for SAFIR2001 – A computer Program for Analysis of Structures Submitted to the Fire. University of Liege, Belgium.

Frannsen J.M. 1990. The Unloading of Building Materials Submitted to Fire. Fire Safety Journal, Vol 16, pp 213–227.

Gamble, W.L. 1989. Predicting Protected Steel Member Fire Endurance Using Spreadsheet Programs. Fire Technology. Vol 25, No. 3, pp256-273.

ISO, 1975. Fire Resistance Tests – Elements of Building Construction. ISO 834 – 1975. International Organisation for Standardisation.

Lawson, R.M. 1990. Behaviour of Steel Beam–to-Column Connections in Fire. The Structural Engineer, Vol 68, No14/17, pp 263-271.

Mason, J.E. 2000. Heat Transfer Programs for the Design of Structures Exposed to Fire. Fire Engineering Research Report 00/9. University of Canterbury, Christchurch, New Zealand.

Milke, J.A. and Hill, S. 1996. Initial Development of Draft Performance Based Fire Protection Standard on Construction. Unpublished report. Department of Fire Protection Engineering. Second Edition. Society of Fire Protection Engineers, USA.

NZS 3404:1992 Steel Structures Standard, Parts 1 & 2, Standards New Zealand, Wellington.

NZS 4203:1992 Code of practice for General Structural Design and Design Loadings for Buildings, Standards New Zealand, Wellington.

Pettersson, O. 1973. The connection between a Real Fire Exposure and the Heating Conditions according to Standard Fire Resistance Tests – with Special Application to Steel Structures. Document CECM 3-73/73. European Commission for Constructional Steelwork.

Rotter, J.M., Sanad, A.M., Usmani, A.S., and Gillie, M. 1999, Structural Performance of Redundant Structures Under Local Fires, Proceedings Interflam'99 Conference, Edinburgh, U.K. pp 1069 – 1080.

Schneider, U. 1988. Concrete at High Temperatures – A General Review. Fire Safety Journal, Vol 13, pp 55-68.

SCI, 1990.Fire Restraint Design of Steel Structures – A Handbook to BS 5950:Part 8., The steel Construction Institute, Publication 080,

Stevenson, P.L. 1993. Computer Modelling of Structural Steel Frames in Fire. Fire Engineering Research Report. University of Canterbury, Christchurch, New Zealand.

APPENDIX

APPENDIX A

Eurocode (EC3 1995 and EC2: 1993) Stress – Strain Relationships at Elevated Temperatures

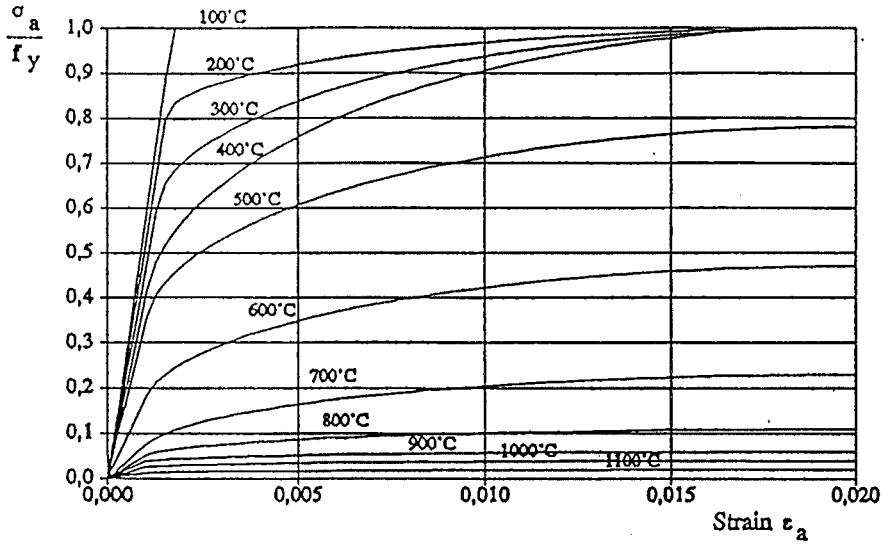

Figure A.1 EC3 Variation of stress-strain relationship with temperature for grade S 355 steel (strain hardening not included).

Table A.1 EC3 Reduction factors for stress-strain relationship of steel at elevated temperatures.

Steel temperature θ_a	Reduction factors at temperature θ_a relative to the value of f_y or E_a at 20°C		
	Reduction factor for effective yield strength	Reduction factor for proportional limit	Reduction factor for the elastic modulus.
20°C	1.000	1.000	1.000
100°C	1.000	1.000	1.000
200°C	1.000	0.807	0.900
300°C	1.000	0.613	0.800
400°C	1.000	0.420	0.700
500°C	0.780	0.360	0.600
600°C	0.470	0.180	0.310
700°C	0.230	0.075	0.130
800°C	0.110	0.050	0.090
900°C	0.060	0.0375	0.0675
1000°C	0.040	0.0250	0.0450
1100°C	0.020	0.0125	0.0225
1200°C	0.000	0.0000	0.0000

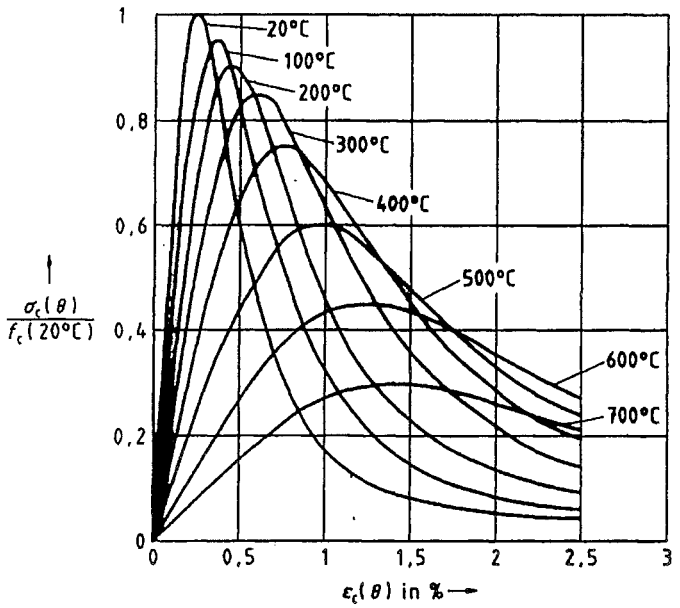

Figure A.2 EC2 Stress-strain relationships of siliceous concrete under uniaxial compression at elevated temperatures.

Table A.2 EC2 Reduction factors for stress-strain relationship of siliceous concrete at elevated temperatures.

Steel temperature θ_a	Reduction factor for compressive strength	$\varepsilon_c1(\theta) \times 10^{-3}$
20°C	1.000	1.000
100°C	0.950	0.960
200°C	0.900	0.920
300°C	0.850	0.810
400°C	0.750	0.630
500°C	0.600	0.440
600°C	0.450	0.260
700°C	0.300	0.080
800°C	0.150	0.060
900°C	0.080	0.050
1000°C	0.040	0.030
1100°C	0.010	0.020
1200°C	0.000	0.000

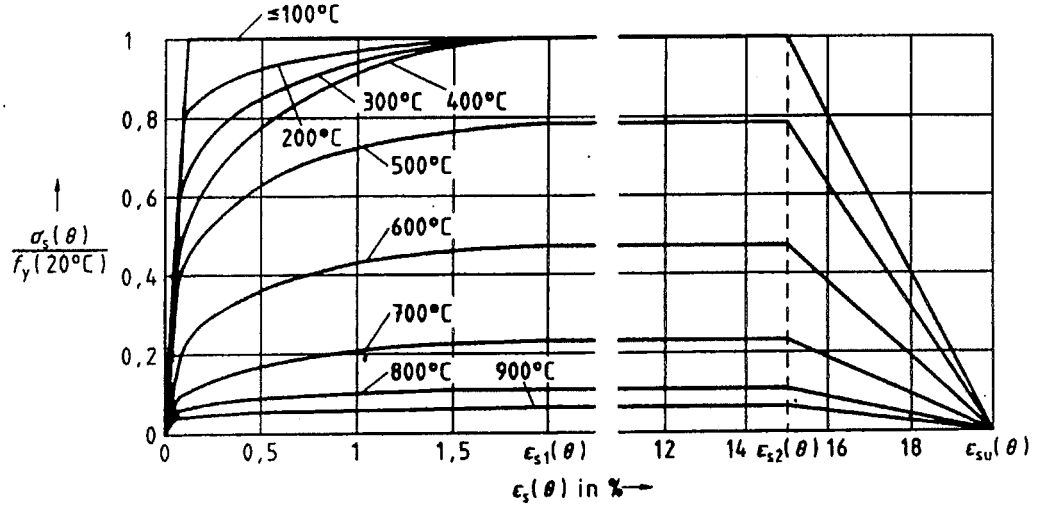

Figure A.3 EC2 Variation of stress-strain relationship with temperature of hot rolled reinforcing steels at elevated temperatures.

Table A.3 EC2 Reduction factors for stress-strain relationship of hot roller reinforcing steel at elevated temperatures.

Steel temperature θ_a	Reduction factors at temperature θ_a relative to the value of f_y or E_a at 20°C		
	Reduction factor for effective yield strength	Reduction factor for proportional limit	Reduction factor for the elastic modulus.
20°C	1.000	1.000	1.000
100°C	1.000	0.960	1.000
200°C	1.000	0.920	0.870
300°C	1.000	0.810	0.720
400°C	0.940	0.630	0.560
500°C	0.670	0.440	0.400
600°C	0.400	0.260	0.240
700°C	0.120	0.080	0.080
800°C	0.110	0.060	0.060
900°C	0.080	0.050	0.050
1000°C	0.050	0.030	0.030
1100°C	0.030	0.020	0.020
1200°C	0.000	0.000	0.000

APPENDIX B

Spreadsheet Method for Calculating the Average Steel Temperature.

The average steel section temperature can be calculated at individual time steps using the spreadsheet method illustrated in Table D1, laid out in Buchanan 2001 (from Milke and Hill, 1996, based on Gamble, 1989). The Eurocode (EC3: 1995) suggests that a time step of no more than 30 seconds and that a minimum value for the section factor F/V of $10m^{-1}$ be used for this method.

Spreadsheet calculation for heat transfer in unprotected steel members.

Time	**Steel temperature T_s**	**FIRE TEMPERATURE T_F**	**Difference in temperature**	**Heat Transfer coefficient**	**Change in steel temperature.**
$T_1 = \Delta t$	Initial steel temperature T_{so}	Fire temperature half way through time step (at $\Delta t/2$)	$T_f - T_{so}$	Use equation [D2] with values of T_f and T_{so} from this row.	Calculate from equation [D1]
$t_2 = t_1 + \Delta t$	T_s from previous time step + ΔT_s from previous row.	Fire temperature half way through time step (at $t_1 + \Delta t/2$)	$T_f - T_s$	Use equation [D2] with values of T_f and T_{so} from this row.	Calculate from equation [D1]
Etc.					

Equations.

$$\Delta T_s = (F/V)\,(h_t/\rho_s c_s)\,(T_f - T_s)\,\Delta t \qquad \text{[Equation D1]}$$

Where ΔT_s is the change in steel temperature in the time step (°C or K)

h_t is the total heat transfer coefficient (W/m^2 K)

P_s is the density of steel (kg/m3)

c_s is the specific heat of steel (J/kg K)

T_f is the temperature in the fire environment (oC or K)

T_s is the temperature of steel (°C or K).

Δ_t is the time interval (s).

The total heat transfer coefficient ht is the sum of the radiative and convective heat transfer coefficients.

$$h_t = h_c + h_r \qquad \text{[Equation D2]}$$

Where h_c is the convective heat transfer coefficient (W/m^2 K)

h_r is the convective heat transfer coefficient (W/m^2 K)

The Eurocode (EC1 1994) recommends a value of 25 W/m^2 K for the convective heat transfer coefficient for the ISO 834 standard fire. For this step by step method the radiative heat transfer coefficient is defined as

$$h_r = \sigma\varepsilon(T_f^4 - T_s^4) / (T_f - T_s) \qquad \text{[Equation D3]}$$

Where σ is the Stefan Boltzmann constant (5.67×10^{-8} W/m^2K^4)

ε is the emissivity

The Eurocode (EC1 1994) recommends that a value of resultant emissivity of 0.56 be used. For the specific heat of the steel a value of 600 J/kgK can be used for simple calculations. For more precise calculations another column inserted into the spreadsheet method containing the formulas listed in Section 2.3.3 Specific Heat c_s.

FIRE ENGINEERING RESEARCH REPORTS

95/1	Full Residential Scale Backdraft	I B Bolliger
95/2	A Study of Full Scale Room Fire Experiments	P A Enright
95/3	Design of Load-bearing Light Steel Frame Walls for Fire Resistance	J T Gerlich
95/4	Full Scale Limited Ventilation Fire Experiments	D J Millar
95/5	An Analysis of Domestic Sprinkler Systems for Use in New Zealand	F Rahmanian
96/1	The Influence of Non-Uniform Electric Fields on Combustion Processes	M A Belsham
96/2	Mixing in Fire Induced Doorway Flows	J M Clements
96/3	Fire Design of Single Storey Industrial Buildings	B W Cosgrove
96/4	Modelling Smoke Flow Using Computational Fluid Dynamics	T N Kardos
96/5	Under-Ventilated Compartment Fires - A Precursor to Smoke Explosions	A R Parkes
96/6	An Investigation of the Effects of Sprinklers on Compartment Fires	M W Radford
97/1	Sprinkler Trade Off Clauses in the Approved Documents	G J Barnes
97/2	Risk Ranking of Buildings for Life Safety	J W Boyes
97/3	Improving the Waking Effectiveness of Fire Alarms in Residential Areas	T Grace
97/4	Study of Evacuation Movement through Different Building Components	P Holmberg
97/5	Domestic Fire Hazard in New Zealand	KDJ Irwin
97/6	An Appraisal of Existing Room-Corner Fire Models	D C Robertson
97/7	Fire Resistance of Light Timber Framed Walls and Floors	G C Thomas
97/8	Uncertainty Analysis of Zone Fire Models	A M Walker
97/9	New Zealand Building Regulations Five Years Later	T M Pastore
98/1	The Impact of Post-Earthquake Fire on the Built Urban Environment	R Botting
98/2	Full Scale Testing of Fire Suppression Agents on Unshielded Fires	M J Dunn
98/3	Full Scale Testing of Fire Suppression Agents on Shielded Fires	N Gravestock
98/4	Predicting Ignition Time Under Transient Heat Flux Using Results from Constant Flux Experiments	A Henderson
98/5	Comparison Studies of Zone and CFD Fire Simulations	A Lovatt
98/6	Bench Scale Testing of Light Timber Frame Walls	P Olsson
98/7	Exploratory Salt Water Experiments of Balcony Spill Plume Using Laser Induced Fluorescence Technique	E Y Yii
99/1	Fire Safety and Security in Schools	R A Carter

99/2	A Review of the Building Separation Requirements of the New Zealand Building Code Acceptable Solutions	J M Clarke
99/3	Effect of Safety Factors in Timed Human Egress Simulations	K M Crawford
99/4	Fire Response of HVAC Systems in Multistorey Buildings: An Examination of the NZBC Acceptable Solutions	M Dixon
99/5	The Effectiveness of the Domestic Smoke Alarm Signal	C Duncan
99/6	Post-flashover Design Fires	R Feasey
99/7	An Analysis of Furniture Heat Release Rates by the Nordtest	J Firestone
99/8	Design for Escape from Fire	I J Garrett
99/9	Class A Foam Water Sprinkler Systems	D B Hipkins
99/10	Review of the New Zealand Standard for Concrete Structures (NZS 3101) for High Strength and Lightweight Concrete Exposed to Fire	M J Inwood
99/12	An Analytical Model for Vertical Flame Spread on Solids: An Initial Investigation	G A North
99/13	Should Bedroom Doors be Open or Closed While People are Sleeping? - A Probabilistic Risk Assessment	D L Palmer
99/14	Peoples Awareness of Fire	S J Rusbridge
99/15	Smoke Explosions	B J Sutherland
99/16	Reliability of Structural Fire Design	JKS Wong
99/17	Heat Release from New Zealand Upholstered Furniture	T Enright
00/1	Fire Spread on Exterior Walls	FNP Bong
00/2	Fire Resistance of Lightweight Framed Construction	PCR Collier
00/3	Fire Fighting Water: A Review of Fire Fighting Water Requirements (A New Zealand Perspective)	S Davis
00/4	The Combustion Behaviour of Upholstered Furniture Materials in New Zealand	H Denize
00/5	Full-Scale Compartment Fire Experiments on Upholstered Furniture	N Girgis
00/6	Fire Rated Seismic Joints	M James
00/7	Fire Design of Steel Members	K R Lewis
00/8	Stability of Precast Concrete Tilt Panels in Fire	L Lim
00/9	Heat Transfer Program for the Design of Structures Exposed to Fire	J Mason
00/10	An Analysis of Pre-Flashover Fire Experiments with Field Modelling Comparisons	C Nielsen
00/11	Fire Engineering Design Problems at Building Consent Stage	P Teo
00/12	A Comparison of Data Reduction Techniques for Zone Model Validation	S Weaver
00/13	Effect of Surface Area and Thickness on Fire Loads	H W Yii
00/14	Home Fire Safety Strategies	P Byrne
00/15	Accounting for Sprinkler Effectiveness in Performance Based Design of Steel Buildings in Fire	M Feeney

00/16	**A Guideline for the Fire Design of Shopping Centres**	**J M McMillan**
01/1	**Flamability of Upholstered Furniture Using the Cone Calorimeter**	**A Coles**
01/2	**Radiant Ignition of New Zealand Upholstered Furniture Composites**	**F Chen**
01/3	**Statistical Analysis of Hospitality Industry Fire Experience**	**T Y A Chen**
01/4	**Performance of Gypsum Plasterboard Assemblies Exposed to Real Building Fires**	**B H Jones**
01/5	**Ignition Properties of New Zealand Timber**	**C K Ngu**
01/6	**Effect of Support Conditions on Steel Beams Exposed of Fire**	**J Seputro**
01/7	**Validation of an Evacuation Model Currently Under Development**	**A Teo**
01/8	**2-D Analysis of Composite Steel - Concrete Beams in Fire**	**R Welsh**
01/9	**Contribution of Upholstered Furniture to Residential Fire Fatalities in New Zealand**	**C R Wong**
01/10	**The Fire Safety Design of Apartment Buildings**	**S Wu**

School of Engineering
University of Canterbury
Private Bag 4800, Christchurch, New Zealand

Phone 643 364-2250
Fax 643 364-2758